Mechanisms of the insulator-to-metal transitions in spinel ferrites/ferroelectric perovskite heterostructures

Kedar Sharma

THÈSE

En vue de l'obtention du

DOCTORAT DE L'UNIVERSITÉ DE TOULOUSE

Délivré par : *l'Université Toulouse 3 Paul Sabatier (UT3 Paul Sabatier)*

Thesis defense date *12/12/2023*

Kedar SHARMA

Mechanisms of the insulator-to-metal transitions in spinel ferrites/ ferroelectric perovskite heterostructures

JURY

Corinne LACAZE-DUFAURE	Professeure des universités	Présidente
Antoine BARBIER	Directeur de recherche	Membre du Jury
Grégory GENESTE	Directeur de recherche	Membre du Jury
Jacek GONIAKOWSKI	Directeur de recherche	Membre du Jury
Rossitza PENTCHEVA	Professeure des universités	Membre du Jury

École doctorale et spécialité :
EDSDM : Ecole Doctorale Sciences de la Matiere
Unité de Recherche :
Centre d'Élaboration de Matériaux et d'Etudes Structurales (CEMES)
Directeur(s) de Thèse :
Rémi ARRAS et *Lionel CALMELS*
Rapporteurs :
Grégory GENESTE et *Jacek GONIAKOWSKI*

Acknowledgement

I would like to express my deepest gratitude to all those who have contributed to the completion of this Ph.D. thesis.

First and foremost, my sincere thanks go to my parents and family members for their unwavering support and understanding throughout this challenging journey. Their love, patience, and encouragement have been my pillars of strength.

I extend my thanks to my thesis advisors, Rémi Arras (CR) and Prof. Lionel Calmels, for their unwavering support, guidance, and encouragement throughout this journey. I am also immensely grateful to the members of my dissertation committee, Prof. Corinne LACAZE-DUFAURE, Grégory GENESTE (DR), Jacek GONIAKOWSKI (DR), Prof. Rossitza PENTCHEVA and Antoine BARBIER (DR) for their constructive feedback, valuable suggestions, and insightful discussions.

I am grateful to the Université Toulouse III - Paul Sabatier for providing a conducive academic environment and resources such as the CALMIP supercomputer, which facilitated my research. I would like to thank the ANR for financing my thesis in the framework of the MULTINANO project.

I am indebted to my experimental collaborators, especially Antoine BARBIER and Haowen LIN with whom I had fruitful discussions about the MULTINANO project. Thanks to the experimental collaborator Helene MAGNAN who was happy to guide me with the experimental work during my visit in their lab. Thanks to the colleagues and fellow researchers who have shared their knowledge and experiences, creating a stimulating intellectual community. Special thanks to my colleagues and friends in the CEMES lab, Dongzhe, Quentin, Sabyasachi, Umamahesh, Akshay, Elio, Romain, Eloïse, Estefania, Sruthi, Megha, Leifeng, Sebastian, Robin, Cecile, Simon, Paul, Anaïs, Kilian, Marine, Martin, Clement, Sara, Liz, Pierre, Shuangying, Youness, Carlos, Jorge, Chiranjit, Astrid, Atzin, and Elodie for the discussions and support.

Finally, I would like to express my gratitude to all my friends Davy, Abdul, Intan, Nicolas, Edelina, Nick, Carlijn, Vivek, Anne, Heidi, Xaviére, Nathalie, Alessandro, Chloé, Alex, Romain, David, Sandra, Malik, Gloria, Kalyan, Feby, Jose, Anagha, Athira, Vishnu, and Sanjay who have stood by my side and provided support and encouragement when it was needed most. Their friendship has brought immeasurable joy to this academic endeavor.

This thesis would not have been possible without the collective contributions of these individuals and institutions. Thank you for being an integral part of my Ph.D. journey.

This thesis, entitled ***Mechanisms of the insulator-to-metal transitions in spinel ferrites/ferroelectric perovskite heterostructures*** was part of the ANR project *Functional nanocircuits at artificial laminar MULTIferroic interfaces by NANOlithography* [MULTINANO project, led by Dr. Antoine Barbier (SPEC, CEA-Saclay), ANR grant ANR-19-CE09-0036 [1]]. It has been realized at the *Centre d'Elaboration de Matériaux et d'Etudes Structurales* (CEMES, CNRS, UPR8011, Toulouse, France) from November 2020 to October 2023. It was supervised by Dr. Rémi Arras and Prof. Lionel Calmels and was included in the activities of the group *Matériaux et dispositifs pour l'Electronique et le Magnétisme* (MEM) [2]. The numerical calculations have been performed using the ressources provided by the high-performance computing center *CALMIP* [3] (Allocations p1229 and p19004, 2020-2023).

1. ANR MULTINANO
2. https://www.cemes.fr/mem/
3. https://www.calmip.univ-toulouse.fr/

Contents

Chapter 1

State of the Art, Motivation and Objectives

1.1 Evolution of electronics and new societal challenges

1.1.1 The end of the standard electronics

Moore's law is the famous observation and prediction made in 1965 by Gordon Moore, an electronic engineer, stating that the growth of electronic components (transistors) per unit area is almost doubled every two years [1], as shown in Fig. 1.1. This prediction had been confirmed by the continuous improvement of computing power over several decades and the reduction of computing costs due to technological innovations [2, 3] and the set up of this roadmap was of a great help for the whole semiconductor industry [4]. Electronic devices continue to play an important role in the rapid evolution of digital technologies resulting in the world-wide economic growth. They indeed allow to process, transfer, and store information and they now take a dominant part in various applications spread over many strategical domains such as communication, education, defense, or medical care. This interaction between the development of electronic devices and the economic growth is double-way and their demand is therefore increasing day by day. In the 21^{th} century, the disruptive evolution of digital technology with the appearance of the internet of things [5], artificial intelligence, big data and exascale supercomputers, imposes more than ever the development of high-performance electronic components.

Despite the more and more crucial place that electronic devices take in our everyday life, the Moore's law is now reaching its physical limit and it starts to be more difficult to improve the performances of conventional devices based on Complementary-Metal-Oxide-Semiconductor (CMOS) technologies. The main factors to explain this limit are directly linked with the miniaturization, which has decreased the size of current transistors down to three nanometers (nm) in the year 2022 [7]. At this length scale, several detrimental issues appear during transistor operations, such as an increase of the read and write times, of the leakage currents and of the heating due to higher

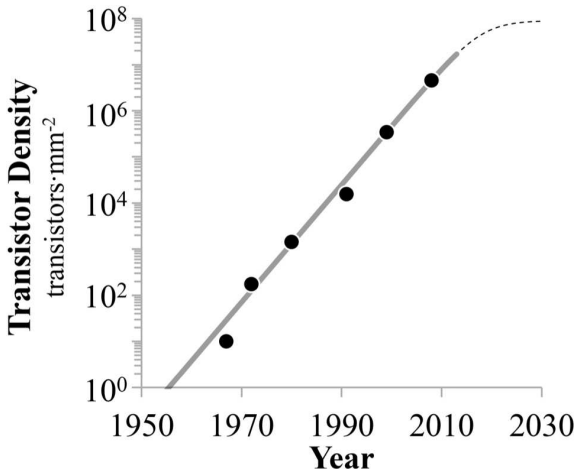

Figure 1.1 – Moore's Law (solid line) and its predicted end (dotted line) around the year 2030 (taken from Ref. [6]).

power density. All these effects result in a decay of the device quality and performances [8–11]. As Moore's law is approaching its limit, there is a need for a change of paradigm and to propose new types of memories or architectures, which will be the start of the more-than-Moore and later the beyond-Moore eras.

1.1.2 Toward more-than-Moore

The predicted growth of the transistor density shown in Fig. 1.1 shows that the trend confirming the Moore's law will start deviating from its linear behavior and will reach a saturation in a few years. To improve the efficiency of current CMOS devices, several possibilities have already been envisioned. The discovery of disruptive technologies necessitates a multiscale research, going through the creation of new architectures, the optimization of new electronic devices, and the understanding of how to precisely control and tune the material properties, which is at the basis of everything and which constitutes the main topic of this thesis.

Regarding the improvements of material properties, several avenues are considered. Firstly, to improve their versatility, one of the most promising idea is to search for multifunctional materials, eventually presenting couplings between their different properties. A second aspect concerns the energy consumption which can be improved by favoring low-voltage operations and by designing non-volatile memories, which do not need an applied electric field to retain their stored information. Lower energy consumption and faster operations could be also obtained by switching to in-memory computing [12] and giving up the von-Neumann architectures, in which the storage and processing units are physically separated. Multistate memories are finally highly sought for their potentialities in neuromorphic applications.

Several kinds of non-volatile memory devices are currently the objects of active researches. They all possess their own advantages and drawbacks. Flash memories have displayed their great advantage in the non-volatile memory market due to their high density and low cost, but they suffer from

many disadvantages such as a low operating speed, a poor endurance, and a high write voltage [13]. Four emerging non-volatile memories are now in the spotlight to replace them: the magnetic, ferroelectric, phase-change and resistive random access memories (respectively MRAM, FeRAM, PCRAM, and ReRAM) [14]. Among these memory devices, FeRAM and MRAM face the problem of miniaturization and PCRAM consumes large power during phase transition [15]. ReRAMs have been considered as a promising next-generation non-volatile memory due to their interesting properties, such as their excellent miniaturization potential down to lower than 10 nm [16], their operating speed lower than 100 ps [17, 18] and their low-energy consumption, below 0.1 pJ [19]. These memories adopt a metal-insulator-metal (MIM) geometry, in which the insulator film is generally an oxide [12].

1.1.3 The need for new materials with regard to the societal constraints

With the need to develop new electronic devices, it is mandatory to improve our knowledge in materials science to propose sustainable compounds with optimized properties. Device materials should be formed by abundant and "economically accessible" chemical species, *i.e.* they should be not critical [1] with regard to the industry demand and the political contexts; they should also be easy to grow and compatible with the current silicon technologies. The use of multifunctional materials, such as for example magnetoelectric multiferroics [20], is certainly a promising route to obtain more versatile devices.

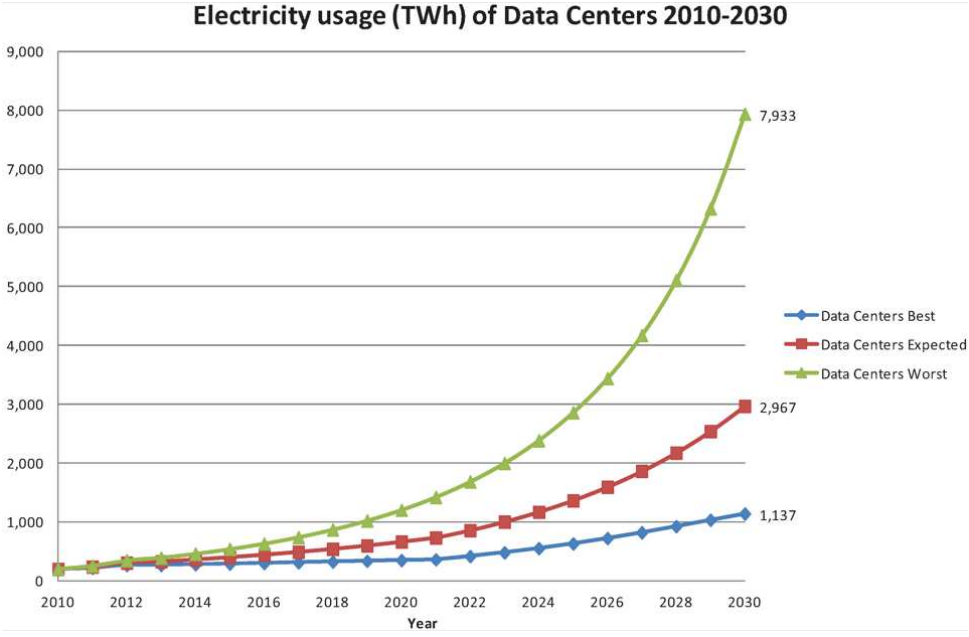

Figure 1.2 – Projected energy demand for data centers (taken from Ref. [21]).

In addition to the economical and industrial concerns, our societies also have to face new challenges imposed by the degradation of our environment and by the global warming. The need of "green" materials is more and more stringent. The increasing use of electronic devices has

1. See the list of critical materials proposed by the EU commission in 2020.

accentuated the amount of electronic waste: In the year 2019, the global production of electronic waste was of 53.6 million tons [22] and it will increase to 74.8 million tons by 2030 [23]. Therefore, it is of critical importance to investigate degradable or easily recyclable, environmentally friendly and non toxic materials. The energy consumption of electronic devices is moreover expected to increase in the coming years, as it is illustrated in Fig. 1.2, in which we can see that the electricity consumption of data centers will be four times higher in 2030 than it was in 2020 [21]. This last point shows the importance of proposing devices with low-energy operating costs.

1.2 Transition-metal oxides

1.2.1 Generalities

With the goal of proposing suitable materials for future electronic devices, the oxides naturally come to mind as they are already part of different devices, as insulating barriers in magnetic tunnel junctions or as dielectric grids in field-effect transitors. These materials can fulfill most of the requirements listed in the previous section. Oxygen is the most abundant chemical element in the Earth's crust and several oxides are formed with the association of other abundant elements such as Si, Al, or Fe, for example.

Oxides may crystallize within different structures and possess a wide range of conductive, magnetic and optical properties, which will depend on the electronic structure (and oxidation state) and ionic radius of the selected cations. Complex oxides, like perovskites and spinels which will be described later, possess at least two different cations, which increases the chance of designing multifunctional materials with rich phase diagrams. Several properties, emerging from the control of the crystal structure and the spin and orbital degrees of freedom, can thus be obtained for a given compound and can eventually coexist or be cross-coupled. The growth of oxides on silicon substrates is still the subject of intensive researches and it often requires the use of wisely-selected buffer layers [24].

The physical properties of most of the oxides are easily tunable by the application of external stimuli such as an electric or magnetic field or stress. Selecting the oxide chemical composition close from a phase transition appears as a good strategy to obtain large responses to those stimuli, for a low energy cost. Many researches have also chosen to focus on low-energy interactions such as electronic correlations, which are responsible for the insulating character of some transition-metal oxides with partially-filled d orbitals [25, 26] or on the spin-orbit interaction found in oxides with heavy elements [27].

Growing heterostructures is finally an additional way to favor the coexistence of different physical properties, which would not be compatible in single bulk compounds, and which can be coupled through their interfaces [28] (see Fig. 7.1, where the degrees of freedom that could be involved at the interfaces between correlated oxides are listed). Heterostructures add several other degrees of freedom to optimize their physical properties like the choice of the substrates, which will impose the growth direction and eventually the strain state, and also the geometry and the nanostructuration

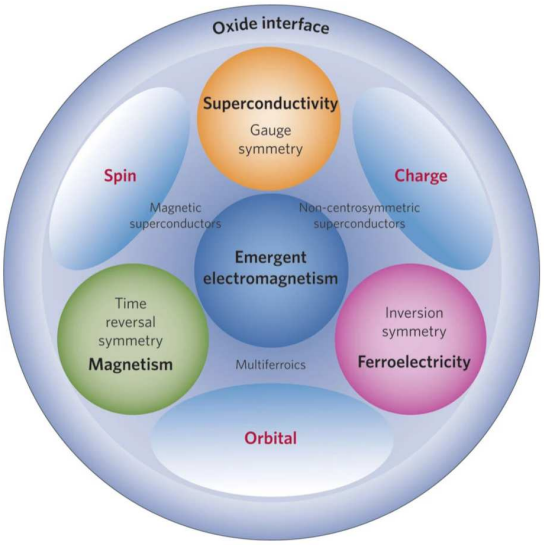

Figure 1.3 – Schematic illustration of the different degrees of freedom in correlated electron systems that could be effectively engineered at the interfaces (Reprinted from Ref. [28] with permission).

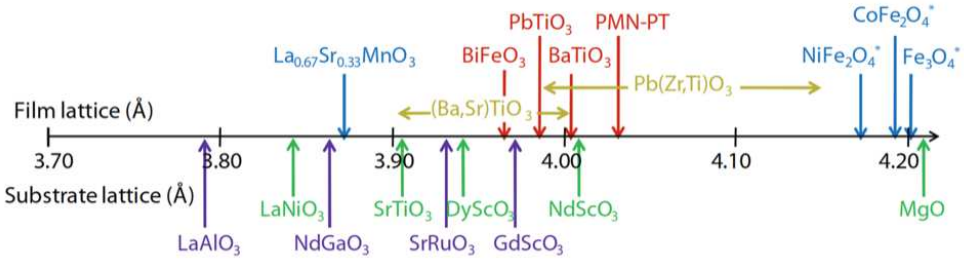

Figure 1.4 – Comparison of the lattice constants (in angstroms) of some single crystal substrates (listed below the number axes), and typical ferroelectric and magnetic oxides of current interest (listed above the number axes). For ferrites (indicated with an asterisk) the numbers correspond to half of their lattice constants. The data are taken with permission from Ref. [30].

of these systems, which are associated to the thicknesses and dimensionalities. Several oxides being regularly used as substrates (see their list in Fig. 1.4), growing full-oxide heterostructures is advantageous as it offers many possibilities, guaranteeing a good compatibility of the crystallographic structure and a continuity of the oxygen sublattice, thus facilitating epitaxial growths. Regarding the possible geometries, they mostly differ by their dimensionalities and can involve nanoparticles (0D), nanowires (1D) or thin films (2D). In the following, we will focus our discussion on the thin-film ("2/2") heterostructures. With the developments of the epitaxial-growth [by pulsed-laser deposition (PLD) or molecular beam epitaxy (MBE)] and of the characterization techniques [by reflection high energy electron diffraction (RHEED)], the quality of the layer-by-layer growth of thin films has strongly improved. The control of the interface quality remains a challenging topic which continues to motivate many studies [29].

For all the reasons described in this section, we can easily understand that oxides are promising

candidates for a large range of applications (see Fig. 1.5), but also to extend our knowledge on many fundamental properties in condensed matter [31].

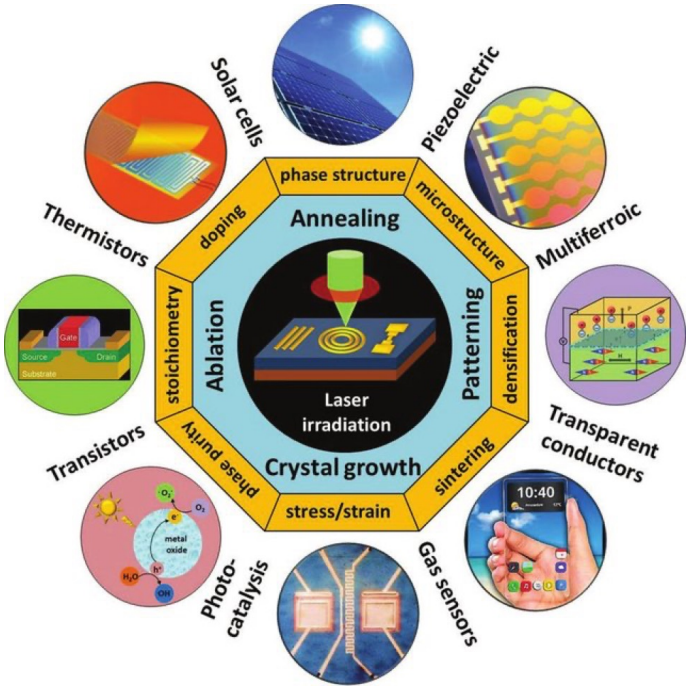

Figure 1.5 – Applications of metal oxide films and nanostructures in various functional devices (Reprinted from Ref. [32] with permission).

1.2.2 Oxides with the perovskite structure

Perovskites stand out as a distinctive group of compounds, characterized by their diverse electronic, chemical, and mechanical characteristics. The name "perovskite" comes from the discovery of the calcium titanate ($CaTiO_3$) mineral, named after the Russian mineralogist L. A. Perovski. The general chemical formula of perovskites is ABX_3, where A and B are cations located in cuboctahedral and octahedral environments defined by the anions X, consisting in O^{2-} ions in the case of oxides (Fig. 1.6). Their crystal structure remains stable, even with extensive variations of their composition, allowing for the incorporation of a wide variety of elements [33]. In 1926, V. M. Goldschmidt proposed a tolerance factor t [34] to predict the stability and structural distortions of a perovskite crystal; this factor is expressed as a function of the A- and B-cation radii $r_{A/B}$:

$$t = \frac{r_A + r_O}{\sqrt{2}(r_B + r_O)} \tag{1.1}$$

For $t > 1.0$, the perovskite is expected to possess a tetragonal or hexagonal structure, which may help for the stabilization of a polar state, with off-centering of the cations and oxygen anions. For $t \sim 0.9$-1.0, the structure may be cubic, and for $t < 0.9$, it may turn to orthorhombic or rhombohedral, with the presence of octahedra tilts.

The different possible distortions, which can partly originate from the values of the cation radii, imply different group symmetries and orbital overlaps. The resulting physical properties of the

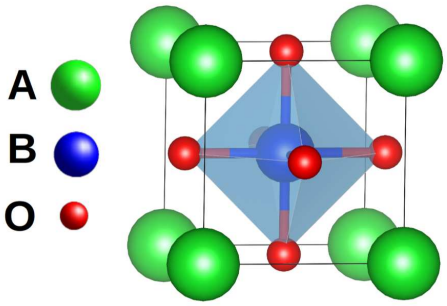

Figure 1.6 – Atomic structure of the undistorted cubic perovskite ABO_3 with the space group 221-$Pm\bar{3}m$. This picture of the crystal structure has been made using VESTA [35].

perovskites will thus strongly depend on these distortions, as well as the electronic configuration of the different cations, in particular the d-shell filling of the transition-metal often occupying the B sites. For example, perovskites with $Ti^{4+}(d^0)$ cations, such as $BaTiO_3$ and $PbTiO_3$, are among the most famous ferroelectrics in their tetragonal phase. Perovskites with transition metals having partially-filled d bands will be magnetic; the magnetic ordering and the conductive or insulating state (and the band-gap width) have been confirmed to strongly depend on the octahedra tilts [36].

In the following, we briefly describe two perovskites, which have been used to build the heterostructures studied in the MULTINANO project (described in Section 1.4), namely $SrTiO_3$ and $BaTiO_3$.

$SrTiO_3$ is commonly used as a substrate. It possesses a cubic and centrosymmetric structure (space group 221-$Pm\bar{3}m$) at room temperature, with a lattice parameter of $a_0 = 3.906$ Å [37] and an indirect band gap of approximately 3.25 eV [38]. At a temperature of $T \sim 105$ K, it undergoes a structural transition to a tetragonal phase (space group 140-$I4/mcm$). $SrTiO_3$ is considered as an incipient ferroelectric (or quantum paraelectric) in which the ferroelectricity can be induced by strain [39, 40]. Oxygen vacancies in STO can be responsible for an insulator-to-metal transition and n-type conductivity [41]; first-principles calculations also predicted that oxygen vacancies can induce the appearance of anti-ferrodistortive oxygen-octahedra rotations in this oxide [42].

$BaTiO_3$ is one of the most known ferroelectric pervoskite [43]. This compound adopts different phases as a function of the temperature. At room temperature, it is tetragonal ($P4mm$), with experimental lattice parameters $a = 3.996$ Å and $c = 4.0285$ Å [44], and an $A - \Gamma$ indirect band gap of 3.18 eV and 3.12 eV for tetragonal and cubic phases, respectively [44]. It has an electric polarization of approximately 0.26 C cm^{-2} and a Curie temperature of $T_C \simeq 390 - 400$ K [44].

1.2.3 Ferrites with a spinel structure

Spinel ferrites MFe_2O_4 (with M representing a transition metal) have captured the imagination of the research community owing to their intriguing magnetic, electrical, optical, and catalytic

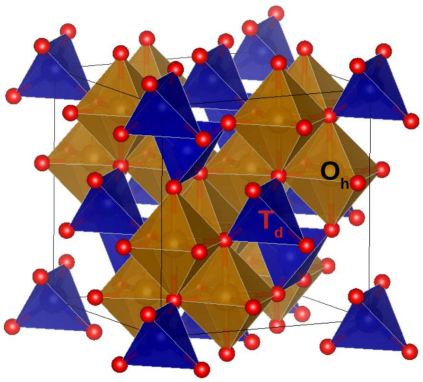

Figure 1.7 – Atomic structure of a normal spinel oxide (space group 227-$Fd\bar{3}m$) made using VESTA [35].

properties, as emphasized by Tetiana, *et al.*, in 2017 [45]. In 2019, there was a notable surge in research publications pertaining to spinel ferrites, with a total of 740 publications, nearly doubling the number reported in 2012, as documented by Narang [46]. This upsurge in interest has spurred a multitude of experimental investigations into spinel ferrite epitaxial films and nanoparticles. They have garnered substantial attention due to their diverse applications in catalysis, energy, electronics, biomedical, and spintronics fields. Their versatility has led to consider them for applications spanning diverse scientific and technical domains, ranging from medicine [47–50], to chemistry and catalysis [51, 52], energy applications [53], water splitting [54], electronics and spintronics [55, 56]. Notably, mixed transition-metal oxides with the spinel structure hold significant promises for energy conversion and storage applications, including lithium-ion batteries and supercapacitors, offering potential for cost-effective and environmentally friendly solutions, as highlighted by Yuan, *et al.*, in 2014 [57]. Various synthesis methods, including sol-gel processes, magnetron sputtering, molecular beam epitaxy, pulsed laser deposition (PLD), solvothermal techniques, co-precipitation methods, mechanical milling, microwave-assisted approaches, and hydrothermal procedures, have been employed in these studies.

The crystal structure of spinel ferrites aligns with that of $MgAl_2O_4$, featuring the 227-$Fd\bar{3}m$ space group. In this arrangement, O^{2-} anions form a distorted face-centered cubic lattice, while cations occupy some of the interstitial sites, precisely one-eighth of the tetrahedral (Td) and half of the octahedral (Oh) sites (see Fig. 1.7). A general chemical formula for spinel ferrites is MFe_2O_4, where M represents a divalent cation (M^{2+}) and Fe stands for Fe^{3+}. Divalent cations can include Mg^{2+}, Mn^{2+}, Fe^{2+}, Co^{2+}, Ni^{2+}, Cu^{2+}, Zn^{2+} or Cd^{2+}, either individually or combined. Spinel ferrites are complex and mixed-valence oxides and their structure is also characterized by their cation distribution. In a so-called normal spinel, all divalent cations (M^{2+}) occupy Td sites, while trivalent cations (Fe^{3+}) occupy Oh sites. Conversely, in an inverse spinel, half of the Fe^{3+} ions occupy Td sites, with the remaining Fe^{3+} and M^{2+} cations residing in Oh sites. Certain spinel structures may exhibit an intermediate distribution, depending on the chemical composition and growth conditions, represented by the chemical formula $[M^{2+}_{1-\lambda}Fe^{3+}_{\lambda}]_{\mathrm{Td}}[M^{2+}_{\lambda}Fe^{3+}_{2-\lambda}]_{\mathrm{Oh}}O_4$, where λ is

the inversion parameter varying from 0 (for normal spinel) to 1 (for inverse spinel). The control of the cation distribution in spinel compounds is important as their physical properties will strongly depend on it; this point will be discussed in more details in Chapter 3.

Table 1.1 – Measured structure type, lattice parameter, magnetic ordering, band gap, and Curie temperature of some spinel ferrites. These data are taken from the literature.

Ferrites	Spinel type	Lattice Parameter (Å)	Magnetic ordering	Band gap (eV)	T_C (K)
$MgFe_2O_4$	Partially inverse	8.38-8.40 [58]		2.0 [59]	
$MnFe_2O_4$	Normal	8.499 [60]			
Fe_3O_4	Inverse	8.396 [60], 8.394 [61]	Ferri.		858, 851 [61]
γ-Fe_2O_3	spinel	a=8.340, c=24.966 [62]	Ferri.	2.00 [63]	
$CoFe_2O_4$	Inverse (λ=0.7-0.9)	8.392 [60]	Ferri.	1.17 [64], 1.31 [65]	790 [66]
$NiFe_2O_4$	Inverse	8.339 [67]	Ferri.	1.52 [65], 1.64 [68], 2.00 [69]	865 [66]
$CuFe_2O_4$		8.412 [70], 8.409 [71]		1.9 [69]	699 [71]
$ZnFe_2O_4$	Normal	8.441 [72]	Antiferro.	2.20, 2.35 [69]	15 K

In Table 1.1, we reported the properties of different spinel ferrites. Among these oxides, Fe_3O_4, γ-Fe_2O_3, $CoFe_2O_4$ and $NiFe_2O_4$ share the common feature of displaying a robust ferrimagnetic ordering, mostly stabilized by the strong antiferromagnetic coupling between the spin magnetic moments of cations in Td and in Oh sites. This results in high Curie temperatures, well above room temperature, rendering these ferrites particularly interesting for spintronic applications, as magnetic electrode or spin-filtering barrier in magnetic tunnel junctions [73], or to design extrinsic-multiferroic heterostructures [74–76]. Because of the large number of vacant atomic sites - only half of the Oh sites and 1/8 of the Td sites are occupied, such materials are also important to develop magneto-ionic systems [77–79]. The magnetite Fe_3O_4 is an exception in this serie, as it is half-metallic at room temperature, while all other spinel ferrites are insulating, which makes them also interesting for resistive switching devices [80–82].

In the following, we discuss the main characteristics of different spinel ferrites relevant for the discussions which will be held throughout the manuscript. A comparative summary of the main properties of these oxides is given in Table 1.1.

Magnetite (Fe_3O_4) is one of the oldest magnetic materials known to mankind. It exhibits a ferrimagnetic ordering below the Curie temperature of 860 K. It is half metallic at room temperature and crystallizes into an inverse spinel structure. The hopping of electrons between Fe^{2+} and Fe^{3+} occupying Oh sites is responsible for its minority spin electronic conductivity. Magnetite exhibits a metal-to-insulator transition, called the Verwey transition [83–85], at the temperature of 120 K. This transition is characterized by an increase of the resistivity by two orders of magnitude. The Verwey transition results from the set up of a charge ordering between Fe cations in Oh sites, which leads to the formation of trimerons [86].

Maghemite (γ-Fe_2O_3) is a ferrimagnetic insulator, with a high Curie temperature of 950 K. Like magnetite, the γ phase of Fe_2O_3 possesses a spinel structure with an additional sub-lattice of Fe(Oh) vacant sites. Experimentally, maghemite crystallizes into a cubic structure with a random distribution of vacancies (space group Fd-3m). Depending on the growth conditions, Fe(Oh) vacancy distribution can lead to a structure in which vacancies have an ordered distribution, with tetragonal symmetry and tripled unit cell along the c-axis (space group $P4_12_12$) [87–89].

$CoFe_2O_4$ has the highest magnetic anisotropy energy of 1.8-3.0 $\times 10^6$ erg cm^{-3} and the highest value of the magnetostriction coefficient (around 350×10^{-6}) among all the spinel ferrites [90]. It is usually experimentally synthesized as a partial inverse spinel with an inversion parameter of 0.7-0.9 [91–95]. Its experimental lattice parameter is 8.392 Å [60] and the reported experimentally measured values of optical band gap are 1.17 eV [64] and 1.31 eV [65].

$NiFe_2O_4$ is an insulating inverse spinel ferrite. It is also a ferrimagnetic crystal with a Curie temperature of about 865 K [66]. Its experimental lattice parameter is 8.339 Å [60] and the reported values of optical band gap measured in experiments are 1.52 eV [65] and 1.64 eV [68]. In 2006, Lüders, *et al.* [96] studied NFO epitaxial heterostructure thin films for spintronic applications. They demonstrated that it is possible to obtain conducting and insulating thin films depending on the growth conditions. The films grown in the Ar/O_2 growth atmosphere are insulating with a resistivity of $\rho \approx 200$ Ωcm, while the films grown in the Ar atmosphere have a conductivity higher by three orders of magnitude ($\rho \approx 200$ mΩcm). They found that NFO has a spin polarization of up to 42% and a spin filtering efficiency of 23% at low temperatures. Dey et al. [97] demonstrated that $NiFe_2O_4$ can be grown with a perfectly inverse spinel structure and a short-range Ni/Fe cation ordering in Oh sites associated to the space group 91-$P4_122$. With such a cation distribution, $NiFe_2O_4$ is found ferroelectric below $T \simeq 98$ K, with a measured electric polarization of 0.29 μC cm^{-2}.

1.2.4 Spinel ferrite/perovskite thin-film heterostructures as extrinsic multiferroics

Multiferroics are (eventually composite) materials which display at least two ferroic orderings [99, 100]. This concept has to be distinguished from the one of (inverse) magnetoelectricity, which design the ability of creating or modifying magnetic/electric dipoles through the application of an electric/magnetic field [101–103] (see Fig. 1.8). These two physical properties are however closely linked in systems associating ferromagnetism and ferroelectricity. Magnetoelectric multiferroics are particularly interesting for the design of non-volatile memories in which the electrode magnetization could be manipulated through the application of an electric field, which would allow a better addressability and miniaturization, as well as significant energy gains [104–108].

With the doping of bulk compounds, growing ferromagnetic/ferroelectric heterostructures has been one of the most investigated way to circumvent the difficulties to find intrinsic multiferroics

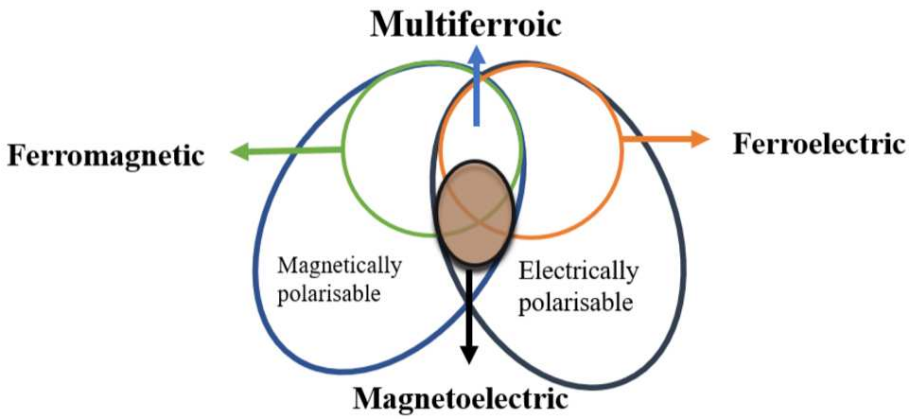

Figure 1.8 – Schematic representation of interrelations between electric and magnetic fields with respect to the electric and magnetic polarizations (Reprinted from Ref. [98] with permission).

with high magnetoelectric coupling (MEC) at room temperature [74, 100]. Intrinsic magnetoelectric multiferroics are indeed rare in the nature because of the incompatible requirements that ferromagnetism and ferroelectricity imposes on the materials symmetries and electronic structures. In terms of symmetries, the ferroelectricity indeed requires the material to be non centrosymmetric, while ferromagnetism is associated with a breaking of the time inversion; fulfilling these two constraints reduces drastically the number of possible space groups. Regarding the electronic structure, the ferroelectricity is usually found in dielectric materials with a d^0 transition-metal electronic configuration, while the ferromagnetism is favoured in metallic systems with partial d-orbital filling [109]. The most famous intrinsic magnetoelectric multiferroic is certainly $BiFeO_3$, in which the electric polarization of 90-95 μC cm^{-2} is driven by the lone pair of electrons of Bi ($T_C \simeq 1100$ K) and a non-compensated antiferromagnetic ordering ($T_N \simeq 653$ K) driven by the $3d$ electrons of Fe cations, lead to a weak ferromagnetism [110, 111].

Heterostructures formed by the association of a ferrimagnetic spinel ferrite and a ferroelectric perovskite have mainly been grown with the goal of designing extrinsic multiferroics with high magnetoelectric coupling at room temperature [74]. Their study has been motivated by the high Curie temperature of the isolated compounds and the relative compatibility of their atomic structures, favoring a continuity of the oxygen sublattice with moderate strain. According to Fig. 1.4, we can for example see that the lattice mismatch [considering a (001) growth] of the nickel ferrite $NiFe_2O_4$ (a = 8.339 Å) is approximately +6.8% with $SrTiO_3$ ($2a$ = 7.81 Å) and +4.4% with $BaTiO_3$ in its tetragonal phase ($2a$ = 7.984 Å). The MEC in heterostructures can be induced indirectly through the piezoelectricity/piezomagnetism or piezostrictive/magnetostrictive effects, or directly through the interface and then be mediated by exchange coupling or charge transfers and chemical bond reorganizations [107]. Several studies have demonstrated the ability to stabilize relatively high linear MEC coefficients α_{ME} at room temperature with heterostructures [74] such as $CoFe_2O_4/BaTiO_3$ has a wide range of α_{ME} varying from 0.5 to 2540 mV cm^{-1} Oe^{-1} depending on the growth method and the magnetic phase content. Only few theoretical studies exist about the multiferroic properties of spinel ferrite/ferroelectric perovskite heterostructures. In 2008, Niranjan,

et al. [112], proposed a first-principle study of the magnetoelectric coupling at the interface between metallic Fe_3O_4 and $BaTiO_3$. They found that the magnetoelectric coupling strongly depends on the interface termination and can be enhanced by a factor 3 if an oxygen-deficient termination is selected. In 2020, Tamerd, *et al.* [113], studied the $NiFe_2O_4/PbZr_{0.5}Ti_{0.5}O_3(001)$ interface and calculated a magnetoelectric coefficient of 3.15×10^{-10} G cm^2 V^{-1}.

1.3 Resistive switching and insulator-to-metal transitions

Resistive-switching (RS) processes correspond to the reversible changes in the electric resistance of a material, which can extend over several orders of magnitude and ultimately correspond to insulator-to-metal transitions (IMT). These processes, which can be triggered by applying an electric voltage, are highly investigated to design efficient non-volatile memories with low energy consumption. The research on RS started in the 1960s, when T. W. Hickmott measured negative differential resistances in metal/oxide/metal sandwiches [114]. Theorized in 1971 [115], the concept of memristor (or memory resistor) was demonstrated in 2008 [116, 117], while patents [2] had already been filed regarding the development of ReRAM a few years before. While the RS processes are generally found in metal/insulator/metal (MIM) heterostructures and involve complex mixing of ions and electrons dynamics (which can be categorized in electromechanical metallization, valence-change or thermodynamical mechanisms [15, 118–120]), purely electronic switches are also possible. It is worthy to note that memristors consist in heterostructures in which the interface effects may play an important role. In the following subsection, we review some of the mechanisms that may contribute to the IMT.

1.3.1 Insulator-to-metal transitions driven by electronic correlations

Mott insulators owe their insulating character to their strong electron-electron interactions, more precisely to the interplay between the electron Coulomb repulsion and their degree of localization. Several transition-metal oxides belong to the Mott insulator family because the width of their partially-filled and already-narrow $3d$ bands is additionally reduced because of their indirect interaction through the $2p$ orbitals of O ligands. Mott insulators generally display small band gaps of a few tenths of eV. Mott transitions [26] are IMT which can be triggered by several kinds of stimuli such as the temperature, the application of an electric voltage or a pressure. Doping the material is also an efficient way of tuning the IMT.

The Mott physics is a complex area of research, which is beyond the scope of this thesis, so it will not be discussed more in details here. It is nonetheless important to remind that magnetite Fe_3O_4 can display a purely electronic IMT (the Verwey transition) at a temperature of $T_V \simeq 120$ K, which has been associated to the formation of a charge ordering at low temperature [83–86, 121]. Other spinel ferrites which will be studied through this manuscript, like $CoFe_2O_4$ and $NiFe_2O_4$, are normally always insulating. As it will be explained later, the correct description of their

2. Patent No.: US6531371B2, US7292469B2

insulating state with first-principles calculations necessitates the use of functionals able to take the strong $3d$ correlations into account [64, 65, 122–131], while standard exchange-correlation functionals would predict these materials as metallic, or at least, strongly underestimate their band-gap width [132]. In the presence of strong distortions and modifications of the lattice, the role of electronic correlations in measured IMT could thus be non negligible in these materials.

It is finally interesting to note that devices based on resistive switching induced by the Mott physics begun to be proposed, opening the road to the developement of a Mottronics [133, 134].

1.3.2 Two-dimensional electron gas: insulator-to-metal transition induced by polar catastrophe and formation of defects

Another type of IMT which is relevant for our future discussions originates from the so-called polar catastrophe, which takes place at the interface between polar materials, where a charge discontinuity exists. Brought to light in the field of oxides with the discovery of the conductive $LaAlO_3/SrTiO_3(001)$ (LAO/STO) interface in 2004 [135], the study of two-dimensional electron gases (2DEG) has then extended to a large variety of perovskite/perovskite interfaces like $LaTiO_3$/STO [136–139], $NdAlO_3$/STO [140] or $LaGaO_3$/STO [141].

One of the first scenarios which was proposed to explain the emergence of the 2DEG at the LAO/STO interface was the one of a Zener breakdown or polar gating. Along the [001] direction, $LaAlO_3$ is polar and is formed by a succession of $(LaO)^+$ and $(AlO_2)^-$ atomic layers, while $SrTiO_3$ is non polar, with only neutral $(SrO)^0$ and $(TiO_2)^0$ layers. The interface between these two oxides introduces a charge discontinuity and breaks the inversion symmetry, which may lead to the formation of an internal electric field in LAO and to an electric-potential build up which diverges when the LAO thickness increases. For a critical thickness of $\sim$ 4 unit cells of LAO [142], the accumulated energy overcomes the band gap of STO and an electron transfer is then possible from the surface of LAO to the interface with STO. These charges will remain localized at the interface, on the STO side, forming a 2DEG, which may extend over a few nanometers away from the interface [143–146]. While, according to the polar catastrophe scenario, 0.5e per formula unit of STO (3.3×10^{14} cm^{-2}) should be transferred to the interface in order to cancel the internal electric field, electron densities 1 or 2 orders of magnitude lower are generally measured [147], with mobilities in the order of 10^3-10^4 cm^2 V^{-1} s^{-1} [147–149] at temperatures of 2-4 K; these quantities may in addition strongly depend on the interface quality, on the strain state [150] and on the presence or not of a capping layer on top of LAO [151, 152]. The Zener breakdown scenario, even if explaining the thickness-dependent IMT, has not been sufficient to explain all the intriguing features of the LAO/STO interfaces [153]. Other scenarios have later been proposed, involving the formation of oxygen vacancies or cation intermixing at the interface [154]. Forming oxygen vacancies by depositing a reducing metal capping layer has been proposed as a solution to form a 2DEG at the surface of $SrTiO_3$ [155].

As reviewed by Bogorin, *et al.* [156, 157], several devices have already been proposed to use the IMT and the peculiar properties of the 2DEG generated at the LAO/STO interface. The

ability to control the IMT and the 2DEG properties by applying an external electric field [158] is particularly interesting to use this interface in field-effect devices with a diode [159, 160] or transistor [161] geometry and in which the interface can naturally form the conductive channel. The demonstration of the possibility to write/erase conductive domains with a width of 2 nm by using a conductive atomic force microscope (AFM) tip [162] is also promising in view of using such an interface to design reconfigurable devices. Finally, let us also mention that the gate-tunable spin-orbit properties associated to the 2DEG [163] are particularly interesting for Rashba-Edelstein spin-to-charge conversions [164], which are particularly demanded in the recent propositions of spinorbitronic devices [106].

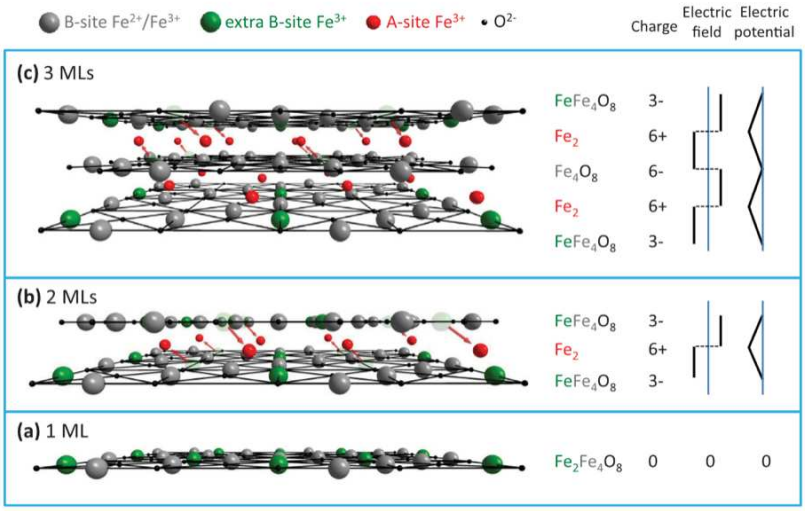

Figure 1.9 – Atomic reconstructions to avoid the polar catastrophe during the growth of Fe_3O_4 on MgO(001). (a,b,c) The mechanisms are shown for three different thicknesses of Fe_3O_4 film, given in number of monolayers (ML). (Reprinted from Ref. [165] with permission)

Considering the fact that the spinel structure is formed by alternating negatively/positively charged (001) layers, it is now reasonable to wonder if spinel-based polar interfaces with a charge discontinuity could be grown and lead to the formation of a 2DEG, similar to the one reported in perovskite heterostructures. In 2014, Arras and Calmels proposed, on the basis of first-principles calculations, that a spin-polarized two-dimensional electron gas could be generated at the interface between a normal and an inverse spinel structures like $CoFe_2O_4/MgAl_2O_4(001)$ [166]. At this interface, the charge discontinuity would originate from the different distribution of divalent and trivalent cations between both oxides. Even if promising, this prediction remains to be confirmed by experiments and the role of defects and atomic reconstructions would deserve to be studied more deeply, as they can cancel the electronic reconstruction and prevent the appearance of a 2DEG. For example, as shown in Fig. 1.9, it was indeed reported that, at the interface between Fe_3O_4 and MgO, Fe_{Td} cations are displaced into the $[Fe_{Oh}]_2O_4$ layer [165] to prevent the polar catastrophe (a similar process was proposed to explain the increase of magnetization at the interface between maghemite γ-Fe_2O_3 and MgO [167]). On the contrary, Ti/Al antisite defects and oxygen vacancies have been

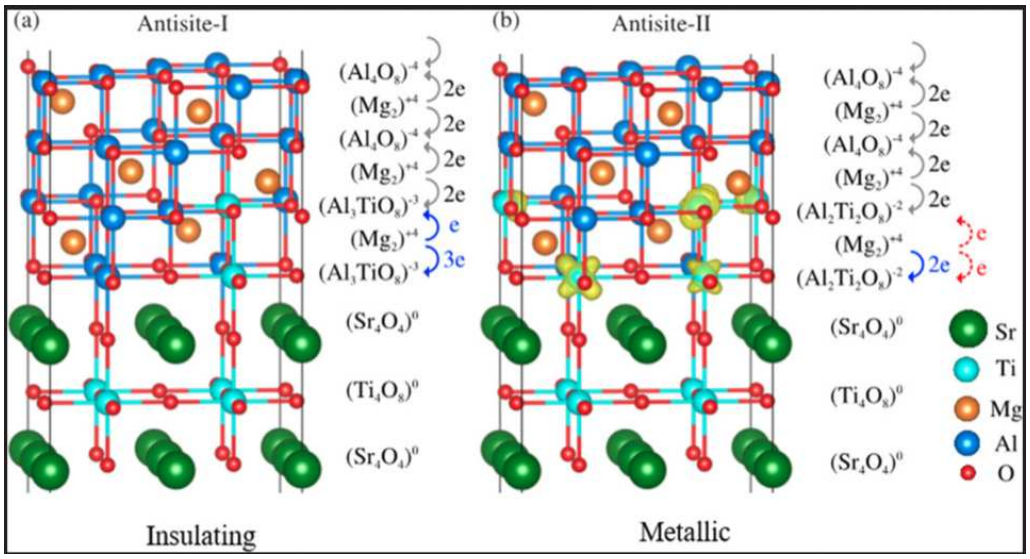

Figure 1.10 – Atomic intermixing at the $MgAl_2O_4/SrTiO_3(001)$ interface. Depending on the antisite model, the interface can (a) remain insulating or (b) become conducting. The model "Antisite-II" could explain the experimental measurements. The charge density of the conducting $3d$ states is printed in yellow. (Reprinted from Ref. [154] with permission)

proposed to explain the emergence of a 2DEG at the interface between $MgAl_2O_4$ and $SrTiO_3$ (see the mechanism proposed in Fig 1.10), with a measured charge density of 5.2×10^{13} cm^{-2} and a mobility of 304 cm^2 V^{-1} s^{-1} [154] at $T = 2$ K. A 2DEG was also measured at the interface between γ-Al_2O_3 and $SrTiO_3$, but this time with much higher electron mobilities, up to 140×10^3 cm^2 V^{-1} s^{-1} (and electron densities of 3.7×10^{14} cm^{-2} at 2 K) [168]. The conductivity at this interface is attributed to the presence of oxygen vacancies [169] and it can disappear after thermal treatments in oxygen-rich atmospheres [170, 171].

1.3.3 Resistive switching and the role of defects

As mentioned in the introduction of this section, the MIM heterostructure and the formation/migration of defects in the insulating (I) film, generally formed by an oxide layer, is at the basis of the ReRAM devices (see Refs. [15, 118–120] and references therein). In ReRAM devices, the switch between low- and high-resistance states (LRS/HRS) results from the formation/destruction of conductive filaments connecting the two metallic electrodes, when pulses of electric currents are applied. Uniform resistance switching have also been reported, but it may necessitate higher programming currents of which the intensity will depend on the film's area [172].

If both the set and reset operations can be performed with the same voltage polarity, the resistive switching is called unipolar; in that case, the formation of connections/disconnections of conductive filaments are mostly triggered by thermal effects at high temperatures. On the other hand, if the set and reset operations must be performed with opposite voltage polarities, the switching is called bipolar. In electrochemical metallization (ECM) or conductive-bridge processes, the insulating layer is an oxide electrolyte and the cap layer is a Cu, Ag, Ni, Ru, Pt-Al, Cu-Ti,

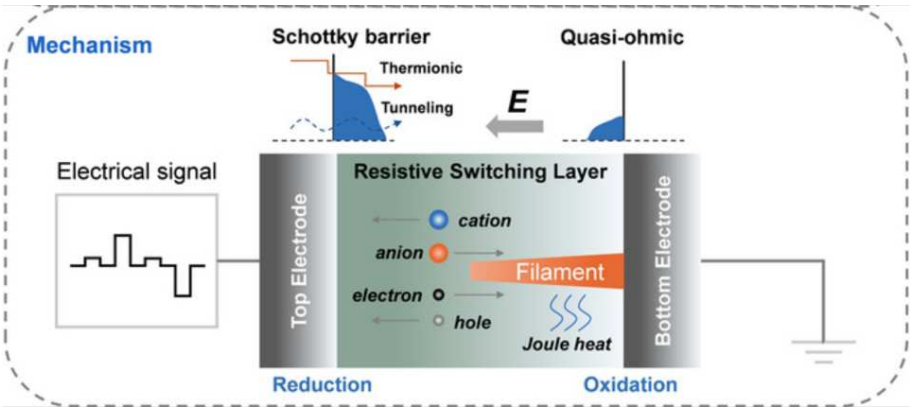

Figure 1.11 – Schematic of a Resistive Switching (RS) device made from a MIM heterostructure. Both ionic and electronic charge carriers may participate to the switching process. The Schottky barrier, the redox reaction of the charge carriers at the interface, their drift diffusion in the bulk, and the Joule heating effect are primary factors in the RS process. (Reprinted from Ref. [119] with permission)

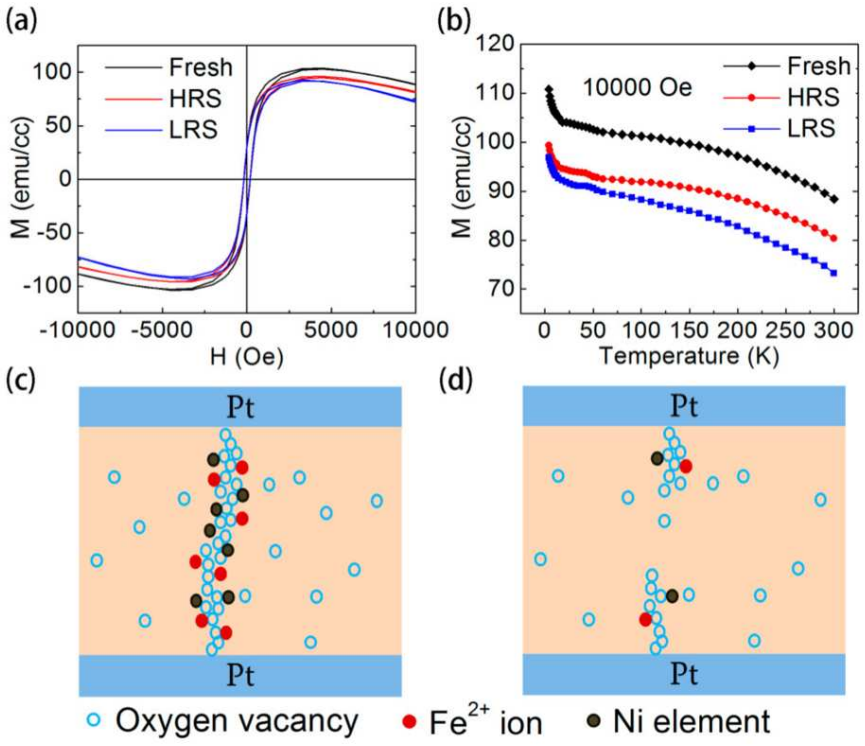

Figure 1.12 – (a) Magnetic hysteresis loops measured at 300 K and (b) temperature dependence of the magnetization of $Pt/NiFe_2O_4/Pt$ devices with different resistance states. (c, d) Diagrams showing the formation and the rupture of the conducting filaments in the LRS and HRS, respectively. (Reprinted from Ref. [80] with permission).

Cu-Te or Ni-Ti electrode [119]. In the initial state, when electric pulses are applied, cations from the cap layer will move in the electrolyte and form conductive bridges. In valence-change memories, the two electrodes are generally different, one being inert and the second one active. The valence-

change switching is associated to exchange of oxygen atoms through the oxidation of the active electrode and the formation of oxygen vacancies in the insulating oxide layer [173]. In addition to the migration and formation of atomic defects, it is important to keep in mind that electronic effects, with trapping/detrapping of charges, can also participate to the resistance switching. A schematics summarizing the different resistive-switching mechanisms is shown in Fig. 1.11.

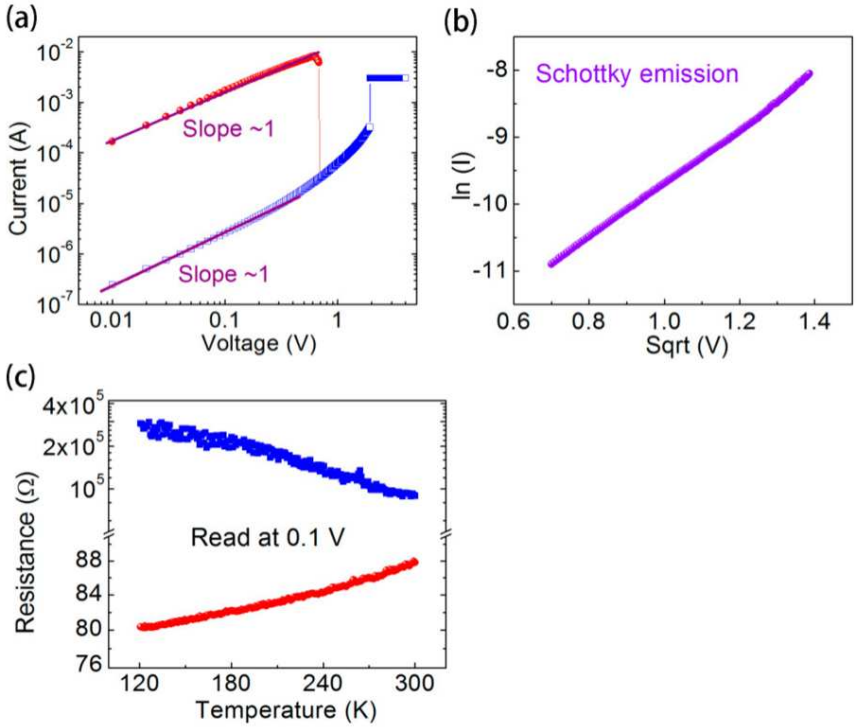

Figure 1.13 – (a) Typical I–V curves for resistive switching of the Pt/$NiFe_2O_4$/Pt devices. (b) Typical ln(I) vs $\sqrt{V}$ plot for the higher-voltage region of the HRS. (c) Temperature dependence of the resistances of the HRS (blue) and LRS (red). (Reprinted from Ref. [80] with permission)

Both unipolar [80, 81, 174] and bipolar [175, 176] device were measured using nickel or cobalt ferrites as insulating oxides. For each system, the switching mechanisms are associated with the formation of filaments made of oxygen vacancies and the consecutive reduction of Fe^{3+} cations into Fe^{2+} occurs. The decreases of the resistance are also accompanied by a consecutive lowering of the spin magnetization as illustrated in Fig. 1.12 for a Pt/$NiFe_2O_4$/Pt heterostructure. The corresponding conductive/resistance states are shown in Fig. 1.13. As it can be seen in this figure, these devices can display variations of resistance by several orders of magnitude, even at room temperature. They have been moreover found to display long retention times (up to 10^5 s) and good endurance.

1.4 The MULTINANO project and objectives of this thesis

A few years ago, the multiferroic properties of ultrathin epitaxial $CoFe_2O_4/BaTiO_3(001)$ layers were studied using synchrotron techniques [93, 94]. Aghavnian, *et al.* [93] investigated the Co/Fe cation ratio and inversion degree for three $CoFe_2O_4/BaTiO_3$ heterostructures with the same thickness (6 nm) of the $CoFe_2O_4$ film and different thicknesses (11, 13, and 15 nm) of the $BaTiO_3$ layer. They found that the inversion degree is close to 80% for every sample. Jedrecy et al [94] studied the thickness dependency of the tetragonal strain in $CoFe_2O_4$ and $BaTiO_3$. The tetragonality is characterized by the c/a ratio, *i.e.* the ratio between the out-of-plane and in-plane lattice parameters, respectively c and a. The c/a ratio of both $CoFe_2O_4$ and $BaTiO_3$ mainly depends on the thickness of $CoFe_2O_4$: it decreases when increasing the thickness of $CoFe_2O_4$ and is equal to 1 when the thickness of $CoFe_2O_4$ is above 10 nm. The thickness of the $CoFe_2O_4$ layer and the tetragonality of $BaTiO_3$ are important parameters which can affect the electric polarization magnitude in $BaTiO_3$ and the coercive electric field needed to rotate it. Finally, the authors also reported oxidoreduction processes in $CoFe_2O_4$ near the interface (in a region thickness of approximately 2.2 nm) with $BaTiO_3$, resulting in the formation of Co^{3+} and Fe^{2+} cations in Oh sites. During his PhD thesis [177], T. Aghavnian demonstrated that the multiferroic properties of this heterostructure were predominantly linked with structural and chemical modifications originating from ionic displacements. He also highlighted that these processes induce reversible changes in the electrical resistance at room temperature, which could therefore be used in resistive memories.

These different works paved the road toward the MULTINANO project (see ANR project ANR-19-CE09-0036) in which it was proposed to use these changes of resistance in spinel ferrite/$BaTiO_3$ thin films to design innovative and reconfigurable devices. Indeed, it has been confirmed that it is possible to write conductive area by applying an electric field using a piezoresponse force microscope (PFM), as it can be seen in Fig. 7.2(a). In addition to this first goal, the MULTINANO project also aimed at understanding the mechanisms responsible for the formation of these conductive domains. In this manuscript, we will present the results of first-principles calculations which were conducted in order to address this question.

Taking into account the review on resistive switching processes described in the previous section, it is possible to understand the complexity of such a system. First of all, spinel ferrites are mixed-valence transition metal oxides in which the electronic correlations must be considered. As discussed in Chapter 2 and in Appendix A, this will have implications on the choice of the exchange-correlation functionals. It will also be important to verify the effect of strain on the electronic structure of the ferrites, as the films are strained on a $SrTiO_3$ substrate. Because *ab initio* calculations based on the density functional theory (DFT) can only be applied on systems consisting in few atoms only, we decided to decompose the problem in four parts, as labelled in Fig. 7.2(b), and which could be sufficient to cover most of the main features and phenomena occuring in this kind of heterostructure. These four different parts of the problem also have the

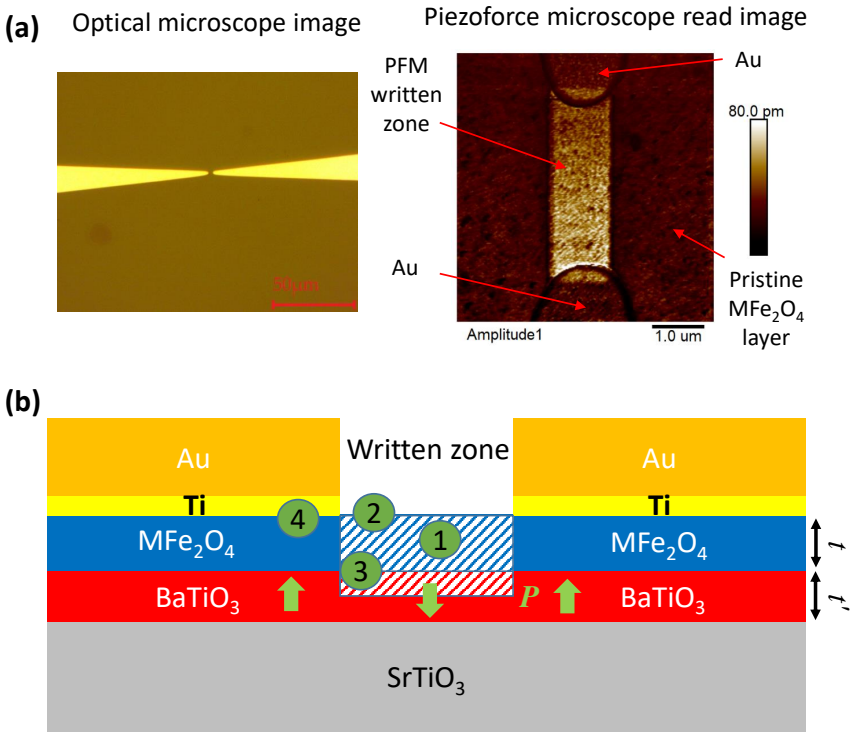

Figure 1.14 – (a) Experimental top-view images of the ferrite/$BaTiO_3$ heterostructure with a conductive domain written by PFM and connecting two Au electrodes. These results have been obtained by Haowen Lin (SPEC, CEA-Saclay) during his on-going PhD thesis. (b) Schematics of the ferrite/$BaTiO_3$(001) thin films, expitaxially deposited on a Nb-doped $SrTiO_3$ substrate and with Au capping electrodes grown over Ti buffer layers. The MFe_2O_4 and $BaTiO_3$ layers are approximately 10-15 nm thick.

advantage to present an increasing difficulty in their treatment.

The first area of interest in the heterostructure corresponds to the center of the ferrite film (which we described as if it was bulk material) and is covered in Chapters 3 and 4. In addition to the electronic correlations, it is important, to correctly calculate the physical properties of the spinel ferrites, to consider the M^{2+}/Fe^{3+} cation distribution, in the Oh-site sublattice, as well as between the tetrahedral and octahedral sites (inversion degree). These effects are described in Chapter 3. The most stable configurations of cation ordering found in this chapter are used as a reference for later comparisons. As proposed in the description of the resistive-switching mechanisms and suggested in the thesis of T. Aghavnian [177], we must consider that the displacement of ions is certainly the cause of the IMT. Consequently, we thus decided to study in Chapter 4 the stability of point defects in bulk spinel ferrites, focusing on $NiFe_2O_4$ and $CoFe_2O_4$ compounds, and their implication on the electronic and magnetic properties. A particular interest was given to the formation of cation and oxygen vacancies.

The second area of interest corresponds to the ferrite surfaces and will be addressed in Chapter 5. Surfaces are particularly important because they can be the host of electronic and atomic

reconstructions. It is worth also to remind that spinel ferrites are polar along the [001] direction and that 2DEG have already been predicted or reported at spinel-based interfaces (see Sect. 1.3.2). The precise understanding of surface properties is also a necessary step before beginning the study the spinel ferrite/$BaTiO_3$ interfaces (area of interest 3). For these interfaces, we intended to investigate how the direction of the electric polarization in $BaTiO_3$ could affect the electronic properties at the interface. Unfortunately, because of a lack of time, only preliminary results will be given at the end of Chapter 5, on the properties of the $NiFe_2O_4/BaTiO_3$ interface for a $NiFeO_4/Ti_2O_4$ termination. Other spinel/$BaTiO_3$ and interfaces with the Ti electrode (area of interest 4) are discussed in the conclusion of this manuscript as perspectives.

Chapter 2

Calculation methods

This chapter covers the methods employed in this thesis for calculating the electronic structure and the thermodynamics properties. It begins by discussing the basis of the Density Functional Theory (DFT), including the Kohn-Sham equations and the exchange-correlation functionals. We then describe the thermodynamic methods, including corrections that must be applied for assessing the stability of the possible cation orderings and calculating the defect formation energies.

2.1 Many-body Schrödinger equation

The time-independent Schrödinger equation [178] is the fundamental equation used to successfully describe the behavior of a set of N_t quantum particles such as electrons in atoms, molecules and solids:

$$\widehat{H}\Psi(\{\vec{r}_i;\vec{R}_I\}) = E\Psi(\{\vec{r}_i;\vec{R}_I\}) \tag{2.1}$$

where, $\widehat{H}$ is the Hamiltonian operator, ψ is the wave function describing the state of the N_t particles and E is the eigenvalue of $\widehat{H}$ or energy of the N-body system. The vectors $\vec{R}_I$ and $\vec{r}_i$ give the positions of the nuclei I and electrons i.

For a molecule or a crystal that has N' nuclei and N electrons ($N_t = N' + N$), the many-body Hamiltonian can be written as:

$$\widehat{H} = -\sum_{I}^{\mathrm{N'}} \frac{\hbar^2}{2M_I}\nabla_I^2 - \sum_{i}^{\mathrm{N}} \frac{\hbar^2}{2m}\nabla_i^2 + \frac{1}{2}\sum_{I\neq J}^{\mathrm{N'}} \frac{\mathrm{Z}_I\mathrm{Z}_J e^2}{4\pi\epsilon_0|\vec{R}_I - \vec{R}_J|} + \frac{1}{2}\sum_{i\neq j}^{\mathrm{N}} \frac{e^2}{4\pi\epsilon_0|\vec{r}_i - \vec{r}_j|} - \sum_{i,I}^{\mathrm{N,N'}} \frac{Z_I e^2}{4\pi\epsilon_0|\vec{r}_i - \vec{R}_I|} \tag{2.2}$$

In this equation, the two first terms correspond to the kinetic energy of nuclei (with masses M_I and atomic numbers Z_I) and electrons (with a mass m), respectively. The third, fourth and fifth terms are the nucleus-nucleus, electron-electron and nucleus-electron Coulomb interactions. $\hbar$ is the reduced Plank's constant.

2.2 Born-Oppenheimer Approximation

Solving Eq. 2.1 is too challenging. Therefore, approximations are necessary to simplify it. The first approximation is the "Born-Oppenheimer approximation" [179], in which nuclei are assumed

to be fixed due to their great mass compared with the electron mass (roughly 1800 times higher). As a result, the kinetic energy of nuclei and nucleus-nucleus Coulombic interaction energy can be omitted from the Hamiltonian of Eq. 2.2. With this approximation, the new Hamiltonian now only possesses three terms as shown below:

$$\left[-\sum_{i}^{N}\frac{\hbar^2}{2m}\nabla_i^2+\frac{1}{2}\sum_{i\neq j}^{N}\frac{e^2}{4\pi\epsilon_0|\vec{r}_i-\vec{r}_j|}-\sum_{i,I}^{N,N'}\frac{Z_I e^2}{4\pi\epsilon_0|\vec{r}_i-\vec{R}_I|}\right]\Psi(\vec{r}_1,\vec{r}_2,...,\vec{r}_N)=E\Psi(\vec{r}_1,\vec{r}_2,...,\vec{r}_N) \tag{2.3}$$

2.3 Hartree-Fock approximation

However, getting a numerical solution of Eq. 2.3 is still impossible due to interaction between electrons. Hartree proposed an approximate method, also known as the Hartree method [180], for solving the many-body Schrödinger equation. In this approach, each electron is treated as moving in an average electrostatic field created by all the other electrons; all other aspects of the electron-electron interaction are neglected. The interacting wave function can be written as a non-interacting wave function also known as Hartree product (HP):

$$\Psi_{\mathrm{HP}}(\vec{r}_1,\vec{r}_2,...,\vec{r}_N)=\psi_1(\vec{r}_1)\psi_2(\vec{r}_2)...\psi_N(\vec{r}_N) \tag{2.4}$$

According to the Hartree approximation, the one-electron Schrodinger equation can be written as:

$$\left[-\frac{\hbar^2}{2m}\nabla_i^2+V_{\mathrm{eff}}\right]\psi_i(\vec{r}_i)=E\psi_i(\vec{r}_i) \tag{2.5}$$

where V_{eff} is the effective potential acting on the i^{th} electron due to nuclei and other remaining electrons. The problem with the Hartree method is that it does not take into account the fact that the wave function must be antisymmetric. However, this method is historically important in the development of more accurate quantum mechanical methods, such as the Hartree-Fock (HF) theory and the DFT.

To antisymmetrize the wave function, the Slater determinant given below can be used as a wave function:

$$\Psi_{HF}(r_1,r_2,...,r_N)=\frac{1}{\sqrt{N!}}\begin{vmatrix}\psi_1(1) & \psi_2(1) & \psi_3(1) & \cdots & \psi_N(1)\\ \psi_1(2) & \psi_2(2) & \psi_3(2) & \cdots & \psi_N(2)\\ \vdots & \vdots & \vdots & \ddots & \vdots\\ \psi_1(N) & \psi_2(N) & \psi_3(N) & \cdots & \psi_N(N)\end{vmatrix} \tag{2.6}$$

In the Hartree-Fock method, the wave function is approximated as a single Slater determinant formed by N orthonormal spin orbitals ψ as shown in Eq. 2.6. It takes the spin exchange (the Pauli exclusion principle) into account but not the electronic correlations: The HF method is a non-correlated method.

2.4 Hohenberg-Kohn theorems

The Thomas-Fermi model gave the main ideas for the development of the DFT, which provides an approximate description of the electron density $n(\vec{r})$ in an atom or a solid.

In the DFT framework, the electron density $n(\vec{r})$ is used instead of the wave function to solve the many-body problem. It is easier to calculate the electron density as the number of electrons increases, because approximations are easier to formulate in this case. More importantly, the equations of the DFT are based on approximations which overcome the main drawback of the HF method, which totally neglects electron correlations.

In 1964, Hohenberg and Kohn laid the foundations of the DFT. They stated two theorems, which show that the electron density can be used as a basic variable to solve the many-body problem. These two theorems, known as Hohenberg-Kohn (HK) [181] theorems are as follows:

1. There is a one-to-one mapping between the external potential due to the nuclei V_{ext} and the ground-state density of interacting electrons moving in this potential, $n(\vec{r})$. The ground-state total energy (E) of the system can thus be expressed as a unique functional of this electron density, $E[n(\vec{r})]$.

2. There exists a functional $\mathrm{F_{HK}}[n(\vec{r})]$ associated with the total energy of the system $E[n(\vec{r})]$. The total energy $E[n(\vec{r})]$ reaches its global minimum or ground state energy when the corresponding electron density is the true ground state density $n_{\text{GS}}(\vec{r})$.

The electron density $n(\vec{r})$ is always a function of three spatial variables, which gives an enormous simplification for solving the Schrödinger equation. The HK theorems guarantee that any ground state property of a system (especially the total energy) can be obtained by using functionals of the electron density. According to HK theorems, the total energy can be written as:

$$E[n(\vec{r})] = T[n(\vec{r})] + E_{ee}[n(\vec{r})] + E_{\text{ext}}[n(\vec{r})] = F_{\text{HK}}[n(\vec{r})] + E_{\text{ext}}[n(\vec{r})] \tag{2.7}$$

where $T[n(\vec{r})]$ is the kinetic energy functional, $E_{ee}[n(\vec{r})]$ and $E_{\text{ext}}[n(\vec{r})]$ describe the electron-electron interaction and the nucleus-electron interaction, respectively.

According to the second HK theorem, the ground state energy can be obtained using the variational principle.

$$E_{\text{GS}} = \min(F_{\text{HK}}[n(\vec{r})] + E_{\text{ext}}[n(\vec{r})]) \tag{2.8}$$

The HK theorems proposed to solve the many-body Schrödinger equation using electron density and energy functionals. Still, until then there was no method to calculate the electron density and its functionals.

2.5 Kohn-Sham equations

The solution to calculate the ground state electron density methods came in 1965, when Kohn and Sham published an article giving practical ways to use the HK theorems and express the

electron density and its functionals [182]. They proposed to replace the interacting many-body problem by a fictitious system of non-interacting particles, chosen in such a way that their electron density is the same as in the original system of interacting particles. The Kohn-Sham (KS) equations thus consist in a set of equations in which the KS Hamiltonian is applied to single-particle wavefunctions:

$$\left[-\frac{\hbar^2}{2m}\nabla_i^2 + V_{\mathrm{KS}}(\vec{r})\right]\phi_i(\vec{r}) = \varepsilon_i\phi_i(\vec{r}) \tag{2.9}$$

where ε_i are the single-particle eigenenergies, $\phi_i(\vec{r})$ are the single-particle eigenfunctions and V_{KS} is an effective KS potential. The electron density is then calculated with the following equation:

$$n(\vec{r}) = \sum_i |\phi_i(\vec{r})|^2 \tag{2.10}$$

V_{KS} contains three terms:

$$V_{\mathrm{KS}} = V_{\mathrm{ext}} + V_{\mathrm{H}} + V_{\mathrm{XC}} \tag{2.11}$$

V_{H} is the classical Hartee potential resulting from the Coulomb interaction between electrons, which is expressed as:

$$V_{\mathrm{H}} = \int \frac{n(\vec{r})}{4\pi\epsilon_0|\vec{r}-\vec{r}'|}d\vec{r}' \tag{2.12}$$

V_{XC} is the exchange-correlation (XC) potential due to the quantum exchange effects and the many-body correlations. We can consider that most of the complexity of the many-body Schrödinger equation has been transferred into this term. The exact analytical form of the exchange-correlation functional for the many-electron system indeed remains unknown and new approximations have to be done.

2.6 Exchange-correlation approximations

Numerous approximations have been proposed to give an expression to the XC potential in order to make possible the DFT calculation of the material properties.

2.6.1 Local Density Approximation

The Local Density Approximation (LDA) is one of the simplest approximations; it was first provided by Kohn and Sham [182]. It is an important and quite accurate exchange-correlation approximation, widely used during the initial years of the development of DFT. The XC potential is constructed assuming the electron density is locally perfectly homogeneous by treating locally the electrons as a uniform electron gas. The XC energy of electrons with the density $n(\vec{r})$ can be written as a simple integral over space since it only depends on the electron density at $\vec{r}$:

$$E_{\mathrm{XC}}^{\mathrm{LDA}}[n(\vec{r})] = \int n(\vec{r})\varepsilon_{\mathrm{XC}}^{\mathrm{LDA}}(n(\vec{r}))d\vec{r} = \int n(\vec{r})\varepsilon_{\mathrm{X}}^{\mathrm{LDA}}(n(\vec{r}))d\vec{r} + \int n(\vec{r})\varepsilon_{\mathrm{C}}^{\mathrm{LDA}}(n(\vec{r}))d\vec{r} \tag{2.13}$$

where $\varepsilon_{\mathrm{X}}^{\mathrm{LDA}}(n(\vec{r}))$ and $\varepsilon_{\mathrm{C}}^{\mathrm{LDA}}(n(\vec{r}))$ are respectively the exchange and correlation energies per electron calculated for a uniform electron gas with the density $n(\vec{r})$. LDA provides reasonable accuracy for

calculating structural properties such as lattice constants and bond lengths, for a wide range of materials. However, it tends to be a poor approximation for bond energies.

2.6.2 Generalized-Gradient Approximation

LDA tends to underestimate the exchange energy and to overestimate the correlation energy [183] due to the assumption that the density is locally homogeneous. To improve the LDA and better take into account of the inhomogeneities of the electron density (which is particularly important when studying oxides), the Generalized Gradient Approximation (GGA) was later proposed. Within this approximation, the XC term not only depends on the local electron density $n(\vec{r})$, but also on its gradient $\nabla n(\vec{r})$:

$$E_{\mathrm{XC}}^{\mathrm{GGA}}[n(\vec{r})] = \int n(\vec{r})\varepsilon_{\mathrm{XC}}(n(\vec{r}), \nabla n(\vec{r}))d\vec{r} \tag{2.14}$$

Many variants of GGA functionals have been developed, such as PW91 [184], PBE [185], PBEsol [186], among the most famous ones. The GGA generally provides a better accuracy compared with LDA. The PBE functional [185], named after Perdew, Burke, and Ernzerhof who developed it, is the most widely used functional for electronic structure calculations. Compared to LDA, it improves atomic and cohesive energies, but it is not as accurate in solid-state physics as it is in chemistry. An improvement of the PBE functional for solid-state calculations was proposed in 2008 [186], leading to the so-called PBESol functional, which has been used during this thesis.

The DFT has been playing a crucial role in the field of physics, chemistry, and material science for the past several decades to predict the electronic and physical properties of materials [187]. It provides an *ab initio*, material-dependent computational framework for efficient geometry optimization, vibrational frequency and energy calculations. There are some drawbacks of the DFT: no universal exchange-correlation energy functional E_{XC} exists and the band gap of semiconductors and insulators is most of the time strongly underestimated with the approximations described previously. To improve the approximation of E_{XC}, many higher order functionals such as meta-GGA and hybrid functionals have been developed. The different levels of DFT exchange-correlation functionals are described by the Jacob's ladder [188], based on increasing accuracy and computational cost, as shown in Fig. 2.1.

2.6.3 The +U correction for strongly localized electrons

Several materials, such as transition-metal oxides and/or Mott insulators, can display strong electron-electron interactions. For these compounds, the standard XC functionals described in the previous sections are not sufficient to correctly calculate their ground state. The use of these approximations generally results in predicting wrong conductive and magnetic states. Indeed, as these approximations tend to underestimate the electron localization due to the spurious self-interaction, they end in the calculations of underestimated band gaps, favorizing ferromagnetic and metallic states, and they fail to correctly describe charge and orbitals ordering when they occur. If

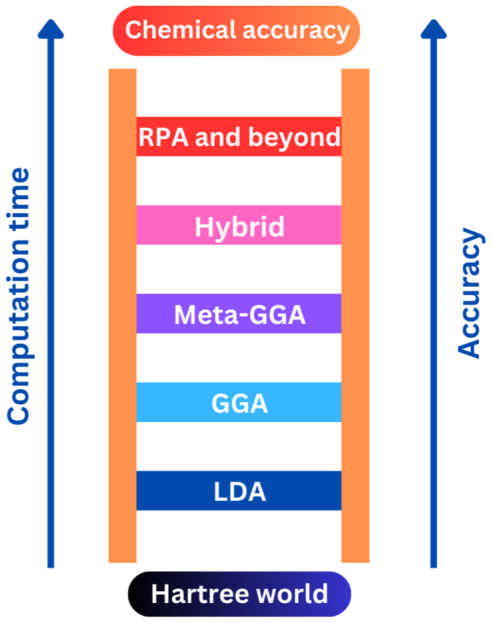

Figure 2.1 – Jacob's ladder to describe the increasing order of accuracy and computation time going from LDA to RPA (Random Phase Approximation) and beyond methods.

these problems can partly be solved by using higher-order functionals, it is at the cost of a higher complexity and higher computational times.

In the 90's, an alternative approach was proposed with the so-called DFT+U method [189], in which a parameter-dependent corrective term is simply added to the LDA or GGA XC functionals. This correction is only added to the correlated orbitals (generally the $3d$ and $4f$ orbitals only) and it depends on the occupancy n_i of these orbitals and on the on-site Coulomb and exchange parameters U and J, defined as in the Hubbard model. Because the $+U$ takes into account of correlation terms already calculated within the standard DFT functionals, it is important to avoid double counting; hence the general formula for the DFT+U writes as follow [190]:

$$E_{\mathrm{DFT}+U}[n(\vec{r})] = E_{\mathrm{DFT}}[n(\vec{r})] + E_{\mathrm{Hub}}[\{n_i\}] - E_{\mathrm{dc}}[\{n_i\}] \tag{2.15}$$

with $E_{\mathrm{Hub}}[\{n_i\}]$ and $E_{\mathrm{dc}}[\{n_i\}]$ the corrective energy and the energy term to avoid a double counting.

The DFT+U method presents the advantage to be computationally cost effective, while maintaining an accuracy comparable to other methods such as the Hybrid functional. A major difference with the HF theory is that the effective interaction in the $+U$ correction is screened and takes the correlation into account. Nonetheless, it is important to keep in mind that this method is only applied on a subset of the electronic states and that the values of U and J have to be chosen. If these parameters can be calculated from constrained DFT calculations, in several studies, as in this thesis, the $+U$ method is used as a semi-empirical method and the U and J parameters are varied so that the calculated electronic structure matches with experimental data or with numerical values calculated with higher-order functionals (see Appendix A). Finally, we have to mention that different versions of the DFT+U method exist. In this thesis, we used the simplified and

rotationnaly invariant approach of Dudarev, *et al.* [191] in which the correction only depends on the effective parameter $U_{eff} = U - J$.

2.7 Self-consistent field

The Self-Consistent Field (SCF) method is an iterative method for calculating the ground state density and energy of a many-body system. An illustration of the SCF in the framework of KS DFT calculations is shown in Fig. 2.2:

1. An initial electron density $n(\vec{r})$ is first provided to compute the KS potential.
2. The KS equations are solved to obtain the single-particle eigenenergies and wave functions
3. A new electron density is calculated from the wave functions, using Eq. 2.10.

When the convergence criteria is reached, the cycle stops and output physical quantities (ground state energy, forces, etc.) can be obtained from post-processing steps.

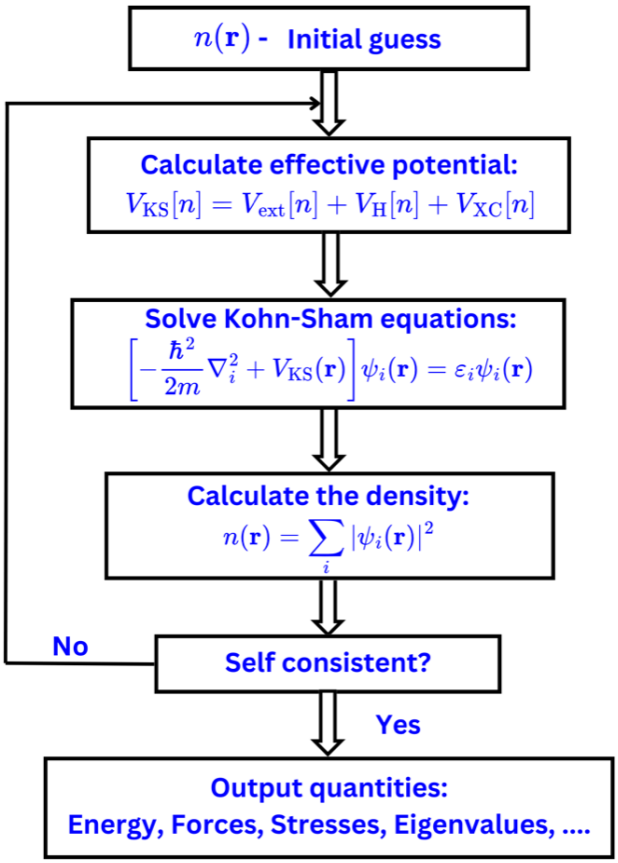

Figure 2.2 – Illustration of the self-consistent cycle in Kohn-Sham density functional theory calculations.

2.8 DFT Code and chosen parameters

In this thesis, the DFT-implemented code Vienna *Ab initio* Simulation Package (VASP.5.4.4) [192, 193] with the projector-augmented wave (PAW) method was used. A plane wave basis set with a cutoff energy of 600 eV was chosen after careful convergence tests to provide an accuracy on the total energy better than 10^{-2} eV for conventional cells containing 8 formula units (f.u.) of $CoFe_2O_4$ or $NiFe_2O_4$.

The PBEsol functional [186] was used for all calculations unless otherwise noted. To calculate the electronic structure of the spinel ferrites $CoFe_2O_4$ and $NiFe_2O_4$, we combined this functional with the $+U$ correction [191] applied to the d electrons of cations. The values of U_{eff} parameters have been set to 4.0, 4.0 and 2.5 eV for the Co, Fe and Ni elements, respectively, this in order to match as much as possible with experimental band gaps (the data are given in table A.4). More explanations about the choice of XC functional and U_{eff} parameters are given in Appendix A, where a comparison with other approximations is given.

To calculate the relative stability between different cation orderings and the vacancy formation energies, we used a cubic conventional unit cell of 8 f.u. of MFe_2O_4 with a Γ-centered and regular 6×6×6 k-grid. To study the surfaces and interfaces, we used slabs and superlattice geometries and a 6×6×1 k-point mesh.

The electronic structure and the forces were optimized until their convergence was better than 10^{-6} eV and 0.05 eV Å^{-1}.

2.9 *Ab initio* thermodynamics

The formation energy of a material depends on the chemical potentials associated to its chemical species. Predicting if this material is thermodynamically stable and if it can be synthesized necessitates to calculate a phase diagram which displays the ranges of chemical potentials for which the formation energy of the considered phase is lower than the formation energies of competing phases.

2.9.1 Calculation of the formation energy:

a. Direct method: Ground state energies of the compounds and of the elements calculated using the PBEsol+U functional

The formation energy of a complex oxide ($A_{n1}B_{n2}O_{n3}$; A, B= Co, Fe, Ni) is defined by Eq. 2.16 as the difference between the ground state energy of this oxide and of its constitutive elements in their standard phases:

$$\Delta E_f(\mathrm{A}_{n1}\mathrm{B}_{n2}\mathrm{O}_{n3}) = E_{\text{tot}}(\mathrm{A}_{n1}\mathrm{B}_{n2}\mathrm{O}_{n3}) - n_1 E^{\text{elem}}(\mathrm{A}) - n_2 E^{\text{elem}}(\mathrm{B}) - n_3 E^{\text{gas}}(\mathrm{O}) \tag{2.16}$$

In the above equation, $\Delta E_f(\mathrm{A}_{n1}\mathrm{B}_{n2}\mathrm{O}_{n3})$ is the formation energy per formula unit of the compound $\mathrm{A}_{n1}\mathrm{B}_{n2}\mathrm{O}_{n3}$, $E_{\text{tot}}(\mathrm{A}_{n1}\mathrm{B}_{n2}\mathrm{O}_{n3})$ is its ground state energy per formula unit, $E^{\text{elem}}(A)$ is the

elemental ground state energy per atom of the chemical species A, $E^{\text{gas}}(\text{O})$ is the ground state energy per oxygen atom of the O_2 molecule and n_1, n_2, n_3 are the numbers of elements A, B and O respectively, in the oxide formula unit.

In this method, all the energies entering in the expression of the formation energy are calculated from first-principles, by performing DFT calculations using the same exchange-correlation functionals. However, there is *a priori* no proof to justify that a given functional can be suitable to calculate at the same time the ground-state energy of the oxide and the ground-state energies of the elemental chemical species. To calculate the correct phase diagram, we need an accurate calculation of these elemental energies. This can alternatively be done using the so-called "Fitted Elemental-Phase Reference Energy" (FERE) method [194], which directly uses the values of the formation energies measured experimentally.

b. FERE method: Ground state energy of the compounds calculated using the DFT+U and of the elemental energies calculated from a fit of the experimental formation energies:

In this method, we use Eq. 2.17 for each oxide, which includes spinel ferrites and their competing phases.

$$\Delta E_f^{\text{Exp}}(\text{A}_{n1}\text{B}_{n2}\text{O}_{n3}) = E_{\text{tot}}^{\text{DFT+}U}(\text{A}_{n1}\text{B}_{n2}\text{O}_{n3}) - n_1 E^{\text{FERE}}(\text{A}) - n_2 E^{\text{FERE}}(\text{B}) - n_3 E^{\text{FERE}}(\text{O}) \quad (2.17)$$

where, $\Delta E_f^{\text{Exp}}(\text{A}_{n1}\text{B}_{n2}\text{O}_{n3})$ and $E_{\text{tot}}^{\text{DFT+}U}(\text{A}_{n1}\text{B}_{n2}\text{O}_{n3})$ are the experimental formation energy and the total ground state energy of $\text{A}_{n1}\text{B}_{n2}\text{O}_{n3}$, respectively (A, B = Co, Fe, Ni; $n1$, $n2$ = 0-3; $n3$ = 1-4). Here, we will consider 9 equations as we will study the 9 competing phases (CoO, FeO, NiO, Fe_2O_3, Ni_2O_3, Fe_3O_4, Co_3O_4, $CoFe_2O_4$, and $NiFe_2O_4$) with 4 unknowns variables(E^{FERE}(Fe), E^{FERE}(Co), E^{FERE}(Ni), and E^{FERE}(O)). Using the least square fit method, the unknown variables are calculated, which are the Fitted Elemental-Phase Reference Energies (FERE).

2.9.2 Phase diagram

The formation energies of the different competing phases of a given compound can be used to plot a phase diagram of the formation energies as a function of the variations of chemical potentials. Such phase diagrams have been calculated for the spinel ferrites and are given in Chapter 4. To define the stability domains, *i.e.* the ranges of chemical potentials, for which $CoFe_2O_4$ and $NiFe_2O_4$ are stable, it is necessary to fulfill a certain number of conditions:

1. We have to prevent elemental precipitation:

$$\Delta\mu_{\text{M}} \leq 0; \Delta\mu_{\text{Fe}} \leq 0; \Delta\mu_{\text{O}} \leq 0 \quad (2.18)$$

2. The MFe_2O_4 compounds have to be stable:

$$\Delta\mu_{\text{M}} + 2\Delta\mu_{\text{Fe}} + 4\Delta\mu_{\text{O}} = \Delta E_f(\text{MFe}_2\text{O}_4) \quad (2.19)$$

3. We must avoid the formation of competing phases like $M_lFe_mO_n$

$$l\Delta\mu_{\text{M}} + m\Delta\mu_{\text{Fe}} + n\Delta\mu_{\text{O}} \leq \Delta E_f(\text{M}_l\text{Fe}_m\text{O}_n) \quad (2.20)$$

where $\Delta\mu_i$ is defined as

$$\Delta\mu_i = \mu_i - E_i^{\text{elem}}; i = \text{M, Fe, O} \tag{2.21}$$

The μ_i and E_i^{elem} are the chemical potential of the chemical species i when it forms its compound and the total energy of the same chemical species i in its pure solid or gas phase. These Eqs. 2.18-2.20 are used to compute the phase diagram showing the ($\Delta\mu_{\text{M}}$, $\Delta\mu_{\text{Fe}}$, and $\Delta\mu_{\text{O}}$) domains, where MFe_2O_4 is more stable than competing phases.

2.9.3 Calculation of the formation energy of vacancy defects

Generalities

Experimentally grown materials always contain defects with a concentration that depends on the growth conditions of these materials. The vacancy formation energy is an important parameter for comparing the relative stability of the different types of vacancy defects. The vacancy formation energies $E_{\text{f}}\left[V_{\text{X}}^q\right]$ of single X-atom vacancies (V_{X}) with the charge state q have been calculated according to the following formula from Refs. [195–197]:

$$E_{\text{f}}\left[V_{\text{X}}^q\right] = E\left[\text{Host} + V_X^q\right] - E\left[\text{Host}\right] + \mu_{\text{X}} + q\left(E_{\text{VBM}}^{\text{H}} + \Delta E_{\text{F}}\right) + E_{\text{corr}} \tag{2.22}$$

where $E\left[\text{Host} + V_X^q\right]$ and $E\left[\text{Host}\right]$ are the total energies calculated by DFT methods for the defective and the non-defective cells of the host material, respectively. μ_{X} is the chemical potential of the atom removed to form the vacancy. q is an integer indicating the charge state of the vacancy X. For each compound that we studied, μ_{X} deviates by $\Delta\mu_{\text{X}}$ from the energy $E_{\text{X}}^{\text{elem}}$. We must consider the values of $\Delta\mu_{\text{X}}$ for which the host material is more stable than other competing materials. $\Delta\mu_{\text{X}}$ is calculated from the bulk stability phase diagram obtained using the methods explained in the previous subsection.

The term $q\left(E_{\text{VBM}}^{\text{H}} + \Delta E_{\text{F}}\right)$ in Eq. 7.1, is also equal to qE_{F}, where E_{F} is the Fermi energy. It corresponds to the chemical potential of the electrons added or removed, *i.e.* the modification of the energy due to the charge state of the defect; this quantity depends on the value of the Fermi level E_{F} within the fundamental band gap E_{g} of the host material [here defined as the energy difference between the conduction band minimum (CBM) and the valence band maximum (VBM), independently of the spin state]. The Fermi energy E_{F} is the sum of $E_{\text{VBM}}^{\text{H}}$, the energy of the VBM for the bulk host crystal, and ΔE_{F}, the variation of the Fermi level in the gap with respect to the VBM. The calculation of ΔE_{F} will be discussed further in this subsection.

Finally, E_{corr} in Eq. 7.1 is the Lany-Zunger correction [199], which includes the Makov-Payne correction [200] and a potential alignment, to correct for the shift of the electrostatic potential due to the limited size of the supercell. This correction is calculated using the PyDEF code [196, 201]; it depends on the values of the relative permittivity of the non-defective host material. An illustration of the terms that are used to calculate the vacancy formation energy is shown in Fig. 2.3.

From the term $q\left(E_{\text{VBM}}^{\text{H}} + \Delta E_{\text{F}}\right)$, we can infer that specific vacancies with a given charge state q are more or less stable depending on the position of the Fermi level ΔE_{F} in the band gap of

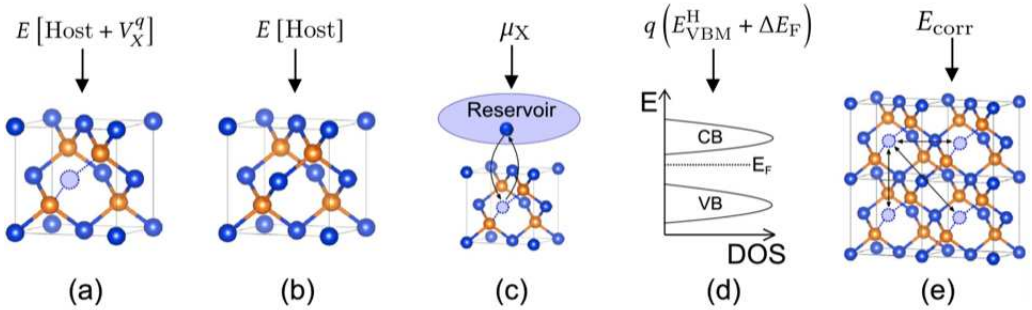

Figure 2.3 – Illustration of the contributions to the defect formation energy $E_f\left[V_X^q\right]$. The contributions are (a) the total energy of a system containing the defect, (b) the total energy of the same system without the defect, (c) chemical potential μ_X of element X that is exchanged between the material and atomic reservoirs to create the defect, (d) the Fermi energy qE_F (i.e. electron chemical potential) for defects with charge state q arising from exchanging electrons with an electron reservoir, and (e) finite-size corrections arising from, for example, potential alignment issues and image-charge interactions for charged defects. (Reprinted with permission from Ref. [198])

the spinel ferrite. The transition energies $\varepsilon(q_1/q_2)$ between two charge states q_1 and q_2 can be expressed as [195]

$$\varepsilon(q_1/q_2) = \frac{E_f\left[V_X^{q_1}, \Delta E_F = 0\right] - E_f\left[V_X^{q_2}, \Delta E_F = 0\right]}{q_2 - q_1} \tag{2.23}$$

The energy of each charged structure has been calculated after optimizing the lattice parameters and atomic coordinates so that each charged state transition energy $\varepsilon(q_1/q_2)$ also takes into account the contribution of the lattice relaxation. If the Fermi level is below $\varepsilon(q_1/q_2)$, charge state q_1 is stable; If the Fermi level is above $\varepsilon(q_1/q_2)$, charge state q_2 is stable. The charge state of a defect can be changed by optical excitation or by applying an electric field to change the Fermi level.

Equilibrium Fermi level and defect concentrations

An equilibrium Fermi level can be calculated for specific growth conditions. It depends on the temperature T and on the concentration of X-atom vacancies with charge state q through the following electrical-neutrality equation [202, 203]:

$$p - n + \sum_{X,q} q\left[V_X^q\right] = 0 \tag{2.24}$$

where n and p are respectively the temperature-dependent concentrations of electrons at the bottom of the conduction band and holes at the top of the valence band for the bulk host material:

$$n = N_c(T) exp\left[\frac{E_F - E_{CBM}^H}{k_B T}\right] \tag{2.25}$$

and

$$p = N_v(T) exp\left[\frac{E_{VBM}^H - E_F}{k_B T}\right]. \tag{2.26}$$

$N_{c(v)}(T) = \left(\frac{2\pi m^*_{e(h)} k_B T}{h^2}\right)^{3/2}$ are the effective carrier densities of states near the bottom of the conduction (c) band and top of the valence (v) band. The effective carrier density of states depends on the effective mass of the electrons or holes, temperature (T) and Fermi energy (E_F). These formulas are derived from the parabolic band approximation and in our calculations we only considered a single and non-degenerate band for the CBM and VBM.

The concentration of the atom vacancies $[V_X^q]$ depends on the formation energy of this defect, on the concentration [X] of the X atoms in the bulk host compound and on the temperature T:

$$[V_X^q] = [X] exp\left[-\frac{E_f\left(V_X^q\right)}{k_B T}\right] \tag{2.27}$$

with k_B the Boltzmann constant.

Because the formation energies $E_f\left(V_X^q\right)$ depend on the value of the Fermi level, the equilibrium Fermi level must be determined self-consistently. We chose to calculate the Fermi level in the framework of the "defect freezing-in" approximation [204]: First, the concentration of each vacancy is calculated according to Eqs. 2.24-2.27 at a high temperature T_g, which is close to some reported growth temperatures [93, 95]; then, considering that the materials are quenched and the Fermi level is further measured at room temperature, we calculate a new value for the Fermi level at T_R = 298 K, with the constrain that the concentration of defects for a given chemical species must stay constant:

$$\sum_q \left[V_X^q(T_g)\right] = \sum_q \left[V_X^q(T_R)\right] \tag{2.28}$$

where $\left[V_X^q(T_g)\right]$ and $\left[V_X^q(T_R)\right]$ are the concentrations of vacancies of atom X with a charge state q at the temperatures T_g and T_R. The Eq. 2.28 is solved self consistently to calculate ΔE_F.

Calculation of the effective masses

The effective mass of the electrons and holes can be calculated from the band dispersion near the CBM and VBM, respectively. To calculate the effective mass, we use the fact that

$$E(k) = E_0 \pm \frac{\hbar^2 k^2}{2m^*} \tag{2.29}$$

in the vicinity of the VBM or of the CBM. In Eq. 2.29, E_0 is the energy of the VBM (CBM), k is the Bloch wave vector with respect to the Bloch vector where the VBM (CBM) is found, and m^* is the electron or hole effective mass. This equation can be used to write:

$$m^* = \pm \lim_{k\to 0} \frac{\hbar^2 k^2}{2(E(k) - E_0)} \tag{2.30}$$

or, in reduced units:

$$\frac{m^*}{m_0} = \pm \lim_{k\to 0} \frac{(k a_0)^2}{(E(k) - E_0)/Ry} \tag{2.31}$$

$$a_0 = \frac{4\pi\epsilon_0 \hbar^2}{m_0 e^2} = 0.52918 \text{ Å} \tag{2.32}$$

$$Ry = \frac{m_0 e^4}{2(4\pi\epsilon_0\hbar)^2} = 13.60569 \text{ eV} \tag{2.33}$$

m_x, m_y, and m_z are the effective masses calculated with Eq. 2.31 when the Bloch wave vector is in the directions [100], [010], and [001], respectively. The so-called density of states effective mass $m_e^*(m_h^*)$ is finally calculated as $|M_c|(m_x m_y m_z)^{1/3}$, where $M_c = 1$ is the number of valleys in the Brillouin zone.

2.9.4 Surface formation energy

The surface formation energy is a crucial quantity in surface thermodynamics that allows us to understand the stability of surfaces. For a (T, P) ensemble, the Gibbs free energy G is an important quantity to study. In this work, we studied MFe_2O_4 surfaces. According to Heifets, *et al.* [205], the surface formation energy is defined by the equation:

$$\gamma = \frac{G^{\text{slab}} - n_M\mu_M - n_{Fe}\mu_{Fe} - n_O\mu_O}{2A} \tag{2.34}$$

where μ_X (X = M, Fe, and O) are the chemical potentials of the elements X and n_X the numbers of X atoms in the slab. A is the surface area of the slab, and the factor 2 takes into account the fact that each slab has two identical surfaces.

The Gibbs free energy of the slab G^{slab} can be defined by Eq. 2.35 [205]:

$$G^{\text{slab}} = E^{\text{slab}} + E^{\text{vib.}} - TS + PV \tag{2.35}$$

In this equation, E^{slab} is the slab energy obtained directly from the DFT calculations. $E^{\text{vib.}}$ is the vibrational contribution to the crystal energy, and T, S, P, and V are the temperature, entropy, pressure, and volume of the crystal, respectively. The term $E^{vib.}$ is generally neglected [205] due to its small contribution, but this approximation fails if the material has soft modes. The calculation of the vibrational spectra of a slab is computationally expensive and it has been neglected in our study. Since our DFT calculations are done at $T = 0$ K, the TS term is zero and the contribution of the PV term is usually less than 5 meV for a pressure of 100 atm (in general, the growth pressure of spinle ferrites is below 100 atm). Therefore, in our calculations, we considered that:

$$G^{\text{slab}} \simeq E^{\text{slab}} \tag{2.36}$$

and the equation used for calculating the surface formation energy in this thesis is:

$$\gamma = \frac{E^{\text{slab}} - n_M\mu_M - n_{Fe}\mu_{Fe} - n_O\mu_O}{2A} \tag{2.37}$$

The chemical potential of the element X (defined by Eq. 2.21) depends on the growth conditions of the slab. The total energy of the bulk MFe_2O_4 can be written as:

$$E^{\text{bulk}}_{MFe_2O_4} = \mu_M + 2\mu_{Fe} + 4\mu_O \tag{2.38}$$

Using the above two equations, the surface formation energy can be written as:

$$\gamma = \frac{E^{\text{slab}} - \frac{n_O}{4}E^{\text{bulk}}_{MFe_2O_4} - \alpha\mu_M - \beta\mu_{Fe}}{2A}; \alpha = (n_M - \frac{n_O}{4}); \beta = (n_{Fe} - \frac{n_O}{2}) \tag{2.39}$$

Finally, using the Eqs. 2.21 and 2.39, we obtain the following expression of the surface energy γ:

$$\gamma = \frac{E^{\text{slab}} - n_{\text{M}} E^{\text{bulk}}_{\text{MFe}_2\text{O}_4} - \alpha E^{\text{metal}}_{\text{M}} - \beta E^{\text{metal}}_{\text{Fe}}}{2A} - \frac{(\alpha \Delta\mu_{\text{M}} + \beta \Delta\mu_{\text{Fe}})}{2A} \tag{2.40}$$

which is only expressed from total energies E which can be obtained from DFT calculations and which is a function of the variations of the chemical potentials $\Delta\mu_i$.

Using the bulk phase diagram defined in Section 2.9.2 and the Eq. 2.40, it is possible to calculate which surface termination, depending on its atomic structure and chemical composition, is stable for the ranges of chemical potentials for which the bulk ferrites are also stable, *i.e.* for the experimental (T,P) growth conditions for which they can be synthesized.

2.10 Other codes and program used

Every calculation was performed using the HPC resources of CALMIP (Grant p19004 and p1229). The VASPKIT program [206] was used for post-processing of VASP calculations to get quantities such as the density of states, the band structure, and the local potential. Home-made bash scripts were written to extract and analyze the calculation data. The VESTA software [35] was used to create structure files and to plot atomic structures. Gnuplot and Python programs were used to plot the data.

Chapter 3

Bulk stoichiometric spinel ferrites

As already explained in Chapter 1, spinel ferrites have many possible short-range cation orderings due to the arrangement of divalent cations (Co or Ni) and trivalent cations (Fe) at the Oh and Td sites. Several computational studies in the literature help to understand the dependence of the electronic and magnetic properties of spinel ferrites on the cation ordering [125, 126, 130, 207]. There is a large variation in the electronic properties due to the cation ordering. Before studying the effect of surfaces and interfaces (with or without defects), it is important to study in detail the physical properties of the perfect bulk spinel structure as a starting point and as a reference for later comparisons. In this chapter, we will discuss detailed results on how the structural, electronic, and magnetic properties of bulk CFO and NFO depend on the cation ordering.

3.1 Cation ordering at Oh sites in the inverse spinel structure

Both CFO and NFO are known to predominantly adopt the inverse spinel structure, which means that the Co(II) or Ni(II) cations share the occupied Oh sites with half of the Fe(III) cations, while the other half of the Fe(III) cations are in the occupied Td atomic sites. If a spinel ferrite MFe_2O_4 (where M is a divalent cation) would adopt the normal structure, all the M(II) cations would be in the occupied Td atomic sites and the space group would be 227-$Fd\bar{3}m$. The inverse spinel structure would retain this space group if the +II and +III cations were randomly distributed within the occupied Oh sites. Cation ordering may also occur in the occupied Oh sites [97, 208], breaking the symmetries and reducing the space group of the inverse spinel to a subgroup of $Fd\bar{3}m$. In this section, we discuss the consequences of this cation ordering on the properties of bulk CFO and NFO with inverse spinel structure.

3.1.1 Atomic structures and their stability

In the conventional cubic cell containing 8 MFe_2O_4 f.u. (*i.e.* 56 atoms), 8 Fe(III) and 8 M(II) cations must be distributed among the 16 occupied Oh sites, resulting in $\binom{16}{8}$ = 12870

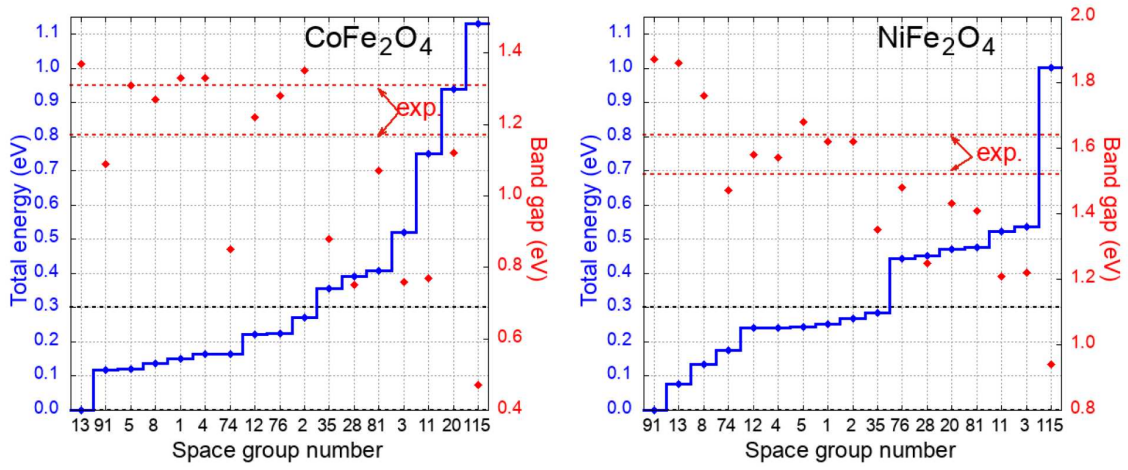

(a) (b)

Figure 3.1 – Total energy E (with respect to the most stable space group) of the cubic conventional cell containing 8 f.u. of the perfect inverse spinels $CoFe_2O_4$ (a) and $NiFe_2O_4$ (b) and band gap width E_g at the Fermi level E_F, as a function of the space group number [209]. The different space groups correspond to different cation distributions in the occupied Oh sites. The ground state energy of the most stable structure is chosen as the origin of the energies and the space groups are ordered by increasing values of E. The band gap width E_g corresponds to the smallest energy difference between the highest occupied band and the lowest unoccupied band for one of the two spin directions.

possible distributions. The number of non-equivalent structures is reduced to 97, distributed over 17 different space groups. While space groups with multiple symmetry operations are associated with only a small number of equivalent structures (e.g. only 6 equivalent structures for the space group 91-$P4_122$), space groups with low symmetry correspond to a larger number of non-equivalent possible structures (the space group 1-P_1 corresponds for instance to 9312 different structures, of which 49 are non-equivalent). We studied the physical properties of structures belonging to the different space groups for the sake of simplicity, we first randomly chose one of the possible structures corresponding to each of the 17 space groups. The corresponding results for the lattice parameters, magnetic moment, band gap, and total energy are given in the tables in appendix B.1 and B.2 for CFO and NFO, respectively.

As suggested in the literature, we found that the structures with the most homogeneous cation distributions are the most stable. Among all the structures studied, we found that the ground state distribution corresponds to the space group 13-$P2/c$ for CFO and 91-$P4_122$ for NFO. The energy difference $\Delta E_{91,13} = E_{91} - E_{13}$ between these two stable phases is of 15 meV/f.u. for CFO and −9 meV/f.u. for NFO (see Fig. 3.1).

The cation distributions of three of the most stable structures (space groups 13, 74, and 91) and of the least stable one (space group 115) are shown in Fig. 3.2. The three stable structures share the characteristic of having a homogeneous distribution of first-neighbor cations, the occupied

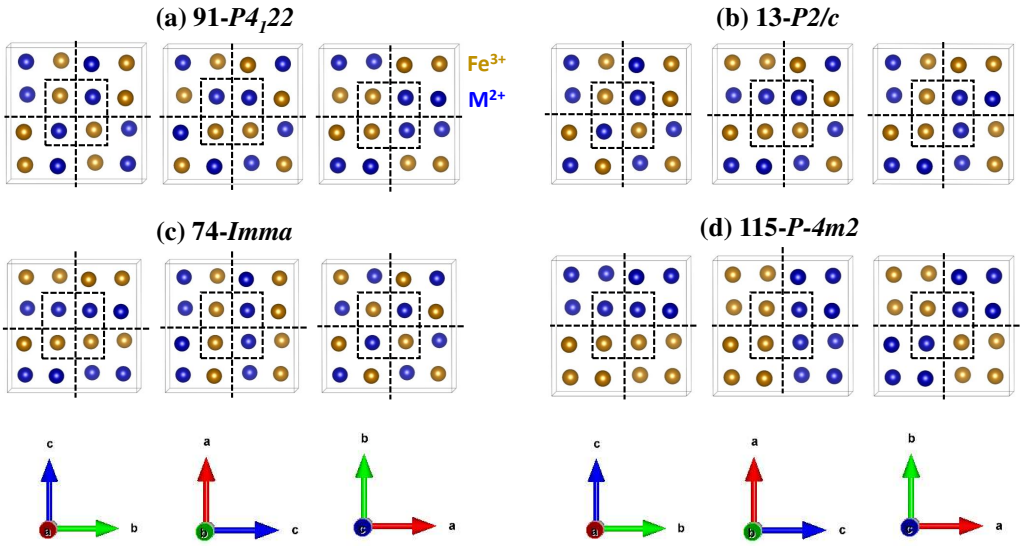

Figure 3.2 – Locations of the Fe^{3+} and M^{2+} cations occupying Oh sites in the 8-f.u. conventional cells with space groups 13, 74, 91 and 115. Black dotted lines delimitate the five tetrahedral formed by occupied octahedra sites; in structures (a-c), they all contain two Fe^{3+} and two M^{2+} cations at their corners. The figures were plotted using VESTA [35].

octahedral sites forming tetrahedra with two M^{2+} and two Fe^{3+} cations at their vertices. These three structures thus satisfy the Anderson conditions based on the predominance of short-range order [210]. For both CFO and NFO, the space group 115-$P\bar{4}m2$, which consists of a superlattice with perfect segregation of M and Fe atoms on each side of the cubic cell, is the least stable, with an energy of about 130 meV/f.u. above that of the most stable structure.

In the cation ordering at the Oh sites of the conventional 8 f.u. cubic cell, we did not study all the structures from the space groups that have more than one inequivalent structure due to computational cost. To verify which cation ordering is the true ground state of the CFO and NFO crystals, we started from the most stable cation configuration and, using the 4 f.u. primitive cell, we generated new structures by exchanging 1 or 2 M/Fe atom pairs located in occupied Oh sites (the inequivalent structures and their multiplicities are shown in the table of the appendix B.3). Fig. 7.3 shows the evolution of the ground state energy and of the band gap width at the Fermi level as a function of the number of swaps. The detailed results for lattice parameters, magnetic moment, band gap, and total energy are shown in the tables in the appendix B.4 and B.5 for CFO and NFO, respectively. The variations of the calculated band gap E_g as a function of total energy for the different cation distributions are more random for CFO than for NFO. However, for both materials, the general trend is a decrease of E_g for the less stable structures. Thus, the calculated values of the fundamental band gap vary from 1.38 to 0.55 eV and from 1.34 to 0.57 eV for CFO and NFO, respectively. The few structures with an energy less than 0.03 eV/f.u. higher than the most stable one shows band gap variations of less than 25% for NFO and 38% for CFO, suggesting that the band gap is more sensitive to cation disorder for CFO.

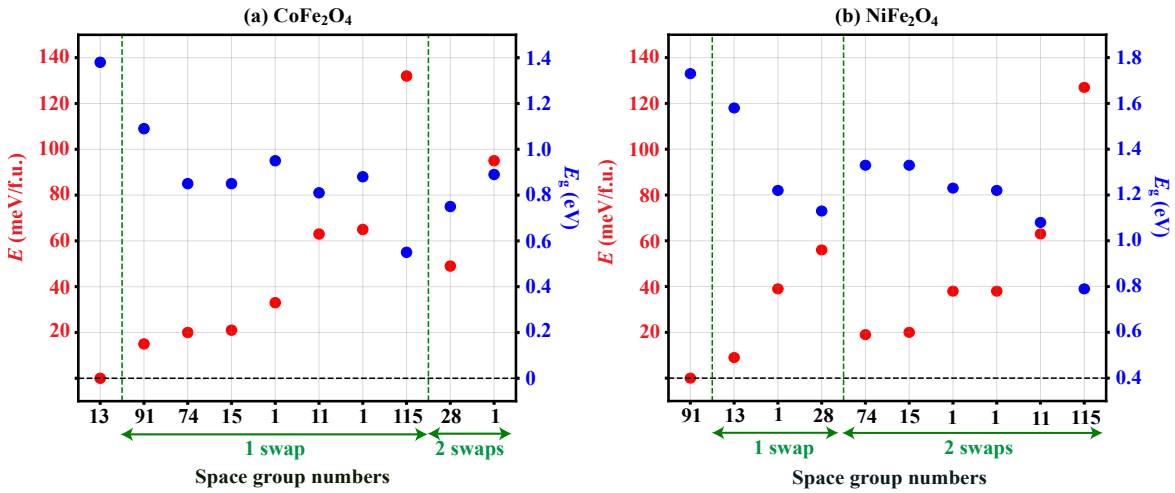

Figure 3.3 – Total energy E of the primitive unit cell containing 4 f.u. of the perfect inverse spinels $NiFe_2O_4$ and $CoFe_2O_4$ and band gap width E_g at the Fermi level E_F, as a function of the space group number [209]. The different space groups correspond to different cation distributions in the occupied Oh sites, which are generated by swapping one or two pair(s) of M/Fe atoms. The ground state energy of the most stable structure is chosen as the origin of the energies and the space groups are ordered by increasing values of E. The band gap width E_g corresponds to the smallest energy difference between the highest occupied band and the lowest unoccupied band for one of the two spin directions.

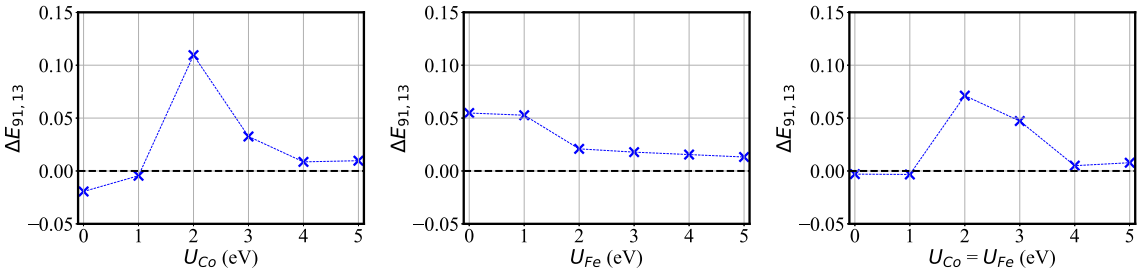

(a) (b) (c)

Figure 3.4 – The variation of $\Delta E_{91,13}$ as a function of Hubbard parameters in CFO: (a) for U_{Fe} = 4 eV, (b) for U_{Co} = 4 eV, and (c) for $U_{Co} = U_{Fe}$.

To our knowledge, the centrosymmetric space group 13-$P2/c$, which has been found to be the most stable for CFO, has never been studied or reported in the literature. To understand the effect of the Hubbard parameter (U) on the relative stability of the space group 13-$P2/c$ with respect to the space group 91-$P4_122$, we compared the $\Delta E_{91,13}$ calculated for CFO at different values of U of Co and Fe atoms. In Fig. 3.4 (a), U_{Fe} is fixed at 4 eV, and as U_{Co} increases above 1 eV, the 13-$P2/c$ space group is more stable than the 91-$P4_122$ space group. In the second case, where U_{Co} is fixed at 4 eV (in Fig. 3.4 (b)), the 13-$P2/c$ space group was always the most stable, regardless of the value of U_{Fe}. In Fig. 3.4 (c), we varied both U_{Co} and U_{Fe} simultaneously and

got similar results as in case (a). These results confirm that the 13-$P2/c$ space group becomes the most stable only when the $+U$ correction is applied to Co (above 1 eV), while the 91-$P4_122$ space group is otherwise more stable. The stability of the supercell with space group 13-$P2/c$ could be a consequence of the electron correlation in CFO and could only be observed at low temperatures and under very specific experimental conditions. In the same way, low symmetry space groups have been demonstrated to explain the low-temperature charge ordering in magnetite [211]. An experimental determination of the actual lowest energy phase of CFO may not be easy, since the CFO crystal is likely to exhibit local fluctuations in its cation distribution, which may be strongly dependent on the growth conditions.

The structure corresponding to space group 91-$P4_122$ is the most stable for NFO. It corresponds to the maximally homogeneous distribution of divalent and trivalent cations over the octahedral sites and thus represents the global minimum of electrostatic energy. According to the point-ion electrostatic (PIE) model [212], this structure has been claimed to correspond to the universal space group for ordered inverse spinels at low temperature; this has been confirmed experimentally on various compounds [213]. Our results for NFO are in agreement with previous DFT studies [126, 128, 214], which however compared only a very small number of well-ordered inverse spinel structures. The predicted lowest energy space group of NFO also corresponds to that measured at 300 K on single crystals by Raman spectroscopy [208] or by synchrotron diffraction [97]. The authors of this last reference demonstrated the appearance of an electric polarization associated with the cation ordering and the non-centrosymmetry of the structure below 98 K, thus making this compound an intrinsic magnetoelectric multiferroic material [97, 129].

In addition to the 91-$P4_122$ space group (sometimes called the α phase), the orthorhombic 74-*Imma* space group (β phase) is often mentioned in the literature as corresponding to the second possible short-range cation ordering for an inverse spinel structure [208, 215]. The corresponding cation distribution shows an alternation of (001) Oh atomic layers with only M(II) or Fe(III) cations, while (100) and (010) layers have equal amounts of M and Fe atoms. For both CFO and NFO, the *Imma* structure is found to be $\simeq 0.02$ eV/f.u. less stable than the lowest energy structure.

Since the energy difference between the crystal cells with the space groups 13-$P2/c$ and 91-$P4_122$ is very small, and for easier comparisons between NFO and CFO, we will mostly give details for the space group $P4_122$, which will be considered as the main reference.

The calculated equilibrium pseudo-cubic lattice parameter $\langle a_0 \rangle = V^{1/3}$ (V is the volume of the conventional cell of 8 f.u.) of the $P4_122$ reference structure is 8.331 Å and 8.283 Å for CFO and NFO, respectively, which is 0.7 % lower than the experimental values [60, 67]. The calculated pseudo-cubic lattice parameter is the same (within 0.02%) for the four most stable structures of NFO. The tetragonal distortion inherent to the $P4_122$ space group is rather small ($c/a = 0.995$ for CFO and 1.002 for NFO).

3.1.2 Magnetic properties

The experimentally measured magnetic ordering is ferrimagnetic (FiM), with all cations ferromagnetically coupled in each of the Td and Oh sublattices, while the magnetic moments have an antiparallel orientation between the Td and Oh sites. This can be summarized by the following formula: $(Fe_{\downarrow})_{Td}[M_{\uparrow},Fe_{\uparrow}]_{Oh}O_4$, where M = Co or Ni and the arrows indicate the orientation of the magnetic moments.

The total spin magnetic moment $M_{f.u.}$ per formula unit can thus be estimated from the formula:

$$M_{f.u.}(MFe_2O_4) = \sum |M_{Oh}| - \sum |M_{Td}| \tag{3.1}$$

which can be simplified as:

$$M_{f.u.}(MFe_2O_4) = M(M^{2+}_{Oh}) \tag{3.2}$$

These equations are based on the hypothesis that all cations in the CFO and NFO crystals with the inverse spinel structure are perfectly ionized and described by the same electronic structures as if they were isolated ($3d^5 4s^0$, $3d^7 4s^0$ and $3d^8 4s^0$ for Fe^{3+}, Co^{2+} and Ni^{2+}, respectively). The total spin magnetic moments remain exactly the same for all inverse structures (*i.e.* independent of the cation distribution in the Oh sites), with values of $M_{f.u.}(CFO) = 3\ \mu_B$ and $M_{f.u.}(NFO) = 2\ \mu_B$.

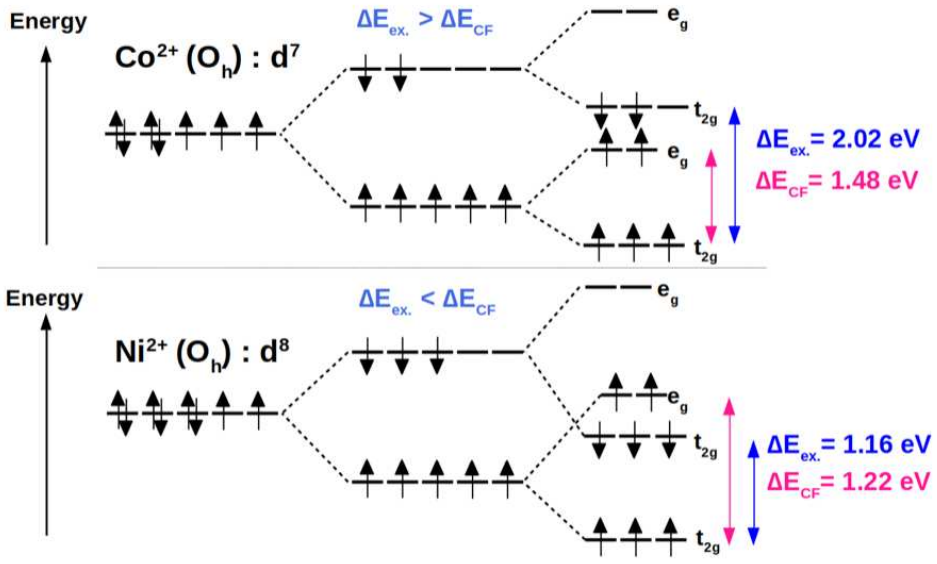

Figure 3.5 – Schematic representation of the *d*-state energies of Co^{2+} and Ni^{2+} cations, located in an octahedral environment and adopting a high and low spin state respectively. Additional lifts of degeneracies resulting from the cation distributions in $CoFe_2O_4$ and $NiFe_2O_4$ are not shown here. Exchange energies $\Delta E_{ex} = E^{\downarrow}(t_{2g}) - E^{\uparrow}(t_{2g})$ and crystal field energies $\Delta E_{cf} = E^{\uparrow}(e_g) - E^{\uparrow}(t_{2g})$ were calculated from averaged values of the projected DOS.

As we will show later, the analysis of the density of states (DOS) curves shows that the Ni^{2+}_{Oh} cations are in a low spin state, while the Co^{2+}_{Oh} cations are in a high spin state with electronic configurations as sketched in Fig. 3.5. The nature of the spin state of the Ni cations does not

affect their spin magnetic moment when they are in the +2 oxidation state; the situation may be different near structural defects due to charge transfer. For CFO, the calculated energy difference between configurations where Co^{2+} cations are in the low and high spin states is 0.63 eV/f.u., and the total spin magnetic moment would decrease from 3 μ_B/f.u. to 1 μ_B/f.u. if a transition between these two states would occur.

3.1.3 Electronic structure

DOS curves are shown in Fig. 7.4(a) and (b) for CFO and NFO, respectively. The fundamental Kohn-Sham band gap is delimited by the highest occupied band energy and the energy of the lowest unoccupied states, independent of the spin direction. For CFO, this band gap is between the minority-spin VBM, where cobalt cations have a major contribution, and the minority spin CBM, which corresponds to Fe(Oh) bands. The CBM of NFO also corresponds to minority-spin unoccupied Fe(Oh), but its VBM corresponds to majority spin bands and to hybridization of Ni(Oh)-*d* and O-*p* orbitals, in agreement with references [125, 126, 130]. The difference in spin polarization of the VBM between CFO and NFO is due to the fact that Co^{2+} cations adopt a high spin state, while Ni^{2+} cations display a low spin state; consequently, the highest occupied *d* bands will correspond to minority-spin t_{2g}-like orbitals for CFO and to majority-spin e_g-like orbitals for NFO (see the energy diagram in Fig. 3.5). The fundamental band gap energy E_g calculated for the space group $P4_122$ is 1.09 eV for CFO and 1.34 eV for NFO.

Experimentally, optical band gaps have been measured in the energy ranges 1.17-1.3 eV for CFO [64, 65] and 1.52-1.65 eV for NFO [65, 68, 127]. The optical band gap widths are associated with spin-state preserving electronic transitions and thus should be larger than the calculated fundamental band gaps. A direct comparison with our numerical calculations would require to know exactly which electronic transitions experiments refer to. The lowest optical band gap is between the highest occupied band and the lowest unoccupied band of the minority spin channel, for both CFO and NFO. The values of this band gap are given in Fig. 3.1. For the space group $P4_122$, it is respectively equal to 1.09 eV for CFO (also corresponding to the fundamental band gap) and to 1.73 eV for NFO, which is close to the experimental measurements. A comparison between our calculated values and other theoretical band gaps reported in the literature is difficult because of their large spread, from 0.63 to 1.5 eV for CFO [64, 65, 122–126, 128, 130] and from 0.98 to 2.27 eV for NFO [65, 122, 123, 126, 127, 129–131]. Such a dispersion reflects the diversity of numerical methods and approximations used to calculate the exchange-correlation potential for these compounds, which in principle includes all user-dependent corrections (+*U*, hybrid or meta-GGA) needed to correctly reproduce the insulating behavior of CFO and NFO [132].

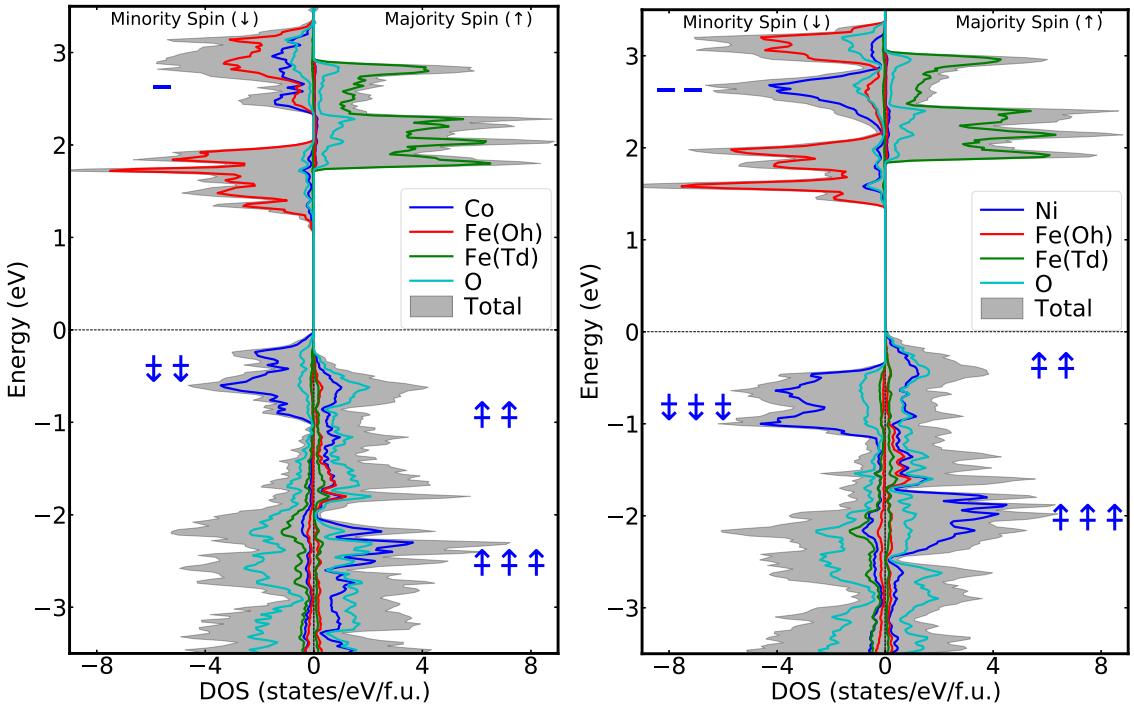

(a) $CoFe_2O_4$ (b) $NiFe_2O_4$

Figure 3.6 – Spin- and site-projected DOS (per formula unit) calculated for the perfect bulk (a) $CoFe_2O_4$ and (b) $NiFe_2O_4$ inverse spinel structures with space group $P4_122$. Majority and minority spin DOS curves are shown in the right and left panels of each figure, respectively. Blue lines next to the DOS peaks, with/without arrows, show the theoretical orbital filling of the Co^{2+} and Ni^{2+} cations.

3.2 Influence of the inversion degree on the physical properties

The experimentally measurable deviations of the M/Fe cation distribution between the Td and Oh atomic sites from that of the perfect inverse spinel must be taken into account because they modify the physical properties of spinel ferrites, such as the magnetization or the lattice parameter. Before being studied by DFT-based methods [125, 126, 130], the influence of the inversion degree parameter λ on the physical properties of spinel oxides was first investigated by phenomenological models based on the concepts of crystal field stabilization energy (CFSE) and octahedral site preference energy (OSPE), which is the difference of CFSE between octahedral and tetrahedral sites. The cation site occupancy depends on the coordination number, on the number of electrons occupying their d orbitals (cations with a higher charge preferentially occupy Oh sites because they offer a higher degree of coordination), and on the orbital radii, which depend on the cation electronegativity [216] (smaller atoms are preferentially located in Td atomic sites). M and Fe cations with high atomic radius will be responsible for a distortion of the oxygen atom sublattice, which allows accommodating the presence of these chemical species in their crystallographic sites.

However, crystal field theory can be insufficient and must be improved by adding the Madelung energy [217, 218] or by including temperature effects through Monte Carlo simulations [212, 219]; such a method allowed Stevanović, *et al.* to determine the inversion character of a spinel crystal as a function of the charges of the two cations and the structural distortion u of the oxygen sublattice [219].

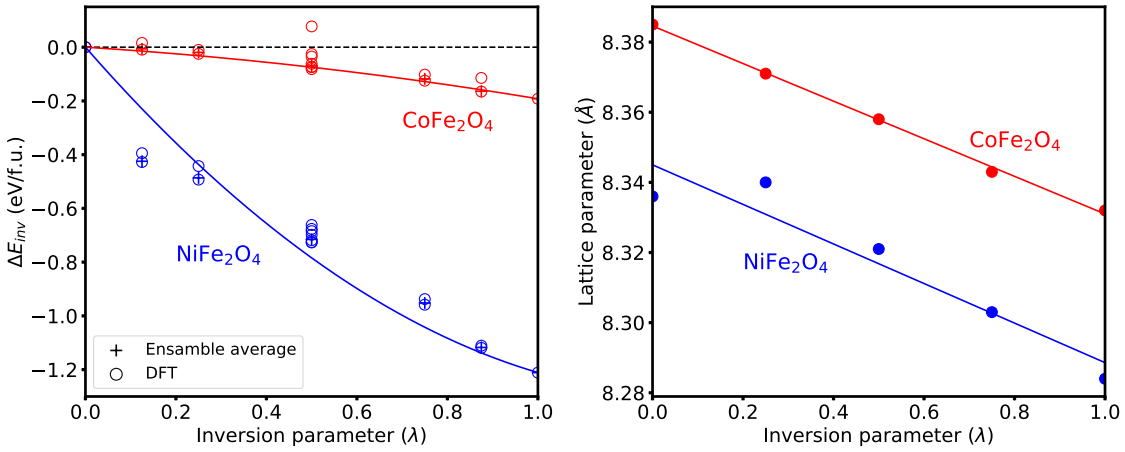

(a) (b)

Figure 3.7 – (a) Variations of the total energy ΔE_{inv} and (b) of the pseudo-cubic lattice parameter a as a function of the inversion parameter λ. ΔE_{inv} is given with respect to the energy of the perfect normal spinel structure: $\Delta E_{\text{inv}}(\lambda) = E(\lambda) - E(0)$. The open circles correspond to the energies calculated by DFT for all possible structures generated from the primitive cell with space group $P4_122$ ($\lambda = 0$, 0.25, 0.5, 0.75, 1) or from the conventional cell ($\lambda = 0.125$, 0.875). The crosses are the ensemble average of these calculated energies, which are used for the quadratic fits represented by the solid lines. Lattice parameters are given for the most stable structures.

3.2.1 Atomic structure versus inversion degree

The cation distribution in a crystal with a not-perfectly inverse spinel structure can be described by the formula $\left(M^{2+}_{1-\lambda}Fe^{3+}_{\lambda}\right)_{\text{Td}}\left[M^{2+}_{\lambda}Fe^{3+}_{2-\lambda}\right]_{\text{Oh}}O^{2-}_{4}$, $\lambda = 0(1)$ corresponding to a normal(inverse) spinel structure.

Fig. 7.5(a) shows the variations ΔE_{inv} of the total energy of the supercell as λ increases from 0 to 1. Several structures corresponding to different cation distributions for a given value of λ have been calculated. Their energy differences spread at most in a range of 0.065 eV/f.u. and 0.159 eV/f.u. for NFO and CFO, respectively, with CFO showing a larger spread than NFO. The λ dependence of the ensemble-averaged value ΔE_{inv} is quadratic [220] and we used the formula $\Delta E_{conf} = a\lambda + b\lambda^2$ for the parabolic fit. The coefficients a and b are -0.086 eV/f.u. and -0.106 eV/f.u. for CFO, 0.715 eV/f.u. and -1.926 eV/f.u. for NFO. These coefficients satisfy the condition for the fully inverse spinel at 0K (b+0.5a < 0) shown by Seko et al. [221]. Our calculated energy difference between the normal and inverse cation distributions $\Delta E_{\text{inv}}(\lambda = 1) = E(\lambda = 1) - E(\lambda = 0)$ is about

−1.21 eV/f.u. for $NiFe_2O_4$ and −0.19 eV/f.u. for CFO, *i.e.* almost 6 times lower, confirming that NFO is more likely to be found with a perfectly inverse spinel structure. A qualitative agreement is found between our data and previously reported results, with $\Delta E_{\mathrm{inv}}(\lambda = 1)$ varying from −0.34 to −0.19 eV/f.u. for CFO [124–126] and from −0.60 to −0.89 eV/f.u. for NFO [126, 222, 223].

Using the variations of $\Delta E_{\mathrm{inv}}(\lambda)$, we calculated the configurational Gibbs free energy, which allows us to determine the equilibrium inversion parameter of each oxide as a function of the growth temperature T_g [224, 225]. The variation of the configurational Gibbs free energy ΔG_{conf} between the spinel structures with different degrees of inversion can be expressed as a function of the temperature by the following equation [224, 225]:

$$\Delta G_{conf} = \Delta E_{conf} + \Delta E_{vib} - T\Delta S_{conf} - T\Delta S_{vib} \tag{3.3}$$

The vibrational energy and entropy are material dependent. Tielens et al. [226] show that the change in vibrational entropy of $CoAl_2O_4$ is negligible compared to its configurational entropy. In another case, Seminovski et al. [224] show that the vibrational entropy of $CdIn_2S_4$ is important to predict its experimental inversion degree. Here, we only consider the configurational energy terms (ΔE_{conf} and $T\Delta S_{conf}$) and neglect the vibrational energy terms (ΔE_{vib} and $T\Delta S_{vib}$) due to computational cost.

The change of the Gibbs free energy due to the inversion of the cations with respect to the normal spinel ($\lambda = 0$) is given by Eq. 3.4.

$$\Delta G_{conf} = \Delta E_{conf} - T\Delta S_{conf} \tag{3.4}$$

where:

$$\Delta E_{conf} = E_{conf}(\lambda) - E_{conf}(\lambda = 0) \tag{3.5}$$

$$\Delta S_{conf} = S_{conf}(\lambda) - S_{conf}(\lambda = 0) \tag{3.6}$$

According to [223], the configuration entropy of spinel ferrite with inversion degree λ is given by Eq. 3.7. This equation is derived from calculating the cation distribution at the Td and Oh sites. Eq. 3.7 shows that the entropy is maximum at $\lambda = 2/3$.

$$S_{conf.}(\lambda) = -R(\lambda \ln \lambda + (1-\lambda)\ln(1-\lambda) + \lambda \ln \lambda/2 + (2-\lambda)\ln(1-\lambda/2)) \tag{3.7}$$

If we use this equation with a conventional unit cell (8 f.u.), we have to do the calculations for 4222 structures (as shown in the table B.6) calculated with the code "supercell" [227]. The DFT calculations of these structures require a lot of computational resources. Therefore, we have chosen a simplified method to study the thermodynamics of inversion in these spinel ferrites. We studied the structures with inversion degrees 0.0, 0.25, 0.5, 0.75, and 1.0 using the tetragonal space group $P4_122$ (a primitive unit cell of 4 f.u.). The total number of possible inequivalent structures generated by the code Supercell is 13 (as shown in the table B.6). The lattice parameters, band gap, and configuration energy are given in the tables B.7 and B.8 for CFO and NFO, respectively. We have also calculated inversion degrees 0.125 and 0.875 using a conventional unit cell of 8 f.u.

(space group $P4_122$), which has only two possible structures for each case. (The results are shown in the table of appendix B.9)

In our case, the entropy given by Eq. 3.7 will change as the number of cation arrangements will differ for space groups 91 and 227. The entropy equation can be derived from the formula (Eq. 3.8) to obtain a total number of configurations for the inversion degree λ.

$$\Omega(\lambda) = \binom{1}{\lambda}\binom{1}{\lambda} \tag{3.8}$$

Eq. 3.9 is used to calculate the configurational entropy.

$$S_{conf.}(\lambda) = R \ln \Omega(\lambda) \tag{3.9}$$

Using Eqs. 3.8 and 3.9, the configurational entropy can be calculated and described by the equation below.

$$S_{conf.}(\lambda) = -2R(\lambda \ln \lambda + (1-\lambda)\ln(1-\lambda)) \tag{3.10}$$

The final configurational Gibbs free energy is given by (using Eq. 3.4):

$$\Delta G_{conf} = \Delta E_{conf} + 2RT(\lambda \ln \lambda + (1-\lambda)\ln(1-\lambda)) \tag{3.11}$$

The energies $\Delta E_{inv}(\lambda) = \Delta E_{conf}(\lambda)$ are obtained from first-principles calculations for different cation distributions. An ensemble-average energy is then calculated for each inversion parameter λ and extrapolated to the entire range of λ by a quadratic polynomial fit (see Fig. 7.5(a)) [220].

The equation we used is simpler than those usually found in the literature [224, 225] because we considered the cation distribution of the space group $P4_122$ as the reference, *i.e.* Td-Oh exchanges do not affect the remaining cation distribution in Oh atomic sites.

Using the calculated $\Delta E_{inv}(\lambda)$ interpolation function and Eq. 3.11, it is possible to calculate an equilibrium value of λ, which corresponds to a minimum of $\Delta G_{\mathrm{conf}}(\lambda)$ for a given temperature. The variation of the equilibrium value of the inversion parameter as a function of the temperature $\lambda(T)$ is shown in Fig. 3.8. The black dotted line at 600K (the growth temperature commonly used for CFO and NFO) shows that CFO undergoes partial inversion with an inversion degree of 0.96 but NFO is almost fully inverse. Experimentally, it has indeed been reported that NFO crystals with a nearly perfect inverse spinel structure can be grown [91, 228], while CFO samples are mostly found with an inversion degree around 0.7-0.9 [91–95].

With the decrease of the inversion degree λ, we also calculated a linear increase of the pseudo-cubic lattice parameter $\langle a \rangle$, with a slope of −5.6 pm for NFO and of −5.4 pm for CFO, as shown in Fig. 7.5(b). Qualitatively similar variations of $\langle a \rangle(\lambda)$ were reported by Fritsch and Ederer [126], while opposite variations were predicted in Ref. [125]. The linear decrease of $a(\lambda)$ is consistent with the equation proposed in Ref. [229, 230], which expresses the variation of the lattice parameter as a function of the inversion parameter λ and of the ionic radii R of the M^{2+} and Fe^{3+} cations:

$$a(\mathrm{MFe_2O_4}) = \frac{8}{3\sqrt{3}}\left[(R_{\mathrm{A}} + R_{\mathrm{O}}) + \sqrt{3}\,(R_{\mathrm{B}} + R_{\mathrm{O}})\right] \tag{3.12}$$

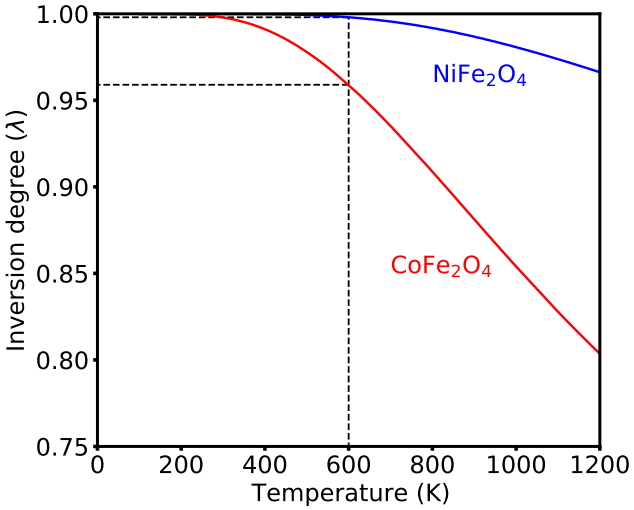

Figure 3.8 – Equilibrium inversion parameter λ calculated as a function of the growth temperature (T_g) for $CoFe_2O_4$ and $NiFe_2O_4$.

with $R_A = (1-\lambda)\,R_{Co^{2+}} + \lambda R_{Fe^{3+}}$ and $R_B = \frac{1}{2}\left[\lambda R_{Co^{2+}} + (2-\lambda)\,R_{Fe^{3+}}\right]$. From this equation, the slope of the variation of $a(\lambda)$ is equal to $\left(1-\frac{\sqrt{3}}{2}\right)(R_{Fe^{3+}} - R_{M^{2+}})$, which is negative considering that $R_{Fe^{3+}} < R_{M^{2+}}$.

Finally, it is also interesting to mention that an auxetic behavior with an increasing volume was measured for CFO samples with an inversion degree of approximately $\lambda = 0.75$; its origin is still not well understood but is certainly related to the presence of cation or anion vacancies, in addition to the relatively high content of Co atoms in Td atomic sites [95]. Depending on the distribution of the Co atoms located in the occupied Td sites, our structure may not strictly preserve its slightly tetragonal shape. We have calculated a small modification of the c/a ratio of CFO, from 0.995 to 0.998 when λ decreases from 1 to 0.875.

3.2.2 Magnetic properties as a function of the inversion degree

We calculated a linear decrease of the total spin magnetic moment per formula unit as the inversion parameter increases. It follows the equation:

$$M_{f.u.}(MFe_2O_4) = 2\,(1-\lambda)\,M(Fe^{3+}) + (2\lambda - 1)\,M(M^{2+}) \tag{3.13}$$

.

Using the perfect ionic model to describe CFO and NFO, which corresponds to the atomic spin magnetic moments $M(Fe^{3+}) = 5\ \mu_B$, $M(Co^{2+}) = 3\ \mu_B$ and $M(Ni^{2+}) = 2\ \mu_B$, the previous equation becomes $M_{f.u.} = (-4\lambda + 7)\,\mu_B$ for CFO and $M_{f.u.} = (-6\lambda + 8)\,\mu_B$ for NFO.

We emphasize that the modifications of the spin magnetic moments reported here have only been calculated approximatively, as we restricted our study to a perfectly-collinear ferrimagnetic order. Recently, Moya *et al.* [231] showed that different values of the inversion parameter lead to different values of the total spin magnetic moment, due to a lowering of the magnetic coupling

and to a canting of the cation magnetic moments, in particular for Co^{2+} cations. Two reasons were given by these authors to explain this effect: the first one is a direct consequence of the non-inverse structure, with Co^{2+}(Td)-O-Fe^{3+}(Oh) antiferromagnetic superexchange interactions lower than the dominant Fe^{3+}(Td)-O-Fe^{3+}(Oh) ones; the second reason potentially comes from structural relaxations induced by other defects [231]. Lüders et al. [232] measured an increase of 250% to 1050 emu cm^{-3} in the total magnetic moment of a 3 nm thick NFO film (corresponding to a 17 % cation inversion). This thin film was found to be conductive, which is consistent with a decrease of the band gap with increasing the NFO cation inversion degree.

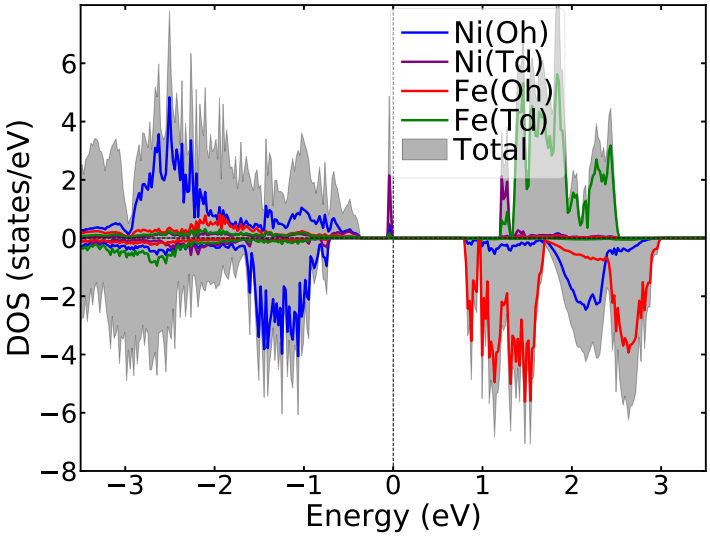

Figure 3.9 – Density of states of NFO with an inversion degree of 0.875. The VBM is at -0.38 eV and an occupied state at the Fermi level corresponds to Ni(Td) (shown in purple color).

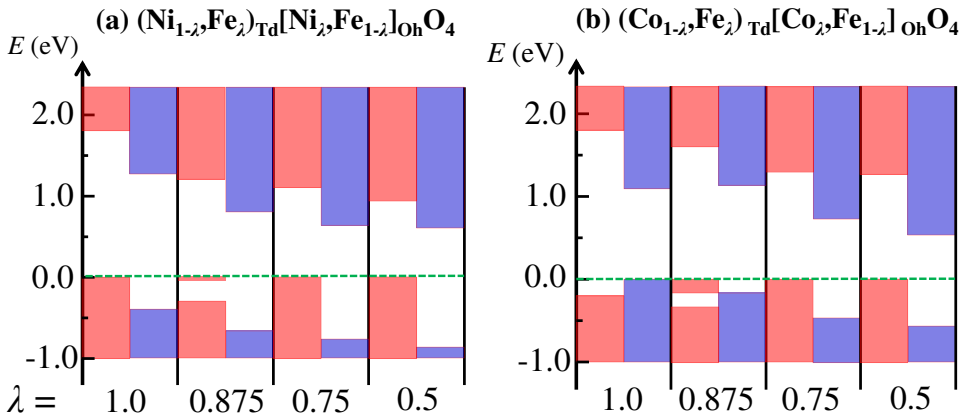

Figure 3.10 – Schematic representation of the calculated density of states (a) for NFO and (b) for CFO and for different values of the inversion degree λ i.e. the occupied defect state at the Fermi level in the majority spin corresponds to Ni(Td) in NFO with inversion degree 0.875 as shown in Fig. 3.9. The energy range of the band gap corresponds to the white area. The majority- and minority-spin DOS are respectively shown in red and blue colors, respectively. The green dashed line corresponds to the highest occupied state.

3.2.3 Electronic structure versus inversion degree

Due to inversion, $Co^{2+}(d^7)$ or $Ni^{2+}(d^8)$ cations substitute $Fe^{3+}(d^5)$ cations in Td sites. Occupied defect states appear in the majority-spin band gap, corresponding to t_2 states created by these divalent cations. The electronic structure due to inversion is shown in Fig. 3.10. The addition of more $Fe^{3+}(d^5)$ cations in the Oh sites (the decrease of λ) will depopulate the minority-spin bands and unoccupied gap states will appear. In summary, when the inversion degree decreases, the minority-spin bands are less occupied for the benefit of the occupation of majority-spin bands and both occupied and unoccupied gap states will merge with the bulk continuum of valence and conduction bands if the inversion degree is too low. Finally, for CFO, it is interesting to note that for $\lambda \neq 1$, the VBM does not belong to the minority-spin channel anymore.

3.3 Effect of strain

Depending on the substrate, the spinel ferrites can be subjected to strain. In particular if an epitaxial growth of the thin film is achieved, the substrate may impose its lattice parameter to the in-plane lattice parameter of the ferrite and therefore induce a tetragonal strain which can modify their electronic and magnetic properties. D. Fritsch and C. Ederer [126] studied the effect of epitaxial strain on the cation distribution in CFO and NFO using *ab initio* calculations. They found that compressive strains tend to increase the inversion degree.

3.4 Conclusion

The cation ordering at Oh sites does not change the magnetic moment but it does change the electronic properties, in particular the value of the band gap. The range of calculated values of the fundamental band gap of CFO and NFO are 0.55-1.09 eV and 0.57-1.34 eV, respectively. The structures with homogeneous cation distribution at Oh sites are the most stable. The most stable cation distribution corresponds to structures with space group 13-$P2/c$ for CFO and 91-$P4_122$ for NFO. The 91-$P4_122$ space group structure is the second most stable for CFO and it only becomes the most stable structure when the Hubbard parameter of Co cations is reduced to 1 eV or less than 1 eV.

The cation inversion modifies both electronic and magnetic properties: with decreasing the inversion degree, the total spin magnetic moment increases and the fundamental band gap decreases. We found that NFO with a lot of cation inversion (17%) tends to become conducting and shows a higher magnetic moment, which confirms the experimental observations of Lüders, *et al.* [232]. According to our results, CFO is more likely to display cation inversion than NFO.

Chapter 4

Non-stoichiometry in bulk spinel ferrites

In the previous Chapter, we have described the effects of cation distribution on the structural, electronic, and magnetic properties of stoichiometric CFO and NFO. In this Chapter, we will describe the consequences on these physical properties of different types of point defects that modify the stoichiometry of these crystals. We will start exploring cation substitutions that lead to a Fe:(Co, Ni) ratio different from 2. Such defects are very likely to exist due to the difficulty of precisely controlling the global and local stoichiometry of $CoFe_2O_4$ and $NiFe_2O_4$ samples. A Fe:(Co, Ni) ratio different from 2 can also result from the presence of cation vacancies, another types of point defects that we have chosen to consider in this Chapter. Cation vacancies are common defects in spinel ferrites, which can even lead to metastable cation-deficient spinel structures, such as maghemite γ-Fe_2O_3 [89], which can be described as an Fe-deficient magnetite crystal. Recent experimental and numerical work [77, 233] has focused on cation diffusion, which can even be controlled by applying an external electric field and could also be promoted by the presence of either oxygen or cation vacancies [77]. The existence of oxygen vacancies has mostly been hypothesized to explain the measured modification of the magnetization and electrical conductivity of metal oxides. S Anjum et al. [234] measured a large decrease in the total magnetic moment of NFO in an O-poor growth condition, which may be due to the presence of cations (Ni, Fe) and O-vacancies. They also found higher electrical conductivity in both O-poor and O-rich growth conditions. Harrison et al. [235] found a decrease of the total magnetic moment of NFO at 1000 °C, due to the presence of B-cation vacancies, which disappeared at the higher temperature of 1200 °C.

4.1 Effects of cation substitutions

We first describe the physical properties of the spinel ferrites $M_{1-\alpha}Fe_{2+\alpha}O_4$ ($\alpha > 0$), in which some of the M=(Co, Ni) atoms have been replaced by Fe atoms and $M_{1+\beta}Fe_{2-\beta}O_4$ ($\beta > 0$), in which some of the Fe atoms have been replaced by M atoms. The detailed structural, magnetic, and band

gap results are shown in table 4.1. We have studied the cation substitution for the values of $\alpha(\beta)$ = 0.125 and 0.25; these values correspond to the substitution of one and two cations, respectively, in the conventional cell of 56 atoms.

Table 4.1 – Lattice parameters, total magnetic moment, band gap energies (majority-spin, minority-spin and fundamental gaps) and total energy (E) calculated for the different cobalt and nickel ferrite supercells. All results are given per conventional cell (of 8 formula units). The calculations are based on the cation distribution in the perfect crystal corresponding to the space group 91-$P4_122$.

α/β	Cations	Lattice parameters				M_{tot}	Band gap			E
	in Oh and Td	a	b	c	$V^{1/3}$		Maj.	Min.	Funda.	
	sites	(Å)	(Å)	(Å)	(Å)	μ_B	(eV)	(eV)	(eV)	(eV)
					$CoFe_2O_4$					
$\alpha = 0$, $\beta = 0$	$[Co_8Fe_8]_{Oh}(Fe_8)_{Td}$	8.346	8.346	8.303	8.331	24	1.98	1.09	1.09	-388.421
$\alpha = 0.125$	$[Co_7Fe_9]_{Oh}(Fe_8)_{Td}$	8.334	8.334	8.327	8.331	25	1.95	0.54	0.54	-390.231
$\alpha = 0.25$	$[Co_6Fe_{10}]_{Oh}(Fe_8)_{Td}$	8.342	8.342	8.328	8.337	26	1.95	0.52	0.52	-391.880
$\beta = 0.125$	$[Co_8Fe_8]_{Oh}(Co_1Fe_7)_{Td}$	8.343	8.355	8.306	8.335	25	0.75	1.27	0.68	-384.439
$\beta = 0.25$	$[Co_8Fe_8]_{Oh}(Co_2Fe_6)_{Td}$	8.328	8.336	8.321	8.328	26	0.66	1.27	0.60	-381.758
$\beta = 0.125$	$[Co_9Fe_7]_{Oh}(Fe_8)_{Td}$	8.326	8.326	8.313	8.321	23	1.97	0.78	0.74	-385.842
$\beta = 0.25$	$[Co_{10}Fe_6]_{Oh}(Fe_8)_{Td}$	8.319	8.318	8.309	8.315	22	1.98	0.75	0.74	-383.143
					$NiFe_2O_4$					
$\alpha = 0$, $\beta = 0$	$[Ni_8Fe_8]_{Oh}(Fe_8)_{Td}$	8.277	8.277	8.294	8.283	16	1.83	1.73	1.34	-382.356
$\alpha = 0.125$	$[Ni_7Fe_9]_{Oh}(Fe_8)_{Td}$	8.292	8.292	8.300	8.295	18	1.83	0.47	0.47	-384.791
$\alpha = 0.25$	$[Ni_6Fe_{10}]_{Oh}(Fe_8)_{Td}$	8.302	8.302	8.298	8.301	20	1.85	0.45	0.45	-387.218
$\beta = 0.125$	$[Ni_8Fe_8]_{Oh}(Ni_1Fe_7)_{Td}$	8.281	8.285	8.292	8.286	18	0.59	1.59	0.59	-377.035
$\beta = 0.25$	$[Ni_8Fe_8]_{Oh}(Ni_2Fe_6)_{Td}$	8.268	8.275	8.286	8.276	20	0.29	1.61	0.29	-373.000
$\beta = 0.125$	$[Ni_9Fe_7]_{Oh}(Fe_8)_{Td}$	8.261	8.261	8.282	8.268	12	0.00	1.76	0.00	-378.603
$\beta = 0.25$	$[Ni_{10}Fe_6]_{Oh}(Fe_8)_{Td}$	8.247	8.247	8.262	8.252	8	0.00	1.88	0.00	-374.961

4.1.1 Atomic structure

For $M_{1+\beta}Fe_{2-\beta}O_4$, we considered two possible substitutions of Fe atoms by Co or Ni atoms: substitutions occurring in Oh or Td sites. Co or Ni substitutions on Fe(Oh) appeared to be the most probable ones, according to the comparison of the total energies that we calculated. Indeed, we found that the substitution of a single Fe atom in a Td site of the conventional cell containing 8 MFe_2O_4 f.u. by an M (Co or Ni) atom costs 1.40 eV and 1.57 eV more for CFO and NFO, respectively, than when the substitution involves an Fe atom located in one of the Oh sites.

Regardless of the Oh site where the substitution occurs, we found that the cell tends to become more cubic after this substitution, with a c/a ratio closer to 1. The averaged lattice parameter does not change significantly when Co is replaced by Fe atoms, while it tends to decrease when Fe is replaced by Co atoms in CFO. For NFO, substituting Fe with Ni atoms decreases the lattice parameter ($\langle a \rangle$ = 8.268 Å for β = 0.125 and 8.252 Å for β = 0.25), while replacing Ni with Fe atoms

increases $\langle a \rangle$ to 8.295 Å for $\alpha = 0.125$ and 8.301 Å for $\alpha = 0.25$.

4.1.2 Electronic structure

As it can be seen in Fig. 7.6, substituting Ni or Co with Fe atoms has a very similar effect in both compounds: it creates occupied minority-spin states near the middle of the band gap. The fact that these gap states are occupied means that Fe replacing Ni or Co atoms in Oh sites are Fe^{2+} cations. The ferrite crystal can then be described by the chemical formula $\left(Fe^{3+}\right)_{Td}\left[M^{2+}_{1-\alpha}Fe^{2+}_{\alpha}Fe^{3+}\right]_{Oh}O^{2-}_{4}$.

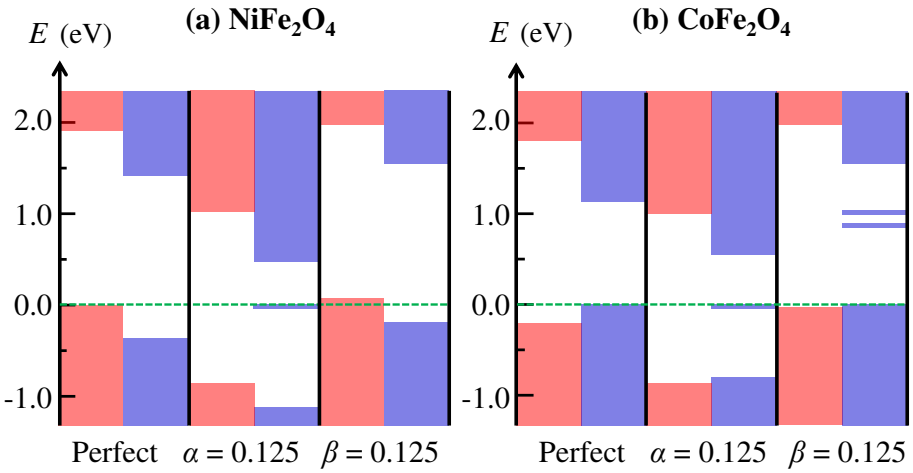

Figure 4.1 – Schematic representation of the density of states calculated for the non-stoichiometric crystals $M_{0.875}Fe_{2.125}O_4$ ($\alpha = 0.125$) and $M_{1.125}Fe_{1.875}O_4$ ($\beta = 0.125$). The energy range of the band gap corresponds to the white area. Majority- and minority-spin DOS are shown in red and blue colors, respectively. The green dashed line corresponds to the highest occupied state.

Conversely, substituting Fe with M atoms leads to the formation of M^{3+} cations in order to preserve the charge neutrality of the crystal, which can be further described by the chemical formula $\left(Fe^{3+}\right)_{Td}\left[M^{2+}M^{3+}_{\beta}Fe^{3+}_{1-\beta}\right]_{Oh}O^{2-}_{4}$, with $\beta > 0$. We have observed some differences between the results that we calculated for NFO and CFO: for CFO, the Co^{3+} cations replacing Fe^{3+} cations have a $d^5_{\uparrow}d^1_{\downarrow}$ electronic structure and the unoccupied minority spin gap states have an energy near the middle of the band-gap, while for NFO the Ni^{3+} cations are in a $d^4_{\uparrow}d^3_{\downarrow}$ low-spin state and the VBM in the majority-spin channel is depopulated and crosses the Fermi level. The depopulated bands have a ($d_{x^2-y^2} + d_{z^2}$ orbitals of the Ni atom and p orbitals of the O atoms) character and an effective mass $m_h = 1.55m_0$, where m_0 is the free electron mass.

4.1.3 Magnetic properties

The electronic structure changes described above are consistent with the calculated total magnetic moments. The corresponding total spin magnetic moment of a MFe_2O_4 crystal with iron overstoichiometry ($\alpha > 0$) is thus given in the ionic approximation by the equation:

$$M_{\text{f.u.}}(M_{1-\alpha}Fe_{2+\alpha}O_4) = (1-\alpha)\,M(M^{2+}) + \alpha M(Fe^{2+}) \tag{4.1}$$

which leads to $M_{\text{f.u.}}(Ni_{1-\alpha}Fe_{2+\alpha}O_4) = 2(\alpha + 1)\ \mu_B$ and $M_{\text{f.u.}}(Co_{1-\alpha}Fe_{2+\alpha}O_4) = (\alpha + 3)\ \mu_B$, in perfect agreement with our DFT results.

On the contrary, if there is an excess of Co or Ni atoms ($\beta > 0$), the spin magnetic moment per formula unit is given, in the ionic approximation, by:

$$M_{\text{f.u.}}(M_{1+\beta}Fe_{2-\beta}O_4) = M(M^{2+}) + \beta\left[M(M^{3+}) - M(Fe^{3+})\right] \tag{4.2}$$

With $M(Co^{3+}) = 4\ \mu_B$ and $M(Ni^{3+}) = 1\ \mu_B$ (in low-spin state), this equation leads to $M_{\text{f.u.}}(Ni_{1+\beta}Fe_{2-\beta}O_4) = (2-4\beta)\ \mu_B$ and $M_{\text{f.u.}}(Co_{1+\beta}Fe_{2-\beta}O_4) = (3-\beta)\ \mu_B$ for non-stoichiometric NFO and CFO, respectively.

In conclusion, we predicted from our calculations that increasing the amount of Fe atoms by substituting Ni or Co atoms will lead to an increase in the total magnetic moment, while on the contrary, substituting Fe atoms with Ni or Co atoms will decrease it.

4.2 Effects of atom vacancies

In this section, we discuss the effects of cation and oxygen vacancies on the electronic structure and on the magnetic properties of CFO and NFO with space group $P4_122$. This $P4_122$ space group has five inequivalent atomic sites: Ni, Fe(Oh), Fe(Td), O1 [bonded to one Ni, two Fe(Oh) and one Fe(Td)] and O2 [bonded to two Ni, one Fe(Oh) and one Fe(Td)]. There is a small difference between the energies of the cell containing O1 and O2 vacancies (0.02 eV and 0.11 eV for CFO and NFO, respectively), and almost no difference in the electronic structure of these vacancies. Therefore, we have taken the averaged effect of O1 and O2 vacancies as one O-vacancy in this chapter. We have studied the oxygen-deficient ferrites $(Fe)_{Td}\,(MFe)_{Oh}\,O_{4-\zeta}$ and the metal deficient compounds $(Fe)_{Td}\,(M_{1-\gamma}Fe)_{Oh}\,O_4$, $(Fe)_{Td}\,(MFe_{1-\delta})_{Oh}\,O_4$ and $(Fe_{1-\epsilon})_{Td}\,(MFe)_{Oh}\,O_4$. Some of these defects have already been studied in spinel ferrites such as Fe_3O_4 [236, 237] or $NiFe_2O_4$ [238]. The detailed structural, magnetic and band gap results of CFO and NFO are shown in tables C.1 and C.2, respectively.

4.2.1 Formation energy of vacancy defects

The vacancy formation energy is an important parameter for comparing the relative stability of the different types of vacancy defects. The vacancy formation energies $E_f\left[V_X^q\right]$ of single X-atom vacancies V_X with charge state q have been expressed according to the Eq. 7.1 in Chapter 2. In this equation, $E\left[\text{Host} + V_X^q\right]$ and $E\left[\text{Host}\right]$ are the energies of the cell with defect and without defect, respectively, calculated by DFT methods. To calculate the vacancy formation energy, we also need to calculate the values of E_X^{elem}, $\Delta\mu_X$, ΔE_F and E_{corr}.

The values of E_X^{elem} are calculated using the FERE method (see subsection 2.9.1(b) of Chapter 2) which is also used for calculating phase diagrams. The values of $\Delta\mu_X$ for which the ferrite crystal can exist are calculated from the stability phase diagram of the ferrites. Therefore, we must first calculate the stability phase diagram. The phase diagram is calculated and plotted in order to determine the favorable range of chemical potentials at which a given compound can be

synthesized and for which competing phases can be avoided. We have used three different methods of calculation of the formation energy to obtain the phase diagrams:

1. The direct method: we used the formation energies of competing phases calculated from the first principles as given in the subsection 2.9.1(a) of Chapter 2. With this method, we used the PBEsol+U functional to calculate the ground state energy of elements and compounds.
2. In the second method, we used experimental values of the formation energies reported in the literature.
3. The FERE method, known as the *Fitted Elemental phase Reference Energy* (FERE) [194] as given in the subsection 2.9.1(b) of Chapter 2.

The competing phases that have been considered for the phase diagrams are listed in Table 4.2, with their corresponding calculated or experimental formation energies. The direct method overestimates the formation energies with respect to the experimental formation energy, partly because of the incorrect values of the elemental energies calculated with this method (the +U method being more adequate to treat transition-metal oxides than metallic systems). It is also important to note that, with this method, the calculated ground state (crystallographic phase and magnetic ordering) of the different competing phases may differ from the experimentally measured one. To correct the overestimation of the formation energy of the direct method, we need a more accurate calculation of the elemental energies. This can be done using the so-called "Fitted Elemental-phase Reference Energy" (FERE) method [194], which uses the experimental formation energies to redefine the elemental energies.

Table 4.2 – The ground state and formation energies, E_{tot} and E_f, of the experimentally stable Co, Fe, and Ni oxides calculated by the direct and FERE methods. Calculated data from Ref. [194] and experimental values from Ref. [239] are also given for comparison. The formation energies $E_f^{[i]}$ ($i = 1, 2, 3$) are numbered according to the three methods ([1] direct, [2] experimental, and [3] FERE) described in the text.

			Our calculations (PBESol+U)			Ref. [194] (PBE+U)	Exp. [239]	
Materials	Space group	Magnetic ordering	E_{tot} (eV/f.u.)	$E_f^{[1]}$ (eV/f.u.)	$E_f^{[3]}$ (eV/f.u.)	$E_f^{[3]}$ (eV/f.u.)	Magnetic ordering	$E_f^{[2]}$ (eV/f.u.)
CoO	R3m	AFM (001)	-12.21	-3.43	-2.53	-2.68	AFM (111)	-2.47
CoO	I4/mmm	AFM (001)	-11.59	-2.81	-1.91	-2.68	AFM (001)	-2.47
FeO	I4/mmm	AFM (111)	-13.81	-3.57	-2.92	-2.64	AFM (001)	-2.83
FeO	R3m	AFM (111)	-13.51	-3.27	-2.62	-2.64	AFM (111)	-2.83
FeO	c2/m	AFM (111)	-13.85	-3.60	-2.96	-2.64	AFM (001)	-2.83
NiO	I4/mmm	AFM (111)	-11.29	-2.37	-2.25	-2.52	AFM (001)	-2.49
NiO	R3m	AFM (111)	-10.93	-2.00	-1.88	-2.52	AFM (111)	-2.49
Fe_2O_3	R-3c	AFM (111)	-35.83	-10.70	-8.46	-8.70	AFM (111)	-8.57
Ni_2O_3	R-3c	AFM (111)	-28.81	-6.33	-5.14	-5.35	AFM (111)	-5.09
Fe3O4	Fd-3m	FiM (001)	-50.08	-14.71	-11.81	-11.97	FiM (001)	-11.63
Co_3O_4	Fd-3m	AFM (001)	-43.99	-13.02	-9.36	-9.87	AFM (001)	-9.27
$CoFe_2O_4$	$P4_122$	FiM (001)	-48.55	-14.65	-11.50	-11.83	FiM (001)	-11.85
$NiFe_2O_4$	$P4_122$	FiM (001)	-47.79	-13.75	-11.38	-11.20	FiM (001)	-11.24

Table 4.3 – Elemental energy in the standard phases that we calculated by the FERE method and the Direct method. The data reported in the literature are also given.

Method	Elemental energy E			
	Co	Fe	Ni	O
	(eV)	(eV)	(eV)	(eV)
Direct (PBEsol+U)	−4.15	−5.62	−4.30	−4.63
FERE (PBEsol+U)	−4.10	−5.32	−3.47	−5.58
FERE (PBE+U, from Ref. [194])	−4.75	−6.15	−3.57	−4.73

The calculated elemental energies are given in table 4.3, with the direct method and the FERE method along with those reported in Ref. [194] (FERE with PBE+U approximation). The elemental energy ($E_{\mathrm{X}}^{\mathrm{elem}}$) calculated using the FERE method in the table 4.3 is used to calculate the vacancy formation energy in this chapter. With our values of U_{eff} (4.0 eV for Co, 4.0 eV for Fe, and 2.5 eV for Ni) and considering only the limited list of oxides mentioned above, we found with the FERE method a mean absolute error with respect to the experimental formation energies of 0.031 eV/atom. Increasing the parameter U_{eff} increases the elemental energy of the transition metals. Therefore, our FERE elemental energies of Co and Fe are higher than the FERE elemental energies given in Ref [194]. In this reference, the authors performed DFT calculations using a PBE+U approximation (with U = 3.0 eV for all transition elements, and U = 5.0 eV for the noble metals Ag and Cu) to calculate $\mathrm{E}_{\mathrm{tot}}^{\mathrm{DFT}+U}$ for 252 binary transition metal compounds; they obtained a mean absolute error, with respect to the experimental formation energies of all these compounds, of 0.054 eV/atom. We will now use the formation energies of the relevant compounds to calculate the phase diagrams of CFO and NFO.

This method gives better values of the elemental energies allowing to calculate a phase diagram that is comparable with the experimental phase diagram.

Phase diagram of stoichiometric CFO and NFO

The formation energies of the different compounds listed in table 4.2 are used to calculate the phase diagrams. The phase diagrams have been plotted using Eqs. 2.18- 2.20 of the subsection 2.9.2 of chapter 2. These equations are used to compute the phase diagram showing the ($\Delta\mu_M$, $\Delta\mu_{Fe}$, and $\Delta\mu_O$) domains, where MFe_2O_4 is more stable than other competing phases.

The phase diagrams of CFO and NFO are shown in Fig. 4.2 and Fig. 4.3 respectively, where they have been calculated from the formation energies: (a) measured experimentally, (b) calculated using the FERE method, and (c) calculated using the direct method. The favorable regions for the stability of CFO and NFO are highlighted with gray shaded areas and the median value is marked with a black cross in each panel (the chemical potentials corresponding to this point are written in Table 4.4).

In the phase diagrams of CFO (Fig. 4.2), both the FERE and direct methods have a good

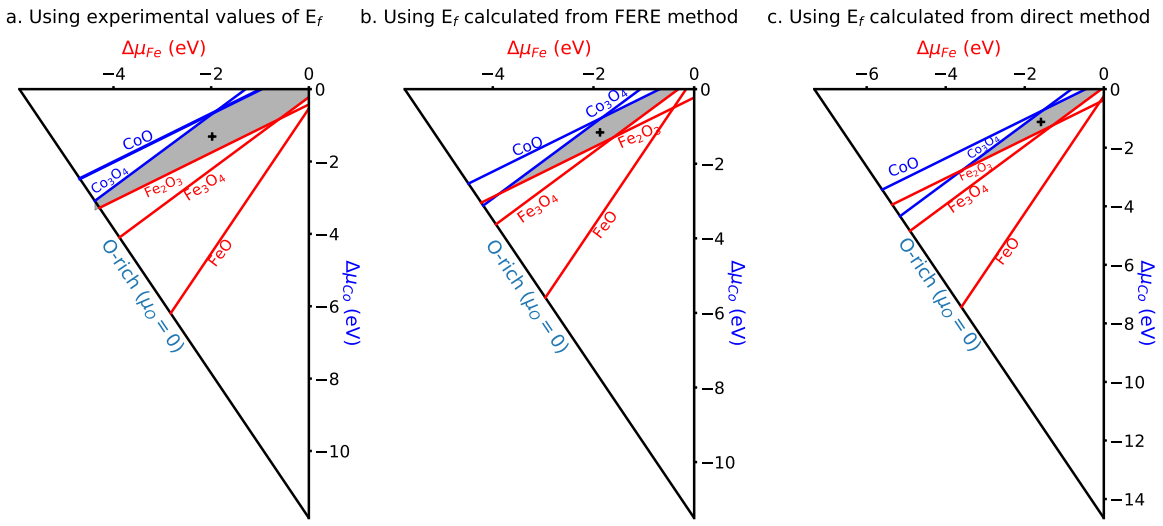

Figure 4.2 – Phase diagram of CFO calculated from the formation energies: (a) measured experimentally, (b) calculated with the FERE method, and (c) calculated using the direct method

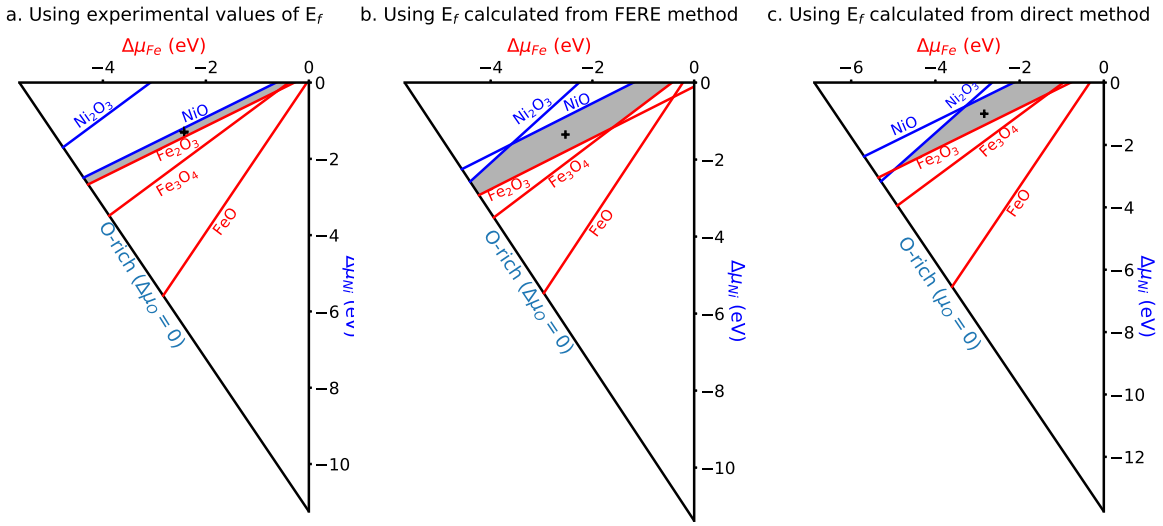

Figure 4.3 – Phase diagram of NFO calculated from the formation energies: (a) measured experimentally, (b) calculated with the FERE method, and (c) calculated using the direct method

enough common region with the experimental phase diagram, while in the case of NFO (Fig. 4.3), only the phase diagram calculated using the FERE method partially agrees with the phase diagram calculated from the experimental formation energies. This could be explained by our chosen value of U_{eff} for Ni atoms, which is smaller (2.5 eV) than the values used in the literature (5-6 eV). However, using larger values of U_{eff}(Ni) would also have the consequence to enlarge the band gap of $NiFe_2O_4$ to values larger than those measured experimentally. The FERE method avoids this

problem.

Table 4.4 – Chemical potentials corresponding to the point of the phase diagram at the center of the stability domain of $CoFe_2O_4$ and $NiFe_2O_4$ (marked by a black cross in Figs. 4.2 and 4.3).

	$CoFe_2O_4$		
	(1) Direct method	(2) Experimental	(3) FERE method
$\Delta\mu_{Co}$ (eV)	−1.12	−1.31	−1.16
$\Delta\mu_{Fe}$ (eV)	−1.59	−1.98	−1.87
$\Delta\mu_{O}$ (eV)	−2.59	−1.64	−1.59
	$NiFe_2O_4$		
	(1) Direct method	(2) Experimental	(3) FERE method
$\Delta\mu_{Ni}$ (eV)	−1.00	−1.31	−1.35
$\Delta\mu_{Fe}$ (eV)	−2.84	−2.42	−2.53
$\Delta\mu_{O}$ (eV)	−1.77	−1.27	−1.24

To calculate the values of $\Delta\mu_i$, for which CFO and NFO are stable, we used the phase diagram plotted using the FERE method. A zoom of the phase diagrams (from Fig. 4.2(b) and Fig. 4.3(b)) is shown in Fig. 7.7, where we can better see the $\Delta\mu_i$-stability domain of NFO and CFO (shaded areas). For NFO, our calculations are in fairly good agreement with those of Rák, *et al.* [240]. In Fig. 7.7, each point of the shaded areas corresponds to a triplet ($\Delta\mu_{Fe}$, $\Delta\mu_{M}$, $\Delta\mu_{O}$). To compare the vacancy formation energies, we choose two cases within the stability domain of CFO or NFO: a first point corresponding to an oxygen-rich growth condition ($\Delta\mu_O$ = −0.5) and a second point corresponding to an oxygen-poor growth condition ($\Delta\mu_O$ = −2.2). These are points A and B in the phase diagram (Fig. 7.7). The values of $\Delta\mu_i$ corresponding to the points A and B used to calculate the vacancy formation energy are given in table 4.5.

Table 4.5 – Chemical potentials corresponding to the points, A [O-rich ($\Delta\mu_O$=-0.5 eV)] and B [O-poor ($\Delta\mu_O$=-2.2 eV)] in the phase diagrams of $CoFe_2O_4$ and $NiFe_2O_4$, respectively.

Growth condition	$\Delta\mu_{Co}$ (eV)	$\Delta\mu_{Fe}$ (eV)	$\Delta\mu_{O}$ (eV)
	$CoFe_2O_4$		
O-rich (A)	-2.50	-3.50	-0.50
O-poor (B)	-0.51	-1.09	-2.20
	$NiFe_2O_4$		
O-rich (A)	-2.12	-3.63	-0.50
O-poor (B)	-0.31	-1.14	-2.20

We now know the values of E_X^{elem} and $\Delta\mu_X$ corresponding to two different growth conditions, but we need to know the two additional variables, ΔE_F and E_{corr}, to calculate the vacancy formation energy. The equilibrium Fermi level ($E_F^{eq} = E_{VBM}^{H} + \Delta E_F^{eq}$) depends on the temperature T and on

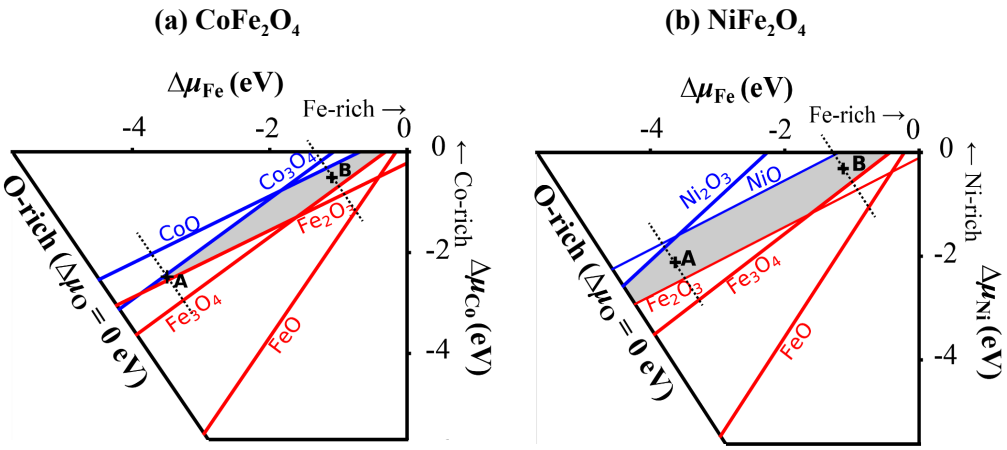

Figure 4.4 – Stability phase diagrams of (a) CFO and (b) NFO. The chemical potential ranges where CFO and NFO are more stable than competing phases are shown by the shaded areas. Points A and B are the median values for oxygen-rich ($\Delta\mu_O$ = −0.5 eV) and oxygen-poor ($\Delta\mu_O$ = −2.2 eV) conditions, respectively.

the concentration of the X-atom vacancies with charge state q and can be calculated by solving the charge neutrality equation given in subsection 2.9.3 of Chapter 2. Note that E_F can also depend on the presence of space charges and can be tuned experimentally by varying the temperature or by applying an electric field when the spinel ferrite oxide is one of the constituent layers of an electronic device. In the charge neutrality equation, the effective concentrations of charge carriers (electrons and holes) depend on their effective masses. The effective masses are calculated according to the method given in subsection 2.9.3 of Chapter 2. The VBM of $CoFe_2O_4$ and $NiFe_2O_4$ are located at the M and Γ points of the first Brillouin zone, respectively. The CBM of these two oxides is located at the Γ point. The calculated effective masses of the electron (conduction band) are m_e^*(CFO) = 1.68 m_0 and m_e^*(NFO) = 8.91 m_0 for CFO and NFO, respectively. The calculated effective masses of the hole (valence band) are m_h^*(CFO) = 2.99 m_0 and m_h^*(NFO) = 1.46 m_0 for CFO and NFO, respectively.

Since the Fermi level depends on formation energies $E_f\left(V_X^q\right)$ that is a function of the Fermi level, the equilibrium Fermi level must be determined self-consistently. We chose to calculate the Fermi level in the framework of the "defect freezing-in" approximation [204]: First, the concentration of each vacancy is calculated according to Eqs. 2.24- 2.27 at a high-temperature T_g = 673 K, which is close to some reported growth temperatures [93, 95]. Then, considering that the materials are quenched and that the Fermi level is further measured at room temperature, we calculate a new value for the Fermi level at T_R = 298 K using Eq. 2.28, with the constraint that the concentration of defects for a given chemical species must remain constant. The Eq. 2.28 is solved self consistently to calculate ΔE_F at the growth temperature T_g.

E_{corr} in Eq. 7.1 is the Lany-Zunger correction [199] used to correct for the shift of the elec-

trostatic potential due to the limited size of the supercell. This correction is calculated using the PyDEF code [196, 201]; it depends on the values of the relative permittivity of 15.58 that we calculated for CFO and of 14.59 that we calculated for NFO. The our calculated value of relative permittivity for CFO is in agreement for with previously calculated (16.05) and measured ($\simeq$ 14) permittivities [241].

4.2.2 Thermodynamic stability of the vacancies in CFO and NFO

The vacancy formation energies $E_f[V_X^q]$ have been calculated using Eq. 7.1 for different values of the chemical potentials $\Delta\mu_X$ within the ranges where CFO and NFO can exist as stable compounds. For each spinel oxide, we will focus our discussions on oxygen-rich ($\Delta\mu_O = -0.5$ eV) and oxygen-poor ($\Delta\mu_O = -2.2$ eV) growth conditions.

Fig. 7.8 shows the values of the formation energies $E_f[V_X^q]$ calculated for the different kinds of atomic vacancies in CFO and NFO and as a function of $\Delta E_F = E_F - E_{VBM}^H$, which varies within the fundamental band gap of these oxides. An equilibrium Fermi level $\Delta E_F^{eq}(T_g, T_R)$ is also given.

For both oxides and under oxygen-poor growth conditions, the formation energy of the oxygen and cation vacancies are all positive, whatever the values taken by ΔE_F within the band gap. These defects are thus unlikely to be formed when CFO and NFO are grown at low temperatures. When the growth temperature increases, due to the exponential factor in Eq. 2.27, the concentration of the atom vacancies with the lowest formation energy will be definitively greater than that of the other kinds of vacancies.

For NFO, the most probable defects *under oxygen-poor growth conditions* will thus be: V_{Ni}^{-2} for $\Delta E_F > 1.31$ eV, V_O^0 for $0.10 < \Delta E_F < 1.31$ eV and V_O^{+1} for $0 < \Delta E_F < 0.10$ eV. V_O^0 and V_O^{+1} should coexist with similar concentrations for $\Delta E_F \approx 0.10$ eV. At the calculated equilibrium Fermi level $\Delta E_F^{eq} = 0.64$ eV, we expect mainly to observe V_O^0 vacancies, with a calculated concentration $[V_O^0] = 3.6 \times 10^{11}$ cm^{-3}, while ionized vacancies will be only present with a concentration of $[V_O^{+1}] = 3.1 \times 10^2$ cm^{-3}. The calculated equilibrium Fermi level being close to the middle of the gap, the numbers of free holes and electrons are balanced to $n = p = 4 \times 10^8$ cm^{-3}. *For CFO under oxygen-poor growth conditions*, the most probable defects are V_{Co}^{-2} for $\Delta E_F > 1.09$ eV and oxygen vacancies for $\Delta E_F < 1.09$ eV. The ionization energy for charge-state transitions is $\varepsilon(+1/0) = 0.28$ eV. At the equilibrium Fermi level $\Delta E_F^{eq} = 0.56$ eV, as in NFO, we also have mostly the presence of neutral oxygen vacancies with a similar concentration of $[V_O^0] = 2.9 \times 10^{11}$ cm^{-3}, 8 orders of magnitude higher than the concentration of Co vacancies. In CFO, the concentration of free carriers $n \simeq p = 2.6 \times 10^{10}$ cm^{-3} is higher than in NFO.

Ni/Co vacancies will be the most stable defects under *oxygen-rich conditions*. *For NFO*, these conditions allowed to calculate a Fermi level of $\Delta E_F^{eq} = 0.30$ eV, for which the Ni vacancies will be mostly partially ionized ($q = -1$), with a concentration $[V_{Ni}^{-1}] = 1.8 \times 10^{14}$ cm^{-3}. At this Fermi level, the concentration of neutral or fully-ionized Ni vacancies, even if 3 to 5 orders of magnitude lower, is however not negligible; $V_{Fe(Oh)}^{-1}$ vacancies will also be present with $[V_{Fe(Oh)}^{-1}] = 4.7 \times 10^6$ cm^{-3}. *For CFO*, we have $\Delta E_F^{eq} = 0.27$ eV (which is below the critical value of $\varepsilon(0/-1) = 0.36$ eV at which

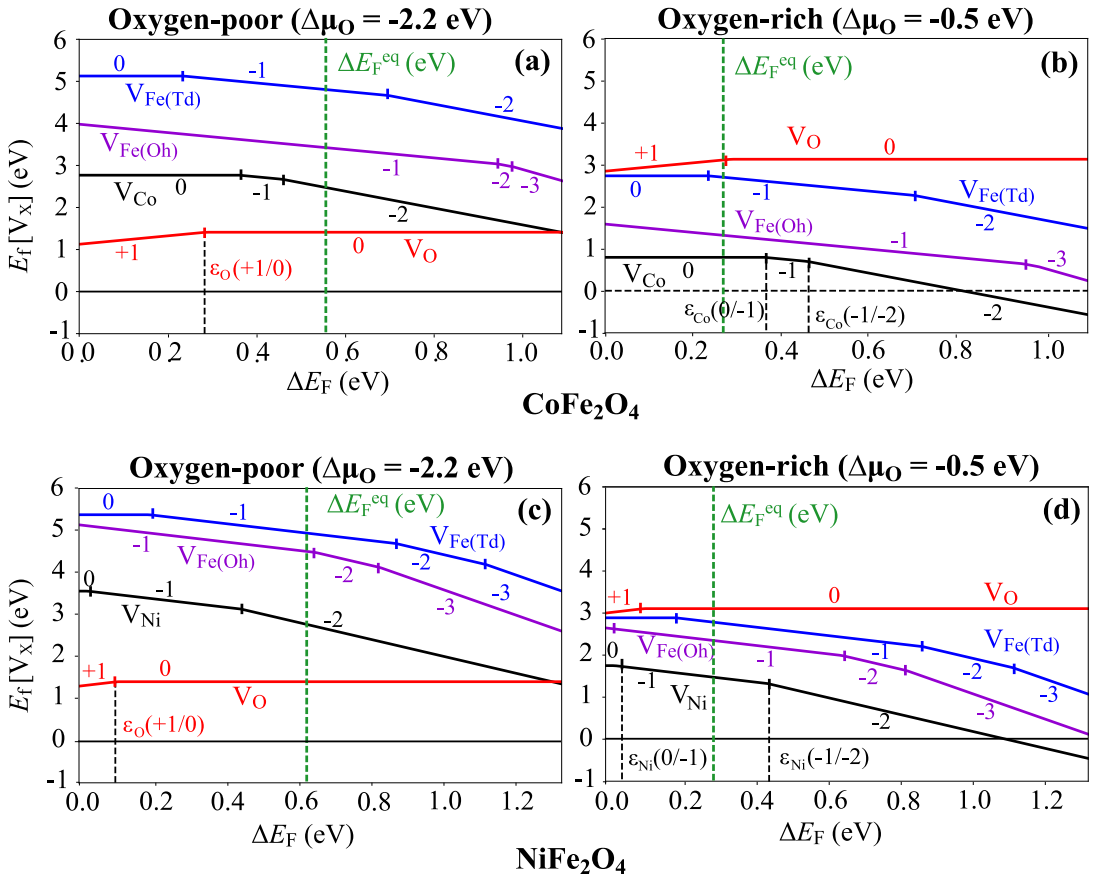

Figure 4.5 – Formation energies $E_f\left[V_X^q\right]$ of charged atomic vacancies in CFO for (a) an oxygen-poor condition ($\Delta\mu_O = -2.2$ eV) and (b) an oxygen-rich condition ($\Delta\mu_O = -0.5$ eV). Formation energies of charged atomic vacancies in NFO under similar oxygen-poor (c) and oxygen-rich (d) conditions. The formation energies are given as a function of the position of the Fermi level ΔE_F, which is given with respect to the VBM of the perfect bulk compounds. Only the energies corresponding to the most stable charge states q of each kind of vacancy are shown and these charge states are indicated close to the lines. The vertical green lines indicate the values of the equilibrium Fermi level $\Delta E_F^{eq}(T_g, T_R)$.

cobalt vacancies with $q = 0$ and $q = -1$ are equally probable) and the Co vacancies will mostly be neutral, with a very high concentration of $[V_{Co}^0] = 9.2 \times 10^{16}$ cm^{-3} and V_{Co}^{-1} vacancies have a concentration 1-2 orders of magnitude lower than $[V_{Co}^0]$. Other defects (V_{Co}^{-2}, $V_{Fe(Oh)}^{-1}$) are present with the concentrations $\sim 10^{11}$-10^{13} cm^{-3}. If we consider oxygen-rich conditions, for both CFO and NFO, the Fermi level is calculated closer to the VBM than in oxygen-poor conditions, and thus we have a larger amount of free holes ($p = 10^{14}$-10^{15} cm^{-3}).

Additional comments can be made about the formation energies of the different defects. First, if we predicted that we will mostly observe Ni or Co vacancies in oxygen-rich conditions, the formation of Fe_{Oh} vacancies cannot totally be excluded, as their formation energy can be close to those of Co/Ni vacancies when the Fermi level approaches the CBM (these vacancies can even become the most stable ones under Fe-poor conditions). Secondly, for all the studied cases, Fe_{Td} vacancies

are always the less stable cation vacancies, in agreement with former calculations performed on iron-deficient Fe_3O_4 [237]. More details about the calculated vacancy concentrations can be found in table C.3. Thirdly, still, in oxygen-rich conditions, we can see that when the Fermi level is close to the CBM, the formation energies $E_f\left[V^{-3}_{Fe(Oh)}\right]$ and $E_f\left[V^{-2}_{M(Oh)}\right]$ become negative and these defects can appear spontaneously, even at low temperatures. In oxygen-poor conditions, where the Fermi level approaches the CBM, the coexistence of Co/Ni and O vacancies is favored.

Our results on vacancies could help to explain some of the experimental studies that aim either at understanding the effects of structural defects in spinel ferrites or at manipulating the structure of these oxides to reach specific functional properties. This is, for instance, the case of the study reported by Chen, *et al.*, who succeeded in reversing the magnetization of an iron-deficient $CoFe_2O_4$ sample by applying an electric field [77]. Their study highlights the role of the Co-atom migration, in agreement with our calculations, which demonstrates that Co vacancies are among the easiest defects to be formed. The authors of this paper also discussed the role of oxygen vacancies in promoting the formation of adjacent iron vacancies and facilitating Co migration, which is also discussed in Ref. [78]. A numerical study of ion migration in spinel ferrites has been reported in Ref. [233]: In comparison with NFO, higher diffusion speeds and lower barrier activation energies have been calculated by these authors for CFO. This partly results from the larger lattice parameter of CFO. In our work, we also found that Co vacancies have lower formation energies than Ni vacancies in oxygen-rich growth conditions.

4.2.3 Atomic structure

The presence of a neutral cation vacancy in the conventional cell systematically lowers the averaged lattice parameter $\langle a \rangle$ of the NFO by 1.4 to 3.6 pm. Conversely, the lattice parameter increases up to 11.7 pm when the charge state q of the cation vacancy decreases. The presence of a Ni vacancy in the cell also increases the ratio c/a to 1.012, which could enhance the electric polarization of the oxide. Fe(Td) vacancies are the defects that induce the strongest variations of the pseudo-cubic lattice parameter, changing the structure from tetragonal to orthorhombic. Similar conclusions are observed for CFO, except that the tetragonality (c/a ratio) of the cell is reduced by Co vacancies. Neutral oxygen vacancies have little effect on the pseudo-cubic lattice parameters $\langle a \rangle$ of both CFO and NFO. Increasing the charge state q of the oxygen vacancies increases $\langle a \rangle$ up to 1% for $q = +2$ in both CFO and NFO.

4.2.4 Electronic structure

Our results show that a cation vacancy enhances the valence state of the Co and Ni cations the closest to this defect. This enhancement depends on the charge state of the vacancy. Conversely, an oxygen vacancy will lower the valence state of the surrounding Fe cations.

A neutral cation vacancy V^0 induces an electronic reconstruction, with the transfer of holes to the Co or Ni cations, first neighbors of the vacancy. As shown in Fig. 7.9, these holes are generated

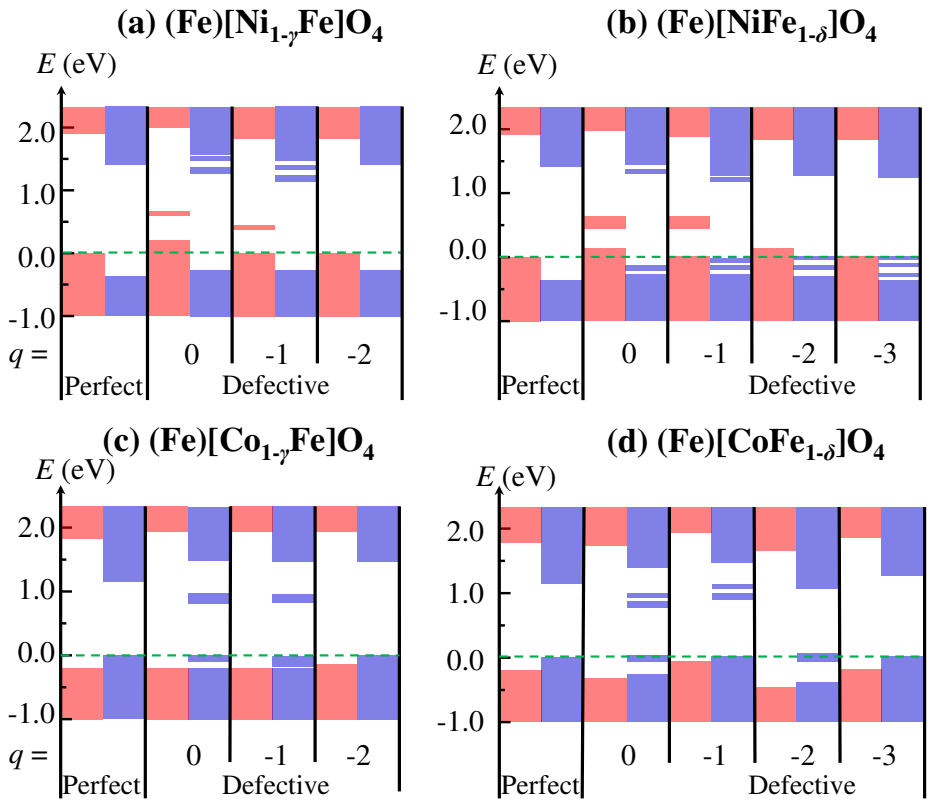

Figure 4.6 – Schematic representation of the density of states calculated for (a,b) NFO and (c,d) CFO crystals with different cation vacancies in the Oh sites and different charge states q. The energy range of the band gap corresponds to the white area. Majority- and minority-spin DOS are shown in red and blue colors, respectively. The green dashed line corresponds to the highest occupied state. The numbers correspond to the values of q.

by depopulating the highest occupied orbitals, which have e_g-like(t_{2g}-like) symmetries and belong to the majority(minority) spin channel for NFO(CFO), thus creating gap states in the same spin channel. When a cation vacancy is charged, the number of transferred holes decreases, down to 0 for both $V^{-2}_{M(Oh)}$ and $V^{-3}_{Fe(Oh)}$. If the electronic reconstruction induced by the defects only implies one hole, this hole is mainly localized in the cations, first neighbors of the vacancy. When more holes are transferred (for neutral vacancies in particular), we observe a delocalization over more Ni/Co cations (which corresponding to a variation of the spin magnetic moments of Ni cations, as it will be shown in Fig. 4.8). The top of the valence band of NFO even crosses the Fermi level for the specific defects $V^{0}_{Ni(Oh)}$, $V^{0}_{Fe(Oh)}$ and $V^{-2}_{Fe(Oh)}$. We remind that neutral cation vacancies are the most stable when the Fermi level is close to the VBM; such a condition would favor p-doping in NFO. Finally, we can notice that occupied gap states are also induced by Fe vacancies, both in CFO and in NFO and their existence is certainly due to the presence of dangling chemical bonds.

Under oxygen-poor growth conditions, oxygen vacancies will most likely exist with the charge state $q = 0$. Their presence goes along with an electronic reconstruction and an occupied state appear one in the majority spin channel and another in the minority spin channel (Fig. 7.10).

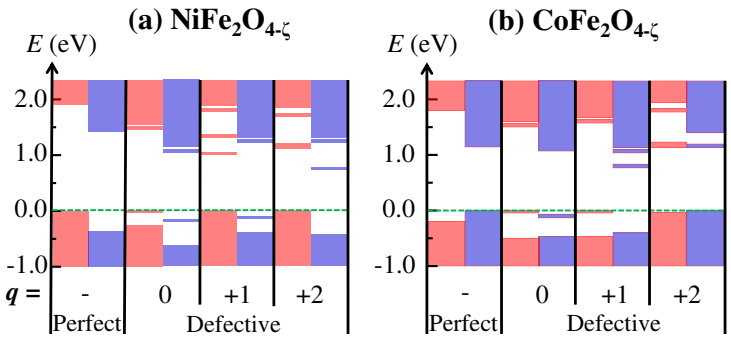

Figure 4.7 – Same as in Fig. 7.9, but for oxygen-deficient (a) NFO and (b) CFO crystals.

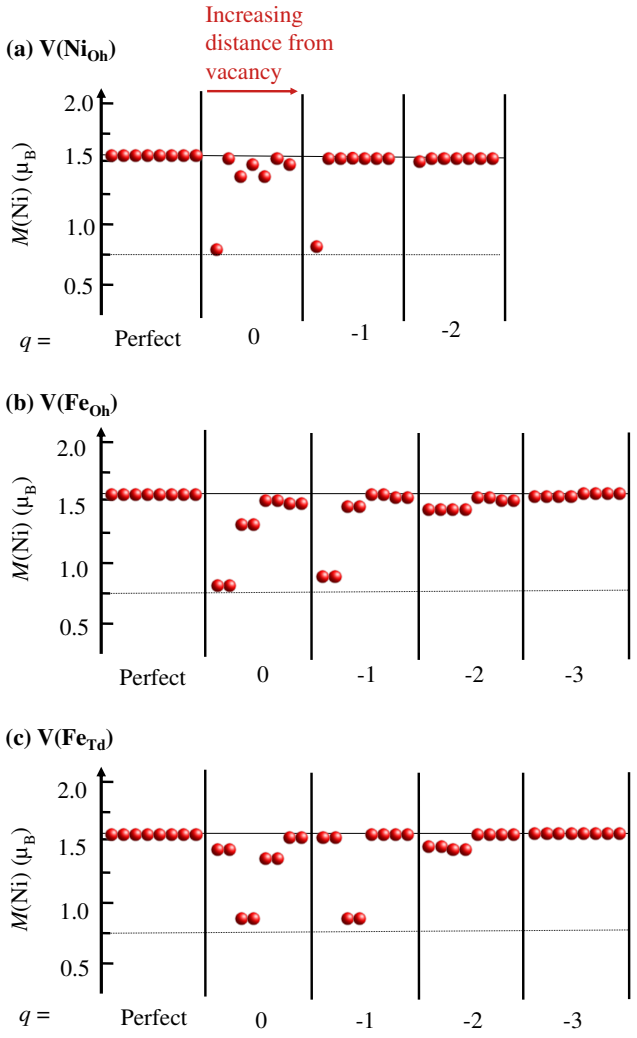

Figure 4.8 – Variations of the spin magnetic moments of Ni cations in $NiFe_2O_4$ when (a) a Ni, (b) a Fe_{Oh} or (c) a Fe_{Td} vacancy is present with different charge states q. The cations are ordered from left to right according to their distance from the vacancy.

Ionized oxygen vacancies can be formed when the Fermi level is close to the VBM. Oxygen vacancies with the charge state $q = +2$ do not lead to a charge imbalance and to an electronic reconstruction.

When the charge state of the oxygen vacancy is $q = +1$, which may happen when the Fermi level is close to the VBM, a single occupied gap state appears in the majority-spin channel for CFO and in the minority-spin channel for NFO.

4.2.5 Magnetic properties

As discussed in a previous study on Fe_3O_4 [237], the variation of total spin magnetic moment induced by vacancies in a spinel ferrite crystal can be decomposed into two different contributions, which are:

1. A decrease(increase) of its value due to the removal of atoms in Oh(Td) atomic sites
2. Its potential increase(decrease) due to the electronic reconstruction, as already discussed in the previous paragraph.

In an oxygen-rich environment, when mostly cation vacancies with the charge state q are created, we can use $M(Co^{2+}) = 3\ \mu_B$, $M(Ni^{2+}) = 2\ \mu_B$ and $M(Fe^{3+}) = 5\ \mu_B$ and the following equations to explain the values of the spin magnetic moment per formula unit that we calculated from first principles:

$$M_{\text{f.u.}}(Co_{1-\gamma}Fe_2O_4) = (1-\gamma)M(Co^{2+}) + [(2-|q|)\gamma]\mu_B \tag{4.3}$$

i.e. $M_{\text{f.u.}} = [3-(1+|q|)\gamma]\ \mu_B$ for $Co_{1-\gamma}Fe_2O_4$, if we consider that only Co vacancies can be stable in CFO and

$$M_{\text{f.u.}}(Ni_{1-\gamma}Fe_2O_4) = (1-\gamma)M(Ni^{2+}) + [(|q|-2)\gamma]\mu_B \tag{4.4}$$

i.e. $M_{\text{f.u.}} = [(|q|-4)\gamma + 2]\ \mu_B$ for $Ni_{1-\gamma}Fe_2O_4$, when only Ni vacancies are present. In iron-poor conditions, we also expect the following value of the spin magnetic moment:

$$M_{\text{f.u.}}(NiFe_{2-\delta}O_4) = M(Ni^{2+}) - \delta M(Fe^{3+}) + [(|q|-3)\delta]\mu_B \tag{4.5}$$

i.e. $M_{\text{f.u.}} = [(|q|-8)\delta + 2]\ \mu_B$ for $NiFe_{2-\delta}O_4$, with only Fe_{Oh} vacancies.

According to our first-principles results, these equations, which should be used at low vacancy contents, hold at least up to $\gamma, \delta = 1/8$. For higher vacancy contents, these equations may not be valid anymore: the stoichiometry being too different from that of MFe_2O_4, other compounds should stabilize. Because the charge state q of a cation vacancy can be at most -3 and because vacancies are most likely to be found in Oh sites, our analysis thus predicts a systematic decrease of the magnetization due to the presence of such defects.

Let us now consider the effects of oxygen vacancies. Oxygen being a non-magnetic atom, changes in total magnetic moments can only be induced by the redistribution of charges for neutral or partially ionized vacancies. As discussed before, no electronic reconstruction will occur for $q = +2$. For $q = 0$, one additional electron is transferred in each spin channel: one electron onto the Fe_{Td} atom first-neighbor of the vacancy, while the other one is spread among Fe_{Oh} atoms,

and stays mostly localized near the vacancy. These two charge transfers induce local decreases of the spin magnetic moments, which compensate for each other on average (Fe_{Td} and Fe_{Oh} atoms being antiferromagnetically coupled) and leave the total spin magnetic moment unchanged for both materials, in agreement with previous predictions reported on Fe_3O_4 [236]. Other reported calculations tend however to predict the transfer of electrons only in the minority-spin channel [238]. In summary, V_O^{+2} and V_O^0 vacancies should not be considered as responsible for a noticeable change in the magnetization:

$$M_{\text{f.u.}} = M(M_{Oh}^{2+}) \tag{4.6}$$

if $q = 0, +2$

For $q = +1$, which is less probable, we do not have the same compensation of the magnetic moments as for $q = 0$: only one electron will be transferred to Fe^{3+} cations located in Td sites for CFO and in Oh sites for NFO. This induces a direct change of the total spin magnetic moment. In this case, the total spin magnetic moment of the $MFe_2O_{4-\zeta}$ crystal will thus decrease(increase) by ζ μ_B:

$$\begin{aligned} M_{\text{f.u.}}(NiFe_2O_{4-\zeta}) &= M(Ni_{Oh}^{2+}) + \zeta \left[M(Fe_{Oh}^{2+}) - M(Fe_{Oh}^{3+})\right] \\ &= (2-\zeta)\ \mu_B \\ M_{\text{f.u.}}(CoFe_2O_{4-\zeta}) &= M(Co_{Oh}^{2+}) + \zeta \left[M(Fe_{Td}^{2+}) - M(Fe_{Td}^{3+})\right] \\ &= (3+\zeta)\ \mu_B \end{aligned} \tag{4.7}$$

In addition to our numerical results, it is important to mention that real samples may be more complex. Munjal and Khare [82], who studied resistive and magnetization switching as a function of an applied electric field, used x-ray photoelectron spectroscopy to measure changes in the oxidation state of Co cations, from Co^{2+} to Co^0. They did not observe the modification of the oxidation state of iron cations, suggesting that this may occur due to the easiest formation of oxygen vacancies near Co than near Fe atoms. Robbennolt, *et al.* also identified the formation of Co^0 atoms, with a smaller concentration of Fe^0 when a sufficiently large voltage is applied on mesoporous CFO [79]. The discrepancy between this experimental study and our calculations may also confirm the necessity to extend our work to the more systematic study of multiple vacancies, as such experimental observations may be the result of the presence of several oxygen vacancies in Co-rich regions.

We only considered single and isolated defects. However, real samples generally possess combinations of these defects and their mutual interaction is not well understood. We have shown for example that a neutral Ni-O bi-vacancy is more stable than the separated Ni and O vacancies, which may be partly explained by the compensating oxidation number of the corresponding ions. The interaction between vacancies and cation distribution would also deserve a deep investigation. In particular, as discussed at the end of this Chapter, the experimental observation of Co^0 or Fe^0 atoms [79, 82] in a sample, which cannot be explained by our calculations, and preferential sites

for the formation of oxygen vacancies, leading to inhomogeneities, should be considered. We also mentioned that p-doping by specific defects could induce the appearance of spin-polarized holes in the VBM of NFO or CFO. In the case of the CFO, the spin state of the VBM depends on the inversion degree: Associating both contributions could certainly alter our results. Another natural extension of this work would also consist of combining the study of point defects with the study of extended defects (like antiphase boundaries which are common in these compounds), of strain effects (which can change both the cation distribution [126] and the formation energy of the vacancies), or also of interfaces.

Finally, the effect of point defects on other material properties is also a possible way to pursue this study: In addition to the magnetization, the electric polarization evidenced in $NiFe_2O_4$ [97, 129] is expected to depend on the cation distribution, but can also be affected by the presence of vacancies, which could lead to tunable magnetoelectric effects. The calculated dependence of the c/a ratio and also of the conductive behavior over different defects discussed in this Chapter may give a first clue of the importance of taking them into account.

There are many other types of more complex defects that are beyond the scope of this thesis, such as Frankel defects (dislocation of crystal ions from its regular lattice site to an interstitial position), Schottky defects (missing of a pair of cation and anion in the crystal), interstitial defects. However, we performed a preliminary calculation on a neutral Ni-O bivacancy created in a supercell containing 8 f.u. of NFO and considering oxygen-poor growth conditions. When both vacancies are as close as possible, *i.e.* separated by a distance of approximately 2 Å, the formation energy of this complex defect is 3.38 eV. If we take the two vacancies away, separated by a distance of 4.6 Å, the formation energy increases by 0.3 eV. The energy increases up to 1.7 eV when we consider the sum of the two formation energies calculated for the isolated neutral or $+1/-1$-charged Ni and O vacancies, that is $E_\mathrm{f}\left[V_\mathrm{Ni}^0\right]+E_\mathrm{f}\left[V_\mathrm{O}^0\right]$ or $E_\mathrm{f}\left[V_\mathrm{Ni}^{-1}\right]+E_\mathrm{f}\left[V_\mathrm{O}^{+1}\right]$. Such a neutral bivacancy does not lead to electronic reconstructions, the oxidation degrees of Ni and O ions canceling out each other, which may explain the stability of this defect.

4.3 Effect of strain

We have performed strain calculations for (001) biaxial strains of -5%, -2.5%, 2.5%, and 5% on bulk NFO with Ni/O vacancy. Compared to the unstrained structure, the electronic and magnetic properties do not change in the presence of an O-vacancy. With Ni vacancy, the electronic and magnetic properties are not changed with compressive strains, but with tensile strains, a change in the electronic and magnetic properties is observed. For a compressive strain, the NFO with Ni-vacancy is conducting, as is the unstrained defective NFO due to the sharing of one of the two-hole defect states by two Ni atoms. However, under tensile strain, this is changed and both hole defect states are localized on two distinct Ni atoms, one on each, leading to the opening of a band gap, and the crystal becomes insulating. These results confirm that strain can alter the electronic properties of spinel ferrites.

4.4 Conclusions

Co/Ni, Fe(Oh), and O vacancies (depending on the growth conditions) are found to be the most likely defects to occur in CFO and NFO. The Fe(Td) vacancy defect is the least probable defect in the bulk spinel ferrite. Only the presence of cation vacancies is expected to strongly decrease the magnetization (this decrease depends on the ionization state of the vacancies), while according to our calculations, no or only few magnetization changes should be due to oxygen vacancies. Cation vacancies will be responsible for a transfer of holes to the VBM of the crystal, in the majority spin channel for NFO and in the minority spin channel for CFO, due to the different spin states of the VBM for the two perfect materials. p-doping with a Ni/Fe ratio above 1/2 can also induce the formation of Ni^{3+} cations with gap states very close to the bulk VBM. In the case where Ni cations replace Fe cations in Oh sites, we observed the formation of Ni^{3+} cations with a low-spin state, promoting a half-metallic state with fully spin-polarized hole conductivity.

Chapter 5

$NiFe_2O_4(001)$ thin films: the role of surfaces and interfaces

In the two previous chapters, we studied the structural, electronic and magnetic properties of bulk stoichiometric and non-stoichiometric spinel ferrites. Because in this thesis, we are interested in the properties of nanometer-thick thin films of spinel ferrites, which are moreover polar along the [001] direction, it is now important to investigate how these properties may change in the vicinity of their surfaces and interfaces.

Only few theoretical studies of spinel ferrite surfaces have already been published, which confirms the importance of the present work. H. Hajiyani and R. Pentcheva [51] have studied (001) and (111) orientations of the $Co_xNi_{1-x}Fe_2O_4$ surfaces (with x = 1.0, 0.5, and 0.0). They studied four types of (001) surface terminations, corresponding to a A layer, a B layer, a 0.5A layer, or a B layer with O vacancies. They found that the (001) surface with an A-layer termination is the most stable under oxygen-poor growth conditions while the surface with a B-layer termination is stable under oxygen-rich growth conditions. X. Shi et al. [238] studied the NFO(001) surface with vacancies on different oxygen sites at the surface, to understand the water adsorption for different catalytic reactions. In their study on $NiCo_2O_4$, Xiao *et al.* [242] found that the β-type surface (associated to a bulk *Imma*-space-group cation distribution) is a more stable surface than the α one ($P4_122$ space group).

In this chapter, we present a detailed study of the NFO(001) surfaces, to understand their electronic and magnetic properties. This study can also help to understand some experimental results. As explained in Section 2.9.4, the growth of surfaces with a specific termination depends on the nature of the substrate and on the growth conditions (*i.e.* the temperature, the oxygen partial pressure, etc.). We have chosen to only study (001) surfaces of $NiFe_2O_4$ corresponding to the samples studied within the MULTINANO project, on which this thesis work is based. The aim of this project was to understand the transport mechanisms at the interface between a spinel ferrite and a perovskite. Therefore, it was important to understand first the electronic and magnetic properties of the spinel ferrite surfaces before studying the (001) interface between a spinel ferrite

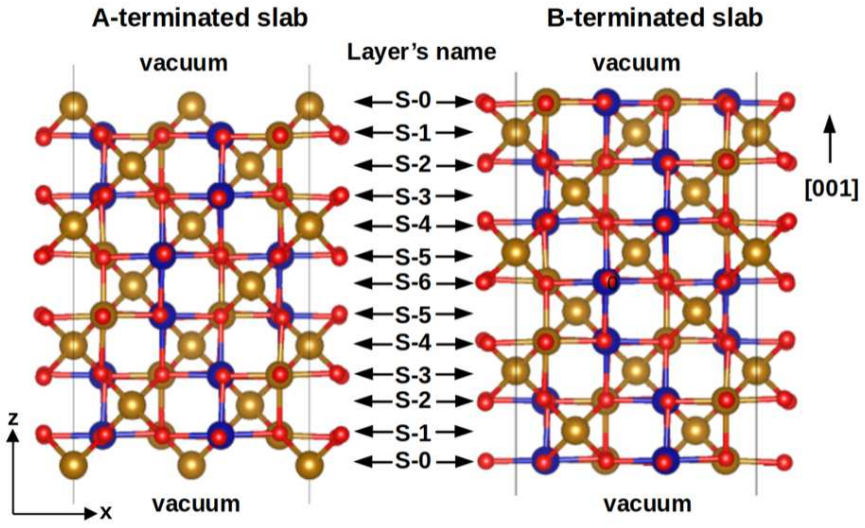

Figure 5.1 – Structure of the NFO slabs with an A-termination (left side; Fe(Td) at the surface) and a B-termination (right side; Ni(Oh), Fe(Oh), and O at the surface). The Ni, Fe, and O atoms are shown in blue, yellow, and red colors, respectively. The labeling of the layers is shown between the two slabs, it will be used later to discuss local results.

and the perovskite $BaTiO_3$ (BTO). Preliminary results about this interface are given at the end of this chapter.

5.1 Computational details

According to Refs. [126, 222] and to our previous calculations, the space group that corresponds to the most stable cation ordering in $NiFe_2O_4$ (NFO) is $P4_122$ (with the space-group number 91). This tetragonal space group is chosen for our study of the NFO(001) surface.

The slabs we used to study the surfaces were made by stacking atomic layers of a conventional unit cell along the [001] direction. The in-plane dimensions of these slabs is a 1×1 square plane with a lattice parameter of 8.277 Å, which corresponds to the calculated equilibrium lattice parameter of bulk NFO. Along the [001] direction, the NFO slabs consist of alternation of A and B layers consisting of $[Fe_2]^{6+}$(Td) and $[Ni_2Fe_2O_8]^{6-}$(Oh), respectively; each bilayer of the supercell thus contains two formula units (f.u.) of NFO.

We used symmetric but non-stoichiometric NFO slabs with two identical surface terminations, as shown in Fig. 7.11 in the case of two perfect A (left) or two perfect B (right) terminations. This choice will allow us to calculate the surface formation energy for a specific termination. A vacuum of at least 15 Å is inserted between the two surfaces to avoid any artificial interaction between them due to the periodic repetition of the atomic structure.

To check the convergence of the surface formation energy with respect to the slab thickness, we used the method proposed by Boettger [243]. In this method, the convergence of the surface formation energy for a given atomic termination can be calculated by taking the energy difference

ΔE between a slab containing $N-1$ atomic layers and another slab containing $(N+1)$ atomic layers:

$$\Delta E(N) = \frac{E_{\text{slab}}(N+1) - E_{\text{slab}}(N-1)}{2} \tag{5.1}$$

Here, N is an even number higher or equal to 4. If the slab is thick enough, this energy difference will converge to the energy of the bulk NFO crystal of one f.u., meaning that the convergence of the surface formation energy is reached.

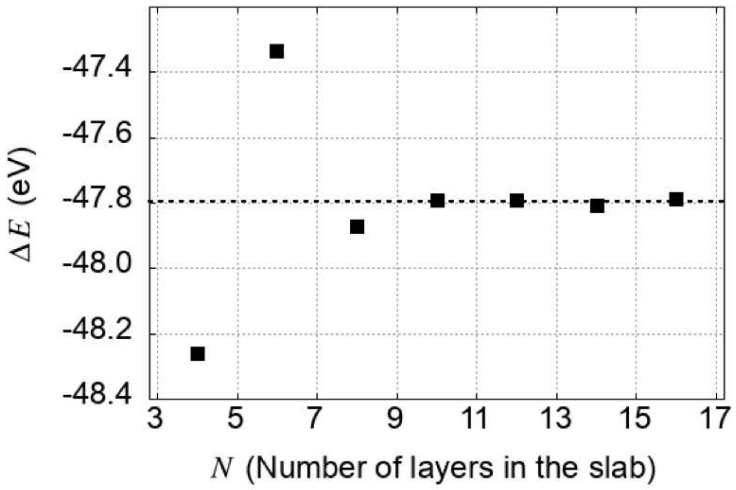

Figure 5.2 – The convergence of ΔE (calculated according to the Boettger's method [243]) with respect to the slab thickness. The energy of one f.u. of bulk NFO is shown by a black dashed line. The x axis gives the number N of NFO layers in the slab. The slabs are symmetric and have an odd number of atomic layers; only slabs with B-terminated surfaces are considered.

The convergence of the surface formation energy of the B-terminated NFO slab calculated by the Boettger's method is shown in Fig. 5.2. If N is sufficiently large, $\Delta E(N)$ is identical to the total energy of bulk NFO (black dashed line in Fig. 5.2). The results show the good convergence of the surface energy of the NFO B-terminated slab from a thickness of 11 layers, where it shows an error of less than 0.01 eV/f.u. To keep a better accuracy, we have used slabs with a thickness of 13 layers for further calculations.

5.2 Properties of the pristine NFO slabs with perfect A or B surface terminations

On the basis of electrostatic energy considerations, Tasker [244] proposed a classification of surfaces into three types. Technically, the (001) surfaces of spinel crystals should belong to the type-III surfaces, *i.e.* to polar surfaces which possess a net dipole. The stabilization of these surfaces is therefore expected to involve electronic reconstructions [245] or atomic reconstructions *via* the formation of defects.

As explained previously, to calculate the surface formation energies, we chose to use symmetric slabs with two identical surface terminations. By construction, such slabs are not stoichiometric: they necessarily possess a number of A/B atomic layers $N_{A/B}$ such as $N_A = N_B \pm 1$. With such a geometric configuration, the slabs are not polar any more (the structure would then be closer from the type II according to the Tasker classification) and the electronic reconstructions will emerge because of the non-stoichiometry of the slabs, rather than because of the presence of electric dipoles and a polar-catastrophe scenario, which we would encouter if we had used an asymmetric and stoichiometric slab, containing one A and one B surface. For sufficiently thick slabs, boths geometry should however give comparable results [246]. A comparison between the results described in this chapter and obtained with symmetric slabs, and the results obtained with an asymmetric slab, are given in the Appendix D.

5.2.1 Atomic structure of the perfect NFO(001) surfaces

At the surface, the forces acting on atoms are not the same than in the bulk NFO crystal, due to the formation of dangling bonds and symmetry breaking. Therefore, after the ionic relaxation, the slab undergoes atomic structural changes near the surface layers. In Fig. 7.12 (a), we plotted the interlayer distances d_{AB} between successive A and B layers for NFO(001) slabs with perfect A or B surface terminations. The interlayer distances d_{AB} are calculated as the difference between the averaged z-coordinates (along the [001] direction, perpendicular to the surfaces) of all the atoms within the adjacent A and B layers. Our calculations show that the distances d_{AB} are smaller near the surface than in bulk NFO: They are indeed of 0.17 and 0.86 Å at the surfaces of the A- and the B-terminated slabs, respectively. As we move away from the surface layer, the interlayer distance oscillates and converges rapidly to the interlayer distance of the bulk NFO crystal ($\simeq$ 1.03 Å).

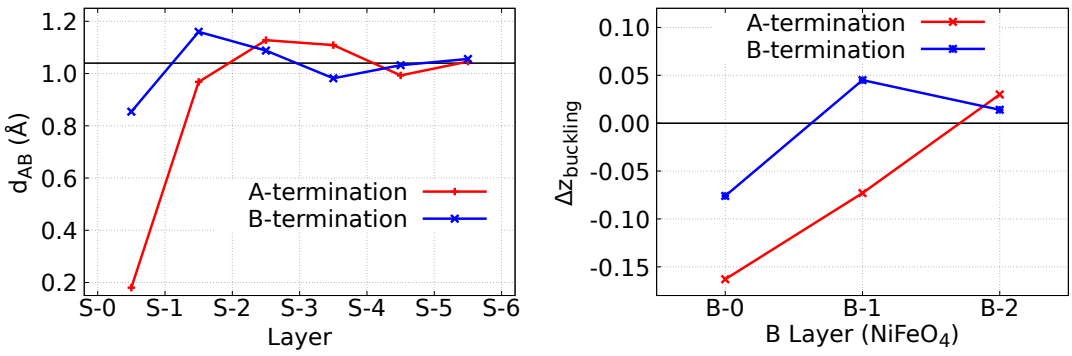

(a) (b)

Figure 5.3 – (a) Interlayer distance between consecutive A and B layers, calculated for the successive atomic layers of the A- and B-terminated slabs, shown with red and blue colors, respectively. The black horizontal line at 1.04 Å represents the interlayer distance of bulk NFO. (b) Anion/cation buckling in the B-layers ($[Ni(Oh)Fe(Oh)O_4]^{3-}$), calculated for the successive atomic layers of the A- and the B-terminated slabs, shown with red and blue colors, respectively.

As shown in Fig. 7.12(b), the B layers near the NFO surface also display a small cation-oxygen rumpling $\Delta z_{buckling}$, defined in Eq. 5.2 as the difference between the averaged z coordinates of cations and oxygen anions located in the same (001) B layers:

$$\Delta z_{buckling} = z_{Cations} - z_{Anions} \tag{5.2}$$

Fig. 7.12(b) shows that the surface cations move slightly toward the center of the slab for both A- and B-terminated slabs. The calculated buckling is higher for the A-terminated slab (-0.163 Å) than for the B-terminated slab (-0.076 Å).

5.2.2 Magnetism at the perfect NFO(001) surfaces

NFO is characterized by an antiferromagnetic coupling between Fe cations located in Td sites and Ni or Fe cations located in Oh sites. The spin magnetic moments of the different cations [Ni, Fe(Oh), and Fe(Td)] are shown in Fig. 7.13(a) and 7.13(b) for the successive atomic layers, respectively for the A- and B-terminated slabs of NFO.

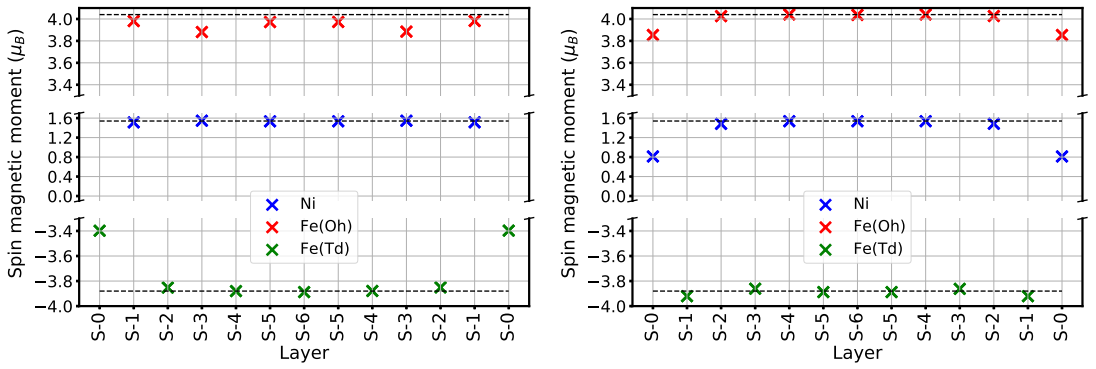

(a) (b)

Figure 5.4 – (a) The spin magnetic moment of cations in the successive atomic layers of the A-terminated NFO slab. The black dashed lines represent the spin magnetic moment of cations in bulk NFO. (b) Same, but for the B-terminated NFO slab.

In the center of the slab, the calculated atomic spin magnetic moments of the cations is found equal to that of the bulk crystal (given by the black dotted lines), which are 1.54 μ_B, 4.04 μ_B, and −3.88 μ_B respectively for the Ni, Fe(Oh), and Fe(Td) cations.

At the surface layers, they are on the contrary different, due to electronic reconstructions which will be explained in the next section. At the perfect A-terminated surface [Fig. 7.13(a)], the Fe(Td) and Fe(Oh) cations change their spin magnetic moment from −3.88 μ_B to −3.40 μ_B for each of the Fe(Td) atoms and from 4.04 μ_B to 3.88 μ_B for each of the Fe(Oh) atoms of the (S-3) layer, respectively. At the perfect B-terminated surface [Fig. 7.13(b)], we observe a slight variation of the atomic spin magnetic moment of cations in the layers the closest to the surface layer: the atomic spin magnetic moment of the Fe(Td) ion of the (S-1) layer becomes −3.92 μ_B, instead of −3.88 μ_B in bulk NFO. We can also see that Ni and Fe(Oh) surface ions change their spin magnetic moment to 0.81 μ_B (for each Ni ion), and 3.86/3.83 μ_B (for each Fe ion).

As in the Chapters 3 and 4, these analyses of the variations of spin magnetic moments will appear to be precious for further understanding the calculated electronic structure and charge reconstructions at the surfaces.

5.2.3 Electronic structure of the perfect NFO(001) surfaces

In the previous subsection, we have commented the changes of spin magnetic moments of the Ni/Fe cations at the perfect (001) A- or B-terminated surfaces of NFO. It is obvious that such changes of the magnetic moments mostly come from the presence of electronic reconstructions arising at the surfaces and resulting in a change of the oxidation degree of the different cations.

Along the [001] direction, the alternating A and B atomic layers respectively carry an electronic charge of σ = +6 e/−6 e (per 2 f.u. of NFO). With a type-III polar surface (corresponding for instance to the termination of a stoichiometric and nonsymmetric slab), an amount of charges equal to -0.5σ should be transferred to the surface in order to cancel the internal electric field and to stabilize the surface [247].

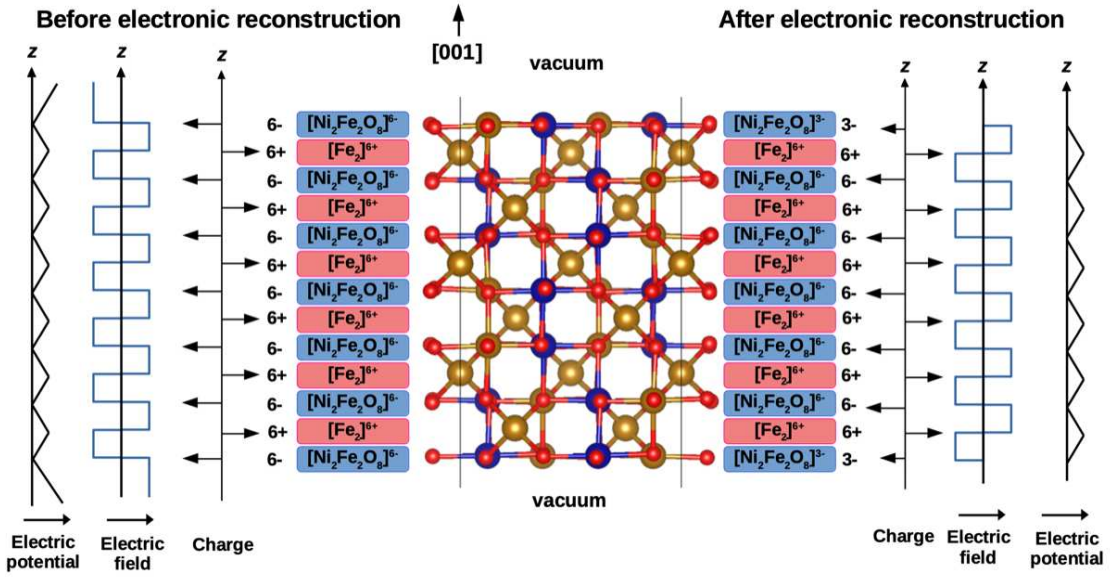

Figure 5.5 – The charges resulting from electronic reconstruction on each atomic layer of the B-terminated NFO(001) slab, along with the electric field and the electric potential between the layers. The Ni, Fe, and O atoms are shown in blue, yellow, and red colors, respectively. It shows that the net averaged electric potential in the slab is uniform. This figure is only valid if each layer of the slab is an infinite 2D layer and the distance between the layers is fixed.

With our slab geometry, a similar amount of charge reorganization is also expected to preserve the global electric neutrality for the non-stoichiometric slab. This charge reconstruction follows the same mechanisms as described in Chapter 4 for non-stoichiometric point defects. For example, the slab with two perfect B-terminated surfaces can be seen as a slab in which an A layer (carrying a charge σ = +6 e) is missing to recover the stoichiometry: in consequences, to preserve the electric neutrality, a surface charge of σ_S = +3 e (corresponding to three holes) has to be distributed onto

each of the two B surfaces, which will thus carry a charge of $-6 + 3 = -3$ e after the electronic reconstruction. Following the same reasoning, a transfer of three electrons ($\sigma_S = -3$ e) should occur toward both A-terminated surfaces (see more details in Fig 5.5).

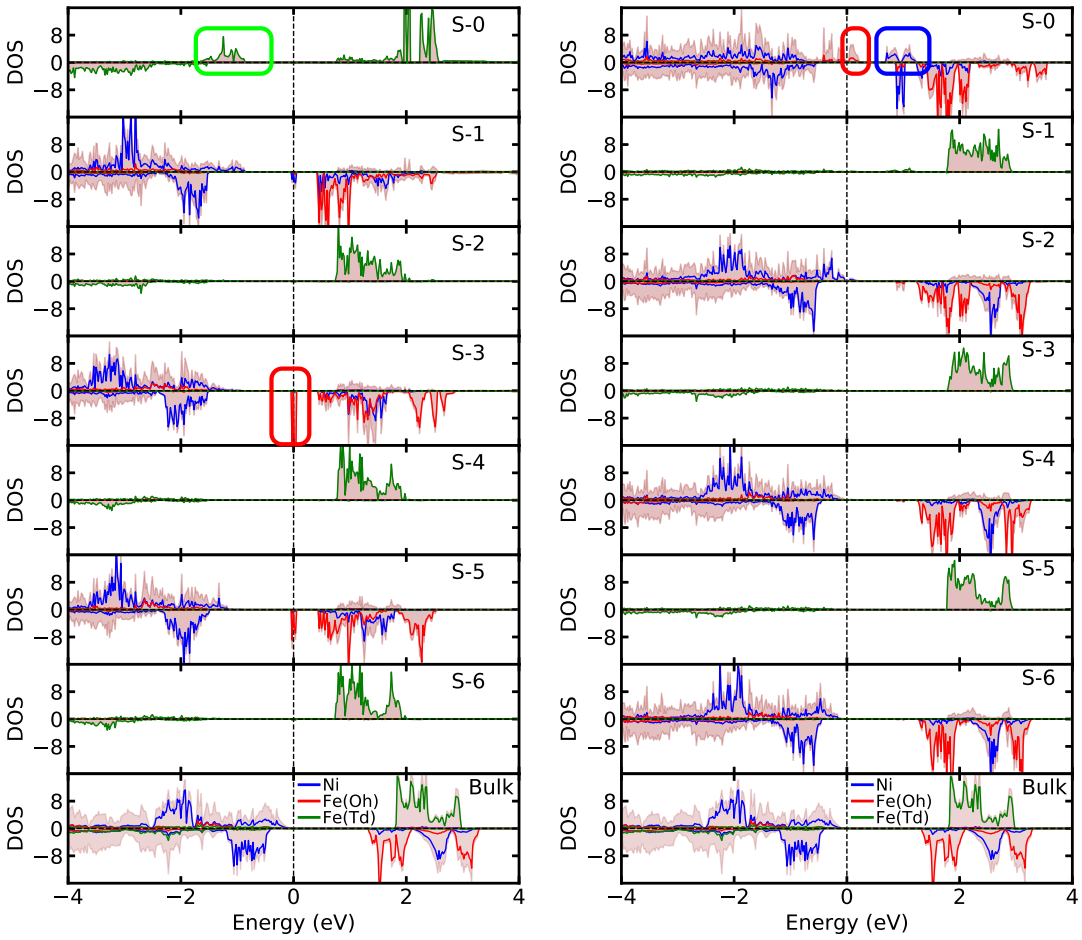

(a) A-terminated slab

(b) B-terminated slab

Figure 5.6 – The LDOS of the atomic layers from (S-0) (surface layer) to (S-6) (the layer at the center of the slab) for the A-terminated (a) and the B-terminated (b) slabs. For comparison, the DOS of bulk NFO is shown in the bottom panel of the two figures. The DOS peaks corresponding to the defect states are highlighted by rectangles drawn with a color that represents the atom to which the defect states belong (blue, red, and green colors for Ni, Fe(Oh), and Fe(Td) cations, respectively).

Defect states corresponding to these charge transfers can be seen in the band gap of the layer-resolved density of states (LDOS) of the A- and B-terminated slabs shown in Fig. 7.14.

For the A-terminated surface [Fig. 7.14(a)], the surface states are expected to correspond to the transfer of three electrons. Two of these electrons will localize on the two Fe^{3+}(Td) cations of the (S-0) surface layer to decrease their oxidation degree to 2+ and to form the defect state highlighted by the green rectangle below the Fermi level. This change of oxidation state is consistent with the calculated decrease, in absolute value, of the spin magnetic moments of the surface Fe(Td)

cations. These defect states on Fe(Td) involves d_{xz}, d_{yz}, d_{z^2} and a small contribution of d_{xy} orbitals. The last electron defect state which involves two Fe(Oh) (d_{xz}) of the (S-3) layer appears in the minority-spin channel and it is shown with a red rectangle just below the Fermi level.

Similarly, we can see that the three-hole defect states of the B-terminated slab are located at the (S-0) surface layer, as shown in Fig. 7.14(b). The first two-hole defect states are shown with a blue rectangle, just above the Fermi level, in the majority spin DOS. They involve the contribution of two Ni atoms and their respective $d_{x^2-y^2}$ orbitals. The last hole defect state, evidenced by the red rectangle, crosses the Fermi level and corresponds to partially-filled $d_{x^2-y^2}$ bands of the two surface Fe(Oh) atoms. Hence, the perfectly-B-terminated NFO surface is found to be a spin-polarized hole conductor because of the electronic reconstruction, which leads to the formation of two Ni^{3+} and two $Fe^{3.5+}$ cations, hence reducing their spin magnetic moment, as explained in the previous section. Analogous results were reported in the literature for a α-NFO(001) surface [238] and for a β-$CoFe_2O_4$(100) surface [248].

5.3 Atomic reconstructions at the $NiFe_2O_4$(001) surfaces

In the previous section, we calculated the physical properties of the perfect A- and B-terminated NFO(001) surfaces and we confirmed the emergence of electronic reconstructions which can make the surface metallic. It is however important to wonder now if atomic reconstructions could happen to avoid such strong reorganizations and to make the surfaces more stable.

5.3.1 Relative stability of the surface terminations

For the symmetric slabs with A- and B-terminated surfaces, many possible surface terminations exist due to different types of surface defects that can form in the surface atomic layers, such as cation exchange within the surface layer or between the surface and sub-surface layers or excess of cations or anions at the surface or in the subsurface layers. The relative stability of the different surface terminations can be compared, using the calculated values of the surface formation energy, according to Eq. 2.34 of Chapter 2. The Fig. 7.15 displays the most stable surface terminations as a function of the variations of the chemical potentials $\Delta\mu_{\mathrm{Fe}}$ and $\Delta\mu_{\mathrm{Ni}}$. In this figure, we superimposed the domain of stability of the bulk NFO, delimitated by the dotted black lines. As in Chapter 4, let us now consider two different growth conditions, an O-rich ($\Delta\mu_{\mathrm{O}} = -0.5$ eV, represented by a black triangle) and an O-poor condition ($\Delta\mu_{\mathrm{O}} = -2.2$ eV, represented by a black dot). With the O-poor growth conditions, the A-terminated surfaces with an excess of Ni atoms at the surface are the most stable surface terminations. As we move from the O-poor growth conditions towards the O-rich growth conditions, the stability of the B-terminated surfaces increases. These results are in agreement with the results calculated for NFO surfaces by Hajiyani, *et al.* [51].

In Fig. 7.15, we can see only the most stable surface for each point ($\Delta\mu_{Fe}$, $\Delta\mu_{Co}$) in the phase diagram, but it does not give any information on the stability of other surface terminations, which may be very close to that of the most stable one for a given growth condition. Therefore,

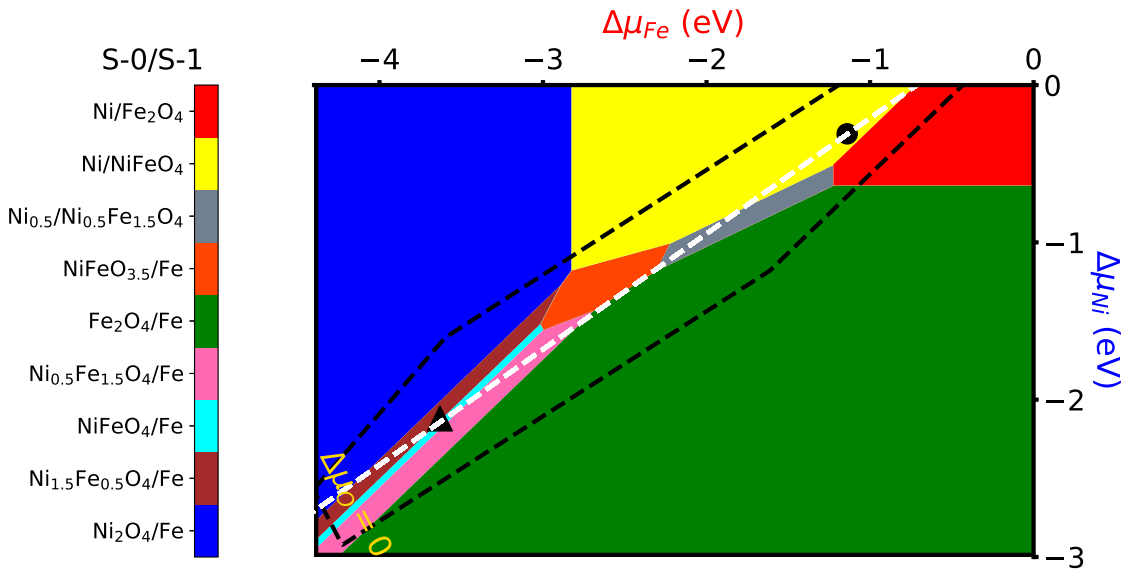

Figure 5.7 – The surface phase diagram of NFO symmetric slabs is plotted for different surface terminations. It is plotted using $\Delta\mu$ of Fe and Ni on the x-axis and y-axis, respectively. The black dashed line represents the stability domain of bulk NFO. The oxygen chemical potential ($\Delta\mu_O$) is zero at the bottom left of the phase diagram. $\Delta\mu_O$ grows towards top-right corner ($\Delta\mu_{Fe}$ = 0, $\Delta\mu_{Co}$ = 0). A black triangle and a black circle on the phase diagram represent O-rich ($\Delta\mu_O$= -0.5 eV) and O-poor ($\Delta\mu_O$= -2.2 eV) growth conditions, respectively. The color bar on the left side of the figure and the notation (S-0/S-1) are used to label the slabs with the (S-0) surface layer and sub-surface (S-1). The white dashed line in the center of the bulk stability domain will be used to calculate the surface formation energy versus the variation of the oxygen chemical potential.

we have plotted the surface formation energies calculated for every surface termination and the two particular growth conditions in Fig. 5.8. In this figure, we show that some surfaces have a surface formation energy lower than 80 meV Å^{-2}. We have chosen this criterion to consider that a termination can be observed even if it is not the most stable one. The first seven data points on the left side of the figure correspond to A-terminated surfaces, while the other data points correspond to B-terminated surfaces. All the stable A-terminated surfaces have Ni atoms at the surface A sites. For the O-rich growth conditions, there are many B-terminated surfaces with a low surface formation energy within an energy range of 10 meV Å^{-2}. Interestingly, the two A-terminated surfaces $Ni_{0.5}/Ni_{0.5}Fe_{1.5}O_4$ and $Ni_{0.5}/NiFeO_4$ are stable in both O-rich and O-poor growth conditions. The B-terminated oxygen deficient surface $NiFeO_{3.5}/Fe$ has nearly the same surface formation energies for the O-rich and O-poor growth conditions (the difference is only of 12 meV Å^{-2}).

In Fig. 5.9, the surface formation energy is plotted as a function of the values taken by $\Delta\mu_O$ along the white dashed line shown on the surface phase diagram (Fig. 7.15). In O-poor growth conditions, the $Ni/NiFeO_4$ surface termination is stable over a wide range of $\Delta\mu_O$, between −2.4 eV and −1.8 eV. For $\Delta\mu_O$ higher than −1.5 eV (O-rich growth conditions) the B-terminated surfaces

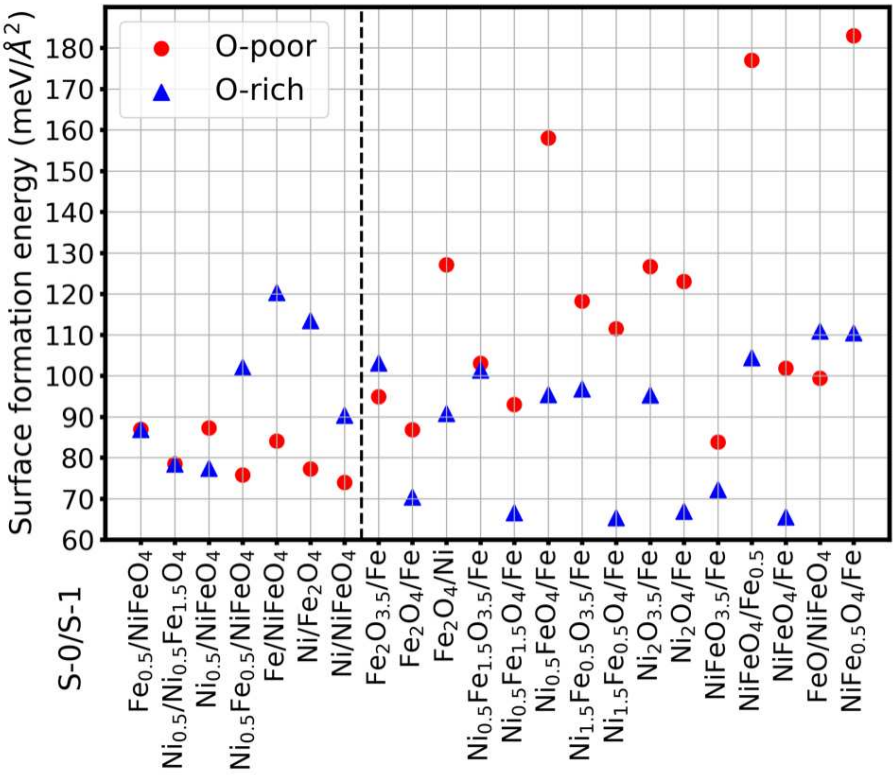

Figure 5.8 – Surface formation energy of NFO surfaces with different (S-0)/(S-1) terminations, calculated for two growth conditions: O-rich (blue triangles) and O-poor (red circles) growth conditions. On the x-axis, the (S-0)/(S-1) surface terminations are indicated. The vertical black dashed line separates the A- and B-terminated surfaces on the left and right sides of this line, respectively.

are the stable ones. The oxygen chemical potential can be expressed in terms of the experimental growth temperature (T) and pressure (P) [249, 250]:

$$\Delta\mu_O(T,P) = \frac{1}{2}\{[H_0 + \Delta H(T)] - T\,[S_0 + \Delta S(T)]\} + \frac{1}{2}k_B T \ln\left(\frac{P}{P_0}\right) \tag{5.3}$$

where $\Delta H(T) = C_p\,(T - T_0)$, $\Delta S(T) = C_p \ln(T/T_0)$. $H_0 = 8.7$ kJ mol^{-1}, $S_0 = 205$ J mol^{-1} K^{-1} are tabulated values [249, 251] and $P_0 = 1$ atm and $T_0 = 298$ K are standard pressure and temperature. This allows to plot the phase diagram for the same range of $\Delta\mu_O$ as in Fig. 5.9. Some examples of experimental growth conditions used to grow NFO thin films are: $T = 923$ K and $P/P_0 = 1.33 \times 10^{-4}$ [252], corresponding to $\Delta\mu_O = -1.35$ eV. Other useful conditions are $T = 673$ K and $P/P_0 = 1.33 \times 10^{-9}$, corresponding to $\Delta\mu_O(T,P) = -1.29$ eV. In Fig. 7.16, we see that the A-terminated surfaces are only stable above 1000 K.

5.3.2 Physical properties of the most stable surface terminations

The charges per surface in the slab before and after the electronic reconstruction has occurred and the work function are given in Table 7.1. These surfaces are divided into two categories: the A-terminated surfaces (top of the table) and the B-terminated surfaces (bottom of the table).

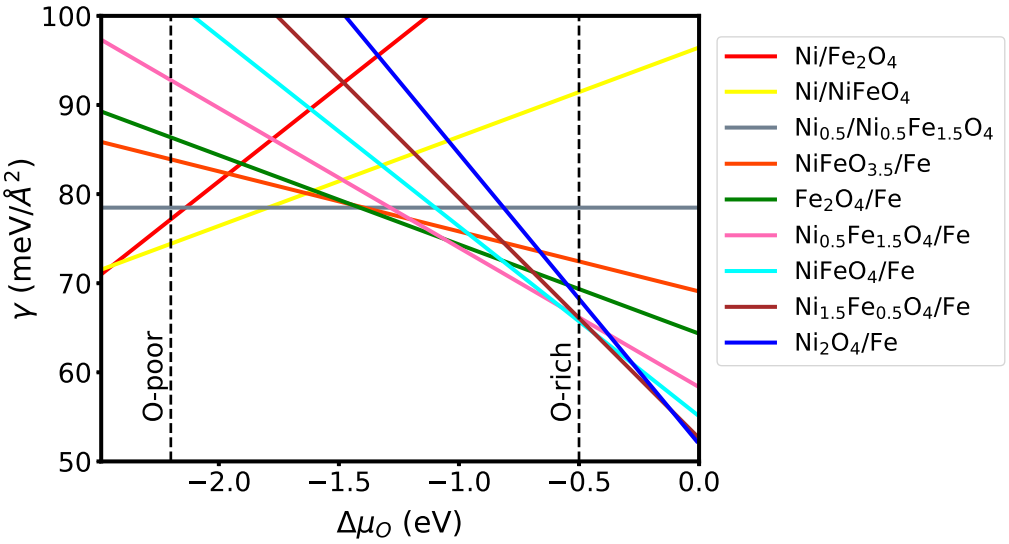

Figure 5.9 – Surface formation energy of NFO surfaces with different terminations versus the variation of the oxygen chemical potential. The range of $\Delta\mu_O$ corresponds to the white dashed line of the surface phase diagram in Fig. 7.15. On the right side of the figure, the labels of the surface terminations are given with the names of the surface and subsurface layers of the slab. The two growth conditions: an O-rich and an O-poor, are represented by the vertical dashed lines $\Delta\mu_O = -0.5$ and $\Delta\mu_O = -2.2$, respectively.

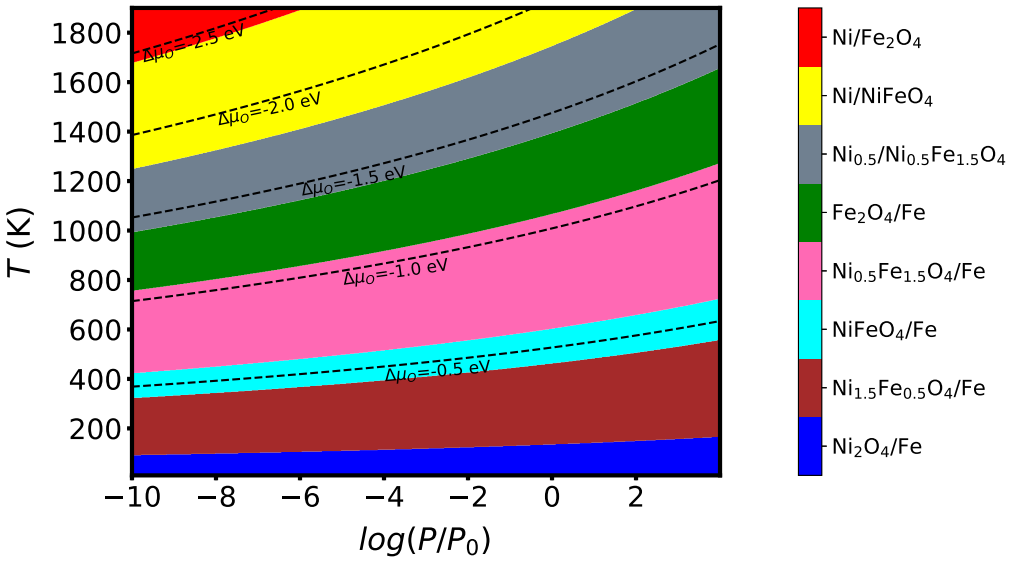

Figure 5.10 – Surface phase diagram plotted with respect to the growth temperature and oxygen partial pressure. The range of $\Delta\mu_O$ corresponds to the white dashed line of the surface phase diagram in Fig. 7.15. On the right side of the figure, the labels of the surface terminations are given with the name of the surface and subsurface layers of the slab. The black dashed lines represent some oxygen iso-chemical potential lines.

The values of the excess charges in the slab before the occurrence of any electronic reconstruction explain why defect electron or hole states appear at the surface or at the sub-surface layers. The

work function of the A-terminated surfaces is smaller than that of the B-terminated surfaces.

From Table 7.1, we can see that, for a given surface termination, when the charge reconstruction involve the delocalization of one hole (h) or one electron (e) over at least two Ni or Fe cations, this surface termination has more chance to become metallic, because of the formation of partially-filled bands which will cross the Fermi level. This situation will occur unless a charge ordering accompanied by structural distortions happens. The possibility of such charge ordering would require some additional verifications. $Ni/NiFeO_4$ and $Ni_{1.5}Fe_{0.5}O_4/Fe$ surfaces are the most stable surfaces of the A-terminated and B-terminated surfaces, respectively. The LDOS of three layers (S-0), (S-1) and (S-2) of these two surfaces are shown in Fig. 5.11. The defect state around the Fermi level of $Ni/NiFeO_4$ surface (shown by a blue ractangle in Fig. 5.11(a)) correspond to $d_{x^2-y^2}$ orbitals of two surface Ni atoms.

Table 5.1 – Physical properties of the surfaces with a surface formation energy lower than 80 meV/Å^2. The surface formation energy is given for two growth conditions: an O-rich and an O-poor. The number of defect charges per surface of the slab before any electronic reconstruction, the location of the defect charges (per surface), the work function, and conducting state (metallic M or Insulating I) of the different surfaces are given in the table.

Surface termination (S-0)/(S-1)	Surface formation energy (meV/Å^2) O-poor	O-rich	Excess charges*	Distribution of defect charges (e or h) on cations (e-electron, h-hole)	Work function (eV)	Conductivity (M/I)
A-terminated surface						
$Ni/NiFeO_4$	74	90	1	1e: → 2 Ni(Td)	4.31	M
$Ni_{0.5}Fe_{0.5}/NiFeO_4$	76	102	2	2e: 1→Fe(Td), 1→Ni(Td)	4.43	I
Ni/Fe_2O_4	77	114	3	3e: 2→2Ni(Td), 1→Fe(Oh)	4.21	M
$Ni_{0.5}/Ni_{0.5}Fe_{1.5}O_4$	78	78	0	Partial e transfer : Ni(Oh) → Ni(Td)	4.92	I
$Ni_{0.5}/NiFeO_4$	87	77	-1	1h: Ni(Td) and 2Ni(Oh)	5.30	I
B-terminated surface						
$NiFeO_{3.5}/Fe$	84	72	-1	1h: Ni(Oh)	5.57	I
Fe_2O_4/Fe	87	70	-1	1h: →2Fe(Oh)	5.50	M
$Ni_{0.5}Fe_{1.5}O_4/Fe$	93	67	-2	2h: 1→Fe(Oh), 1→Ni(Oh)	5.69	I
$NiFeO_4/Fe$	102	66	-3	3h: 1→2Fe(Oh), 2→2Ni(Oh)	5.77	M
$Ni_{1.5}Fe_{0.5}O_4/Fe$	112	65	-4	4h: 3Ni(Oh); Ni(Oh)(S-2)	5.85	I
Ni_2O_4/Fe	123	67	-5	5h: 4→4Ni(Oh), 1→2Ni(Oh)(S-2)	5.90	I

*The excess charges before electronic reconstruction are the net charges per surface calculated by assuming that the Ni, Fe, and O are in the +2, +3, and -2 oxidation states, respectively.

5.3.3 Effect of atomic vacancies at the NFO(001) surface

In Chapter 4, we studied the stability of vacancy defects in the bulk NFO crystal and we found that Ni and O vacancies are the most stable of these defects, for the O-poor and O-rich growth conditions, respectively. Similarly, we want to study the stability of vacancy defects in the NFO slab, to check whether they are more stable at the surface layer or near the center of the slab. These vacancies may stabilize the surfaces by diminishing the bounded surface charges and the effect of the electronic reconstructions. The stabilization of the surface defects could moreover

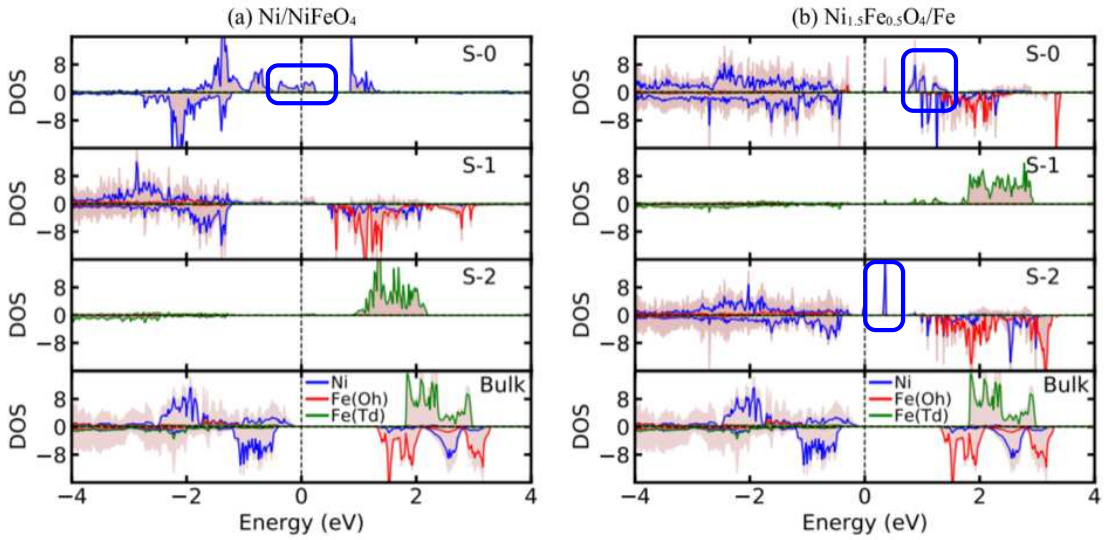

Figure 5.11 – The LDOS of the atomic layers from (S-0) (surface layer) to (S-2) for $Ni/NiFeO_4$ (a) and $Ni_{1.5}Fe_{0.5}O_4/Fe$ (b) slabs. For comparison, the DOS of bulk NFO is shown in the bottom panel of the two figures. The DOS peaks corresponding to the defect states belonging to Ni atoms are highlighted by blue colored rectangles.

result in the germination of the conductive domains observed experimentally.

In the bulk NFO crystal with a cation distribution corresponding to the space group $P4_122$, there are two types of O atoms, located at two different atomic sites: The oxygen atom O1 is bound to one Ni(Oh), two Fe(Oh) and one Fe(Td) atoms, while the oxygen O2 is bound to two Ni, one Fe(Oh), and one Fe(Td) atoms. We found that the O2 vacancy is more stable than the O1 vacancy by 0.11 eV. Shi, *et al.* [238] found the O1 vacancy more stable than the O2 vacancy, which might be due to the DFT parameters that they have chosen in their calculations.

We then tried to perform the same kind of calculations near the surface of a symmetric slab with two perfect B-terminated surfaces. At the S-0 surface layer, the O atom has only three neighboring cations. Three inequivalent O vacancies can be created, which differ by the nature of their neighboring cations, as shown in Fig. 5.12(a). These O vacancies are named O1 [bound to one Ni and two Fe(Oh)], O2 [bound to two Ni and one Fe(Oh)], and O3 [bound to one Ni and one Fe(Oh), and one Fe(Td)]. The total spin magnetic moment of the oxygen deficient slab is of 36 μ_B for these three vacancies, instead of 32 μ_B for the slab without vacancy. The total energy per slab cell with respect to the most stable one is of 0.457 eV, 0.000 eV and 3.951 eV for the slabs with an O1, O2, and O3 vacancy on each surface, respectively. The O2 vacancy is thus the most stable one and the O3 vacancy is the least stable one. The energy difference between the most stable and the least stable O vacancies in the surface layer is of 1.97 eV per O vacancy. These results are in good agreement with the calculations of the NFO slab by Shi, *et al.* [238].

The perfect B-terminated slab is subject to an electronic reconstruction, consisting in the transfer of three holes to the surface cations. Due to the O vacancy at the S-0 layer, the electronic reconstruction changes and is restricted to one hole only transferred to one surface Ni atom. The

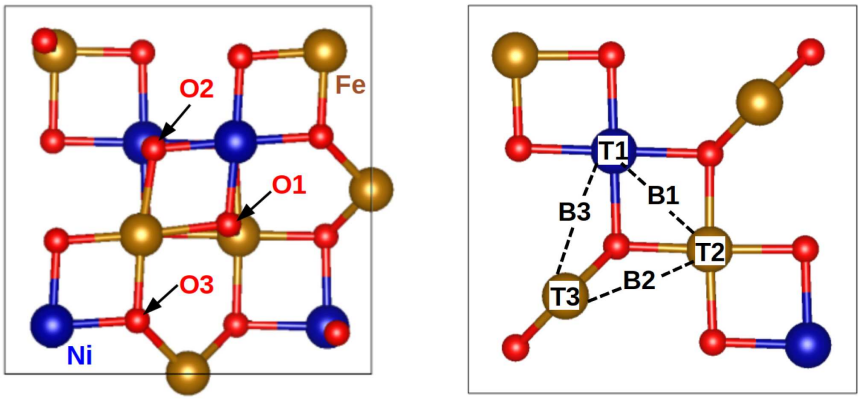

(a) (b)

Figure 5.12 – (a) Structure of the slab cell with the three inequivalent O vacancy sites on the S-0 surface layer of the B-terminated NFO(001) slab. (b) Location of the three possible top sites (T) and three bridge sites (B) for the adsorption of an O atom on the S-0 surface layer of the B-terminated NFO(001) slab. The Ni, Fe, and O atoms are shown in blue, yellow, and red colors, respectively.

corresponding defect state can be seen in the LDOS of the B-terminated slab with O2 vacancy shown in Fig. 5.13. Our results are in agreement with the references [238, 245, 253], which show that the B-terminated slabs are stabilized by an oxygen vacancy and the transfer of a hole to a surface divalent cation. According to Shi, *et al.* [238], the ease of forming an oxygen vacancy at the surface layer of NFO(001) makes it a promising catalytic material for oxidation reactions occurring through the Mars–Van Krevelen mechanism. Unlike for the pristine B-terminated slab, the one-hole defect state is not shared by several cations and the B-terminated slab with O vacancies is insulating. The total energy of the slabs with an O vacancy located in the atomic layers (S-0), (S-2), and (S-4) with respect the the most stable one is of 0.000 eV, 3.068 eV, and 5.054 eV, respectively. The comparison of these energies shows that the O vacancy is more stable in the (S-0) layer than in the (S-2) or (S-4) layers. The energy difference between the vacancy formation in the (S-0) and (S-4) layers is of 2.527 eV per O vacancy. The total spin magnetic moment of the slabs with an O vacancy in the (S-0), (S-2), and (S-4) layers is of 36 μ_B, 32 μ_B, and 32 μ_B, respectively.

In the same way, we also studied Ni vacancies in the (S-0), (S-2), and (S-4) layers. The total energy of the corresponding slabs (with respect to the most stable one) is of 0.964 eV, 0.326 eV, and 0.000 eV, respectively. The stability of the Ni vacancy is higher when it is located far from the surface. The total spin magnetic moment of the slabs with a Ni vacancy on the (S-0), (S-2), and (S-4) layers is of 28 μ_B, 24 μ_B, and 24 μ_B, respectively.

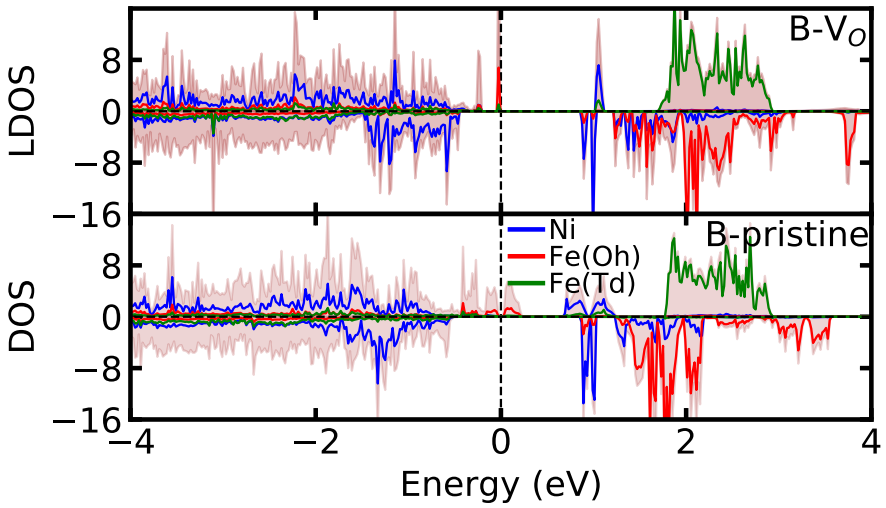

Figure 5.13 – Comparison of the LDOS of the NFO(001) surface layer (S-0) of the B-terminated pristine surface and of the B-terminated surface with O2 vacancy (at the S-0 surface).

5.3.4 Effect of oxygen adsorption

The surface of the A-terminated NFO(001) slab is cation-rich or oxygen-deficient. We expect that the adsorption of O atoms on this surface can stabilize the A-terminated surface. The adsorption of an O atom on the A-terminated surface can lower the number of electrons contributing to the electronic reconstruction, from three for the defect-free surface to one for the surface with an adsorbed O atom. There are many sites for O adsorption on the A-terminated surface. The top and bridge sites are shown in Fig. 5.12(b). The O adsorption energy is given in the table 5.2. The results show that the O atom at the bridge position between Fe(Td) and Fe(Oh) (B2 site) is the most stable one and that the O atom at the top position of Fe(Td) (T3 site) is the second most stable site for O adsorption. The O atom located at T2 (top of Fe(Oh)) or B1 (between Ni(Oh) and Fe(Oh)) site has an adsorption energy about 1 eV higher per O atom adsorbed on the surface of the slab cell. We found that the O-adsorption at the T1 site is unstable as the O atom moves to the bride site during ionic relaxation. All the O-adsorbed A-terminated slabs have the same total spin magnetic moment of 16 μ_B (same as unadsorbed A-terminated slab).

5.4 Effect of strain on the NFO surface

The strain applied to NFO thin films depends on the substrate on which they are epitaxially grown. Our study of strain on thin films is limited to two NFO slabs: the B-terminated slab and the perfect B-terminated slab with an oxygen vacancy at the surface layer (S-0). We applied −5% and 5% strains to both of these slabs, and found that the electronic and magnetic properties of the B-terminated NFO slab with O vacancy did not change much with respect to the unstrained slab. The 5% strained perfect B-terminated slab also shows the same electronic and magnetic properties

Table 5.2 – Slab energy of the A-terminated NFO with different possible O adsorption sites.

Adsorption site	Energy with respect to the most stable O adsorption per surface (eV)
T2	1.176
T3	0.278
B1	1.750
B2	0.359
B3	0.000

as the unstrained and perfect B-terminated NFO slab, but a −5% compressive strain changes the electronic properties of the perfect slab and makes it insulating, by transferring a hole on only one Fe(Oh) atom instead of sharing it between two Fe(Oh) atoms. From these results, we can say that under strain the defect state induced by the presence of the perfect surface will try to localize on a single atom and makes it insulating, instead of being delocalized on many cations which makes the surface a hole conductor.

5.5 $NiFe_2O_4/BaTiO_3(001)$ interface

In this section, we will describe preliminary results that we obtained on the $NiFe_2O_4$ /$BaTiO_3$(001) heterostructure.

As shown in Fig. 7.17, the properties of the interfaces were studied using a superlattice containing by construction two non-equivalent interfaces perpendicular to the z[001] axis (respectively IF-1 and IF-2), which only differ by the orientation of the electric polarization in $BaTiO_3$: at the interface IF-1 (IF-2), the polarization is pointing outward(inward) from the interface, *i.e.* toward the center of the $NiFe_2O_4$ layer (toward the center of the $BaTiO_3$ layer). In this first study, we considered that the two interfaces have a perfect $[NiFe]_{Oh}O_4/Ti_2O_4$ atomic terminations. The lateral dimensions of $NiFe_2O_4$ and $BaTiO_3$ in the x- and y-directions are $(\frac{1}{\sqrt{2}}\times\frac{1}{\sqrt{2}})R45°$ and $(\sqrt{2}\times\sqrt{2})R45°$, respectively: every (001) layer contain either two formula units of $BaTiO_3$ or one formula unit of $NiFe_2O_4$ (of which the latteral dimensions is half that used for the study of the surfaces). The in-plane lattice parameter common to each material was fixed to 5.61 Å, which corresponds to the equilibrium in-plane lattice parameter of bulk $BaTiO_3$ (a_{BTO} = 3.967 Å) calculated with the PBESol functional. This structure thus mimics an epitaxial growth of $NiFe_2O_4$ on top of $BaTiO_3$. According to our calculated lattice parameters, the in-plane lattice mismatch between these two materials is of ($\frac{a_{NFO}-a_{BTO}}{a_{BTO}}$ =) 4.32%. The Ni/Fe cation distribution in the Oh sites still corresponds to the one of the $P4_122$ space group and the tetragonal axis of this structure is along the z-axis normal to the interfaces. The superlattice contains a total of 124 atoms spread over 15 (001) atomic layers of $BaTiO_3$ and 13 atomic layers of $NiFe_2O_4$.

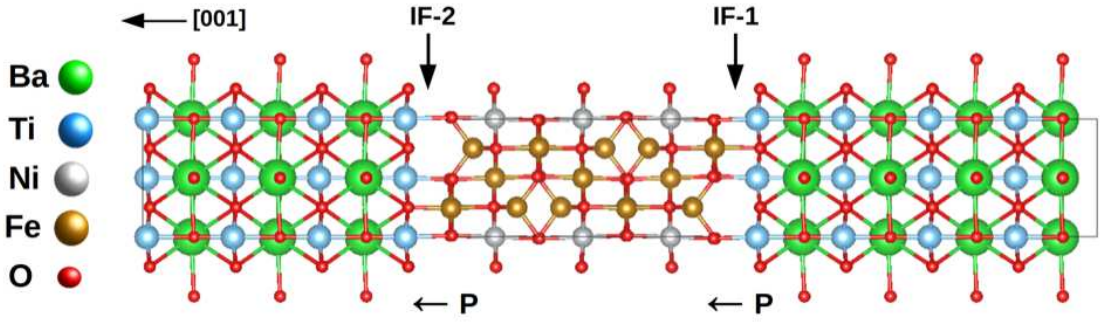

Figure 5.14 – $NiFe_2O_4/BaTiO_3(001)$ superlattice used for the calculations and formed with two interfaces (IF-1 and IF-2) with $NiFeO_4/Ti_2O_4$ atomic terminations.

The calculated LDOS are shown in Fig. 7.18 for the NFO atomic layers located at the interfaces IF-1 and IF-2. We can see on these spectra that the electronic occupation of the Ni cations is strongly changed compared to the bulk compound. The DOS curves are also different for the two interfaces, witnessing an effect of the orientation of the electric polarization. In particular, we can see that some Ni majority-spin bands which are fully occupied in bulk NFO are now unoccupied. As reported in Table 7.2, these changes in the DOS correspond to variations of the atomic spin magnetic moments: We can indeed see a decrease of the Ni spin magnetic moment by $\sim 0.7\ \mu_B$ between the bulk and IF-1 and another decrease by $\sim 0.7\ \mu_B$ between IF-1 and IF-2, Ni cations at IF-2 having a vanishing spin magnetic moment. The variations of the spin magnetic moment of the other atoms are negligible.

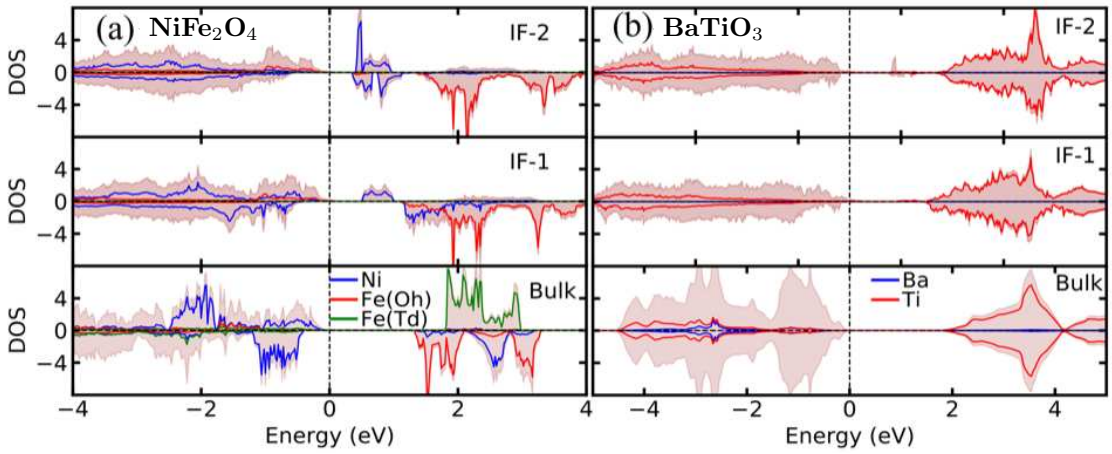

Figure 5.15 – Atomic resolved layered DOS of interface layers of NFO (a) and BTO (b) at the interfaces IF-1 and IF-2. The bulk DOS of both NFO and BTO are shown in the bottom panel for reference.

In our superlattice, the (001) atomic bilayers contain only one formula unit of $NiFe_2O_4$. Atomic layers therefore possess alternatively ±3 e charges. Because of the symmetry of the structure, as for the slabs used for the study of the surfaces, the $NiFe_2O_4$ film is not stoichiometric. With two B-terminated interfaces, we have three holes which have to be re-distributed among the two

interfaces. According to our results, we can state a scenario in which one of the three holes is localized on the Ni atom of the IF-1 interface, decreasing its oxidation state from Ni^{2+} to Ni^{3+}, while the two other holes localize on the Ni atom of the IF-2 interface, changing its oxidation state from Ni^{2+} to Ni^{4+}. The formation of Ni^{4+} has already been reported in perovskite compounds in which the Ni cations is in a Oh environment and also display a low-spin state with a null spin magnetic moment [254, 255]. The absence of variations in the oxidation degrees of Fe(Oh) cations shows nonetheless that this interface does behave differently than the B-terminated surface, which can be a result from the interface structure and chemistry, but also from their non-equivalence resulting from the electric polarization. As we can see from Table 7.3, the Ni-O bond length displays a change of 0.25 Å when the electric polarization is reversed, i.e. between the interfaces IF-2 and IF-1.

Table 5.3 – Spin magnetic moment of atoms in the atomic layers near the interfaces IF-1 and IF-2. Multiplicities for each atoms is given between parentheses

	Atomic spin magnetic moment (μ_B)					
	$NiFeO_4$			Ti_2O_4		Total
	Ni	Fe	O (×4)	Ti (×2)	O (×4)	
Bulk	1.541	4.036	0.079	0.000	0.000	
IF-1	0.773	4.018	0.079	0.005	0.045	5.295
IF-2	0.001	4.011	0.078	0.006	0.027	4.440
Difference between total atomic spin magnetic moments						0.855

As observed in the bulk calculations described in Chapter 4 and in the surface calculations in this chapter, the added holes depopulate majority-spin states rather than minority-spin ones, because of the position of the valence-band maximum, thus explaining why we calculated a systematic decrease of the spin magnetic moments. The Ni contribution to the LDOS at the interface IF-2 is consistent with its stabilization of in a low-spin state, in agreement with the DOS reported at the interface between $NiFe_2O_4$ and $Pb(Zr,Ti)O_3$ [113]. We also observe that the minority-spin unoccupied bands appear at lower energies than in the bulk compound. This result is particularly interesting to understand the possible insulator-to-metal transitions which could occur at the $NiFe_2O_4/BaTiO_3$ interface, because we calculated that more charges are transferred to this interface when the electric polarization in $BaTiO_3$ is pointing outward from the interface (toward the center of $BaTiO_3$ film). In that case, the band gap is strongly reduced for both spin channels, down to 0.28 eV. These results are in agreement with the experimental data shown in Fig. 7.2, which show that the conductive domains written in the spinel ferrites are associated with an inward electric polarization in $BaTiO_3$, while the electric polarization is otherwise pointing outward (from $BaTiO_3$ to $NiFe_2O_4$).

From the change in the total atomic spin magnetic moment, it is possible to calculate the surface magnetoelectric coefficient α_S using the formula, $\mu_0 \Delta M = \alpha_S E_c$, where ΔM is the change in the interface magnetization, μ_0 is the vacuum permittivity and E_c = 100 kV cm^{-1} is the coercive field used to switch the electric polarization of $BaTiO_3$. As shown in Table 7.2 the calculated

Table 5.4 – Bond lengths between cations and oxygen anions accross the interfaces IF-1 and IF-2, along the [001] direction.

Interface	Fe-O (Å)	Ni-O (Å)	Ti-O (Å)
IF-1	2.01	2.12	1.98
IF-2	1.95	1.87	2.09

change of interface magnetization is $\Delta M = 0.855\ \mu_B$ per surface unit. Using these values, we thus obtain a linear magnetoelectric coefficient of 3.16×10^{-10} G cm^2 V^{-1}.

Our calculated magnetoelectric coefficient is of the same order of magnitude than those reported in the literature. Indeed, it is very close from the coefficient $\alpha_S = 3.15 \times 10^{-10}$ G cm^2 V^{-1} calculated by Tamerd, *et al.* [113], for the $NiFe_2O_4/PbZr_{0.5}Ti_{0.5}O_3(001)$ bilayer, with $NiFeO_4/ZrTiO_4$ interface terminations. Lower values ($\alpha_S = 0.52 \times 10^{-10}$ G cm^2 V^{-1}) have however been calculated for a $NiFeO_4/Pb_2O_2$ termination. Considering the first interface, the magnetoelectric coefficients were in agreement with previous calculations performed on the $Ni/BaTiO_3$ (2.3×10^{-10} G cm^2 V^{-1}) [256] and $Ni/PbTiO_3$ (6.7×10^{-10} G cm^2 V^{-1}) [257] interfaces. Studying a $Fe_3O_4/BaTiO_3$ bilayer, Niranjan, *et al.* [112], found a much lower coefficient of 0.7×10^{-10} G cm^2 V^{-1} at the $[Fe_2]_{Oh}O_4/Ti_2O_4$ interface, but they also found that that it could be increased by a factor 3 for a O-deficient interface, which would consist in a Fe_{Td}/Ti_2O_4 termination. For this termination, a coefficient of 2.1×10^{-10} G cm^2 V^{-1} is calculated, which is close from the one obtained at the $Fe/BaTiO_3$ interface [258]. The strength of the magnetoelectric coupling will mostly depend on the magnetic interaction between the interface cations, which may be direct or indirect (*via* the oxygen ligands) and which will vary with the changes of the bond lengths when the electric polarization is reversed in $BaTiO_3$. In consequences, inteface magnetoelectric properties are also expected to strongly depend on the interface atomic terminations.

5.6 Conclusion

In summary, we can say that in the A-terminated and B-terminated surfaces are stable in the O-poor and O-rich growth environments, respectively. Due to the presence of the surface, there are defect holes or electrons located in the surface or subsurface layers, depending on the surface termination. The conducting behavior of the surface also depends on the surface termination: a B-terminated surface is conducting, but becomes insulating if it contains an O-vacancy. O vacancies will preferably form at the surface and Ni vacancies in the center of the slab for the B-terminated slabs. A Ni-rich environment favors O vacancy on the surface of the B-terminated slab. The change in the electronic and magnetic properties of the NFO slabs induced by an external strain depends on the surface termination. In the case of a B-terminated slab with an O vacancy, there is no significant change of the electronic and the magnetic properties of the surface due to external strain; in the case of a compressive strain applied on the B-terminated slab, we calculated a transition from a conducting to an insulating surface.

We finally presented preliminary results of the physical properties of the $NiFe_2O_4/BaTiO_3(001)$ interface with a $NiFeO_4/Ti_2O_4$ termination. We demonstrated that, depending on the direction of the electric polarization, Ni^{2+} cations transform into Ni^{3+} (polarization outward) or Ni^{4+} (polarization inward), reducing both the band gap and the local spin magnetization. It would be now interesting to try to perform similar calculations with an interface displaying a larger lateral dimension, which would allow more complex charge/atomic reconstructions. In particular, as it was demonstrated for B-terminated surfaces, we can expect that, it is likely that such interface termination can favor the formation of oxygen vacancies, in particular in the case of an inward electric polarization; the formation of a neutral oxygen vacancy per formula unit of $NiFe_2O_4$ would indeed cancel the changes of oxidation degree of the Ni cations. Finally, we intend in the future to also study the properties of other (001) interface terminations, such as $NiFeO_4/Ba_2O_2$, Fe/Ti_2O_4, or Fe/Ba_2O_2.

Chapter 6

Conclusions and perspectives

During this thesis, we intended to understand the mechanisms which were responsible for the formation of conductive domains in $MFe_2O_4/BaTiO_3(001)$ (M = Co, Ni) thin films, when an electric field was applied.

We first considered the bulk ferrite crystals. In Chapter 3, we analyzed the effects of the M/Fe cation ordering. We first found that the oxidation state and the magnetization were not significantly changed as a function of the cation distribution in Oh sites, but the band gap can be decreased by 25% to 40% when a mix of the most stable phases are present. Exchanges of divalent and trivalent cations between the Td and Oh sites, *i.e.* decreasing the inversion degree, also induce a systematic decrease of the band gap widths and is associated with an increase of the total spin magnetic moment. In every tested scenario, we always found that $NiFe_2O_4$ and $CoFe_2O_4$ remain insulating, whatever the cation distribution. We then examined, in Chapter 4, the electronic properties of non-stoichiometric ferrites, focusing on the effects of atomic vacancies. We found that in oxygen-poor conditions, the most stable defects are the neutral oxygen vacancies, which, on the contrary to what is usually admitted, do not change the spin magnetization. They however induce the appearance of localized gap states in the band gap for the two spin channels. In oxygen-rich conditions, we rather expect to stabilize neutral Co vacancies or partially ionized Ni vacancies. In that case, a decrease of the spin magnetization is expected. Again, these defects are not expected to turn the spinel ferrites into a conductor. On the contrary, in $NiFe_2O_4$, if the formation of neutral Ni vacancies or Fe(Oh) vacancies occurred, the material would turn into a spin-polarized hole conductor.

When the nickel ferrite is grown as thin film, the surface and interface effects may play an important role and cancel its insulating behavior. This is particularly true if a perfect B-terminated film (*i.e.* with a $NiFeO_4$ surface termination) is stabilized. For such a surface, a charge reconstruction will induce the localization of 3 holes per 2 formula unit of $NiFe_2O_4$ at the surface, among which, 1 hole will be shared by the two Fe(Oh) cations located at the surface, enabling a metallic state from double-exchange hole hopping mechanisms. We however found that the formation of neutral oxygen vacancies, which are more stable at this B surface than in the bulk, can help to

recover the insulating character of the surface. The insulating behavior can also be recovered by applying a compressive strain of −5%, which is of the order of the strain which would be induced by an epitaxial growth on $BaTiO_3$ or $SrTiO_3$. The insulating state originates in that case from the formation of a charge ordering. It can thus be expected from these results that any modification of the strain state or healing/forming oxygen vacancies could trigger the insulating-to-metal transition. Further analyses of the electronic structure of other stable surface terminations would be determining in reaching a final conclusion about the role of surfaces. Considering interfaces add another contribution coming from the direction of the electric polarization in $BaTiO_3$. At an interface with a $NiFeO_4/Ti_2O_4$ termination, unlike at the B-terminated surface, we did not calculate any hole transfer to the interfacial Fe(Oh) atoms, but only to the Ni atoms. The amount of redistributed charges depends on the direction of the electric polarization and is higher in the case of an outward polarization (from $NiFe_2O_4$ to $BaTiO_3$). The band gap width of the interfacial atomic layer is strongly decreased, down to $\simeq$ 0.3 eV. Additional perturbations could then easily make it conductive.

In terms of perspectives, several routes could be followed in order to improve our understanding of the insulator-to-metal transitions in the spinel ferrites.

In this thesis, we studied the effects on the electronic structure coming from different isolated structural features. It is reasonable to think that these different features would coexist in realistic thin films and that they would interact together. The effects on the electronic structure originating from these interactions could be different than the simple sum of the different effect taken separately. As it was partly shown in Chapter 4, the combination of strain and the presence of atomic vacancies can change the conductive state of $NiFe_2O_4$, while strain alone does not affect significantly the band gap width. The formation of a neutral defect complexes associating two point defects with an opposite charge state can allow to avoid electronic reconstructions. The atomic vacancies were all studied for a given initial cation distribution, while they could behave differently and we could expect that neutral oxygen vacancies would change differently the electronic structure if they were formed in a partially inverse spinel ferrite, rather than in a totally inverse one [259].

As mentioned previously, the analysis of the interface properties is still undergoing. The results presented on the $NiFe_2O_4/BaTiO_3(001)$ interface have only been obtained for one interface termination, which might not be the most stable one. Other terminations, involving Fe(Td)- and BaO atomic layers, should be considered, as well as defective interfaces, which would however be more complicated and necessitates to perform the calculations for larger superlattices.

When presenting the experimental system (See Fig. 7.2), in addition to the center of the ferrite film, its surface and its interface with the ferroelectric oxide $BaTiO_3$, we also identified a fourth area of interest, which is the interface between the spinel ferrite and the metallic electrode. This electrode is made of gold, but it is separated from the spinel ferrite by a Ti buffer layer with a thickness of a few nanometers. The conductive domains in the spinel ferrite are written by applying an out-of-plane electric field. Transport measurements are however in plane. We can make the

hypothesis that structural defects are formed in the spinel ferrite during the writing process. These defects are certainly stabilized by the reversal of the electric polarization in $BaTiO_3$. Taking the metallic electrode into account and calculating the electronic structure at the $Ti/NiFe_2O_4$ interface could be useful to firstly estimate the Schottky barrier height, if $NiFe_2O_4$ is still slightly insulating, or to simply understand the band alignment at the interface. When high voltages are applied during the transport measurements, it would be interesting to verify also if the diffusion of Ti atoms in the (defective) ferrite could happen, or if additional oxygen vacancies could be created through the oxidization of the Ti interface, hence allowing the formation of several resistance states. Unfortunately, such calculations could be difficult to realize because of the large lattice mismatch (in terms of lattice parameters and lattice symmetries) between the two structures.

Finally, we hope we will succeed to correlate our numerical calculations with experimental data before the end of the MULTINANO project.

Chapitre 7

Résumé en français

7.1 Introduction

Le domaine de l'électronique a connu une croissance sans précédent au cours des dernières décennies, confirmant la loi de Moore qui prévoyait le doublement de la densité des composants électroniques tous les deux ans. Les appareils électroniques font désormais partie intégrante de divers domaines d'application tels que la communication, l'éducation, la défense et de la santé. Les limites physiques des dispositifs conventionnels basés sur les technologies CMOS (*Complementary Metal-Oxide Semiconductor*) deviennent évidentes à mesure que la loi de Moore atteint ses limites. La miniaturisation continue des composants électroniques fait apparaître des problèmes liés aux temps de lecture et d'écriture accrus, à la présence de courants de fuite élevés et à la densité de puissance plus élevée qui entraîne des surchauffes. Ces problèmes compromettent la qualité et les performances des dispositifs, ce qui incite à explorer de nouveaux types de mémoire et de nouvelles architectures.

Lorsqu'il s'agit de proposer des matériaux appropriés pour les futurs dispositifs électroniques, les oxydes viennent naturellement à l'esprit car ils sont déjà utilisés dans divers dispositifs actuels, en tant que barrières isolantes dans les jonctions tunnel magnétiques ou en tant que grilles diélectriques dans les transistors à effet de champ, par exemple. Les oxydes complexes, comme les oxydes de structure pérovskite ou spinelle, possèdent au moins deux cations différents, ce qui augmente les chances de concevoir des matériaux multifonctionnels avec des diagrammes de phase riches. Plusieurs propriétés, résultant du contrôle de la structure cristalline et des degrés de liberté de spin et d'orbite, peuvent ainsi être obtenues pour un composé donné et peuvent éventuellement coexister ou faire l'objet d'un couplage croisé. La croissance d'hétérostructures est finalement un moyen supplémentaire de favoriser la coexistence de différentes propriétés physiques qui ne seraient pas compatibles dans des cristaux massifs isolés, mais qui, dans les hétérostructures, peuvent être couplées aux travers de leurs interfaces [28] (voir Fig. 7.1 dans laquelle les degrés de liberté qui pourraient être manipulés aux interfaces entre les oxydes corrélés sont énumérés).

Les ferrites de structure spinelle MFe_2O_4 (avec M représentant un métal de transition) ont sus-

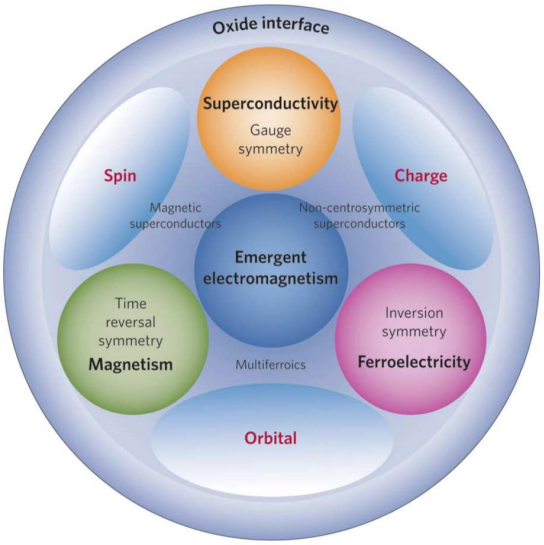

FIGURE 7.1 – Degrés de liberté pouvant exister aux interfaces d'oxydes (Reproduit de Ref. [28] avec permission).

cité l'attention de la communauté scientifique en raison de leurs propriétés magnétiques, électriques, optiques et catalytiques intrigantes [45]. Parmi ces oxydes, Fe_3O_4, γ-Fe_2O_3, $CoFe_2O_4$, et $NiFe_2O_4$ ont en commun de présenter un ordre ferrimagnétique robuste, principalement stabilisé par le fort couplage antiferromagnétique entre les moments magnétiques de spin des cations occupant les sites tétraèdriques (Td) et ceux situés dans les sites octaédriques (Oh). La magnétite (Fe_3O_4) est l'un des plus anciens matériaux magnétiques connus. Elle présente une transition métal-isolant, appelée transition de Verwey [83-85], à la température de 120 K. $CoFe_2O_4$ possède l'énergie d'anisotropie magnétique la plus élevée de 1,8 à 3,0 $\times 10^6$ erg cm^{-3} et la valeur la plus élevée du coefficient de magnétostriction (environ 350 $\times 10^{-6}$) parmi tous les ferrites spinelles [90]. $NiFe_2O_4$ est un ferrite de structure spinelle inverse isolante et ferrimagnétique, dont la température de Curie est d'environ 865 K [66].

Les hétérostructures formées par l'association d'un ferrite de structure spinelle ferrimagnétique et d'un oxyde de structure pérovskite ferroélectrique ont été principalement étudiées dans le but de concevoir des systèmes dits multiferroïques extrinsèques pouvant présenter un couplage magnétoélectrique élevé à température ambiante [74]. Niranjan, *et al.* [112] ont proposé une étude numérique, basée sur des calculs *ab initio*, du couplage magnétoélectrique à l'interface entre le composé métallique Fe_3O_4 et le matériau ferroélectrique $BaTiO_3$. Ils ont constaté que le couplage magnétoélectrique dépend fortement de la terminaison atomique à l'interface et peut être amélioré d'un facteur 3 si une terminaison déficiente en oxygène est sélectionnée. En 2020, Tamerd, *et al.* [113], ont étudié l'interface $NiFe_2O_4/PbZr_{0.5}Ti_{0.5}O_3(001)$ et ont calculé un coefficient magnétoélectrique de $3,15 \times 10^{-10}$ G cm^2 V^{-1}. Au cours de sa thèse [177], T. Aghavnian a démontré que les propriétés multiferroïques de l'hétérostructure $CoFe_2O_4/BaTiO_3(001)$ étaient principalement liées à des modifications structurales et chimiques provenant de déplacements ioniques. Il a également souligné que ces processus induisent des changements réversibles de la résistance

électrique à température ambiante, qui pourraient donc être utilisés dans les mémoires résistives.

Les processus de commutation résistive (RS pour *resistive switching*) correspondent aux changements réversibles de la résistance électrique d'un matériau, qui peuvent s'étendre sur plusieurs ordres de grandeur, allant jusqu'à des transitions isolant-métal. Différents mécanismes contribuent à la transition isolant-métal (TIM), notamment les corrélations électroniques dans les isolants de Mott et l'émergence de gaz d'électrons bidimensionnels (2DEG) aux interfaces polaires. Les isolants de Mott doivent leur caractère isolant à de fortes interactions électron-électron et à l'interaction entre la répulsion de Coulomb et la localisation des électrons. Les oxydes de métaux de transition, tels que la magnétite (Fe_3O_4), peuvent présenter une TIM purement électronique, comme la transition de Verwey. Les spinelles comme le $CoFe_2O_4$ et le $NiFe_2O_4$ sont normalement isolants en raison de fortes corrélations entre les électrons des couches $3d$. La formation de 2DEG dans $LaAlO_3/SrTiO_3(001)$ résulte de la discontinuité de charge et des effets de polarisation. Des scénarios similaires sont proposés pour les interfaces spinelles-perovskites potentielles, prédisant l'émergence de 2DEG à l'interface entre $MgAl_2O_4$ et $SrTiO_3$ [154]. Enfin, les ferrites de structure spinelle peuvent présenter des propriétés de RS [80, 81, 174-176] résultant de la formation et de la destruction de filaments de conduction via la formation et le déplacement de lacunes d'oxygène.

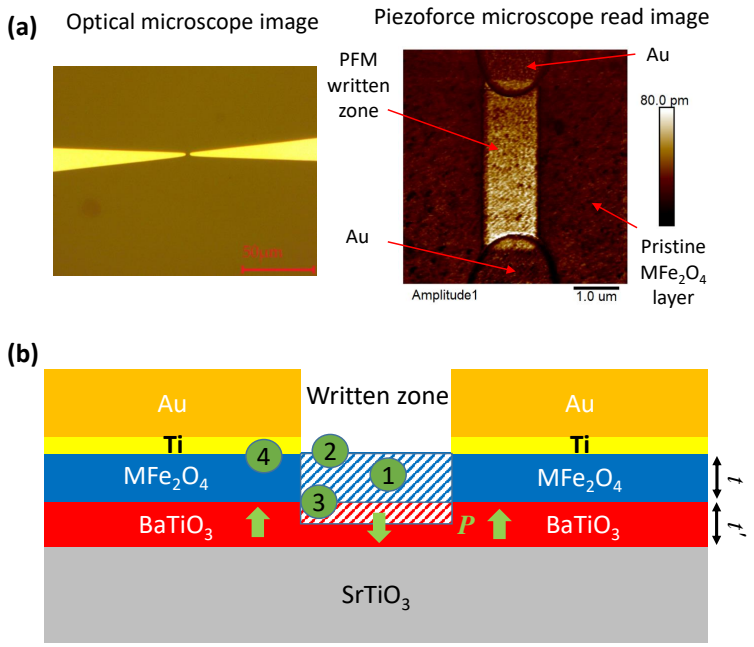

FIGURE 7.2 – (a) Images expérimentales (vue de dessus) de l'hétérostructure ferrite/$BaTiO_3$ avec un domaine conducteur écrit par PFM pour connecter deux électrodes d'Au. Ces résultats ont été obtenus par Haowen Lin (SPEC, CEA-Saclay) dans le cadre de sa thèse de doctorat en cours. (b) Schémas du dispositif expérimental (vue latérale) associant des couches minces de ferrite/$BaTiO_3(001)$, déposés épitaxialement sur un substrat $SrTiO_3(001)$ dopé au Nb. Le dépôt des électrodes d'Au a nécessité l'utilisation de couches tampons de Ti. Les couches de MFe_2O_4 et de $BaTiO_3$ ont une épaisseur d'environ 10-15 nm.

Cette thèse s'inscrit dans le projet ANR MULTINANO (voir projet ANR-19-CE09-0036) dans lequel il a été proposé d'utiliser les variations de résistance dans les couches minces de ferrite spinelle/$BaTiO_3$ pour concevoir des dispositifs électroniques innovants et reconfigurables. En effet, il a été confirmé qu'il est possible d'écrire une zone conductrice en appliquant un champ électrique à l'aide d'un microscope à force de piézo-réponse (PFM), comme on peut le voir sur la Fig. 7.2(a). Outre ce premier objectif, le projet MULTINANO visait également à comprendre les mécanismes responsables de la formation de ces domaines conducteurs. Dans ce manuscrit de thèse, nous présentons les résultats issus de calculs premiers principes qui ont été menés pour répondre à cette question. Dans les différents chapitres, nous détaillons nos études réalisées sur des systèmes de complexité croissante et correspondant à différentes zones du dispositif expérimental décrit dans la Fig. 7.2(b). Nous avons essayé durant notre étude d'envisager différents scénarios associés aux mécanismes potentiels énoncés précédemment. Nous avons pour ce faire tout d'abord étudié la stabilité et les effets de la distribution de cations dans les cristaux massifs de structure spinelle $CoFe_2O_4$ (CFO) et $NiFe_2O_4$ (NFO). Nous avons ensuite étudié la formation de défauts ponctuels de types lacunes de cations ou d'oxygène dans ces composés. Finalement, nous nous sommes intéressés aux propriétés de surface et d'interface de la ferrite de Ni avec $BaTiO_3$, celles-ci étant susceptibles de contribuer fortement compte tenu des faibles épaisseurs des couches d'oxydes déposées expérimentalement.

7.2 Méthodes de calculs

Pour réaliser notre étude, nous avons effectué des calculs numériques basés sur la théorie de la fonctionnelle de la densité (DFT pour *Density Functional Theory* à l'aide de l'utilisation du code *Vienna Ab initio Simulation Package* (VASP.5.4.4) [192, 193] et de la méthode dite PAW (*Projector Augmented Wave*) [260]. La fonctionnelle PBEsol [186] a été utilisée pour calculer l'énergie d'échange et de corrélations. Pour calculer la structure électronique des ferrites de structure spinelle $CoFe_2O_4$ et $NiFe_2O_4$, nous avons combiné cette fonctionnelle avec la correction $+U$ [191] appliquée aux électrons $3d$ des cations. Les valeurs des paramètres U_{eff} ont été fixées à 4,0, 4,0 et 2,5 eV pour les éléments Co, Fe et Ni, respectivement, afin de calculer des largeurs de bandes interdites autour du niveau de Fermi proches des valeurs mesurées expérimentalement.

Chaque calcul a été effectué en utilisant les ressources informatique fournie par le mésocentre de calculs CALMIP (Allocations p19004 et p1229). Le programme VASPKIT [206] a été utilisé pour le post-traitement des calculs VASP afin de tracer des quantités telles que la densité d'états (DOS), la structure de bandes et le potentiel électrostatique. Des scripts bash maison ont été écrits pour extraire et analyser les données de calcul. Le logiciel VESTA [35] a été utilisé pour créer des fichiers de structure et pour tracer des structures atomiques. Les programmes Gnuplot et Python ont également été utilisés pour tracer les données.

7.3 Cristaux massifs de ferrites spinelles stœchiométriques

Les ferrites CFO et NFO sont connus pour adopter principalement une structure spinelle dite inverse, ce qui signifie que les cations Co(II) ou Ni(II) partagent les sites Oh occupés avec la moitié des cations Fe(III), tandis que l'autre moitié des cations Fe(III) se trouve dans les sites atomiques Td occupés. Si un ferrite de structure spinelle MFe_2O_4 (où M est un cation divalent) adoptait la structure normale, tous les cations M(II) se trouveraient dans les sites atomiques Td occupés et le groupe spatial serait 227-$Fd\bar{3}m$. La structure spinelle inverse conserverait ce groupe spatial si les cations +II et +III étaient distribués au hasard dans les sites Oh occupés. Un ordre dans la distribution des cations peut également se produire dans les sites Oh occupés [97, 208], brisant ainsi les symétries et réduisant le groupe d'espace du composé de structure spinelle inverse à un sous-groupe de $Fd\bar{3}m$.

Pour réaliser nos calculs, nous avons utilisé une cellule cubique conventionnelle contenant 8 MFe_2O_4 formules unités (f.u.), *i.e.* 56 atomes, dont 8 cations Fe(III) et 8 cations M(II) doivent être répartis entre les 16 sites Oh occupés, ce qui donne $\binom{16}{8} = 12870$ distributions possibles. Le nombre de structures non équivalentes est réduit à 97, réparties sur 17 groupes d'espace différents. Nous avons choisi au hasard une des structures possibles correspondant à chacun des 17 groupes d'espace et nous avons trouvé que la distribution de cations la plus stable correspond aux structures avec le groupe d'espace 13-$P2/c$ pour CFO et 91-$P4_122$ pour NFO (également le deuxième groupe le plus stable pour CFO).

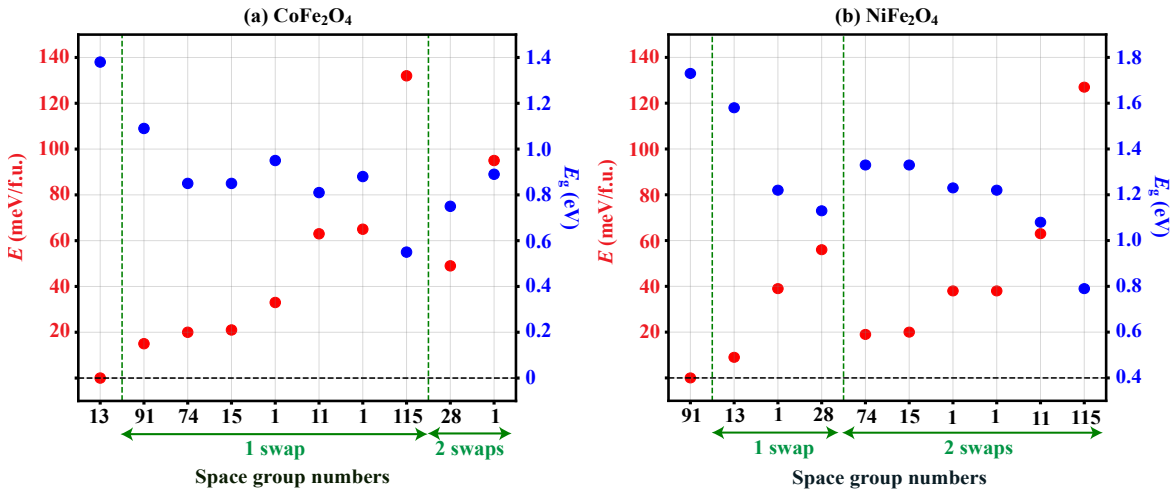

FIGURE 7.3 – Energie totale E de la cellule primitive contenant 4 f.u. de spinelles inverses parfaites $NiFe_2O_4$ et $CoFe_2O_4$ et largeur de bande interdite E_g au niveau de Fermi E_F, en fonction du nombre de groupes d'espace [209]. Les différents groupes d'espace correspondent à différentes distributions de cations dans les sites Oh occupés, qui sont générés en échangeant une ou deux paire(s) d'atomes M/Fe. L'énergie de l'état fondamental de la structure la plus stable est choisie comme origine des énergies et les groupes d'espace sont classés par valeurs croissantes de E. La largeur de la bande interdite E_g correspond à la plus petite différence d'énergie entre le maximum des bandes de valence et le minimum des bandes de conduction pour l'une des deux directions de spin.

Pour vérifier quel ordre cationique est le véritable état fondamental des cristaux CFO et NFO, nous sommes partis de la configuration cationique la plus stable et, en utilisant la cellule primitive de 4 f.u., nous avons généré de nouvelles structures en échangeant 1 ou 2 paires d'atomes M/Fe situés dans des sites Oh occupés. La Fig. 7.3 montre l'évolution de l'énergie de l'état fondamental et de la largeur de la bande interdite au niveau de Fermi en fonction du nombre d'échanges de cations. La mise en ordre des cations sur les sites Oh ne modifie pas le moment magnétique, mais elle modifie les propriétés électroniques, en particulier la valeur de la bande interdite. Les valeurs calculées de la bande interdite fondamentale du CFO et du NFO sont respectivement de 0,55-1,09 eV et de 0,57-1,34 eV. Les structures avec une distribution homogène des cations sur les sites Oh sont les plus stables.

Les courbes de DOS calculées sont présentées dans les Fig. 7.4(a) et (b), respectivement pour CFO et NFO présentant une distribution de cations correspondant au groupe d'espace $P4_122$. La largeur de bande interdite fondamentale de Kohn-Sham est délimitée par l'énergie de la bande occupée la plus élevée et l'énergie des états inoccupés la plus basse, indépendamment de la direction du spin. Pour CFO, cette bande interdite se situe entre le maximum des bandes de valence (VBM) pour les électrons de spin minoritaire, où les cations de cobalt ont une contribution majeure, et le minimum des bandes de conduction (CBM) de direction de spin minoritaire, qui correspond aux bandes de Fe(Oh). Le CBM de NFO correspond également aux bandes de Fe(Oh) de spin minoritaire, mais son VBM correspond aux bandes de spin majoritaire et dont la contribution provient de l'hybridation des orbitales Ni(Oh)-d et O-p, en accord avec les références [125, 126, 130]. La différence de polarisation en spin du VBM entre CFO et NFO est due au fait que les cations Co^{2+} adoptent un état « haut spin », tandis que les cations Ni^{2+} sont dans un état « bas spin ». L'énergie de la bande interdite fondamentale E_g calculée pour le groupe d'espace $P4_122$ est de 1,09 eV pour CFO et de 1,34 eV pour NFO.

Après avoir étudié l'ordre dans la distribution des cations dans le sous-réseau des sites Oh, nous avons considéré la distribution des cations entre les sites atomiques Td et Oh, caractérisée par le degré d'inversion λ de la structure. Ce paramètre d'inversion est connu pour être déterminant pour comprendre les propriétés électroniques et magnétiques des oxydes de structure spinelle. La distribution des cations dans un cristal avec une structure spinelle inverse non parfaite peut ainsi être décrite par la formule $\left(M^{2+}_{1-\lambda}Fe^{3+}_{\lambda}\right)_{Td}\left[M^{2+}_{\lambda}Fe^{3+}_{2-\lambda}\right]_{Oh}O^{2-}_{4}$, avec $\lambda = 0(1)$ correspondant à une structure spinelle normale (inverse).

La Fig. 7.5(a) montre les variations ΔE_{inv} de l'énergie totale de la supercellule lorsque λ augmente de 0 à 1. Plusieurs structures correspondant à différentes distributions de cations pour une valeur donnée de λ ont été calculées. Leurs différences d'énergie s'étendent au maximum dans une plage de 0,065 eV/f.u. et 0,159 eV/f.u. pour NFO et CFO, respectivement, CFO présentant un écart plus important que NFO. La dépendance en λ de la valeur moyenne de l'ensemble ΔE_{inv} est quadratique [220] et nous avons utilisé la formule $\Delta E_{conf} = a\lambda + b\lambda^2$ pour l'ajustement parabolique. Les coefficients a et b sont de $-0,086$ eV/f.u. et $-0,106$ eV/f.u. pour CFO, $0,715$ eV/f.u. et $-1,926$ eV/f.u. pour NFO. Ces coefficients satisfont la condition pour le spinelle complètement

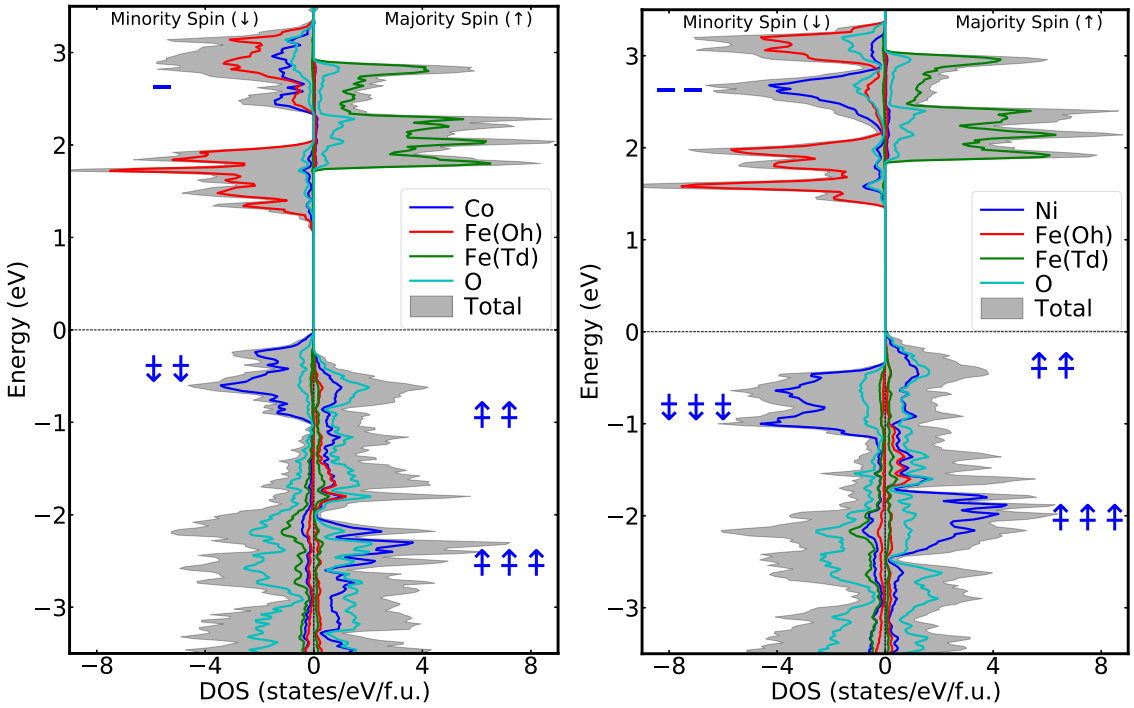

(a) $CoFe_2O_4$ (b) $NiFe_2O_4$

FIGURE 7.4 – DOS projetées en spin et par atome calculées pour (a) $CoFe_2O_4$ et (b) $NiFe_2O_4$ avec des structures spinelles inverses parfaites et une distribution de cations correspondant au groupe d'espace $P4_122$. Les courbes DOS pour les états de spin majoritaire et minoritaire sont représentées respectivement dans les panneaux de droite et de gauche de chaque figure. Les lignes bleues à côté des pics de DOS, avec/sans flèches, montrent le remplissage théorique des orbitales des cations Co^{2+} et Ni^{2+}.

inverse à 0 K ($b + 0,5a < 0$) montré par Seko, *et al.* [221]. La différence d'énergie que nous avons calculée entre les distributions de cations normale et inverse $\Delta E_{\text{inv}}(\lambda = 1) = E(\lambda = 1) - E(\lambda = 0)$ est d'environ −1.21 eV/f. u. pour $NiFe_2O_4$ et $-0,19$ eV/f.u. pour CFO, *i.e.* presque 6 fois plus faible, confirmant que NFO est plus susceptible d'être trouvé avec une structure spinelle parfaitement inverse. Un accord qualitatif est trouvé entre nos données et les résultats précédemment rapportés dans la littérature, avec $\Delta E_{\text{inv}}(\lambda = 1)$ variant de $-0,34$ à $-0,19$ eV/f.u. pour CFO [124-126] et de $-0,60$ à $-0,89$ eV/f.u. pour NFO [126, 222, 223].

En exprimant l'énergie libre de Gibbs comme la somme de l'énergie interne et d'un terme d'entropie configurationnelle dépendant de λ, il est possible de calculer une valeur d'équilibre de λ, qui correspond à un minimum d'énergie libre de Gibbs configurationnelle ($\Delta G_{\text{conf}}(\lambda)$) pour une température et une énergie configurationnelle données ($\Delta E_{conf}(\lambda)$). La variation de la valeur d'équilibre du paramètre d'inversion à une température de 600 K (température de croissance couramment utilisée pour CFO et NFO) montre que la structure de CFO devient partiellement inverse avec un degré d'inversion de 0,96, alors que la distribution de cation dans NFO reste presque totalement inverse. Expérimentalement, il a en effet été mesuré que les cristaux de NFO peuvent

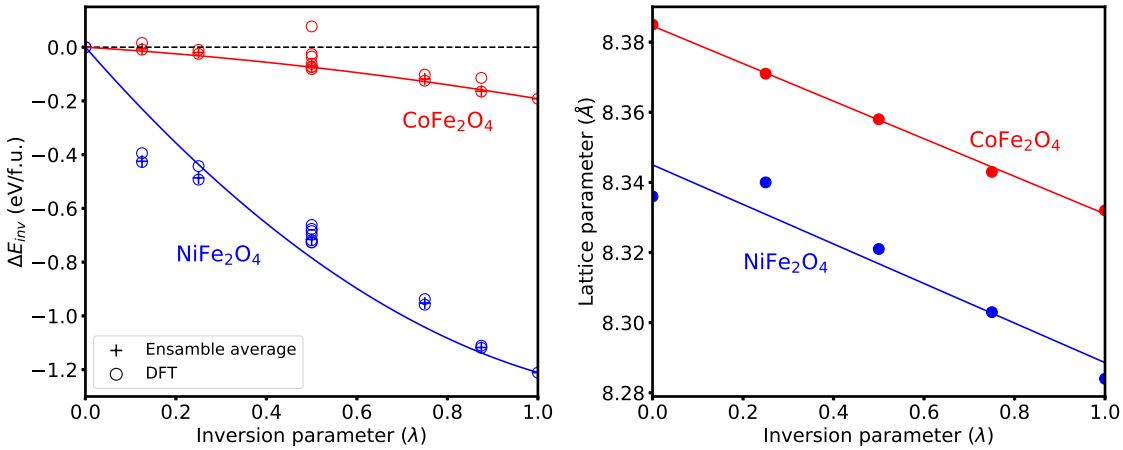

(a) (b)

FIGURE 7.5 – (a) Variations de l'énergie totale ΔE_{inv} et (b) du paramètre de maille pseudo-cubique a en fonction du paramètre d'inversion λ. L'énervie ΔE_{inv} est donnée par rapport à l'énergie de la structure spinelle normale parfaite : $\Delta E_{\text{inv}}(\lambda) = E(\lambda) - E(0)$. Les cercles ouverts correspondent aux énergies calculées par DFT pour toutes les structures possibles générées à partir de la cellule primitive de groupe d'espace $P4_122$ (λ = 0 ; 0,25 ; 0,5 ; 0,75 ; 1) ou de la cellule conventionnelle ($\lambda = 0,125$, 0,875). Les croix représentent la moyenne de l'ensemble de ces énergies calculées, qui sont utilisées pour les ajustements quadratiques représentés par les lignes pleines. Les paramètres de maille sont donnés pour les structures les plus stables.

être élaborés avec une structure spinelle inverse presque parfaite ($\lambda \simeq 1,0$) [91, 228], tandis que les échantillons de CFO sont principalement trouvés avec un degré d'inversion autour de 0,7-0,9 [91-95]. L'inversion cationique modifie les propriétés électroniques et magnétiques. En diminuant le degré d'inversion, nous avons calculé que la largeur de bande interdite diminue et qu'il serait possible de rendre NFO conducteur pour un taux d'inversion suffisamment faible ($\lambda = 0,17$). La diminution du degré d'inversion a également pour effet d'augmenter les valeurs de moments magnétiques de spin totaux, ce qui confirme les observations expérimentales de Lüders, *et al.* [232].

7.4 Cristaux massifs de ferrites non-stœchiométriques

Dans cette section, nous allons maintenant décrire les conséquences sur les propriétés électroniques et magnétiques de différents types de défauts ponctuels qui modifient la stœchiométrie des cristaux massifs de CFO et NFO.

Nous avons tout d'abord étudié les substitutions de cations qui conduisent à un rapport Fe :(Co,Ni) différent de 2. Nous avons pour cela effectué des calculs sur des ferrites de structure spinelle de formule chimique $M_{1-\alpha}Fe_{2+\alpha}O_4$ ($\alpha > 0$), dans lesquelles certains des atomes M = (Co, Ni) ont été remplacés par des atomes de Fe et $M_{1+\beta}Fe_{2-\beta}O_4$ ($\beta > 0$), dans lesquelles certains des atomes Fe ont été remplacés par des atomes M. Nous avons considéré des taux de substitution de cations correspondant aux valeurs de $\alpha(\beta) = 0,125$ et 0,25 ; ces valeurs correspondent à la

substitution d'un ou deux cations, respectivement, dans la cellule conventionnelle de 56 atomes.

Nos calculs nous ont permis de prédire que l'augmentation de la quantité d'atomes de Fe par substitution d'atomes de Ni ou de Co entraîne une augmentation du moment magnétique total, alors qu'au contraire, la substitution d'atomes de Fe par des atomes de Ni ou de Co le diminue.

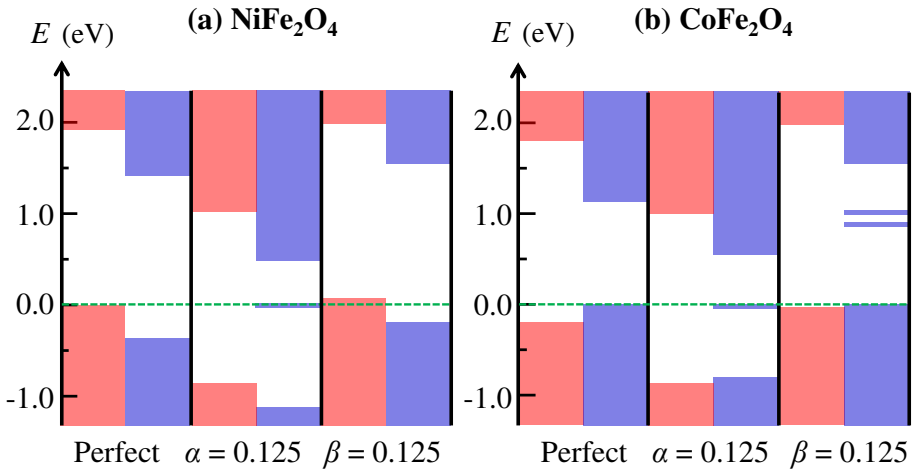

FIGURE 7.6 – Représentation schématique de la densité d'états calculée pour les cristaux massifs non stœchiométriques $M_{0,875}Fe_{2,125}O_4$ ($\alpha = 0,125$) et $M_{1,125}Fe_{1,875}O_4$ ($\beta = 0,125$). La largeur de la bande interdite en énergie correspond à la zone blanche. Les DOS de spins majoritaires et minoritaires sont représentées en rouge et en bleu, respectivement. La ligne verte en pointillés correspond à l'état d'occupation le plus élevé.

Les structures électroniques calculées en présence de substitutions de cations sont représentées schématiquement dans la Fig. 7.6. La substitution d'atomes de Ni ou de Co par des atomes de Fe ($\alpha = 0,125$) a un effet très similaire dans les deux composés, CFO et NFO : elle crée des états de défauts occupés proche du milieu de la bande interdite pour le canal de spin minoritaire. Le fait que ces états soient occupés signifie que les cations de Fe remplaçant les atomes de Ni ou de Co dans les sites Oh adoptent le même degré d'oxydation, donant lieu à la présence de Fe^{2+}. Inversement, la substitution des atomes de Fe par des atomes M ($\beta = 0,125$) conduit à la formation de cations M^{3+} afin de préserver la neutralité de charge du cristal, qui peut être décrite par la formule chimique $\left(Fe^{3+}\right)_{\mathrm{Td}}\left[M^{2+}M_{\beta}^{3+}Fe_{1-\beta}^{3+}\right]_{\mathrm{Oh}}O_4^{2-}$, avec $\beta > 0$. Dans le cas de cette substitution, nous avons observé quelques différences entre les résultats que nous avons calculés pour NFO et CFO : pour CFO, les cations Co^{3+} remplaçant les cations Fe^{3+} ont une structure électronique $d_{\uparrow}^5 d_{\downarrow}^1$ et les états de spin gap minoritaires inoccupés ont une énergie proche du milieu de la bande interdite, tandis que pour NFO, les cations Ni^{3+} sont dans un état de type « bas spin » $d_{\uparrow}^4 d_{\downarrow}^3$ et le VBM dans le canal de spin majoritaire est dépeuplé et traverse le niveau de Fermi. Les bandes dépeuplées (constituées des orbitales $d_{x^2-y^2} + d_{z^2}$ de l'atome de Ni et des orbitales p des atomes d'O) ont une masse effective $m_{\mathrm{h}} = 1,55m_0$, où m_0 est la masse de l'électron libre. La formation d'un composé $Ni_{1,125}Fe_{1,875}O_4$ favorise donc l'apparition d'un état semi-métallique avec une conductivité des trous entièrement polarisée en spin.

Après l'étude des substitutions cationiques, nous nous sommes intéressés aux effets induits par la présence de lacunes atomiques. Les calculs ont été réalisés en conservant la distribution des cations correspondant au groupe d'espace $P4_122$ dans la structure spinelle inverse parfaite. Dans cette structure atomique, nous pouvons distinguer cinq sites atomiques non équivalents dans lesquels vont pouvoir se créer les lacunes V : Ni, Fe(Oh), Fe(Td), O1 [lié à un Ni, deux Fe(Oh) et un Fe(Td)] et O2 [lié à deux Ni, un Fe(Oh) et un Fe(Td)]. Nous avons calculé une légère différence entre les énergies de formation des lacunes d'oxygène formées dans les sites O1 et O2 (0,02 eV et 0,11 eV pour le CFO et le NFO, respectivement), mais presque aucune différence dans les modifications induites dans la structure électronique par ces lacunes. Par conséquent, pour décrire l'effets des lacunes d'oxygène, nous avons choisi de présenter dans la suite l'effet moyen produit par les lacunes créées dans les sites O1 et O2.

L'énergie de formation des lacunes est une grandeur importante pour comparer la stabilité relative des différents types de lacunes. Les énergies de formation $E_\mathrm{f}\left[\mathrm{V}_\mathrm{X}^q\right]$ sont calculées pour des lacunes isolées d'un élément chimique X ($\mathrm{V_X}$), avec l'état de charge q, et suivant la formule suivante tirée de Refs. [195-197] :

$$E_\mathrm{f}\left[\mathrm{V}_\mathrm{X}^q\right] = E\left[\mathrm{Host} + V_X^q\right] - E\left[\mathrm{Host}\right] + \mu_\mathrm{X} + q\left(E_\mathrm{VBM}^\mathrm{H} + \Delta E_\mathrm{F}\right) + E_\mathrm{corr} \tag{7.1}$$

où $E\left[\mathrm{Host} + V_X^q\right]$ et $E\left[\mathrm{Host}\right]$ sont les énergies totales calculées par des méthodes DFT pour les cellules défectueuses et non défectueuses du matériau hôte, respectivement. μ_X est le potentiel chimique de l'atome X supprimé pour former l'espace vacant. Pour chaque composé étudié, μ_X s'écarte de $\Delta\mu_\mathrm{X}$ de l'énergie $E_\mathrm{X}^\mathrm{elem}$. Il faut considérer les valeurs de $\Delta\mu_\mathrm{X}$ pour lesquelles le matériau hôte est plus stable que les différentes phases en compétition. L'ensemble des valeurs $\Delta\mu_\mathrm{X}$ est calculée à partir du diagramme de phase de stabilité globale (réalisé à partir de l'énergie de formation calculée par la méthode FERE [194]) présentée dans la Fig 7.7.

Le terme $q\left(E_\mathrm{VBM}^\mathrm{H} + \Delta E_\mathrm{F}\right)$ dans l'Eq. 7.1 est également égal à qE_F, où E_F est l'énergie de Fermi. Ce terme correspond au potentiel chimique des électrons ajoutés ou retirés, *i.e.* la modification de l'énergie due à l'état de charge du défaut ; cette quantité dépend de la valeur du niveau de Fermi E_F dans la bande interdite fondamentale E_g du matériau hôte [définie ici comme la différence d'énergie entre le minimum de la bande de conduction et le maximum de la bande de valence, indépendamment de l'état de spin]. L'énergie de Fermi E_F est donc définie comme la somme de $E_\mathrm{VBM}^\mathrm{H}$, l'énergie du VBM pour le cristal hôte massif, et ΔE_F, la variation du niveau de Fermi dans le gap par rapport au VBM. Enfin, E_corr dans l'Eq. 7.1 est la correction de Lany-Zunger [199], qui comprend la correction de Makov-Payne [200] et un alignement du potentiel électrostatique pour corriger son décalage dû à la taille limitée de la supercellule utilisée. Cette correction est calculée à l'aide du code PyDEF [196, 201] ; elle dépend des valeurs de la permittivité relative du matériau hôte non défectueux.

La Fig. 7.8 montre les valeurs des énergies de formation $E_\mathrm{f}[\mathrm{V}_\mathrm{X}^q]$ calculées pour les différents types de lacunes atomiques dans CFO et NFO et en fonction de ΔE_F qui varie à l'intérieur de la bande interdite fondamentale de ces oxydes.

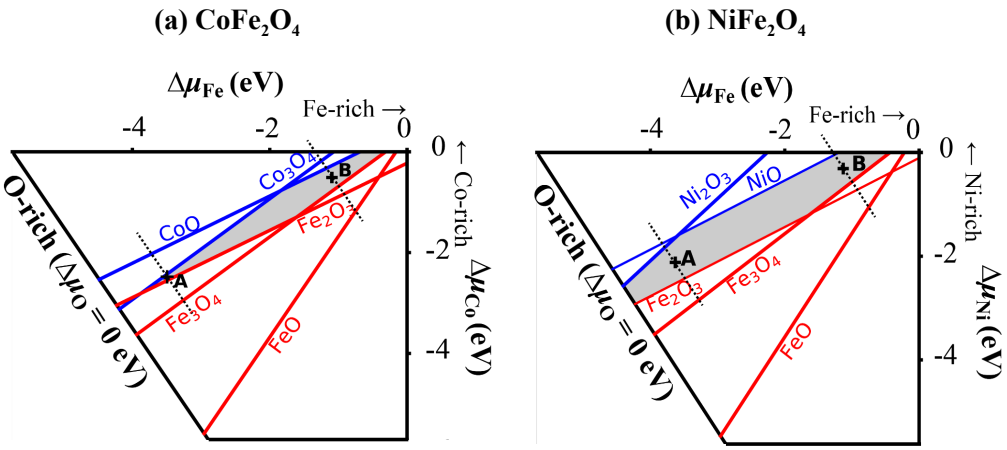

FIGURE 7.7 – Diagrammes de phase de stabilité de (a) CFO (b) et NFO. Les gammes de potentiels chimiques pour lesquelles CFO et NFO sont plus stables que les phases concurrentes sont indiquées par les zones grises. Les points A et B sont les valeurs médianes pour des conditions de croissance dans des atmosphères dites riches ($\Delta\mu_O = -0,5$ eV) ou pauvres ($\Delta\mu_O = -2,2$ eV) en oxygène, respectivement.

Pour NFO, les défauts que nous avons calculés comme étant les plus probables *dans des conditions de croissance pauvres en oxygène* sont donc : V_{Ni}^{-2} pour $\Delta E_F > 1.31$ eV, V_O^0 pour $0,10 < \Delta E_F < 1,31$ eV et V_O^{+1} pour $0 < \Delta E_F < 0,10$ eV. *Pour CFO dans des conditions de croissance pauvres en oxygène*, les défauts les plus probables sont V_{Co}^{-2} pour $\Delta E_F > 1.09$ eV et les lacunes d'oxygène pour $\Delta E_F < 1.09$ eV.

Les lacunes de Ni/Co seront les défauts les plus stables dans *des conditions riches en oxygène*. *Pour NFO*, ces conditions ont permis de calculer un niveau de Fermi (en utilisant une équation d'électroneutralité [202, 203]) de $\Delta E_F^{eq} = 0,30$ eV, pour lequel les lacunes de Ni seront principalement partiellement ionisées ($q = -1$), et seront présentes avec une concentration $[V_{Ni}^{-1}] = 1,8\times10^{14}$ cm^{-3}. *Pour CFO*, nous avons $\Delta E_F^{eq} = 0,27$ eV (ce qui est inférieur à la valeur d'énergie critique $\varepsilon(0/-1) = 0,36$ eV à laquelle les lacunes dans le cobalt transitent d'un état de charge $q = 0$ à un état $q = -1$) et les lacunes dans le Co seront principalement neutres et présentes avec une concentration très élevée de $[V_{Co}^0] = 9,2\times10^{16}$ cm^{-3} (les lacunes chargées V_{Co}^{-1} ont une concentration de 1 à 2 ordres de grandeur inférieure à $[V_{Co}^0]$). Si on considère des conditions riches en oxygène, pour CFO et NFO, le niveau de Fermi est calculé plus près du VBM que dans des conditions pauvres en oxygène et nous avons donc une plus grande quantité de trous libres ($p = 10^{14}$-10^{15} cm^{-3}).

La structure électronique des ferrites présentant des lacunes de cations et d'oxygène est présentée dans les Figs. 7.9 et 7.10, respectivement. Une lacune de cation neutre V^0 induit une reconstruction électronique, avec le transfert de trous vers les cations Co ou Ni, premiers voisins de la lacune. Comme le montre la Fig. 7.9, ces trous sont générés par la dépopulation des orbitales les plus occupées, créant ainsi des états de lacune dans le même canal de spin. Lorsqu'une lacune de cation

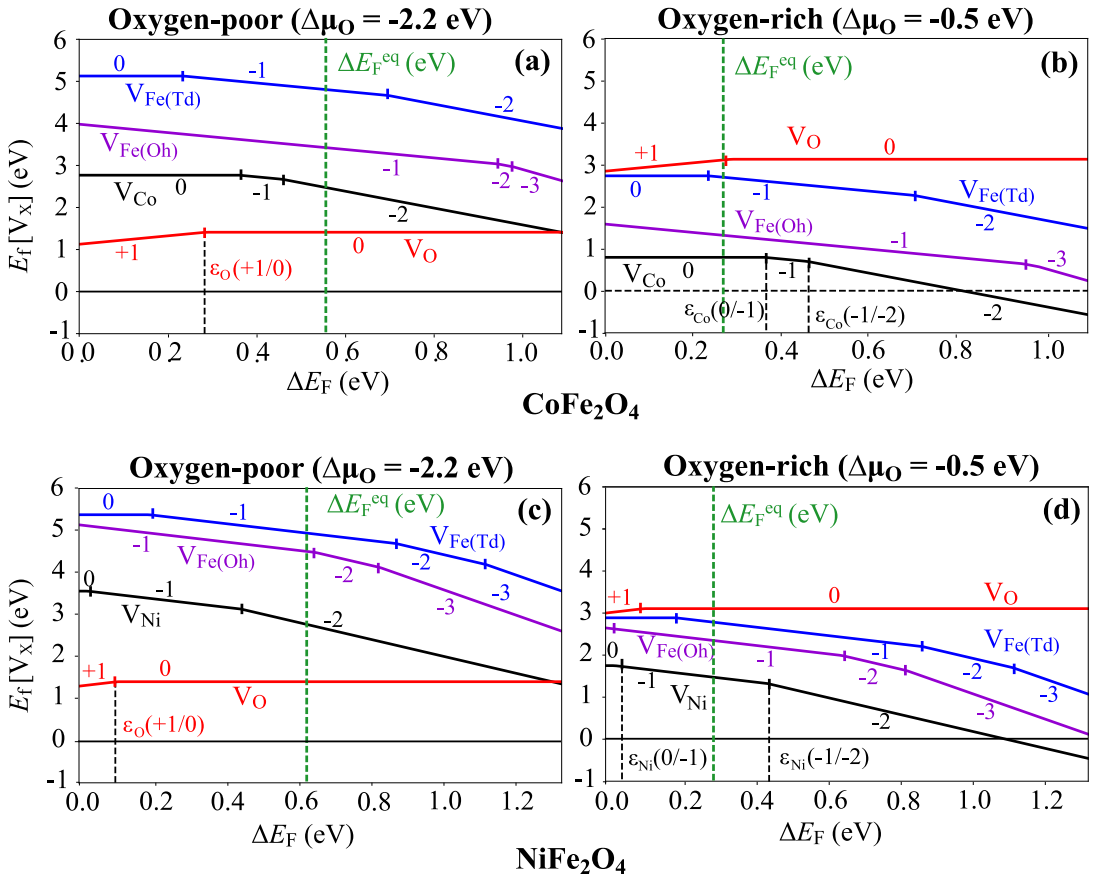

FIGURE 7.8 – Energies de formation $E_f\left[V_X^q\right]$ des lacunes atomiques chargées dans CFO pour (a) une atmosphère pauvre en oxygène ($\Delta\mu_O = -2,2$ eV) et (b) une atmosphère riche en oxygène ($\Delta\mu_O = -0,5$ eV). Énergies de formation des lacunes atomiques chargées dans NFO dans des conditions de croissance similaires : (c) pauvre et (d) riche en oxygène. Les énergies de formation sont données en fonction de la position du niveau de Fermi ΔE_F qui est donnée par rapport au VBM des cristaux massifs des composés parfaits. Les énergies correspondant aux états de charge les plus stables q de chaque type de lacune sont représentées et ces états de charge sont indiqués à proximité des lignes. Les lignes verticales vertes indiquent les valeurs du niveau de Fermi d'équilibre.

est chargée, le nombre de trous transférés diminue, jusqu'à 0 pour $V^{-2}_{M(Oh)}$ et $V^{-3}_{Fe(Oh)}$. Si la reconstruction électronique induite par les défauts n'implique qu'un seul trou, celui-ci est principalement localisé dans les cations, premiers voisins de la lacune. Lorsque plus de trous sont transférés (pour les lacunes neutres en particulier), on observe une délocalisation sur plus de cations Ni/Co. Le sommet de la bande de valence de NFO traverse le niveau de Fermi lorsque des lacunes $V^0_{Ni(Oh)}$, $V^0_{Fe(Oh)}$ et $V^{-2}_{Fe(Oh)}$ sont présentes.

Pour des conditions de croissance dans une atmosphère pauvre en oxygène, les lacunes d'oxygène existeront très probablement avec l'état de charge $q = 0$. Leur présence s'accompagne d'une reconstruction électronique et d'un état occupé apparaissant l'un dans le canal de spin majoritaire et l'autre dans le canal de spin minoritaire (Fig. 7.10). Des lacunes d'oxygène ionisées peuvent être formées lorsque le niveau de Fermi est proche du VBM. Les lacunes d'oxygène avec l'état de charge

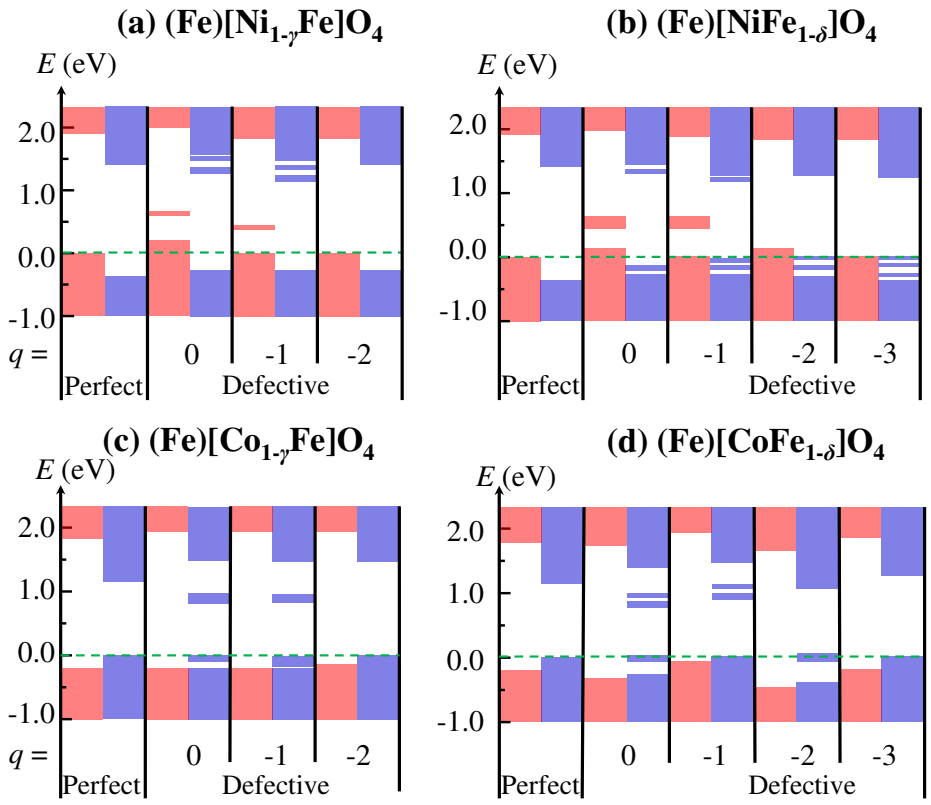

FIGURE 7.9 – Représentation schématique de la densité d'états calculée pour les cristaux (a,b) de NFO et (c,d) de CFO avec différentes lacunes de cations dans les sites Oh et différents états de charge q. La largeur en énergie de la bande interdite correspond à la zone blanche. Les DOS des spins majoritaire et minoritaire sont représentées respectivement en rouge et en bleu. La ligne verte en pointillés correspond à l'état d'occupation le plus élevé. Les nombres correspondent aux valeurs de q.

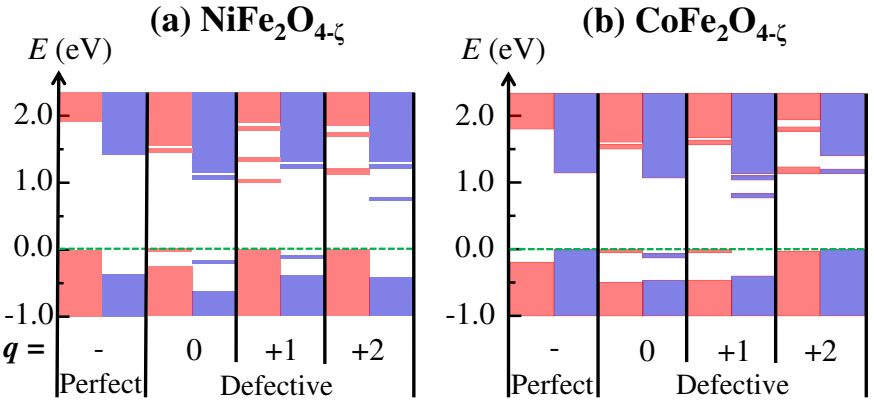

FIGURE 7.10 – Identique à la Fig. 7.9, mais pour des cristaux massifs de a) NFO et (b) CFO déficients en oxygène.

q = +2 ne conduisent pas à un déséquilibre de charge et à une reconstruction électronique. Lorsque l'état de charge de la lacune d'oxygène est q = +1, ce qui peut se produire lorsque le niveau de

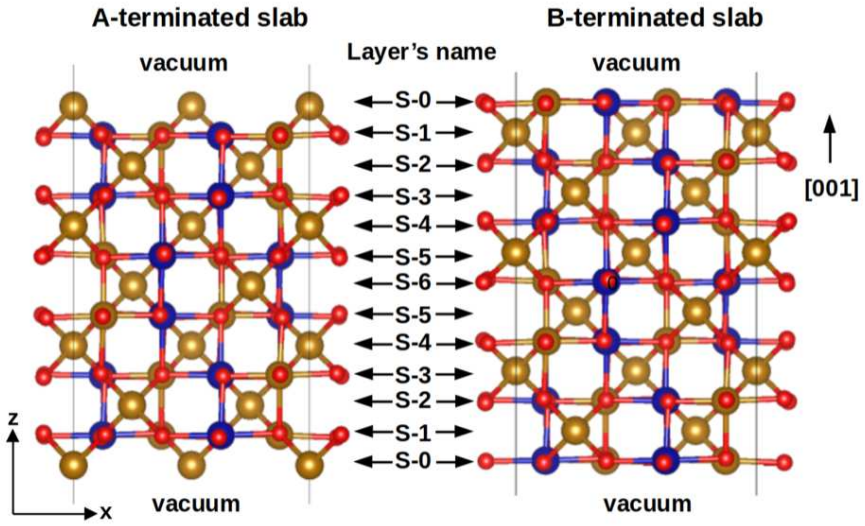

FIGURE 7.11 – Structure atomique des couches de NFO avec une terminaison de surface A [Fe(Td) à la surface] et une terminaison B [Ni(Oh), Fe(Oh), et O à la surface]. Les atomes de Ni, Fe et O sont représentés respectivement en bleu, marron et rouge. Les différents plans atomiques de la surface au centre de la couche sont numérotés comme indiqué sur la figure.

Fermi est proche du VBM, un seul état de lacune occupé apparaît dans le canal de spin majoritaire pour CFO et dans le canal de spin minoritaire pour NFO.

7.5 Couches minces de $NiFe_2O_4(001)$: Rôle des surfaces et des interfaces

Expérimentalement, les épaisseurs des couches de $NiFe_2O_4$ déposées pour réaliser les dispositifs étudiés sont d'environ 10-15 nm, de sorte que les contributions des surfaces/interfaces peuvent être significatives. Dans cette section, nous présentons une étude détaillée des surfaces dans les couches de NFO(001), afin de comprendre leurs propriétés électroniques et magnétiques. Nous avons choisi de n'étudier que les surfaces d'orientation (001) correspondant aux échantillons étudiés dans le cadre du projet MULTINANO. Le but de ce projet était de comprendre les mécanismes expliquant la transition isolant vers métal lorsque la ferrite de structure spinelle choisie est interfacée avec l'oxyde ferroélectrique de structure pérovskite $BaTiO_3(001)$. Il était donc important de comprendre d'abord les propriétés électroniques et magnétiques des surfaces libres avant d'étudier directement ces interfaces. Des résultats préliminaires concernant cette interface sont donnés à la fin de cette section.

7.5.1 Surfaces $NiFe_2O_4(001)$

Tout d'abord, nous avons examiné les surfaces de terminaison A (correspondant à un plan atomique $[Fe_2]^{6+}$(Td)) et de terminaison B (de plan atomique $[Ni_2Fe_2O_8]^{6-}$(Oh)) idéales, i.e. qui respectent l'empilement des plans atomiques dans le cristal massif ; les structures atomiques des

couches utilisées pour étudier ces surfaces sont représentées dans la Fig. 7.11. Dans la Fig. 7.12 (a), nous avons tracé les distances intercouches d_{AB} entre les plans A et B successifs dans les couches NFO(001) avec des terminaisons de surface A ou B parfaites. Les distances intercouches d_{AB} sont calculées comme la différence entre les coordonnées z moyennes (le long de la direction [001] perpendiculaire aux surfaces) de tous les atomes dans les plans A et B adjacents. Nos calculs montrent que les distances d_{AB} sont plus petites près de la surface que dans le NFO massif : Elles sont en effet de 0,17 et 0,86 Å aux surfaces des couches de terminaison A et B, respectivement. Au fur et à mesure que l'on s'éloigne de la surface, la distance intercouche oscille et converge rapidement vers la distance intercouche du cristal massif de NFO ($\simeq 1,03$ Å).

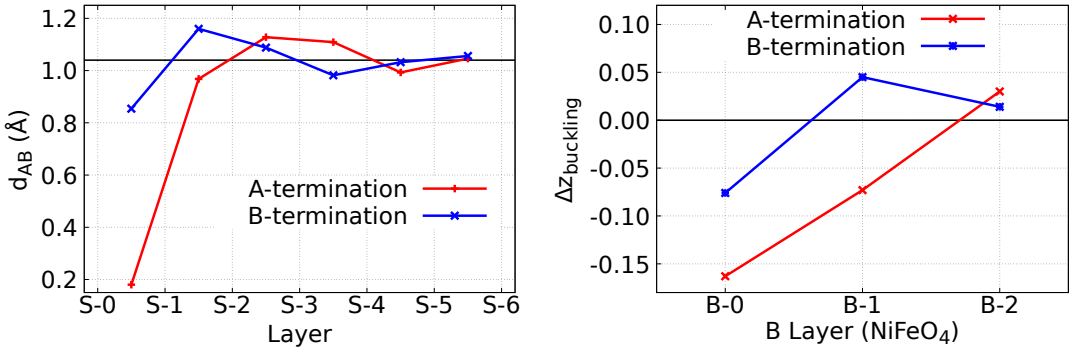

(a) (b)

FIGURE 7.12 – (a) Distance intercouche d_{AB} entre les plans A et B consécutifs. La ligne horizontale noire à 1,04 Å représente la distance intercouche calculée pour le cristal massif de NFO. (b) Distorsion polaire entre les anions et cations dans les plans B, calculée le long de la direction [001].

Comme le montre la Fig. 7.12(b), les plans atomiques B proches de la surface de NFO présentent également une légère distorsion polaire cation-oxygène ($\Delta z_{buckling} = z_{Cations} - z_{Anions}$) définie comme la différence entre les coordonnées z moyennes des cations et des anions d'oxygène situés dans les mêmes plans B(001). La Fig. 7.12(b) montre que les cations de surface se déplacent légèrement vers le centre de la couche du fait de la présence des surfaces de terminaison A et B. La distorsion calculée est plus élevée pour les couches de terminaison A ($-0,163$ Å) que pour celles de terminaison B ($-0,076$ Å).

Nous rappelons que l'ordre magnétique dans NFO est caractérisé par un couplage antiferromagnétique entre les cations de Fe situés dans les sites Td et les cations de Ni ou de Fe situés dans les sites Oh. La variation des moments magnétiques de spin des différents cations [Ni, Fe(Oh), et Fe(Td)] en fonction de leur distance par rapport à la surface est montrée dans les Fig. 7.13(a) et 7.13(b) pour les deux terminaisons de surface parfaites étudiées. Au centre de la couche de NFO, les moments magnétiques de spin des cations sont égaux à ceux obtenus pour le cristal massif (donnés par les lignes noires pointillées), qui sont de 1,54 μ_B, 4,04 μ_B, et $-3,88$ μ_B respectivement pour les cations Ni, Fe(Oh), et Fe(Td). Dans les plans superficiels, ces moments magnétiques sont au contraire différents, en raison des reconstructions électroniques induites par les surfaces. A la surface parfaite de terminaison A [Fig. 7.13(a)], les cations Fe(Td) et Fe(Oh) voient leur moment

magnétique de spin changer de $-3,88$ μ_B à $-3,40$ μ_B pour chacun des atomes de Fe(Td) et de 4,04 μ_B à 3,88 μ_B pour chacun des atomes de Fe(Oh) de la couche (S-3). A la surface B parfaite [Fig. 7.13(b)], nous observons une légère variation du moment magnétique de spin des cations dans les plans les plus proches de la surface : le moment magnétique de spin de l'ion Fe(Td) de la couche (S-1) devient -3.92 μ_B, au lieu de -3.88 μ_B dans le cristal massif de NFO. Nous pouvons également constater que les ions de surface Ni et Fe(Oh) ont leur moment magnétique de spin modifier à 0,81 μ_B pour chaque ion Ni et 3,86/3,83 μ_B pour chaque ion Fe.

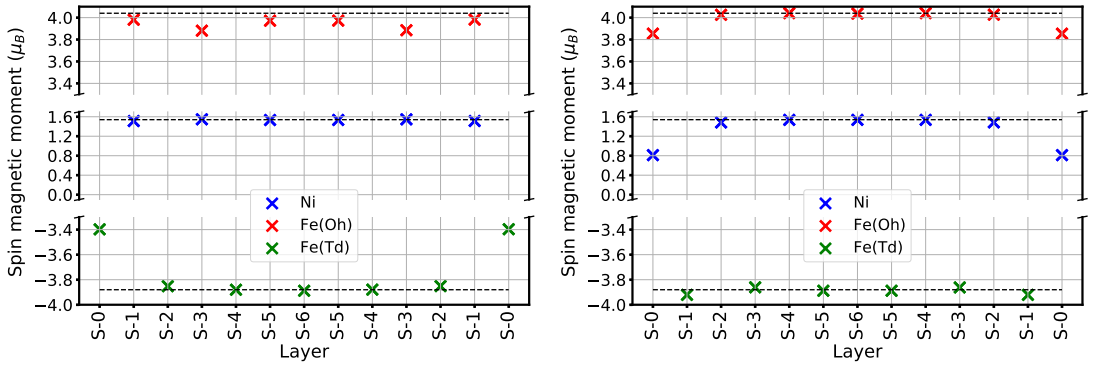

(a) (b)

FIGURE 7.13 – (a) Moment magnétique de spin des cations dans les plans atomiques (001) successifs de la couche de NFO de surface de terminaison A. Les lignes pointillées noires représentent le moment magnétique de spin des cations dans le cristal massif de NFO. (b) Idem pour la couche dont la surface est de terminaison B.

Le long de la direction [001], les plans atomiques A et B alternés portent respectivement une charge électronique de $\sigma = +6$ e/-6 e (pour 2 f.u. de NFO). Dans une couche réelle, la présence d'une unique surface polaire peut induire l'apparition de reconstruction électronique pour garantir sa stabilité [247]. Comme nous avons choisi de modéliser nos couches par des structures symmétriques présentant deux terminaisons de surface identiques, l'origine des reconstructions électroniques calculées permet de garantir la neutralité électrique globale de la couche, cette dernière étant par construction non-stœchiométrique. Il est attendu que ces reconstructions électroniques correspondent à la localisation d'une charge surfacique $\sigma_S = -0,5\sigma$. Les états de surface correspondant à ces transferts de charge peuvent être observés dans la bande interdite des DOS projetées dans les différents plans atomiques (LDOS), calculées pour les couches présentant des surfaces de terminaisons A et B (voir Fig. 7.14). Pour la surface de terminaison A [Fig. 7.14(a)], les états de surface devraient correspondre au transfert de trois électrons. Deux de ces électrons vont se localiser sur les deux cations Fe^{3+}(Td) de la couche de surface (S-0) pour réduire leur degré d'oxydation à 2+ et former l'état de défaut mis en évidence par le rectangle vert sous le niveau de Fermi. De même, nous pouvons voir que les états de défaut correspondant au transfert de 3 trous dans la couche dont les surfaces sont de terminaison B sont situés dans le plan de surface (S-0), comme le montre la Fig. 7.14(b). Les premiers états de défaut correspondant à la répartition de deux

trous sont représentés par un rectangle bleu, juste au-dessus du niveau de Fermi, dans la DOS de spin majoritaire. Ils impliquent la contribution de deux atomes de Ni et de leurs orbitales $d_{x^2-y^2}$ respectives. Le dernier état de défaut inoccupé, mis en évidence par le rectangle rouge, traverse le niveau de Fermi et correspond à des bandes $d_{x^2-y^2}$ partiellement remplies par les deux atomes Fe(Oh) de surface. Par conséquent, la surface NFO de terminaison B parfaite est un conducteur de trous polarisés en spin.

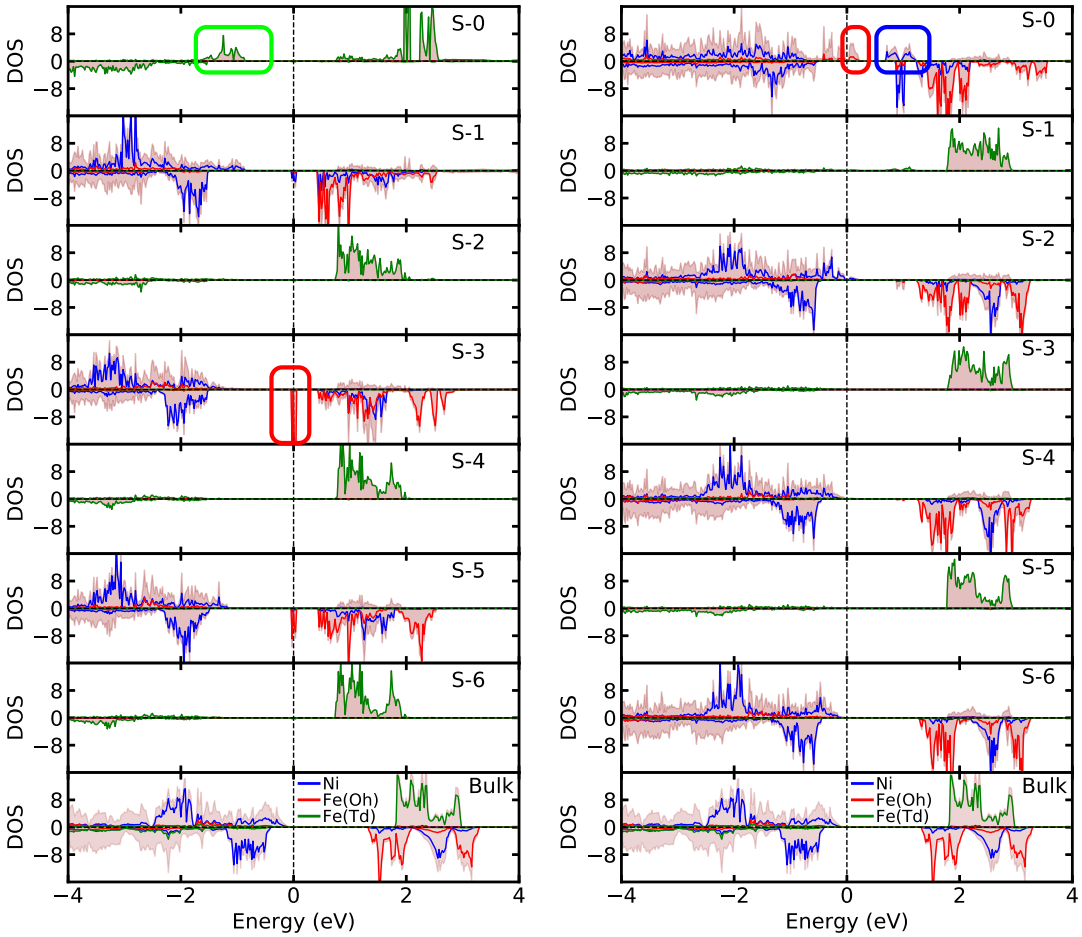

(a) A-terminated slab

(b) B-terminated slab

FIGURE 7.14 – LDOS projetées dans les plans atomiques (S-0) (plan de surface) à (S-6) (plan au centre de la couche) pour les couches de NFO de surfaces (a) de terminaison A et (b) de terminaison B. À titre de comparaison, la DOS du cristal massif de NFO est indiquée dans le panneau inférieur des deux figures. Les pics de DOS correspondant aux états de défauts sont mis en évidence par des rectangles tracés avec une couleur représentant l'atome auquel appartiennent ces états (couleurs bleue, rouge et verte pour les cations Ni, Fe(Oh) et Fe(Td), respectivement).

Une fois que la structure électronique des surfaces de terminaisons A et B parfaites a été étudiée, nous avons cherché à savoir si d'autres terminaisons de surface pourraient être, ou non, plus stables, et donc plus susceptibles d'être observées expérimentalement. La Fig. 7.15 montre les terminaisons de surface calculées comme étant les plus stables en fonction des variations des potentiels chimiques

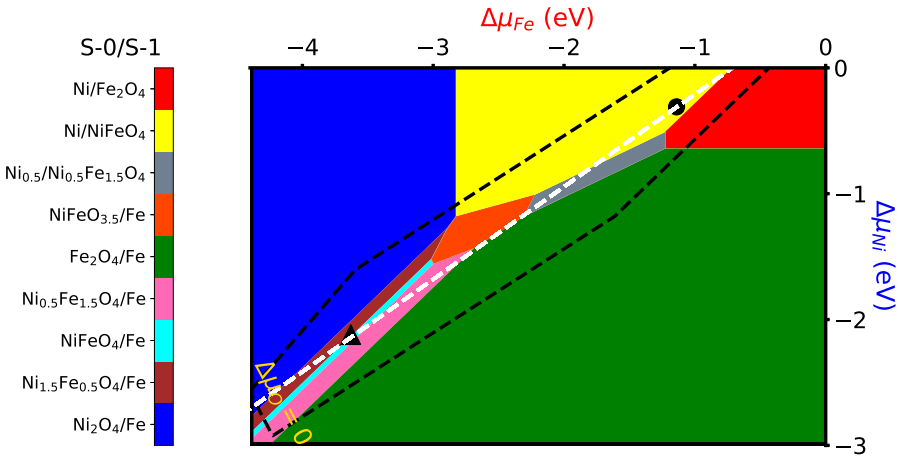

FIGURE 7.15 – Diagramme de phase de la stabilité des terminaisons de surface calculé pour des couches symétriques de NFO et tracé en fonction des variations des potentiels chimiques $\Delta\mu$ des atomes de Fe et de Ni. La ligne noire en pointillés représente le domaine de stabilité calculé pour le cristal massif de NFO (voir Fig. 7.7(b)). Le potentiel chimique des atomes d'oxygène ($\Delta\mu_O$) est nul en bas à gauche du diagramme de phase et augmente vers le coin supérieur droit ($\Delta\mu_{Fe} = 0$, $\Delta\mu_{Co} = 0$). Le triangle noir et le cercle noir sur le diagramme de phase représentent les conditions de croissance dans des atmosphères riches ($\Delta\mu_O = -0,5$ eV) et pauvres ($\Delta\mu_O = -2,2$ eV) en O. La barre de couleur sur le côté gauche de la figure et la notation (S-0/S-1) sont utilisées pour préciser les compositions chimiques des plans de surface (S-0) et de sous-surface (S-1). La ligne blanche en pointillés au centre du domaine de stabilité du cristal massif sera utilisée pour calculer l'énergie de formation de la surface en fonction de la variation du potentiel chimique de l'oxygène.

$\Delta\mu_{Fe}$ et $\Delta\mu_{Ni}$. Dans cette figure, nous avons superposé le domaine de stabilité du cristal massif de NFO, délimité par les lignes noires pointillées. Pour des conditions de croissance dans une atmosphère pauvre en O, la terminaison de surface $Ni/NiFeO_4$ est stable sur une large gamme de $\Delta\mu_O$, entre $-2,4$ eV et $-1,8$ eV. Pour $\Delta\mu_O$ supérieur à $-1,5$ eV (conditions de croissance riches en O), les surfaces de terminaisons B sont les plus stables. Le potentiel chimique de l'oxygène peut être exprimé en fonction des paramètres expérimentaux utilisés lors de la croissance des couches, qui sont la température de croissance (T) et la pression partielle en oxygène (P) [249, 250] :

$$\Delta\mu_O(T,P) = \frac{1}{2}\{[H_0 + \Delta H(T)] - T\,[S_0 + \Delta S(T)]\} + \frac{1}{2}k_B T \ln\left(\frac{P}{P_0}\right) \tag{7.2}$$

où $\Delta H(T) = C_p\,(T - T_0)$, $\Delta S(T) = C_p \ln(T/T_0)$. $H_0 = 8,7$ kJ mol^{-1}, $S_0 = 205$ J mol^{-1} K^{-1} sont des valeurs tabulées [249, 251] et $P_0 = 1$ atm et $T_0 = 298$ K sont la pression et la température standard. Voici quelques exemples de conditions de croissance expérimentales utilisées pour produire des couches minces de NFO : $T = 923$ K et $P/P_0 = 1,33 \times 10^{-4}$ [252], correspondant à $\Delta\mu_O = -1,35$ eV. D'autres conditions utiles sont $T = 673$ K et $P/P_0 = 1,33 \times 10^{-9}$, correspondant à $\Delta\mu_O(T,P) = -1,29$ eV. Comme le montre la Fig. 7.16, le diagramme de phase de surface est tracé par rapport à T et P correspondant aux valeurs de $\Delta\mu_O$ le long de la ligne blanche en pointillés montrée dans

la Fig. 7.15. Dans la Fig. 7.16, nous voyons que les surfaces de terminaison A ne sont stables qu'au-dessus de T = 1000 K.

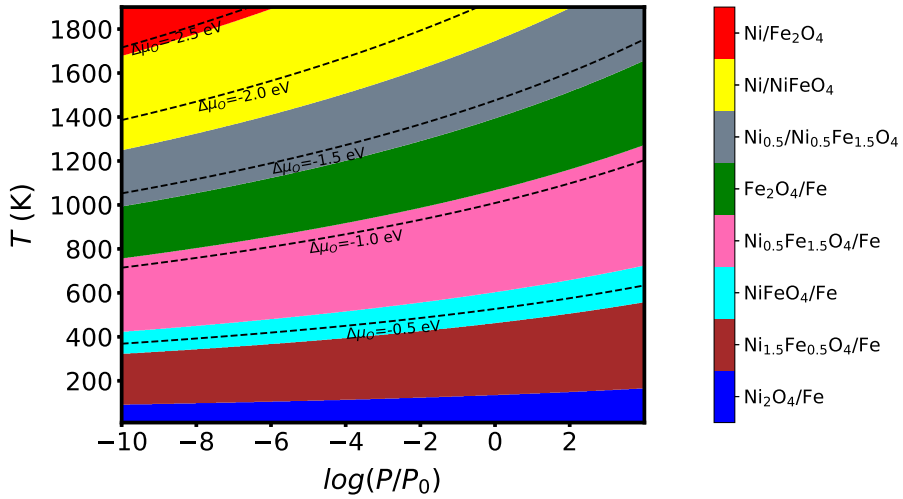

FIGURE 7.16 – Diagramme de phase de surface tracé en fonction de la température de croissance T et de la pression partielle en oxygène P. Les valeusr de T et de P sont définies suivant l'ensemble des valeurs de $\Delta\mu_O$ correspondant à la ligne blanche en pointillés du diagramme de phase de surface de la Fig. 7.15. Les lignes noires en pointillés représentent les courbes d'iso-potentiel de l'oxygène.

Le Tableau 7.16 montre que, pour une terminaison de surface donnée, lorsque la reconstruction de charge implique la délocalisation d'un trou (h) ou d'un électron (e) sur au moins deux cations Ni ou Fe, cette terminaison de surface a plus de chances de devenir métallique, en raison de la formation de bandes partiellement remplies qui vont croiser le niveau de Fermi. Cette situation doit se produire à moins qu'un ordre de charge accompagné de distorsions structurales n'apparaisse. La vérification que de tels ordres de charge puissent être présents nécessiterait des études supplémentaires. Les terminaisons $Ni/NiFeO_4$ et $Ni_{1,5}Fe_{0,5}O_4/Fe$ correspondent aux surfaces les plus stables de terminaisons de type A et B, respectivement.

D'après nos résultats, nous pouvons affirmer que les surfaces de terminaison A et de terminaison B sont stables dans les environnements de croissance pauvres en O et riches en O, respectivement. En raison de la présence de la surface, des trous ou des électrons sont situés vont se localiser dans les plans de surface ou de sous-surface, en fonction de la terminaison atomique. Le comportement conducteur de la surface dépend du type de terminaison de la surface. Du fait que les terminaisons de surface les plus stables ne correspondent pas forcément aux terminaisons A et B parfaites, nous avons ensuite cherché à savoir si les défauts ponctuels de structure étudiés dans la section précédente pouvaient, ou non, se former plus facilement au niveau des surfaces que dans le centre des couches. Si nous examinons la stabilité des lacunes de Ni et O en fonction de leur position par rapport à la surface, nous constatons que les lacunes d'O se forment de préférence au niveau de la surface alors que les lacunes de Ni sont plus stables au centre de la couche de terminaison B.

TABLE 7.1 – Propriétés physiques des surfaces dont l'énergie de formation γ est inférieure à 80 meV/Å^2. L'énergie de formation de surface est donnée pour les deux conditions de croissance étudiées. Le nombre de charges par surface avant toute reconstruction électronique σ, la localisation des charges (σ_S), électrons (e) ou trous (h), induites par la reconstruction électronique (par surface), le travail de sortie ϕ_M et l'état conducteur (métallique M ou isolant I) des différentes terminaisons de surfaces sont indiqués.

Terminaison de surface (S-0)/(S-1)	γ (meV/Å^2) pauvre en O	riche en O	σ^*	Distribution de σ_S (e ou h) sur les cations	ϕ_M (eV)	Conductivité (M/I)
Terminaisons de surface de type A						
$Ni/NiFeO_4$	74	90	1	1e : → 2 Ni(Td)	4,31	M
$Ni_{0.5}Fe_{0.5}/NiFeO_4$	76	102	2	2e : 1→Fe(Td), 1→Ni(Td)	4,43	I
Ni/Fe_2O_4	77	114	3	3e : 2→2Ni(Td), 1→Fe(Oh)	4,21	M
$Ni_{0.5}/Ni_{0.5}Fe_{1.5}O_4$	78	78	0	Transfert partiel d'e : Ni(Oh) → Ni(Td)	4,92	I
$Ni_{0.5}/NiFeO_4$	87	77	-1	1h : Ni(Td) and 2Ni(Oh)	5,30	I
Terminaisons de surface de type B						
$NiFeO_{3.5}/Fe$	84	72	-1	1h : Ni(Oh)	5,57	I
Fe_2O_4/Fe	87	70	-1	1h : →2Fe(Oh)	5,50	M
$Ni_{0.5}Fe_{1.5}O_4/Fe$	93	67	-2	2h : 1→Fe(Oh), 1→Ni(Oh)	5,69	I
$NiFeO_4/Fe$	102	66	-3	3h : 1→2Fe(Oh), 2→2Ni(Oh)	5,77	M
$Ni_{1.5}Fe_{0.5}O_4/Fe$	112	65	-4	4h : 3Ni(Oh) ; Ni(Oh)(S-2)	5,85	I
Ni_2O_4/Fe	123	67	-5	5h : 4→4Ni(Oh), 1→2Ni(Oh)(S-2)	5,90	I

*Les charges excédentaires avant la reconstruction électronique sont les charges nettes par surface calculées en supposant que le Ni, le Fe et l'O sont respectivement dans les états d'oxydation +2, +3 et -2.

7.5.2 Interface $NiFe_2O_4(001)/BaTiO_3(001)$

Après avoir étudié les surfaces de NFO(001), nous avons cherché à savoir s'il serait possible de moduler les propriétés électroniques d'interface avec un matériau ferroélectrique en fonction de l'orientation de la polarisation électrique de ce dernier. Nous avons choisi de considérer l'interface avec l'oxyde de structure pérovskite $BaTiO_3$ (BTO) dans sa phase tétragonale. Comme le montre la Fig. 7.17, les propriétés des interfaces ont été étudiées à l'aide d'un super réseau contenant, par construction, deux interfaces non équivalentes perpendiculaires à l'axe z[001] (respectivement IF-1 et IF-2), qui ne diffèrent que par l'orientation de la polarisation électrique dans $BaTiO_3$: à l'interface IF-1 (IF-2), la polarisation pointe vers l'extérieur (vers l'intérieur) depuis l'interface, c'est-à-dire vers le centre de la couche de $NiFe_2O_4$ (vers le centre de la couche de $BaTiO_3$). Dans cette étude préliminaire, nous avons considéré que les deux interfaces ont des terminaisons atomiques $[NiFe]_{Oh}O_4/Ti_2O_4$ parfaites. Les dimensions latérales de $NiFe_2O_4$ et $BaTiO_3$ dans les directions x et y sont respectivement $(\frac{1}{\sqrt{2}}\times\frac{1}{\sqrt{2}})R45°$ et $(\sqrt{2}\times\sqrt{2})R45°$, chaque couche (001) contenant soit 2 f.u. de $BaTiO_3$ ou 1 f.u. de $NiFe_2O_4$ (dont les dimensions latérales sont la moitié de celles utilisées pour l'étude des surfaces). Le paramètre de maille dans le plan commun à chaque matériau a été fixé à 5,61 Å, ce qui correspond au paramètre de maille dans le plan calculé pour le cristal massif de structure tétragonale de $BaTiO_3$ à l'équilibre ($a_{BTO} = 3,967$ Å) avec la fonctionnelle PBESol. Cette structure imite ainsi une croissance épitaxiale de $NiFe_2O_4$ sur $BaTiO_3$(001). Selon

nos paramètres de maille calculés, le désaccord de maille dans le plan entre ces deux matériaux est de $\frac{a_{\mathrm{NFO}}-a_{\mathrm{BTO}}}{a_{\mathrm{BTO}}} = 4,32\%$. La distribution des cations Ni/Fe dans les sites Oh correspond toujours à celle du groupe spatial $P4_122$ et l'axe tétragonal de cette structure est le long de l'axe z normal aux interfaces. Le super réseau contient un total de 124 atomes répartis sur 15 couches atomiques (001) de $BaTiO_3$ et 13 couches atomiques de $NiFe_2O_4$.

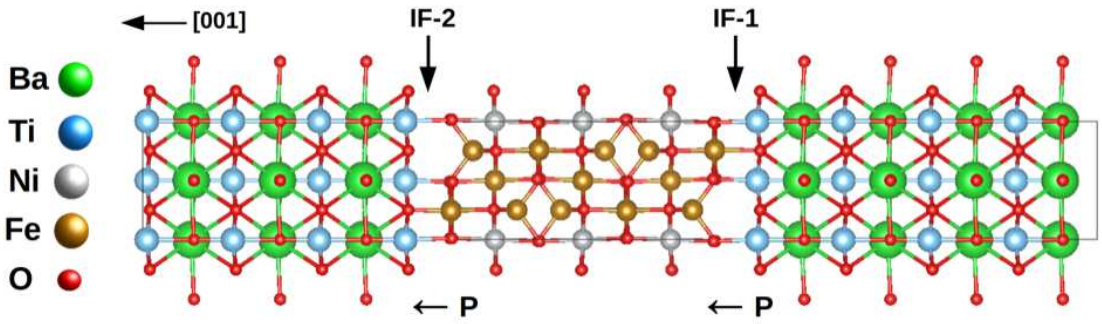

FIGURE 7.17 – Super-réseau constitué de bi-couches $NiFe_2O_4/BaTiO_3(001)$ utilisé pour les calculs et formé de deux interfaces (IF-1 et IF-2) avec des terminaisons atomiques $NiFeO_4/Ti_2O_4$.

Nous pouvons voir dans les LDOS de la Fig. 7.18 que l'occupation électronique des bandes des cations Ni est fortement modifiée par rapport au cristal massif. Les courbes de LDOS sont également différentes pour les deux interfaces, témoignant d'un effet de l'orientation de la polarisation électrique. En particulier, nous pouvons voir que certaines bandes de spin majoritaire du Ni, entièrement occupées pour le cristal massif de $NiFe_2O_4$, ne sont plus occupées. Comme indiqué dans le Tableau 7.2, ces changements dans les LDOS sont également associés à des variations des moments magnétiques de spin atomiques : on observe en effet une diminution du moment magnétique de spin du Ni d'environ $\sim 0.7\ \mu_B$ entre le cristal massif et IF-1, puis une autre diminution d'environ $\sim 0.7\ \mu_B$ entre IF-1 et IF-2, les cations Ni à IF-2 ayant un moment magnétique de spin nul. Les variations du moment magnétique de spin des autres atomes sont négligeables. L'absence de variations dans les degrés d'oxydation des cations Fe(Oh) montre que cette interface se comporte différemment de la surface terminée en B, ce qui peut être le résultat de la structure et de la chimie de l'interface choisies, mais aussi de leur non-équivalence résultant de la polarisation électrique. Comme on peut le voir dans le Tableau 7.3, la longueur de la liaison Ni-O varie de 0,25 Å lorsque la polarisation électrique est inversée, c'est-à-dire entre les interfaces IF-2 et IF-1.

À partir des variations de moments magnétiques de spin aux interfaces, il est possible de calculer un coefficient magnétoélectrique de surface α_S en utilisant la formule $\mu_0 \Delta M = \alpha_S E_c$, où ΔM est le changement dans l'aimantation à l'interface, μ_0 est la permittivité du vide et $E_c = 100$ kV cm^{-1} est le champ coercitif utilisé pour renverser la polarisation électrique de $BaTiO_3$. Comme indiqué dans le Tableau 7.2, le changement calculé de l'aimantation d'interface est $\Delta M = 0,855\ \mu_B$ par unité de surface. En utilisant ces valeurs, nous obtenons ainsi un coefficient magnétoélectrique linéaire de $3,16 \times 10^{-10}$ G cm^2 V^{-1}. Ce coefficient magnétoélectrique est du même ordre que celui calculé par Tamerd, *et al.* ($3,15 \times 10^{-10}$ G cm^2 V^{-1}), pour une bicouche $NiFe_2O_4/PbZr_{0,5}Ti_{0,5}O_3(001)$, avec

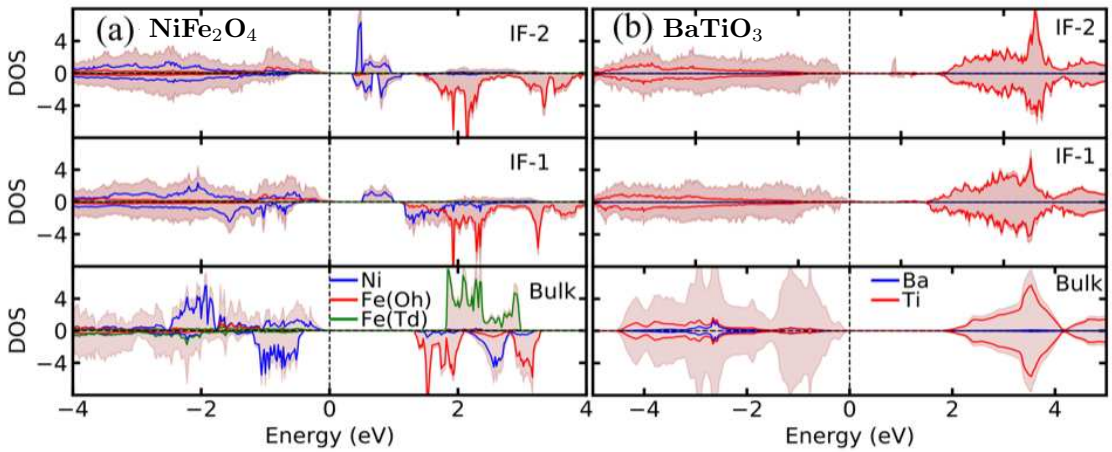

FIGURE 7.18 – Contribution à la DOS des plans atomiques d'interfaces IF-1 et IF-2 (a) côté NFO et (b) côté BTO.

TABLE 7.2 – Moment magnétique de spin des atomes dans les plans atomiques près des interfaces IF-1 et IF-2. Les multiplicités pour chaque atome sont données entre parenthèses.

	Moment magnétique de spin atomique (μ_B)					
	$NiFeO_4$			Ti_2O_4		Total
	Ni (×1)	Fe (×1)	O (×4)	Ti (×2)	O (×4)	
Cristal massif	1,541	4,036	0,079	0,000	0,000	
IF-1	0,773	4,018	0,079	0,005	0,045	5,295
IF-2	0,001	4,011	0,078	0,006	0,027	4,440
Différence entre les moments magnétiques de spin atomiques totaux						0.855

TABLE 7.3 – Longueurs de liaison chimique entre les cations et les anions d'oxygène à travers les interfaces IF-1 et IF-2, le long de la direction [001].

Interface	Fe-O (Å)	Ni-O (Å)	Ti-O (Å)
IF-1	2,01	2,12	1,98
IF-2	1,95	1,87	2,09

des terminaisons d'interface $NiFeO_4/ZrTiO_4$ [113].

7.6 Conclusions et perspectives

Au cours de cette thèse, nous avons cherché à comprendre les mécanismes responsables de la formation de domaines conducteurs dans les couches minces $MFe_2O_4/BaTiO_3(001)$ (M = Co, Ni) lors de l'application d'un champ électrique.

Nous avons d'abord considéré les cristaux massifs de ferrite et analysé les effets de l'arrangement des cations M/Fe dans le réseau. Nous avons constaté que l'état d'oxydation et l'aimantation ne changeaient pas significativement en fonction de la distribution des cations dans les sites Oh, mais la bande interdite pouvait être réduite de 25% à 40% en présence d'un mélange des phases les

plus stables. Les échanges de cations divalents et trivalents entre les sites Td et Oh, c'est-à-dire la diminution du degré d'inversion, entraînent également une diminution systématique de la largeur de la bande interdite et sont associés à une augmentation du moment magnétique de spin total. Nous avons ensuite examiné les propriétés électroniques des ferrites non stœchiométriques, en mettant l'accent sur les effets des lacunes atomiques. Nous avons constaté que dans des conditions de croissance correspondant à une atmosphère pauvre en oxygène, les défauts les plus stables sont les lacunes d'oxygène neutres qui n'altèrent pas l'aimantation de spin, elles induisent cependant l'apparition d'états électroniques locaux de lacunes dans la bande interdite pour les deux canaux de spin. Si la croissance est réalisée dans une atmosphère riche en oxygène, on s'attend plutôt à stabiliser des lacunes de Co neutres ou des lacunes de Ni partiellement ionisées, entraînant une diminution de l'aimantation de spin. Encore une fois, ces défauts, si isolés, ne devraient pas rendre les ferrites spinelles conductrices. En revanche, dans $NiFe_2O_4$, la présence moins probable de lacunes de Ni neutres ou de lacunes de Fe(Oh) pourrait induire la transformation du matériau en un conducteur de trous polarisés en spin.

Dans les couches minces de ferrites de nickel, les effets de surface et d'interface peuvent jouer un rôle important et annuler son comportement isolant. Cela est particulièrement vrai si la couche possède une surface de terminaison B parfaite (c'est-à-dire une terminaison correspondant à un plan (001) $NiFeO_4$). Pour une telle surface, une reconstruction de charge induira la localisation de 3 trous pour 2 f.u. de $NiFe_2O_4$ à la surface, parmi lesquels 1 trou sera partagé par les deux cations Fe(Oh) situés à la surface, permettant l'apparition d'un comportement métallique par des mécanismes de saut de trous par double échange. Cependant, nous avons constaté que la formation de lacunes d'oxygène neutres, plus stables à cette surface B que dans le matériau massif, peut contribuer à restaurer le caractère isolant de la surface. On peut donc s'attendre, à partir de ces résultats, à ce que toute modification de l'état de contrainte ou de la création/destruction de lacunes d'oxygène puisse déclencher la transition d'un caractère isolant vers métal. Des analyses plus approfondies de la structure électronique des autres terminaisons de surface calculées comme potentiellement stables permettraient de parvenir à une conclusion définitive sur le rôle des surfaces. La prise en compte des interfaces ajoute une autre contribution provenant de la direction de la polarisation électrique dans $BaTiO_3$. À une interface avec une terminaison $NiFeO_4/Ti_2O_4$, contrairement à la surface parfaite de terminaison B, nous n'avons calculé aucun transfert de trous dans les atomes de Fe(Oh) interfaciaux, mais seulement dans atomes de Ni. La quantité de charges redistribuées dépend de la direction de la polarisation électrique et est plus élevée dans le cas d'une polarisation orientée vers l'extérieur (de $NiFe_2O_4$ vers $BaTiO_3$). La largeur de la bande interdite de la couche atomique interfaciale est fortement réduite, jusqu'à $\simeq 0,3$ eV. Des perturbations supplémentaires pourraient alors facilement la rendre conductrice.

En termes de perspectives, plusieurs voies pourraient être suivies afin d'améliorer notre compréhension des transitions isolant-métal dans les ferrites spinelles.

Tout d'abord, lors de l'étude des défauts de structure dans les cristaux massifs de ferrite, nous nous sommes cantonnés à une étude indépendante de chaque type de défauts. Dans de vrais

échantillons, il est tout à fait raisonnable d'émettre l'hypothèse que ces défauts pourraient ne pas être isolés, mais pourraient s'ordonner ou s'agglomérer pour former des complexes, et que différents types de défauts pourraient coexister. Dans une étude non décrite dans ce manuscrit, nous avons par exemple mis en évidence une interaction entre le degré d'inversion de la structure spinelle et la présence de lacunes d'oxygène [259] ; nous avons de plus démontré que lorsque le degré d'inversion est inférieur à 1 et que ces lacunes sont présentes, NFO peut facilement devenir métallique. L'interaction entre plusieurs défauts mériterait ainsi une étude plus systématique.

Lors de la présentation du système expérimental (voir Fig. 7.2), en plus du centre de la couche de ferrite, de sa surface, et de son interface avec l'oxyde ferroélectrique $BaTiO_3$, nous avons également identifié une quatrième zone d'intérêt, à savoir l'interface entre le ferrite spinelle et l'électrode métallique. Cette électrode est en Au, mais elle est séparée du ferrite spinelle par une couche tampon en Ti d'une épaisseur de quelques nanomètres. Les domaines conducteurs dans la ferrite spinelle sont écrits en appliquant un champ électrique hors plan. Cependant, les mesures de transport sont réalisées dans le plan. Nous pouvons faire l'hypothèse que des défauts structurels se forment dans le ferrite spinelle pendant le processus d'écriture. Ces défauts sont certainement stabilisés par l'inversion de la polarisation électrique dans $BaTiO_3$. Prendre en compte l'électrode métallique et calculer la structure électronique à l'interface $Ti/NiFe_2O_4$ pourrait être utile pour estimer d'abord la hauteur de la barrière de Schottky si $NiFe_2O_4$ est encore légèrement isolant, ou simplement comprendre l'alignement des bandes à l'interface. Lorsque des tensions élevées sont appliquées pendant les mesures de transport, il serait également intéressant de vérifier si la diffusion des atomes de Ti dans la ferrite (défectueuse) pourrait se produire, ou si des lacunes d'oxygène supplémentaires pourraient être créées par l'oxydation de l'interface avec la couche de Ti, permettant ainsi la formation de plusieurs états de résistance. Malheureusement, de telles calculs pourraient être difficiles à réaliser en raison du grand désaccord de maille (en termes de paramètres de maille et de symétries de maille) entre les deux structures.

Appendix A

Choice of the exchange-correlation functionals and +U parameters

A.1 Choice of the exchange-correlation functionals

In this section, we compare different relevant physical properties (band gap, lattice parameter, magnetic moments) calculated for bulk spinel ferrites with different exchange-correlation functionals. In particular, owing to the goal of this thesis, which is to understand the mechanisms responsible of the conductivity in ferrites, an accurate calculation of the electronic structure and of the band gap at the Fermi level is essential. Because one of the objectives was also to calculate the effects of the interface between the ferrites and the ferroelectric oxide $BaTiO_3$, the chosen approximation also had to be suitable to calculate the properties of this last oxide, notably its tetragonality c/a, associated to its electric polarization. The final choice of the functional and of the U_{eff} parameters then came from a compromise between the results calculated for every material.

In Tables A.1, A.2 and A.3, we provide different physical properties of bulk $CoFe_2O_4$, $NiFe_2O_4$ and $BaTiO_3$, respectively, calculated using the CA+U (LDA) [261], the PBE+U (GGA), the PBEsol+U (GGA), the SCAN+U (METAGGA) and the HSE06 (hybrid) functionals.

When comparing these different functionals, it is important to keep in mind that they do not all belong to the same level of accuracy in the Jacob's ladder presented in Chapter 2 and that they can therefore be split in two groups:

1. The LDA and GGA belong to the two first levels and they display comparable computational times. These functionals however poorly describe the electronic structure if no +U correction is added as shown in Fig. A.1. We thus describe in the following the results obtained with the applied correction. For the sake of simplicity, when comparing the three functionals, the U_{eff} parameters are kept fixed to the values optimized with the PBESol functional (see next section) even if it is important to keep in mind that optimal values of the U_{eff} parameters had to be selected independently for every functional.
2. The SCAN functional, which is a META-GGA approximation, requires more computational

Table A.1 – Pseudo-cubic lattice parameter a, total and atomic spin magnetic moments M, and spin-dependent band gaps E_g calculated for the bulk $CoFe_2O_4$ oxide with different exchange-correlation functionals. The values of U_{Co} and U_{Fe} are 4.0 eV and 4.0 eV, respectively. The reported experimental values of the lattice parameters and the band gap are given in the last row.

Functional	a	M (μ_B)				E_g (eV)	
	(Å)	Total (per f.u.)	Co	Fe(Oh)	Fe(Td)	Maj.	Min.
LDA+U	8.226	3	2.55	3.96	-3.80	1.76	0.73
PBE+U	8.443	3	2.63	4.06	-3.94	2.03	1.34
PBEsol+U	8.331	3	2.60	4.03	-3.90	1.98	1.08
SCAN+U	8.334	3	2.73	4.15	-4.08	2.81	0.33
HSE06	8.350	3	2.62	4.10	-3.96	3.37	1.93
Experimental	8.396 [60]					1.17 [64], 1.31 [65]	

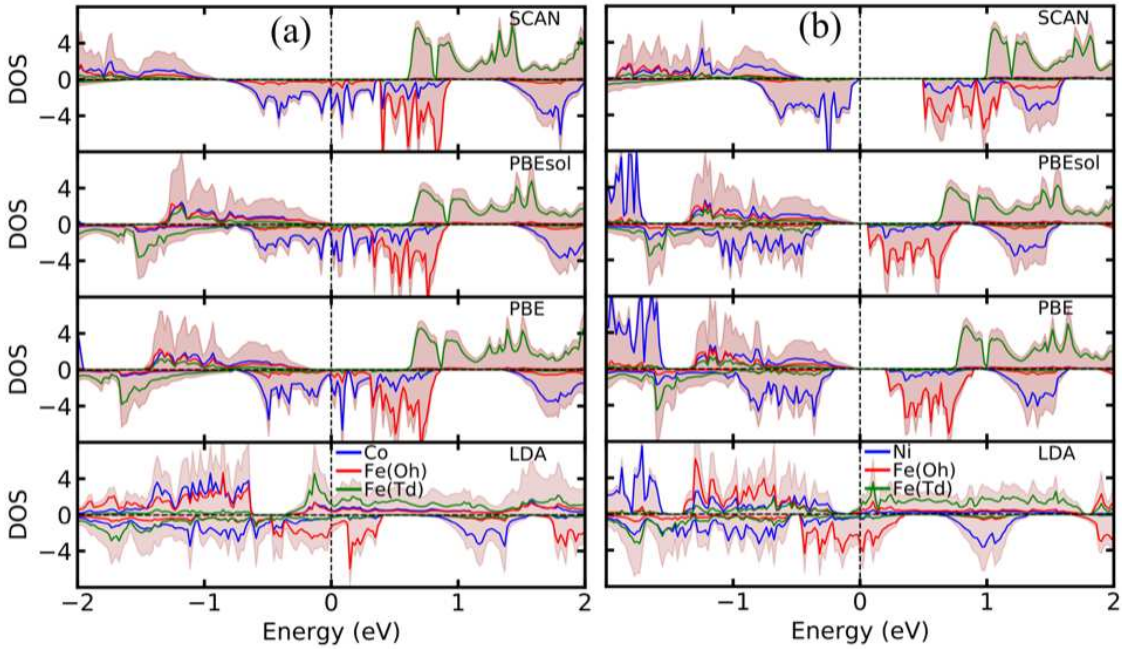

Figure A.1 – Densities of states of (a) $CoFe_2O_4$ and (b) $NiFe_2O_4$ (space group $P4_122$), calculated with different exchange-correlation functionals and without the $+U$ correction. For all the functionals, CFO is found conducting, while NFO is insulating for all the functionals (except the LDA), but displaying a low band-gap energy.

time and is more difficult to converge, while the hybrid HSE06 functional is even much more demanding in terms of resources. Independently of their accuracy, these two functionals are thus difficult to use for large-scale systems or for a large number of systems; the results obtained on perfect structures with these functionals are thus given for information only. We must also precise that every calculation has been performed using the primitive $P4_122$ cell with 4 formula units of MFe_2O_4, unless the hybrid-functional calculations which, in

Table A.2 – Pseudo-cubic lattice parameter a, total and atomic spin magnetic moments M, and spin-dependent band gaps E_g calculated for the bulk $NiFe_2O_4$ oxide with different exchange-correlation functionals. The values of U_{Ni} and U_{Fe} are 2.5 eV and 4.0 eV, respectively. The reported experimental values of the lattice parameters and the band gap are given in the last row.

Functional	a	M (μ_B)				E_g (eV)	
	(Å)	Total (per f.u.)	Ni	Fe(Oh)	Fe(Td)	Maj.	Min.
LDA+U	8.180	2.00	1.48	3.97	−3.78	1.60	1.48
PBE+U	8.396	2.00	1.57	4.06	−3.92	1.91	1.86
PBEsol+U	8.283	2.00	1.54	4.04	−3.88	1.84	1.73
SCAN+U	8.310	2.00	1.57	4.19	−4.07	2.56	1.92
HSE06	8.310	2.00	1.66	4.10	−3.96	3.47	3.01
Experimental	8.339 [67]					1.64 [68], 1.52 [65]	

Table A.3 – In-plane and out-of-plane lattice parameters a and c, and band gap energy E_g around the Fermi level calculated for the tetragonal bulk $BaTiO_3$ with different exchange-correlation functionals. The reported experimental values of the lattice parameters and the band gap are given in the last row.

Functional	a (Å)	c (Å)	c/a	E_g (eV)
LDA	3.942	3.988	1.012	1.75
PBE	3.996	4.218	1.056	1.77
PBEsol	3.967	4.065	1.025	1.76
SCAN	3.983	4.084	1.025	2.15
HSE06	3.958	4.156	1.050	3.32
Experimental	3.996 [44]	4.028 [44]	1.008	3.18 [44]

order to gain time, have been performed with the *Imma* primitive cell of 2 formula units.

A.1.1 Lattice parameters

The LDA+U approximation is the one which gives the lowest accuracy with an underestimation of the lattice parameter according to the experimental values by 1.91% and 2.02% for $NiFe_2O_4$ and $CoFe_2O_4$, respectively. If this approximation also underestimates the lattice parameters of $BaTiO_3$, it nonetheless gives the best c/a ratio. The PBE functional gives rather good in-plane lattice parameters for $BaTiO_3$ but it overestimates the c/a ratio, which might be a problem for the study of the interfaces. The PBESol(+U) functional thus seems to give results that are good compromises for the calculations of the three materials with lattice parameters which are only 0.67% and 0.77% lower than the experimental parameters of $NiFe_2O_4$ and $CoFe_2O_4$, and a c/a

ratio for $BaTiO_3$ overestimated only by 1.69%.

Regarding the SCAN and HSEO6 functionals, the calculated lattice parameters are close to the experimental value with an error of only 0.34% (same for both SCAN and HSEO6 functionals) for $NiFe_2O_4$ and 0.74% (SCAN) and 0.55% (HSE06) for $CoFe_2O_4$.

A.1.2 Electronic structure

To compare the accuracy with which the electronic structure is calculated, the reader can refer to the band gaps given in Tables A.1, A.2 and A.3 and to the (projected) densities of states (DOS) of Figs. A.2, A.3 and A.4.

Considering first the calculations performed on $BaTiO_3$, for which no +U correction is used, we can see that the band-gap energy E_g at the Fermi level is underestimated by approximately 50% when compared with the experimental value. This problem is common with DFT calculations. The band gap is slightly increased using the SCAN functional, and it reaches a value very close from the experiment with the HSE06 hybrid functional.

Regarding $CoFe_2O_4$ and $NiFe_2O_4$, the band gap energies the closest from the experimental values are obtained with the PBE+U (1.34 eV) and PBESol+U (1.73 eV) functionals, respectively.

If we consider the relative energies of the different sets of bands, we also have to mention some discrepancy between the different functionals. In particular, the SCAN+U functional appears to be an exception. In the case of $CoFe_2O_4$, the spin-dependent band gap is delimited by the Co-3d valence bands and Fe(Oh)-3d conduction bands in the minority-spin channel for every functional, while it is delimited by Co-3d bands only with the SCAN+U approximation, with a small band gap of only 0.33 eV. For $NiFe_2O_4$, the valence band maximum consists in majority-spin Ni-3d+O-2p bands with all the functionals (even the hybrid HSE06), except again with the SCAN+U for which the valence-band maximum is located in the minority-spin channel. For these reasons, we preferred not to refer to this functional for the study of the spinel ferrites.

About the calculations performed on $NiFe_2O_4$, due to our choice of U_{eff}(Ni) = 2.5 eV, we can see that the minority-spin unoccupied bands involving Ni atoms appear at lower energies with all the DFT+U methods (they appear between the unoccupied t_{2g} and e_g bands of the Fe(Oh) atoms) except the HSE06 functional (see Fig. A.4. However, it is also worth to point out that the band gap is strongly overestimated with the hybrid functional, by almost a factor 2 (we calculated a band gap E_g of 3.01 eV with HSE06, which is comparable to the band gap of 2.7 eV reported by Sun, *et al.* [68]). Due to the lack of experimental data to confirm the position of these unoccupied bands, it was difficult to set accurately the value of U_{eff}(Ni).

A.2 Choice of U_{eff} parameters

With the choice of the exchange-correlation functional described in the previous section, we tried to optimize the values of the U_{eff} parameters entering the +U corrections added to the 3d bands of Fe, Co and Ni atoms. This optimization was performed by comparing the calculated

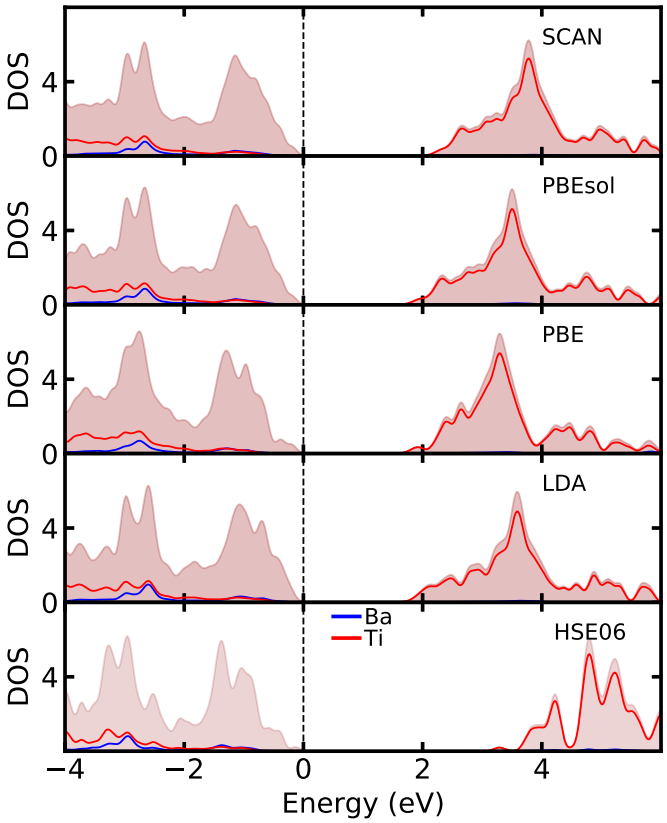

Figure A.2 – Densities of states of the tetragonal $P4mm$ phase of $BaTiO_3$ calculated with different exchange-correlation functionals.

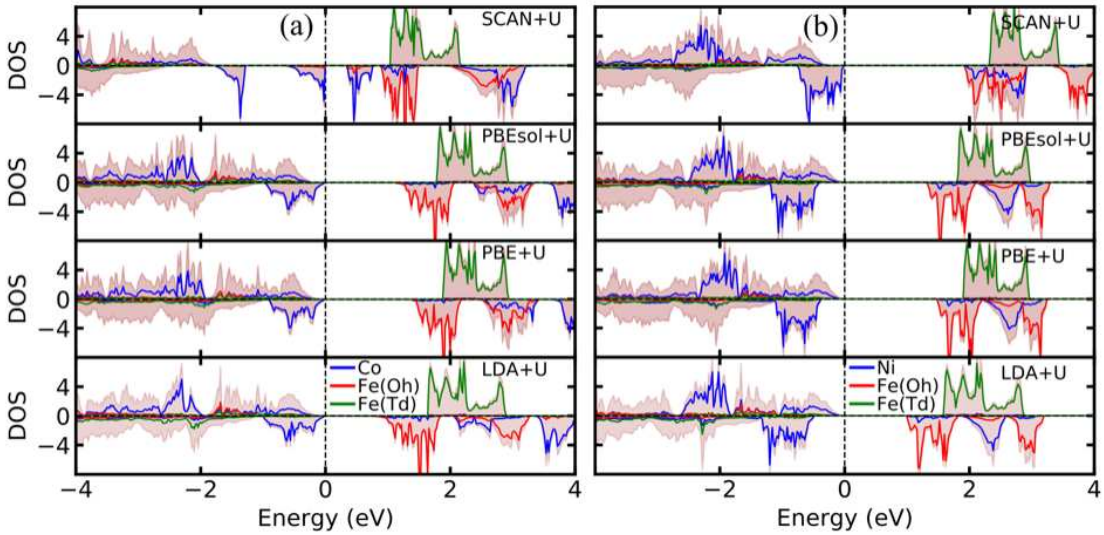

Figure A.3 – Densities of states of (a) $CoFe_2O_4$ and (b) $NiFe_2O_4$ (space group $P4_122$), calculated with different exchange-correlation functionals including a $+U$ correction.

band gaps with the experimental values obtained from the literature, as shown in Fig. A.5. We also decided to keep a constant value for U_{eff}(Fe) to study $CoFe_2O_4$ and $NiFe_2O_4$. Finally we selected the values U_{eff}(Fe) = 4.0 eV, U_{eff}(Co) = 4.0 eV and U_{eff}(Ni) = 2.5 eV.

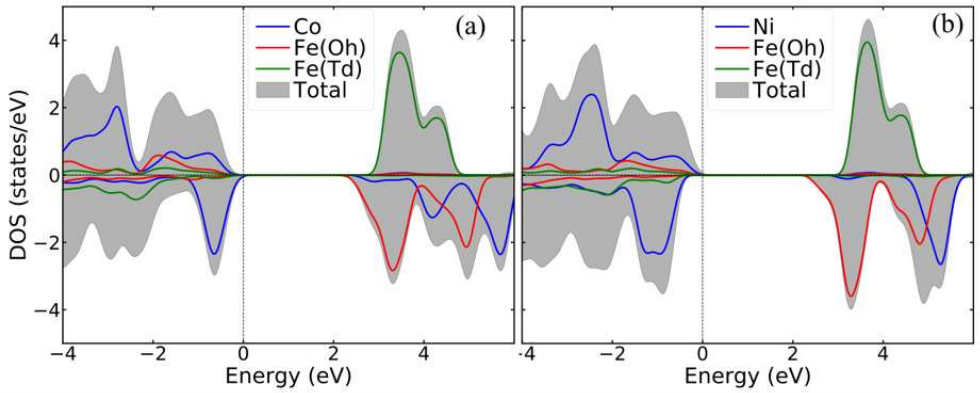

Figure A.4 – Densities of states of (a) $CoFe_2O_4$ and (b) $NiFe_2O_4$ (space group *Imma*) calculated with the HSE06 hybrid functional.

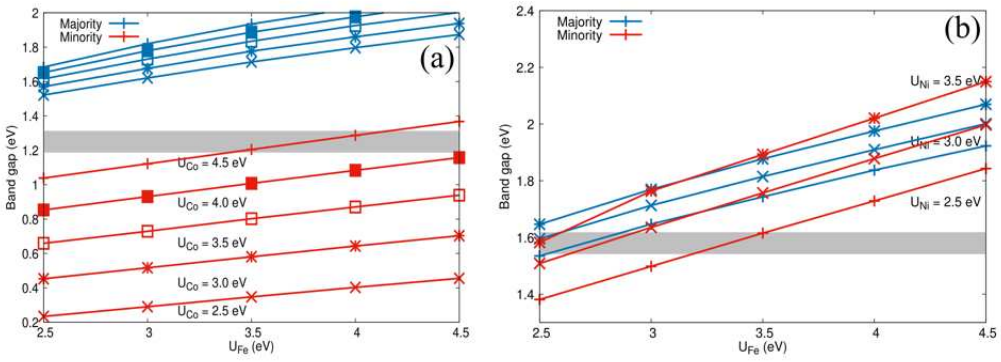

Figure A.5 – Majority and minority-spin band gap energy at the Fermi level of (a) $CoFe_2O_4$ and (b) $NiFe_2O_4$ calculated as a function of U_{eff}(X) (X = Fe, Co, Ni). The range of experimental band gap values is displayed by the gray-color area.

Table A.4 – Majority (Maj.) and Minority (Min.) spin band gap energies of CFO and NFO with different values of U_{eff} for the cations Co, Ni, and Fe.

U_{eff} parameters (eV)			Band gap (eV)		Band gap (eV)	
			CFO		NFO	
Co	Ni	Fe	Maj.	Min.	Maj.	Min.
2.5	2.5	2.5	1.52	0.23	1.53	1.38
2.5	2.5	3.0	1.62	0.29	1.65	1.50
2.5	2.5	3.5	1.71	0.35	1.74	1.62
2.5	**2.5**	**4.0**	1.80	0.40	**1.84**	**1.73**
2.5	2.5	4.5	1.87	0.46	1.92	1.84
3.0	3.0	2.5	1.57	0.45	1.60	1.51
3.0	3.0	3.0	1.68	0.52	1.71	1.64
3.0	3.0	3.5	1.78	0.58	1.81	1.76
3.0	3.0	4.0	1.86	0.64	1.91	1.88
3.0	3.0	4.5	1.94	0.70	2.00	2.00
3.5	3.5	2.5	1.62	0.66	1.65	1.58
3.5	3.5	3.0	1.73	0.73	1.77	1.76
3.5	3.5	3.5	1.83	0.80	1.88	1.89
3.5	3.5	4.0	1.93	0.87	1.98	2.02
3.5	3.5	4.5	2.00	0.94	2.07	2.15
4.0	4.0	2.5	1.65	0.85	1.69	1.61
4.0	4.0	3.0	1.78	0.93	1.82	1.80
4.0	4.0	3.5	1.89	1.01	1.93	1.98
4.0	4.0	**4.0**	**1.98**	**1.09**	2.03	2.15
4.0	4.0	4.5	2.06	1.16	2.13	2.29
4.5	4.5	2.5	1.68	1.04	1.73	1.61
4.5	4.5	3.0	1.82	1.12	1.86	1.81
4.5	4.5	3.5	1.93	1.20	1.98	2.00
4.5	4.5	4.0	2.03	1.29	2.08	2.19
4.5	4.5	4.5	2.11	1.37	2.18	2.36

Appendix B

Results of cation ordering in stoichiometric spinel ferrites

Table B.1 – Space group, lattice parameters, magnetic moment, band gap and total energy calculated for the different cation ordering at Oh sites of a stoichiometric CFO conventional cell (8 f.u.) with the inverse spinel structure.

Space group		Lattice parameters				Magnetic Moment (M)					Band gap			E
No.	Name	a	b	c	$V^{1/3}$	tot	Co	Fe_{Oh}	Fe_{Td}	O	Maj.	Min.	Funda.	
		(Å)	(Å)	(Å)	(Å)	μ_B	μ_B	μ_B	μ_B	(eV)	(eV)	(eV)	(eV)	(eV)
13	P2/c	8.308	8.338	8.338	8.328	24	2.61	4.03	-3.90	0.06	1.97	1.38	1.38	-388.540
91	$P4_122$	8.303	8.346	8.346	8.331	24	2.60	4.03	-3.90	0.06	1.98	1.09	1.09	-388.421
5	C2	8.331	8.328	8.328	8.329	24	2.61	4.03	-3.90	0.06	1.97	1.31	1.31	-388.419
8	Cm	8.325	8.325	8.330	8.327	24	2.60	4.03	-3.90	0.06	1.99	1.27	1.27	-388.403
1	P1	8.319	8.333	8.329	8.327	24	2.60	4.03	-3.90	0.06	1.94	1.33	1.33	-388.389
4	$P2_1$	8.324	8.329	8.335	8.329	24	2.60	4.03	-3.90	0.06	1.93	1.33	1.33	-388.375
74	Imma	8.319	8.347	8.319	8.329	24	2.60	4.04	-3.90	0.06	1.96	0.85	0.85	-388.375
12	C2/m	8.321	8.333	8.333	8.329	24	2.60	4.03	-3.89	0.06	1.91	1.22	1.22	-388.318
78	$P4_3$	8.325	8.333	8.325	8.328	24	2.60	4.03	-3.89	0.06	1.94	1.27	1.27	-388.277
2	P-1	8.353	8.353	8.353	8.353	24	2.61	4.03	-3.90	0.06	1.93	1.35	1.34	-388.269
35	Cmm2	8.330	8.330	8.330	8.330	24	2.60	4.03	-3.89	0.06	1.92	0.88	0.88	-388.183
28	Pma2	8.315	8.337	8.337	8.329	24	2.60	4.03	-3.89	0.06	1.88	0.75	0.75	-388.149
81	P-4	8.333	8.328	8.333	8.331	24	2.60	4.03	-3.89	0.06	1.85	1.07	1.07	-388.131
3	P2	8.353	8.353	8.353	8.353	24	2.60	4.04	-3.90	0.06	1.82	0.76	0.76	-388.020
11	$P2_1/m$	8.336	8.311	8.336	8.327	24	2.59	4.03	-3.89	0.06	1.81	0.77	0.77	-387.790
20	$C222_1$	8.372	8.239	8.239	8.283	24	2.59	4.02	-3.88	0.06	1.66	1.12	1.09	-387.602
115	P-4m2	8.367	8.367	8.279	8.338	24	2.59	4.04	-3.89	0.06	1.69	0.47	0.47	-387.409

Table B.2 – Space group, lattice parameters, magnetic moment, band gap and total energy calculated for the different cation ordering at Oh sites of a stoichiometric NFO conventional cell (8 f.u.) with the inverse spinel structure.

Space group		Lattice parameters				Magnetic Moment (M)					Band gap			E
No.	Name	a	b	c	$V^{1/3}$	tot	Ni	Fe_{Oh}	Fe_{Td}	O	Maj.	Min.	Funda.	
		(Å)	(Å)	(Å)	(Å)	μ_B	μ_B	μ_B	μ_B	(eV)	(eV)	(eV)	(eV)	(eV)
91	$P4_122$	8.294	8.277	8.277	8.283	16	1.54	4.04	-3.88	0.08	1.83	1.73	1.34	-382.356
13	P2/c	8.275	8.275	8.296	8.282	16	1.54	4.04	-3.88	0.08	1.84	1.58	1.23	-382.281
8	Cm	8.283	8.283	8.286	8.284	16	1.54	4.04	-3.88	0.08	1.83	1.64	1.28	-382.225
74	Imma	8.305	8.240	8.305	8.283	16	1.54	4.04	-3.88	0.08	1.81	1.33	1.01	-382.197
5	C2	8.279	8.286	8.286	8.284	16	1.53	4.04	-3.88	0.08	1.80	1.58	1.25	-382.123
4	$P2_1$	8.291	8.278	8.282	8.284	16	1.53	4.04	-3.88	0.08	1.74	1.46	1.14	-382.118
12	C2/m	8.288	8.282	8.282	8.284	16	1.53	4.04	-3.88	0.08	1.79	1.44	1.14	-382.117
1	P1	8.289	8.280	8.281	8.283	16	1.53	4.04	-3.88	0.08	1.77	1.51	1.17	-382.117
2	P-1	8.281	8.291	8.279	8.284	16	1.53	4.04	-3.88	0.08	1.77	1.51	1.20	-382.099
35	Cmm2	8.295	8.263	8.295	8.284	16	1.53	4.04	-3.88	0.08	1.76	1.21	0.91	-382.068
78	$P4_3$	8.283	8.287	8.283	8.284	16	1.53	4.04	-3.88	0.08	1.74	1.39	1.11	-381.930
28	Pma2	8.274	8.288	8.288	8.284	16	1.53	4.04	-3.88	0.08	1.66	1.13	0.75	-381.907
20	$C222_1$	8.285	8.284	8.284	8.284	16	1.53	4.04	-3.88	0.08	1.74	1.34	1.09	-381.900
81	P-4	8.284	8.287	8.284	8.285	16	1.53	4.04	-3.88	0.08	1.67	1.30	1.05	-381.879
11	$P2_1/m$	8.288	8.277	8.288	8.284	16	1.53	4.04	-3.87	0.08	1.65	1.08	0.74	-381.850
3	P2	8.301	8.268	8.289	8.286	16	1.53	4.04	-3.87	0.08	1.66	1.08	0.85	-381.817
115	P-4m2	8.303	8.303	8.257	8.288	16	1.51	4.04	-3.87	0.08	1.50	0.79	0.57	-381.342

Table B.3 – Space group and its degeneracy for the different cation swapping at Oh sites of inverse spinel ferrite primitive cell of space group 91 (4 f.u.).

No. of cation swaps	Space group	Degeneracy
0	91 ($P4_122$)	1
1	1 (P1)	8
	13 (P2/c)	4
	28 (Pma2)	4
2	115 (P-4m2)	4
	1 (P1)	8
	11 (P21/m)	8
	15 (C2/c)	4
	1 (P1)	8
	74 (Imma)	2
	91 ($P4_122$)	2
3	1 (P1)	8
	13 (P2/c)	4
	28 (Pma2)	4
4	91 ($P4_122$)	1
Total structures		70

Table B.4 – Space group, Lattice parameters, magnetic moment, band gap and total energy calculated for the different cation swapping at Oh sites of CFO primitive cell with space group 91.

Space group	Lattice parameters				Magnetic Moment (M)					Band gap			E
	a	b	c	$V^{1/3}$	tot	Co	Fe_{Oh}	Fe_{Td}	O	Maj.	Min.	Funda.	
	(Å)	(Å)	(Å)	(Å)	μ_B	μ_B	μ_B	μ_B	(eV)	(eV)	(eV)	(eV)	(eV)
1 swap													
P1	8.312	8.344	8.334	8.330	12	2.60	4.03	-3.89	0.06	1.80	0.89	0.89	-193.885
Pma2	8.335	8.340	8.317	8.331	12	2.60	4.03	-3.89	0.06	1.87	0.75	0.75	-194.072
P2/c	8.341	8.338	8.305	8.328	12	2.61	4.03	-3.90	0.06	1.97	1.38	1.38	-194.267
2 swaps													
P-4m2	8.333	8.333	8.338	8.335	12	2.59	4.03	-3.89	0.06	1.63	0.55	0.55	-193.740
P1	8.338	8.353	8.296	8.329	12	2.60	4.03	-3.89	0.06	1.81	0.88	0.88	-194.008
$P2_1/m$	8.342	8.324	8.326	8.331	12	2.60	4.03	-3.89	0.06	1.82	0.81	0.81	-194.014
C2/c	8.335	8.335	8.318	8.329	12	2.60	4.04	-3.90	0.06	1.96	0.85	0.85	-194.184
P1	8.312	8.333	8.340	8.329	12	2.60	4.03	-3.89	0.06	1.86	0.95	0.95	-194.136
Imma	8.288	8.350	8.350	8.329	12	2.60	4.04	-3.90	0.06	1.96	0.85	0.85	-194.186
$P4_322$	8.348	8.348	8.300	8.332	12	2.60	4.03	-3.90	0.06	1.98	1.09	1.09	-194.207

Table B.5 – Space group, Lattice parameters, magnetic moment, band gap, and total energy calculated for the different cation swapping at Oh sites of NFO primitive cell with space group 91.

Space group	Lattice parameters				Magnetic Moment (M)					Band gap			E
	a	b	c	$V^{1/3}$	tot	Ni	Fe_{Oh}	Fe_{Td}	O	Maj.	Min.	Funda.	
	(Å)	(Å)	(Å)	(Å)	μ_B	μ_B	μ_B	μ_B	(eV)	(eV)	(eV)	(eV)	(eV)
1 swap													
P1	8.282	8.300	8.270	8.284	8	1.53	4.04	-3.88	0.08	1.74	1.22	0.88	-191.023
Pma2	8.264	8.316	8.270	8.283	8	1.53	4.04	-3.88	0.08	1.67	1.13	0.76	-190.953
P2/c	8.278	8.276	8.296	8.283	8	1.54	4.04	-3.88	0.08	1.84	1.58	1.24	-191.142
2 swaps													
P-4m2	8.305	8.305	8.254	8.288	8	1.51	4.04	-3.87	0.08	1.50	0.79	0.57	-190.670
P1	8.287	8.305	8.268	8.287	8	1.53	4.04	-3.88	0.08	1.74	1.23	0.88	-191.026
$P2_1/m$	8.316	8.263	8.275	8.285	8	1.53	4.04	-3.87	0.08	1.65	1.08	0.74	-190.926
C2/c	8.273	8.273	8.304	8.283	8	1.54	4.04	-3.88	0.08	1.81	1.33	1.01	-191.099
P1	8.282	8.300	8.272	8.285	8	1.53	4.04	-3.88	0.08	1.74	1.22	0.88	-191.024
Imma	8.293	8.321	8.237	8.283	8	1.54	4.04	-3.88	0.08	1.81	1.33	1.01	-191.100
$P4_322$	8.279	8.279	8.291	8.283	8	1.54	4.04	-3.88	0.08	1.84	1.73	1.34	-191.177

Table B.6 – The number of possible structures with different cation ordering in spinel ferrite with different inversion degrees (λ).

Inversion	Conventional unit cell (227)		Primitive unit cell (91)	
degree (λ)	Total structures	Inequivalent structures	Total structures	Inequivalent structures
0	1	1	1	1
0.125	128	2		
0.25	3360	31	16	2
0.375	31360	186		
0.5	127400	762	36	7
0.625	244608	1337		
0.75	224224	1291	16	2
0.875	91520	515		
1	12870	97	1	1
Total	735471	4222	70	13

Table B.7 – The relative stability of CFO with cation inversion with the supercell of 4 f.u.

Inversion degree (λ)	space group	Lattice parameter (Å) a (Å)	b (Å)	c (Å)	$V^{1/3}$ (Å)	Magnetic moment (μ_B)	Band gap Maj. (eV)	Min. (eV)	Funda. (eV)	ΔE_{conf} (per f.u) (eV)
0	$I4_1/amd$	8.385	8.385	8.383	8.385	28	2.49	1.23	0.29	0.000
0.25(near)	Pm	8.365	8.385	8.363	8.371	24	1.31	1.01	0.37	-0.025
0.25(far)	Pm	8.362	8.374	8.375	8.371	24	1.15	0.93	0.23	-0.010
0.5	P1	8.360	8.368	8.344	8.357	20	1.32	1.05	0.46	-0.074
0.5	C2	8.360	8.360	8.347	8.356	20	1.07	0.78	0.30	-0.025
0.5	P1	8.354	8.358	8.366	8.359	20	1.02	0.84	0.16	-0.035
0.5	C2	8.383	8.383	8.315	8.360	20	0.99	0.95	0.20	0.077
0.5	P2/m	8.342	8.374	8.358	8.358	20	1.17	1.11	0.35	-0.082
0.5	$Pmn2_1$	8.344	8.372	8.348	8.354	20	1.22	1.16	0.50	-0.062
0.5	Pma2	8.345	8.374	8.353	8.357	20	1.16	1.10	0.33	-0.073
0.75(near)	P1	8.345	8.357	8.327	8.343	16	1.34	1.12	0.69	-0.125
0.75(far)	P1	8.341	8.358	8.332	8.344	16	1.22	0.81	0.42	-0.102
1	$P4_122$	8.345	8.345	8.304	8.332	12	1.98	1.09	1.09	-0.192

Table B.8 – The relative stability of NFO with cation inversion in the supercell with 4 f.u.

Inversion degree (λ)	space group	Lattice parameter (Å) a (Å)	b (Å)	c (Å)	$V^{1/3}$ (Å)	Magnetic moment (μ_B)	Band gap Maj. (eV)	Min. (eV)	Funda. (eV)	ΔE_{conf} (per f.u) (eV)
0	$I4_1/amd$	8.434	8.434	8.144	8.336	31.43	0.00	0.87	0.00	0.000
0.25	Pm	8.278	8.293	8.452	8.340	26	1.02	1.19	0.45	-0.493
0.25	Pm	8.226	8.284	8.488	8.332	26	0.84	1.01	0.17	-0.443
0.5	P1	8.290	8.315	8.369	8.324	20	1.04	1.28	0.55	-0.718
0.5	C2	8.296	8.296	8.373	8.321	20	1.07	1.07	0.33	-0.685
0.5	P1	8.288	8.295	8.394	8.325	20	0.93	0.99	0.21	-0.676
0.5	C2	8.296	8.296	8.348	8.313	20	0.65	1.04	0.07	-0.662
0.5	P2/m	8.277	8.319	8.380	8.325	20	0.86	1.44	0.52	-0.726
0.5	$Pmn2_1$	8.293	8.328	8.341	8.321	20	1.07	1.46	0.59	-0.726
0.5	Pma2	8.282	8.468	8.218	8.322	20	0.66	1.28	0.20	-0.698
0.75	P1	8.285	8.305	8.320	8.303	14	1.11	1.40	0.62	-0.958
0.75	P1	8.264	8.302	8.343	8.303	14	1.22	1.18	0.49	-0.937
1	$P4_122$	8.280	8.280	8.293	8.284	8	1.84	1.73	1.34	-1.211

Table B.9 – The relative stability of CFO and NFO with cation inversion in the supercell of 8 f.u.

Inversion degree (λ)	space group	Lattice parameter (Å) a (Å)	b (Å)	c (Å)	$V^{1/3}$ (Å)	Magnetic moment (μ_B)	Band gap Maj. (eV)	Min. (eV)	Funda. (eV)	ΔE_{conf} (per f.u) (eV)
					$CoFe_2O_4$					
0.125	Cm	8.376	8.379	8.376	8.377	52	1.35	0.96	0.30	-0.009
0.125	R3m	8.378	8.378	8.378	8.378	52	1.27	0.91	0.36	0.016
0.875	P1	8.339	8.344	8.325	8.336	28	1.58	1.41	1.10	-0.165
0.875	P1	8.341	8.335	8.344	8.340	28	1.48	1.16	0.91	-0.114
					$NiFe_2O_4$					
0.125	Cm	8.275	8.503	8.275	8.350	58	1.10	1.10	0.43	-0.427
0.125	R3m	8.357	8.357	8.357	8.357	58	0.90	1.15	0.36	-0.395
0.875	P1	8.294	8.286	8.301	8.294	22	1.22	1.51	0.80	-1.119
0.875	P1	8.304	8.260	8.308	8.291	22	1.20	1.48	0.72	-1.111

Appendix C

Study of vacancy defect

Table C.1 – Lattice parameters, total magnetic moment, and total energy (E) calculated for the vacancy defect in CFO. All results are given per conventional cell (of 8 formula units). Calculations have been made starting from a cation distribution in the perfect crystal corresponding to the 91-$P4_122$ space group.

Vacancy	q	space	Lattice parameters				M_{tot}	Band gap			E
		group	a	b	c	$V^{1/3}$		Maj.	Min.	Funda.	
			(Å)	(Å)	(Å)	(Å)	μ_B	(eV)	(eV)	(eV)	(eV)
No vacancy		$P4_122$	8.345	8.345	8.304	8.332	24	1.98	1.09	1.09	-388.421
Co	0	C2	8.300	8.316	8.316	8.311	23	2.04	0.83	0.83	-381.026
Co	-1	C2	8.347	8.380	8.38	8.369	22	1.94	0.57	0.57	-374.485
Co	-2	C2	8.394	8.443	8.443	8.427	21	1.94	1.43	1.43	-368.276
Fe(Oh)	0	C2	8.274	8.320	8.32	8.305	22	2.05	0.01	0.01	-377.995
Fe(Oh)	-1	C2	8.341	8.372	8.372	8.362	21	2.01	1.00	1.00	-371.735
Fe(Oh)	-2	C2	8.407	8.427	8.427	8.420	20	1.97	0.00	0.00	-365.205
Fe(Oh)	-3	C2	8.474	8.486	8.486	8.482	19	1.86	1.31	1.31	-359.339
Fe(Td)	0	P2	8.300	8.348	8.337	8.328	32	1.91	0.55	0.55	-376.868
Fe(Td)	-1	P1	8.380	8.376	8.414	8.390	31	1.80	0.90	0.90	-370.522
Fe(Td)	-2	P1	8.424	8.459	8.481	8.455	30	1.64	0.91	0.80	-364.404
Fe(Td)	-3	P2	8.503	8.528	8.526	8.519	29	1.64	1.40	1.38	-358.511
O1	0	P1	8.313	8.339	8.339	8.330	24	1.40	1.19	1.06	-379.177
O1	1	P1	8.283	8.297	8.303	8.294	25	1.49	1.11	0.70	-386.51
O1	2	P1	8.216	8.258	8.256	8.243	24	1.16	1.22	1.16	-393.936
O2	0	P1	8.317	8.330	8.329	8.325	24	1.40	1.19	1.06	-379.198
O2	1	P1	8.282	8.295	8.299	8.292	25	1.54	1.14	0.76	-386.584
O2	2	P1	8.228	8.231	8.245	8.235	24	0.76	0.83	0.76	-393.876

Table C.2 – Lattice parameters, total magnetic moment, and total energy (E) calculated for the vacancy defect in NFO. All results are given per conventional cell (of 8 formula units). Calculations have been made starting from a cation distribution in the perfect crystal corresponding to the 91-$P4_122$ space group.

Vacancy	q	space	Lattice parameters				M_{tot}	Band gap			E
		group	a	b	c	$V^{1/3}$		Maj.	Min.	Funda.	
			(Å)	(Å)	(Å)	(Å)	μ_B	(eV)	(eV)	(eV)	(eV)
No vacancy		$P4_122$	8.280	8.280	8.293	8.284	16	1.84	1.73	1.34	-382.357
Ni	0	C2	8.336	8.231	8.231	8.265	12	0.00	1.51	0.00	-375.018
Ni	-1	C2	8.381	8.296	8.296	8.324	13	0.34	1.32	0.34	-369.239
Ni	-2	C2	8.385	8.379	8.379	8.381	14	1.81	1.69	1.42	-363.536
Fe(Oh)	0	C2	8.237	8.252	8.252	8.247	8	0.00	1.40	0.00	-370.803
Fe(Oh)	-1	C2	8.286	8.310	8.310	8.302	9	0.27	1.24	0.27	-365.053
Fe(Oh)	-2	C2	8.374	8.362	8.362	8.366	10	0.00	1.35	0.00	-359.370
Fe(Oh)	-3	C2	8.436	8.421	8.421	8.426	11	1.66	1.24	1.24	-354.069
Fe(Td)	0	P1	8.294	8.278	8.236	8.269	18	0.00	1.55	0.00	-370.521
Fe(Td)	-1	P2	8.363	8.332	8.305	8.333	19	0.37	1.43	0.37	-364.744
Fe(Td)	-2	P1	8.406	8.395	8.381	8.394	20	0.00	1.67	0.00	-358.925
Fe(Td)	-3	P2	8.468	8.467	8.450	8.462	21	1.46	1.51	1.15	-353.560
O1	0	P1	8.300	8.286	8.280	8.289	16	1.40	1.11	0.92	-373.056
O1	1	P1	8.240	8.229	8.202	8.224	15	0.79	1.28	0.79	-379.804
O1	2	P1	8.218	8.183	8.203	8.201	16	1.00	1.17	0.75	-386.698
O2	0	P1	8.293	8.279	8.277	8.283	16	1.39	1.21	0.97	-373.172
O2	1	P1	8.230	8.225	8.200	8.218	15	0.79	1.47	0.79	-379.981
O2	2	P1	8.216	8.188	8.191	8.198	16	0.94	0.92	0.49	-386.656

Table C.3 – Fermi levels, Electrons (n), and holes (p) carrier concentrations with the corresponding cation and oxygen vacancy concentrations of (a) CFO and (b) NFO. The calculations have been performed for a growth temperature T_g = 673 K and a measurement temperature T_R = 298 K.

		(a) $CoFe_2O_4$				(b) $NiFe_2O_4$			
Vacancy	q	Concentration (cm^{-3})				Concentration (cm^{-3})			
		Oxygen-rich		Oxygen-poor		Oxygen-rich		Oxygen-poor	
		673 K	298 K	673 K	298 K	673 K	298 K	673 K	298 K
n		1.2E+15	3.2E+05	1.2E+16	2.6E+10	2.6E+15	9.1E+02	2.8E+15	4.0E+08
p		1.1E+17	2.0E+15	1.2E+16	2.5E+10	3.0E+15	1.8E+14	2.8E+15	4.0E+08
Co/Ni	-2	3.3E+16	9.7E+11	3.1E+03	3.5E+03	1.6E+14	5.2E+11	3.7E+00	4.0E+00
Co/Ni	-1	4.8E+16	2.0E+15	4.5E+02	7.9E+01	1.4E+13	1.8E+14	3.1E-01	2.6E-03
Co/Ni	0	1.3E+16	9.2E+16	1.2E+01	3.9E-02	7.9E+08	3.3E+09	1.6E-05	9.6E-14
$Fe(O_h)$	-3	3.0E+05	3.5E-11	1.8E-10	1.8E-18	1.4E+04	2.8E-09	2.2E-15	7.2E-17
$Fe(O_h)$	-2	3.9E+09	6.4E+01	2.3E-07	3.5E-11	1.1E+06	3.9E+00	1.6E-13	2.0E-13
$Fe(O_h)$	-1	2.8E+13	2.8E+13	1.7E-04	1.7E-04	3.6E+06	4.7E+06	5.0E-13	4.6E-13
$Fe(O_h)$	0	9.9E+09	3.9E+08	6.0E-09	2.6E-14	2.7E+02	1.8E+02	3.5E-17	3.5E-23
$Fe(T_d)$	-3	6.0E-05	5.3E-20	3.6E-20	3.7E-27	8.6E-04	1.5E-21	1.3E-22	5.5E-29
$Fe(T_d)$	-2	1.0E+01	3.0E-05	6.1E-16	2.2E-17	1.1E+01	2.3E-07	1.6E-18	1.6E-20
$Fe(T_d)$	-1	9.9E+02	7.9E+02	5.8E-15	6.4E-15	1.8E+03	1.8E+03	2.5E-16	2.5E-16
$Fe(T_d)$	0	2.9E+01	2.4E+02	1.8E-17	2.3E-20	2.0E+00	2.9E+01	2.5E-19	7.8E-24
O	2	1.8E-09	1.8E-12	1.4E+02	2.3E-09	4.3E-12	7.5E-14	2.8E+01	2.2E-12
O	1	2.3E-03	2.3E-02	1.7E+09	5.4E+06	1.1E-05	2.1E-05	7.7E+07	3.1E+02
O	0	3.8E-02	1.8E-02	2.8E+11	2.9E+11	4.9E-02	4.9E-02	3.6E+11	3.6E+11
Fermi level (eV):		0.438	0.266	0.570	0.556	0.588	0.301	0.591	0.635

Appendix D

Surface properties calculated with a stoichiometric and asymmetric polar $NiFe_2O_4(001)$ slab

In this appendix, we will describe the electronic structure calculated using a polar NFO slab possessing two non-equivalent surfaces with different atomic terminations, to make a comparison with the results obtained with symmetric slabs and presented in Chapter 5. As shown in Fig. D.1, this slab has a surface with a perfect A termination, consisting in a layer with 2Fe(Td) atoms and a surface with a perfect B, *i.e.* terminated by a 2[$NiFeO_4$] atomic layer. (S_B-0) and (S_A-0) denote the surface layers having B-termination and A-termination, respectively. The two surfaces are still separated by a vacuum layer of at least 15 Å. Moreover, to avoid any spurious interaction between these two surfaces and the appearance of an electric field in the vacuum region, we applied a dipolar correction [262] along the [001] direction.

Because the slab is asymmetric and the structure is polar along the [001] direction, with a succession of atomic planes carrying alternatively 6+/6− charges (for two formula units of $NiFe_2O_4$), we expect a polar catastrophe and a transfer of electrons from the B-terminated surface to the A-terminated surface. This is indeed what we observe in Fig. D.2, which shows the LDOS of the successive bilayers (see labeling in Fig. D.1). The defect states corresponding to changes in the oxidation states of the surface cations Fe(Oh) and Fe(Td) are shown with colored rectangles in the DOS curves of the bi-layers (BL-0) and (BL-5). The self-consistent calculation shows that an electronic reconstruction occurs and Fe^{3+} cations at the surface layer (S_A-0) change their oxidation state and become Fe^{2+} cations. At the surface layer (S_B-0), Fe^{3+} cations change their oxidation state and become Fe^{4+} cations. The electronic charges of the atomic layers after the electronic reconstruction are summarized in Fig. D.1.

Fig. D.3 shows the spin magnetic moment of the cations in the different layers of the asymmetric slab after the electronic reconstruction has occurred. The calculated variations of spin magnetic

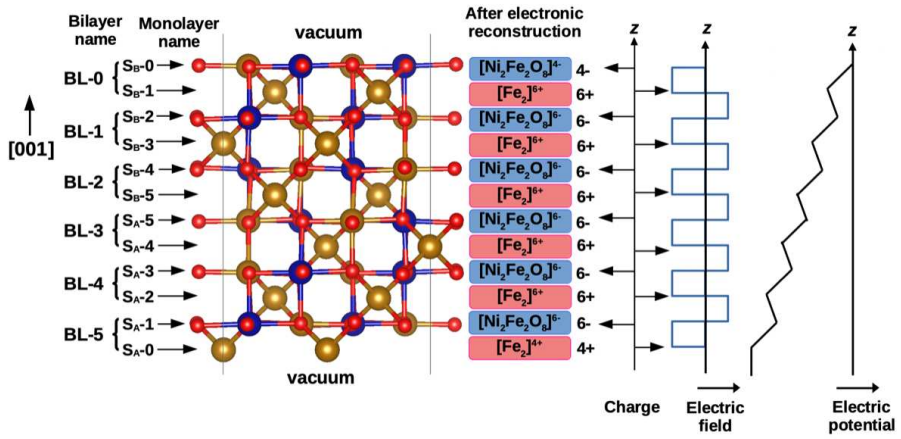

Figure D.1 – The charges on each layer of the AB-terminated NFO(001) slab. The electric field and the electric potential between the layers are also shown. It shows that the net electric field is finite in the slab. The labeling of the layers indicates the surface terminations: A-terminated (S_A) or B-terminated (S_B) surfaces. The labeling of successive bilayers (BL-0 to BL-5) is also shown by adding two consecutive A and B layers. This notation will be used to describe the DOS of the bilayers. This figure is only valid if each layer of the slab is an infinite 2D layer and the distance between the layers is fixed.

moment of cations at the surface are in good agreement with the changes observed in the surface LDOS and the changes of oxidation degrees written previously. We thus see a decrease of the magnetic moment of Fe(Oh) cations from 4.04 μ_B to 3.47 μ_B at the B surface due to the transfer of one electron per Fe atom and an increase from −3.88 μ_B to −3.42 μ_B of the spin magnetic moments of the two Fe(Td) of the S_A-0 layer because of the transfer of holes to this surface layer.

By comparing the results obtained with two symmetric slabs (Chapter 5) and with an asymmetric slab (this appendix), we can see that the charge reconstructions at the A- and B-terminated surfaces are different. While with the symmetric slabs, we calculated surface charges of $\sigma_S = \pm 3$ e, here, the charge transfer between the two surfaces only involve two electrons and the oxidation state of Ni atoms does not change. If we cannot explain precisely this discrepancy, we can however make the hypothesis that, for the asymmetric slab, the chosen thickness is maybe too thin. Indeed, we can observe in Fig. D.2 a positive shift in energy of the different LDOS when going from the A-terminated (BL-5) to the B-terminated (BL-0) surface. This shift is characteristics of the presence of a non-zero internal electric field 0.07 eV/Å, which tends to prove that the electronic reconstruction calculated with this slab thickness is not complete, which might, at least partially, explain the different results.

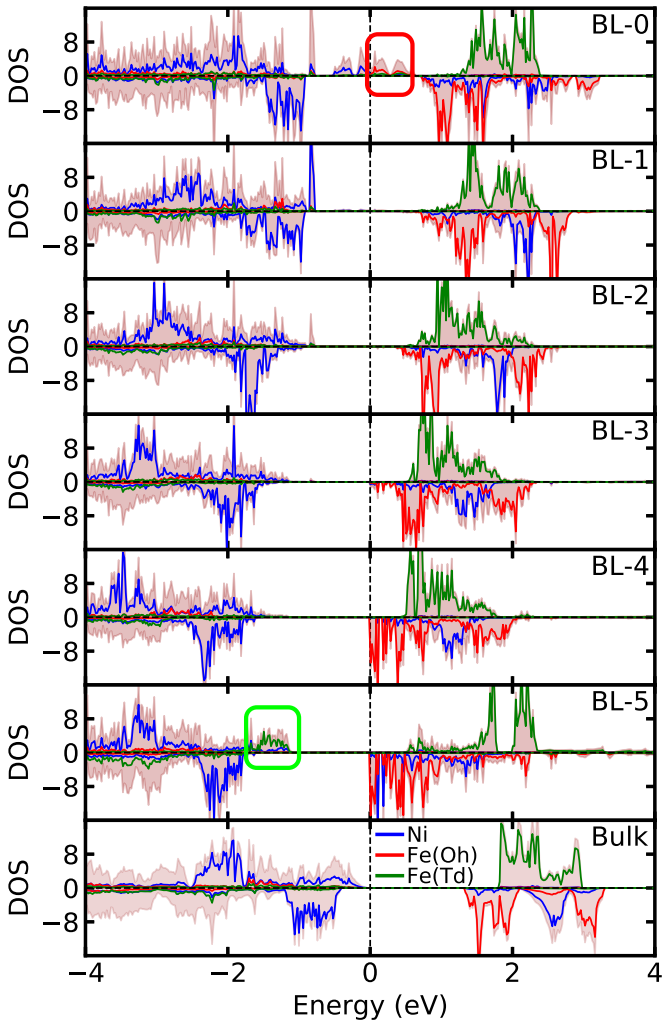

Figure D.2 – DOS of the successive bilayers (A+B) of the polar AB-terminated NFO slab. (BL-0) has a B-terminated surface and (BL-5) has an A-terminated surface. The defect states are shown by colored rectangles: red for defect states involving Fe(Oh) and green for defect states involving Fe(Td) cations.

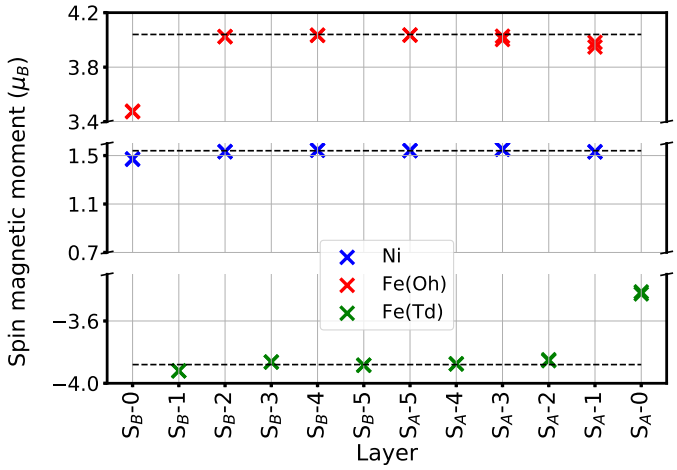

Figure D.3 – The atomic spin magnetic moment of cations in the different layers of the AB-terminated slab. S_B and S_A denote the surface layer having the B-termination and the A-termination at the surface layer, respectively. The black dashed lines represent the spin magnetic moment of cations in bulk NFO.

Bibliography

[1] Moore, G. E. Gramming more components onto integrated circuits. *Electronics* **1965**, *38*, 8.

[2] Moore, G. Cramming More Components Onto Integrated Circuits. *Proceedings of the IEEE* **1998**, *86*, 82–85.

[3] Mollick, E. Establishing Moore's Law. *IEEE Annals of the History of Computing* **2006**, *28*, 62–75.

[4] ITRS Reports, International Technology Roadmap for Semiconductors http://www.itrs2.net/itrs-reports.html.

[5] Liu, X.; Lam, K.; Zhu, K.; Zheng, C.; Li, X.; Du, Y.; Liu, C.; Pong, P. W. Overview of spintronic sensors with internet of things for smart living. *IEEE Transactions on Magnetics* **2019**, *55*, 1–22.

[6] Burg, D.; Ausubel, J. H. Moore's Law revisited through Intel chip density. *PloS one* **2021**, *16*, 1–18.

[7] Samsung Begins Chip Production Using 3nm Process Technology With GAA Architecture https://news.samsung.com/global/samsung-begins-chip-production-using-3nm-process-technology-with-gaa-architecture.

[8] Meindl, J. D.; Chen, Q.; Davis, J. A. Limits on silicon nanoelectronics for terascale integration. *Science* **2001**, *293*, 2044–2049.

[9] Zhirnov, V. V.; Cavin, R. K. Negative capacitance to the rescue? *Nature Nanotechnology* **2008**, *3*, 77–78.

[10] Chien, A. A.; Karamcheti, V. Moore's Law: The First Ending and a New Beginning. *Computer* **2013**, *46*, 48–53.

[11] Waldrop, M. M. The chips are down for Moore's law. *Nature News* **2016**, *530*, 144–147.

[12] Ielmini, D.; Wong, H.-S. P. In-memory computing with resistive switching devices. *Nature electronics* **2018**, *1*, 333–343.

[13] Pan, F.; Gao, S.; Chen, C.; Song, C.; Zeng, F. Recent progress in resistive random access memories: Materials, switching mechanisms, and performance. *Materials Science and Engineering: R: Reports* **2014**, *83*, 1–59.

[14] Chen, A. A review of emerging non-volatile memory (NVM) technologies and applications. *Solid-State Electronics* **2016**, *125*, 25–38.

[15] Banerjee, W. Challenges and applications of emerging nonvolatile memory devices. *Electronics* **2020**, *9*, 1029.

[16] Ho, C.; Hsu, C.-L.; Chen, C.-C.; Liu, J.-T.; Wu, C.-S.; Huang, C.-C.; Hu, C.; Yang, F.-L. In *2010 International Electron Devices Meeting*, 2010, pp 19.1.1–19.1.4.

[17] Torrezan, A. C.; Strachan, J. P.; Medeiros-Ribeiro, G.; Williams, R. S. Sub-nanosecond switching of a tantalum oxide memristor. *Nanotechnology* **2011**, *22*, 485203.

[18] Choi, B. J.; Torrezan, A. C.; Norris, K. J.; Miao, F.; Strachan, J. P.; Zhang, M.-X.; Ohlberg, D. A.; Kobayashi, N. P.; Yang, J. J.; Williams, R. S. Electrical performance and scalability of Pt dispersed SiO_2 nanometallic resistance switch. *Nano letters* **2013**, *13*, 3213–3217.

[19] Cheng, C.-H.; Tsai, C.-Y.; Chin, A.; Yeh, F. In *2010 International Electron Devices Meeting*, 2010, pp 19.4.1–19.4.4.

[20] Trassin, M. Low energy consumption spintronics using multiferroic heterostructures. *Journal of Physics: Condensed Matter* **2015**, *28*, 033001.

[21] Andrae, A. S. G.; Edler, T. On Global Electricity Usage of Communication Technology: Trends to 2030. *Challenges* **2015**, *6*, 117–157.

[22] Forti, V.; Balde, C. P.; Kuehr, R.; Bel, G. The Global E-waste Monitor 2020: Quantities, flows and the circular economy potential. **2020**.

[23] Shreyas Madhav, A.; Rajaraman, R.; Harini, S.; Kiliroor, C. C. Application of artificial intelligence to enhance collection of E-waste: A potential solution for household WEEE collection and segregation in India. *Waste Management & Research* **2022**, *40*, 1047–1053.

[24] Bachelet, R.; De Coux, P.; Warot-Fonrose, B.; Skumryev, V.; Niu, G.; Vilquin, B.; Saint-Girons, G.; Sanchez, F. Functional spinel oxide heterostructures on silicon. *CrystEngComm* **2014**, *16*, 10741–10745.

[25] Wilson, J. Systematics of the breakdown of Mott insulation in binary transition metal compounds. *Advances in Physics* **1972**, *21*, 143–198.

[26] Imada, M.; Fujimori, A.; Tokura, Y. Metal-insulator transitions. *Rev. Mod. Phys.* **1998**, *70*, 1039–1263.

[27] Gosteau, J.; Arras, R.; Chen, P.; Zhao, H. J.; Paillard, C.; Bellaiche, L. Spin-orbit effects in ferroelectric $PbTiO_3$ under tensile strain. *Phys. Rev. B* **2021**, *103*, 024416.

[28] Hwang, H. Y.; Iwasa, Y.; Kawasaki, M.; Keimer, B.; Nagaosa, N.; Tokura, Y. Emergent phenomena at oxide interfaces. *Nature materials* **2012**, *11*, 103–113.

[29] Huang, Z.; Ariando; Renshaw Wang, X.; Rusydi, A.; Chen, J.; Yang, H.; Venkatesan, T. Interface Engineering and Emergent Phenomena in Oxide Heterostructures. *Advanced Materials* **2018**, *30*, 1802439.

[30] Ma, J.; Hu, J.; Li, Z.; Nan, C.-W. Recent progress in multiferroic magnetoelectric composites: from bulk to thin films. *Advanced materials* **2011**, *23*, 1062–1087.

[31] Coll, M. et al. Towards Oxide Electronics: a Roadmap. *Applied Surface Science* **2019**, *482*, 1–93.

[32] Palneedi, H.; Park, J. H.; Maurya, D.; Peddigari, M.; Hwang, G.-T.; Annapureddy, V.; Kim, J.-W.; Choi, J.-J.; Hahn, B.-D.; Priya, S.; Lee, K. J.; Ryu, J. Laser Processing of Metal Oxides: Laser Irradiation of Metal Oxide Films and Nanostructures: Applications and Advances (Adv. Mater. 14/2018). *Advanced Materials* **2018**, *30*, 1870094.

[33] Peña, M. A.; Fierro, J. L. G. Chemical Structures and Performance of Perovskite Oxides. *Chemical Reviews* **2001**, *101*, 1981–2018.

[34] Goldschmidt, V. M. Die gesetze der krystallochemie. *Naturwissenschaften* **1926**, *14*, 477–485.

[35] Momma, K.; Izumi, F. VESTA 3 for three-dimensional visualization of crystal, volumetric and morphology data. *Journal of applied crystallography* **2011**, *44*, 1272–1276.

[36] Varignon, J.; Malyi, O. I.; Zunger, A. Dependence of band gaps in d-electron perovskite oxides on magnetism. *Physical Review B* **2022**, *105*, 165111.

[37] Cao, L.; Sozontov, E.; Zegenhagen, J. Cubic to Tetragonal Phase Transition of $SrTiO_3$ under Epitaxial Stress: An X-Ray Backscattering Study. *physica status solidi (a)* **2000**, *181*, 387–404.

[38] Van Benthem, K.; Elsässer, C.; French, R. H. Bulk electronic structure of $SrTiO_3$: Experiment and theory. *Journal of Applied Physics* **2001**, *90*, 6156–6164.

[39] Haeni, J. H. et al. Room-temperature ferroelectricity in strained $SrTiO_3$. *Nature* **2004**, *430*, 758–761.

[40] Xu, R.; Huang, J.; Barnard, E. S.; Hong, S. S.; Singh, P.; Wong, E. K.; Jansen, T.; Harbola, V.; Xiao, J.; Wang, B. Y.; Crossley, S.; Lu, D.; Liu, S.; Hwang, H. Y. Strain-induced room-temperature ferroelectricity in $SrTiO_3$ membranes. *Nature Communications* **2020**, *11*, 3141.

[41] Ohtomo, A.; Hwang, H. Y. Growth mode control of the free carrier density in $SrTiO_{3-\delta}$ films. *Journal of Applied Physics* **2007**, *102*, 083704.

[42] Choi, M.; Oba, F.; Kumagai, Y.; Tanaka, I. Anti-ferrodistortive-Like oxygen-octahedron rotation induced by the oxygen vacancy in cubic $SrTiO_3$. *Advanced Materials* **2013**, *25*, 86–90.

[43] Acosta, M.; Novak, N.; Rojas, V.; Patel, S.; Vaish, R.; Koruza, J.; Rossetti Jr., G. A.; Rödel, J. $BaTiO_3$-based piezoelectrics: Fundamentals, current status, and perspectives. *Applied Physics Reviews* **2017**, *4*, 041305.

[44] Mishra, V.; Sagdeo, A.; Kumar, V.; Warshi, M. K.; Rai, H. M.; Saxena, S. K.; Roy, D. R.; Mishra, V.; Kumar, R.; Sagdeo, P. R. Electronic and optical properties of $BaTiO_3$ across tetragonal to cubic phase transition: An experimental and theoretical investigation. *Journal of Applied Physics* **2017**, *122*, 065105.

[45] Tatarchuk, T.; Bououdina, M.; Judith Vijaya, J.; John Kennedy, L. In *Nanophysics, Nanomaterials, Interface Studies, and Applications*, ed. by Fesenko, O.; Yatsenko, L., Springer International Publishing: Cham, 2017, pp 305–325.

[46] Narang, S. B.; Pubby, K. Nickel Spinel Ferrites: A review. *Journal of Magnetism and Magnetic Materials* **2021**, *519*, 167163.

[47] Demirci Dönmez, Ç. E.; Manna, P. K.; Nickel, R.; Aktürk, S.; van Lierop, J. Comparative Heating Efficiency of Cobalt-, Manganese-, and Nickel-Ferrite Nanoparticles for a Hyperthermia Agent in Biomedicines. *ACS Applied Materials & Interfaces* **2019**, *11*, 6858–6866.

[48] Balakrishnan, P. B.; Silvestri, N.; Fernandez-Cabada, T.; Marinaro, F.; Fernandes, S.; Fiorito, S.; Miscuglio, M.; Serantes, D.; Ruta, S.; Livesey, K.; Hovorka, O.; Chantrell, R.; Pellegrino, T. Exploiting Unique Alignment of Cobalt Ferrite Nanoparticles, Mild Hyperthermia, and Controlled Intrinsic Cobalt Toxicity for Cancer Therapy. *Advanced Materials* **2020**, *32*, 2003712.

[49] Dutta, S.; Akhter, M.; Ahmed, J.; Amin, M.; Dhar, P. Synthesis and catalytic activity of spinel ferrites: A brief review, Biointerface Res. *Appl. Chem* **2021**, *12*, 4399–4416.

[50] Paswan, S. K.; Kumar, P.; Singh, R. K.; Shukla, S. K.; Kumar, L. Spinel ferrite magnetic nanoparticles: an alternative for wastewater treatment. *Pollutants and water management: resources, strategies and scarcity* **2021**, 273–305.

[51] Hajiyani, H.; Pentcheva, R. Surface Termination and Composition Control of Activity of the $Co_xNi_{1-x}Fe_2O_4(001)$ Surface for Water Oxidation: Insights from DFT+ U Calculations. *ACS Catalysis* **2018**, *8*, 11773–11782.

[52] Kharisov, B. I.; Dias, H. R.; Kharissova, O. V. Mini-review: Ferrite nanoparticles in the catalysis. *Arabian Journal of Chemistry* **2019**, *12*, 1234–1246.

[53] Bohra, M.; Alman, V.; Arras, R. Nanostructured $ZnFe_2O_4$: An Exotic Energy Material. *Nanomaterials* **2021**, *11*, 1286.

[54] Taffa, D. H.; Dillert, R.; Ulpe, A. C.; Bauerfeind, K. C. L.; Bredow, T.; Bahnemann, D. W.; Wark, M. Photoelectrochemical and theoretical investigations of spinel type ferrites ($M_xFe_{3-x}O_4$) for water splitting: a mini-review. *Journal of Photonics for Energy* **2016**, *7*, 012009.

[55] Valenzuela, R. Novel Applications of Ferrites. *Physics Research International* **2012**, *2012*, 1–9.

[56] Hirohata, A.; Sukegawa, H.; Yanagihara, H.; Zutic, I.; Seki, T.; Mizukami, S.; Swaminathan, R. Roadmap for Emerging Materials for Spintronic Device Applications. *IEEE Transactions on Magnetics* **2015**, *51*, 1–11.

[57] Yuan, C.; Wu, H. B.; Xie, Y.; Lou, X. W. Mixed transition-metal oxides: design, synthesis, and energy-related applications. *Angewandte Chemie International Edition* **2014**, *53*, 1488–1504.

[58] O'neill, H. S. C.; Annersten, H.; Virgo, D. The temperature dependence of the cation distribution in magnesioferrite ($MgFe_2O_4$) from powder XRD structural refinements and Mössbauer spectroscopy. *American Mineralogist* **1992**, *77*, 725–740.

[59] Hou, Y.; Zuo, F.; Dagg, A.; Feng, P. A three-dimensional branched cobalt-doped α-Fe_2O_3 nanorod/$MgFe_2O_4$ heterojunction array as a flexible photoanode for efficient photoelectrochemical water oxidation. *Angewandte Chemie International Edition* **2013**, *52*, 1248–1252.

[60] Li, Z.; Fisher, E. S.; Liu, J. Z.; Nevitt, M. V. Single-crystal elastic constants of Co-Al and Co-Fe spinels. *Journal of Materials Science* **1991**, *26*, 2621–2624.

[61] Wakihara, M.; Shimizu, Y.; Katsura, T. Preparation and magnetic properties of the FeV_2O_4-Fe_3O_4 system. *Journal of Solid State Chemistry* **1971**, *3*, 478–483.

[62] Greaves, C. A powder neutron diffraction investigation of vacancy ordering and covalence in γ-Fe_2O_3. *Journal of Solid State Chemistry* **1983**, *49*, 325–333.

[63] Litter, M. I.; Blesa, M. A. Photodissolution of iron oxides. IV. A comparative study on the photodissolution of hematite, magnetite, and maghemite in EDTA media. *Canadian Journal of Chemistry* **1992**, *70*, 2502–2510.

[64] Holinsworth, B. S.; Mazumdar, D.; Sims, H.; Sun, Q.-C.; Yurtisigi, M. K.; Sarker, S. K.; Gupta, A.; Butler, W. H.; Musfeldt, J. L. Chemical tuning of the optical band gap in spinel ferrites: $CoFe_2O_4$ vs $NiFe_2O_4$. *Applied Physics Letters* **2013**, *103*, 082406.

[65] Dileep, K.; Loukya, B.; Pachauri, N.; Gupta, A.; Datta, R. Probing optical band gaps at the nanoscale in $NiFe_2O_4$ and $CoFe_2O_4$ epitaxial films by high resolution electron energy loss spectroscopy. *Journal of Applied Physics* **2014**, *116*, 103505.

[66] Caffrey, N. M.; Fritsch, D.; Archer, T.; Sanvito, S.; Ederer, C. Spin-filtering efficiency of ferrimagnetic spinels $CoFe_2O_4$ and $NiFe_2O_4$. *Phys. Rev. B* **2013**, *87*, 024419.

[67] Liebermann, R. C. Pressure and temperature dependence of the elastic properties of polycrystalline trevorite ($NiFe_2O_4$). *Physics of the Earth and Planetary Interiors* **1972**, *6*, 360–365.

[68] Sun, Q. .-. C.; Sims, H.; Mazumdar, D.; Ma, J. X.; Holinsworth, B. S.; O'Neal, K. R.; Kim, G.; Butler, W. H.; Gupta, A.; Musfeldt, J. L. Optical band gap hierarchy in a magnetic oxide: Electronic structure of $NiFe_2O_4$. *Physical Review B* **2012**, *86*, 205106.

[69] Shetty, K.; Renuka, L.; Nagaswarupa, H.; Nagabhushana, H.; Anantharaju, K.; Rangappa, D.; Prashantha, S.; Ashwini, K. A comparative study on $CuFe_2O_4$, $ZnFe_2O_4$ and $NiFe_2O_4$: morphology, impedance and photocatalytic studies. *Materials Today: Proceedings* **2017**, *4*, 11806–11815.

[70] Patil, S.; Otari, S.; Mahajan, V.; Patil, M.; Patil, A.; Soudagar, M.; Patil, B.; Sawant, S. Structural, IR and magnetisation studies on La3+ substituted copper ferrite. *Solid state communications* **1991**, *78*, 39–42.

[71] Naik, A.; Patil, S.; Powar, J. X-ray and magnetization studies on Li-Cu mixed ferrites. *Journal of materials science letters* **1988**, *7*, 1034–1036.

[72] Li, Z.; Fisher, E. Single crystal elastic constants of zinc ferrite ($ZnFe_2O_4$). *Journal of materials science letters* **1990**, *9*, 759–760.

[73] Moussy, J.-B. From epitaxial growth of ferrite thin films to spin-polarized tunnelling. *Journal of Physics D: Applied Physics* **2013**, *46*, 143001.

[74] Vaz, C. A. F.; Hoffman, J.; Ahn, C. H.; Ramesh, R. Magnetoelectric Coupling Effects in Multiferroic Complex Oxide Composite Structures. *Advanced Materials* **2010**, *22*, 2900–2918.

[75] Yang, X.; Zhou, Z.; Nan, T.; Gao, Y.; Yang, G. M.; Liu, M.; Sun, N. X. Recent advances in multiferroic oxide heterostructures and devices. *Journal of Materials Chemistry C* **2016**, *4*, 234–243.

[76] Song, C.; Cui, B.; Li, F.; Zhou, X.; Pan, F. Recent progress in voltage control of magnetism: Materials, mechanisms, and performance. *Progress in Materials Science* **2017**, *87*, 33–82.

[77] Chen, X.; Zhu, X.; Xiao, W.; Liu, G.; Feng, Y. P.; Ding, J.; Li, R.-W. Nanoscale Magnetization Reversal Caused by Electric Field-Induced Ion Migration and Redistribution in Cobalt Ferrite Thin Films. *ACS Nano* **2015**, *9*, 4210–4218.

[78] Dhanapal, P.; Guo, S.; Wang, B.; Yang, H.; Agarwal, S.; Zhan, Q.; Li, R.-W. High-throughput investigation of orientations effect on nanoscale magnetization reversal in cobalt ferrite thin films induced by electric field. *Applied Physics Letters* **2017**, *111*, 162401.

[79] Robbennolt, S.; Menéndez, E.; Quintana, A.; Gómez, A.; Auffret, S.; Baltz, V.; Pellicer, E.; Sort, J. Reversible, Electric-Field Induced Magneto-Ionic Control of Magnetism in Mesoporous Cobalt Ferrite Thin Films. *Scientific Reports* **2019**, *9*, 10804.

[80] Hu, W.; Qin, N.; Wu, G.; Lin, Y.; Li, S.; Bao, D. Opportunity of Spinel Ferrite Materials in Nonvolatile Memory Device Applications Based on Their Resistive Switching Performances. *Journal of the American Chemical Society* **2012**, *134*, 14658–14661.

[81] Hu, W.; Zou, L.; Chen, R.; Xie, W.; Chen, X.; Qin, N.; Li, S.; Yang, G.; Bao, D. Resistive switching properties and physical mechanism of cobalt ferrite thin films. *Applied Physics Letters* **2014**, *104*, 143502.

[82] Munjal, S.; Khare, N. Valence Change Bipolar Resistive Switching Accompanied With Magnetization Switching in $CoFe_2O_4$ Thin Film. *Scientific Reports* **2017**, *7*, 12427.

[83] Verwey, E. Electronic conduction of magnetite (Fe_3O_4) and its transition point at low temperatures. *Nature* **1939**, *144*, 327–328.

[84] Verwey, E.; Haayman, P. Electronic conductivity and transition point of magnetite ("Fe_3O_4"). *Physica* **1941**, *8*, 979–987.

[85] Verwey, E. J.; Haayman, P. W.; Romeijn, F. C. Physical Properties and Cation Arrangement of Oxides with Spinel Structures II. Electronic Conductivity. *The Journal of Chemical Physics* **1947**, *15*, 181–187.

[86] Senn, M. S.; Wright, J. P.; Attfield, J. P. Charge order and three-site distortions in the Verwey structure of magnetite. *Nature* **2012**, *481*, 173–176.

[87] Shmakov, A.; Kryukova, G.; Tsybulya, S.; Chuvilin, A.; Solovyeva, L. Vacancy ordering in γ-Fe_2O_3: Synchrotron X-ray powder diffraction and high-resolution electron microscopy studies. *Journal of Applied Crystallography* **1995**, *28*, 141–145.

[88] Jørgensen, J.-E.; Mosegaard, L.; Thomsen, L. E.; Jensen, T. R.; Hanson, J. C. Formation of γ-Fe_2O_3 nanoparticles and vacancy ordering: An in situ X-ray powder diffraction study. *Journal of Solid State Chemistry* **2007**, *180*, 180–185.

[89] Grau-Crespo, R.; Al-Baitai, A. Y.; Saadoune, I.; De Leeuw, N. H. Vacancy ordering and electronic structure of γ-Fe_2O_3 (maghemite): a theoretical investigation. *Journal of Physics: Condensed Matter* **2010**, *22*, 255401.

[90] Zheng, H. et al. Multiferroic $BaTiO_3$-$CoFe_2O_4$ Nanostructures. *Science* **2004**, *303*, 661–663.

[91] Carta, D.; Casula, M. F.; Falqui, A.; Loche, D.; Mountjoy, G.; Sangregorio, C.; Corrias, A. A Structural and Magnetic Investigation of the Inversion Degree in Ferrite Nanocrystals MFe_2O_4 (M = Mn, Co, Ni). *The Journal of Physical Chemistry C* **2009**, *113*, 8606–8615.

[92] Sawatzky, G. A.; Van Der Woude, F.; Morrish, A. H. Mössbauer Study of Several Ferrimagnetic Spinels. *Physical Review* **1969**, *187*, 747–757.

[93] Aghavnian, T.; Moussy, J.-B.; Stanescu, D.; Belkhou, R.; Jedrecy, N.; Magnan, H.; Ohresser, P.; Arrio, M.-A.; Sainctavit, P.; Barbier, A. Determination of the cation site distribution of the spinel in multiferroic $CoFe_2O_4/BaTiO_3$ layers by X-ray photoelectron spectroscopy. *Journal of Electron Spectroscopy and Related Phenomena* **2015**, *202*, 16–21.

[94] Jedrecy, N.; Aghavnian, T.; Moussy, J.-B.; Magnan, H.; Stanescu, D.; Portier, X.; Arrio, M.-A.; Mocuta, C.; Vlad, A.; Belkhou, R.; Ohresser, P.; Barbier, A. Cross-Correlation between Strain, Ferroelectricity, and Ferromagnetism in Epitaxial Multiferroic $CoFe_2O_4/BaTiO_3$ Heterostructures. *ACS Applied Materials & Interfaces* **2018**, *10*, 28003–28014.

[95] Martin, E. et al. Non-auxetic/auxetic transitions inducing modifications of the magnetic anisotropy in $CoFe_2O_4$ thin films. *Journal of Alloys and Compounds* **2020**, *836*, 155425.

[96] Lüders, U.; Barthélémy, A.; Bibes, M.; Bouzehouane, K.; Fusil, S.; Jacquet, E.; Contour, J.-P.; Bobo, J.-F.; Fontcuberta, J.; Fert, A. $NiFe_2O_4$: A Versatile Spinel Material Brings New Opportunities for Spintronics. *Advanced Materials* **2006**, *18*, 1733–1736.

[97] Dey, J. K.; Chatterjee, A.; Majumdar, S.; Dippel, A.-C.; Gutowski, O.; Zimmermann, M. v.; Giri, S. Ferroelectric order associated with ordered occupancy at the octahedral site of the inverse spinel structure of multiferroic $NiFe_2O_4$. *Physical Review B* **2019**, *99*, 144412.

[98] NV, S.; Vinayakumar, K.; Nagaraja, K. Magnetoelectric coupling in bismuth ferrite—challenges and perspectives. *Coatings* **2020**, *10*, 1221.

[99] Eerenstein, W.; Mathur, N. D.; Scott, J. F. Multiferroic and magnetoelectric materials. *Nature* **2006**, *442*, 759–765.

[100] Fiebig, M.; Lottermoser, T.; Meier, D.; Trassin, M. The evolution of multiferroics. *Nature Reviews Materials* **2016**, *1*, 16046.

[101] Debye, P. Bemerkung zu einigen neuen Versuchen über einen magneto-elektrischen Richteffekt. *Zeitschrift für Physik* **1926**, *36*, 300–301.

[102] E., D. I. On the magneto-electrical effects in antiferromagnets. *Soviet Physics JETP* **1960**, *10*, 628–629.

[103] Fiebig, M. Revival of the magnetoelectric effect. *Journal of Physics D: Applied Physics* **2005**, *38*, R123.

[104] Bibes, M.; Barthélémy, A. Oxide Spintronics. *IEEE Transactions on Electron Devices* **2007**, *54*, 1003–1023.

[105] Bibes, M.; Barthélémy, A. Towards a magnetoelectric memory. *Nature materials* **2008**, *7*, 425–426.

[106] Manipatruni, S.; Nikonov, D. E.; Lin, C.-C.; Gosavi, T. A.; Liu, H.; Prasad, B.; Huang, Y.-L.; Bonturim, E.; Ramesh, R.; Young, I. A. Scalable energy-efficient magnetoelectric spin–orbit logic. *Nature* **2019**, *565*, 35–42.

[107] Wang, J.; Chen, A.; Li, P.; Zhang, S. Magnetoelectric memory based on ferromagnetic/ferroelectric multiferroic heterostructure. *Materials* **2021**, *14*, 4623.

[108] Spaldin, N. A.; Ramesh, R. Advances in magnetoelectric multiferroics. *Nature materials* **2019**, *18*, 203–212.

[109] Hill, N. A. Why Are There so Few Magnetic Ferroelectrics? *The Journal of Physical Chemistry B* **2000**, *104*, 6694–6709.

[110] Lebeugle, D.; Colson, D.; Forget, A.; Viret, M. Very large spontaneous electric polarization in $BiFeO_3$ single crystals at room temperature and its evolution under cycling fields. *Applied Physics Letters* **2007**, *91*, 022907.

[111] Spaldin, N. A.; Cheong, S.-W.; Ramesh, R. Multiferroics: Past, present, and future. *Physics Today* **2010**, *63*, 38–43.

[112] Niranjan, M. K.; Velev, J. P.; Duan, C.-G.; Jaswal, S. S.; Tsymbal, E. Y. Magnetoelectric effect at the $Fe_3O_4/BaTiO_3$ (001) interface: A first-principles study. *Physical Review B* **2008**, *78*, 104405.

[113] Tamerd, M. A.; Abraime, B.; Lahmar, A.; El Marssi, M.; Hamedoun, M.; Benyoussef, A.; El Kenz, A. Magnetoelectric coupling at the $NiFe_2O_4$/PZT (001) interface: A density functional theory investigation. *Superlattices and Microstructures* **2020**, *139*, 106401.

[114] Hickmott, T. Low-frequency negative resistance in thin anodic oxide films. *Journal of Applied Physics* **1962**, *33*, 2669–2682.

[115] Chua, L. Memristor-the missing circuit element. *IEEE Transactions on circuit theory* **1971**, *18*, 507–519.

[116] Strukov, D. B.; Snider, G. S.; Stewart, D. R.; Williams, R. S. The missing memristor found. *nature* **2008**, *453*, 80–83.

[117] Yang, J. J.; Pickett, M. D.; Li, X.; Ohlberg, D. A.; Stewart, D. R.; Williams, R. S. Memristive switching mechanism for metal/oxide/metal nanodevices. *Nature nanotechnology* **2008**, *3*, 429–433.

[118] Ielmini, D. Resistive switching memories based on metal oxides: mechanisms, reliability and scaling. *Semiconductor Science and Technology* **2016**, *31*, 063002.

[119] Shi, T.; Wang, R.; Wu, Z.; Sun, Y.; An, J.; Liu, Q. A review of resistive switching devices: performance improvement, characterization, and applications. *Small Structures* **2021**, *2*, 2000109.

[120] Kamble, G. U.; Patil, A. P.; Kamat, R. K.; Kim, J. H.; Dongale, T. D. Promising Materials and Synthesis Methods for Resistive Switching Memory Devices: A Status Review. *ACS Applied Electronic Materials* **2023**, *5*, 2454–2481.

[121] Attfield, J. P. Magnetism and the trimeron bond. *Chemistry of Materials* **2022**, *34*, 2877–2885.

[122] Antonov, V. N.; Harmon, B. N.; Yaresko, A. N. Electronic structure and x-ray magnetic circular dichroism in Fe_3O_4 and Mn-, Co-, or Ni-substituted Fe_3O_4. *Physical Review B* **2003**, *67*, 024417.

[123] Szotek, Z.; Temmerman, W. M.; Ködderitzsch, D.; Svane, A.; Petit, L.; Winter, H. Electronic structures of normal and inverse spinel ferrites from first principles. *Physical Review B* **2006**, *74*, 174431.

[124] Walsh, A.; Wei, S.-H.; Yan, Y.; Al-Jassim, M. M.; Turner, J. A.; Woodhouse, M.; Parkinson, B. A. Structural, magnetic, and electronic properties of the Co-Fe-Al oxide spinel system: Density-functional theory calculations. *Physical Review B* **2007**, *76*, 165119.

[125] Hou, Y. H.; Zhao, Y. J.; Liu, Z. W.; Yu, H. Y.; Zhong, X. C.; Qiu, W. Q.; Zeng, D. C.; Wen, L. S. Structural, electronic and magnetic properties of partially inverse spinel $CoFe_2O_4$: a first-principles study. *Journal of Physics D: Applied Physics* **2010**, *43*, 445003.

[126] Fritsch, D.; Ederer, C. Effect of epitaxial strain on the cation distribution in spinel ferrites $CoFe_2O_4$ and $NiFe_2O_4$: A density functional theory study. *Applied Physics Letters* **2011**, *99*, 081916.

[127] Meinert, M.; Reiss, G. Electronic structure and optical band gap determination of $NiFe_2O_4$. *Journal of Physics: Condensed Matter* **2014**, *26*, 115503.

[128] Odkhuu, D.; Taivansaikhan, P.; Yun, W. S.; Hong, S. C. A first-principles study of magnetostrictions of Fe_3O_4 and $CoFe_2O_4$. *Journal of Applied Physics* **2014**, *115*, 17A916.

[129] Jong, U.-G.; Yu, C.-J.; Park, Y.-S.; Ri, C.-S. First-principles study of ferroelectricity induced by p–d hybridization in ferrimagnetic $NiFe_2O_4$. *Physics Letters A* **2016**, *380*, 3302–3306.

[130] Ulpe, A. C.; Bauerfeind, K. C. L.; Bredow, T. Influence of Spin State and Cation Distribution on Stability and Electronic Properties of Ternary Transition-Metal Oxides. *ACS Omega* **2019**, *4*, 4138–4146.

[131] Sharifi, S.; Yazdani, A.; Rahimi, K. Incremental substitution of Ni with Mn in $NiFe_2O_4$ to largely enhance its supercapacitance properties. *Scientific Reports* **2020**, *10*, 10916.

[132] Pénicaud, M.; Siberchicot, B.; Sommers, C.; Kübler, J. Calculated electronic band structure and magnetic moments of ferrites. *Journal of Magnetism and Magnetic Materials* **1992**, *103*, 212–220.

[133] Cario, L.; Vaju, C.; Corraze, B.; Guiot, V.; Janod, E. Electric-field-induced resistive switching in a family of Mott insulators: Towards a new class of RRAM memories. *Advanced Materials* **2010**, *22*, 5193–5197.

[134] Chen, J.; Mao, W.; Gao, L.; Yan, F.; Yajima, T.; Chen, N.; Chen, Z.; Dong, H.; Ge, B.; Zhang, P., et al. Electron-Doping Mottronics in Strongly Correlated Perovskite. *Advanced Materials* **2020**, *32*, 1905060.

[135] Ohtomo, A.; Hwang, H. A high-mobility electron gas at the $LaAlO_3/SrTiO_3$ heterointerface. *Nature* **2004**, *427*, 423–426.

[136] Biscaras, J.; Bergeal, N.; Kushwaha, A.; Wolf, T.; Rastogi, A.; Budhani, R. C.; Lesueur, J. Two-dimensional superconductivity at a Mott insulator/band insulator interface $LaTiO_3/SrTiO_3$. *Nature communications* **2010**, *1*, 89.

[137] Choi, W. S.; Lee, S. A.; You, J. H.; Lee, S.; Lee, H. N. Resonant tunnelling in a quantum oxide superlattice. *Nature communications* **2015**, *6*, 7424.

[138] Ohtomo, A.; Muller, D.; Grazul, J.; Hwang, H. Y. Artificial charge-modulationin atomic-scale perovskite titanate superlattices. *nature* **2002**, *419*, 378–380.

[139] Veit, M.; Arras, R.; Ramshaw, B.; Pentcheva, R.; Suzuki, Y. Nonzero Berry phase in quantum oscillations from giant Rashba-type spin splitting in $LaTiO_3/SrTiO_3$ heterostructures. *Nature communications* **2018**, *9*, 1458.

[140] Annadi, A.; Putra, A.; Liu, Z.; Wang, X.; Gopinadhan, K.; Huang, Z.; Dhar, S.; Venkatesan, T., et al. Electronic correlation and strain effects at the interfaces between polar and nonpolar complex oxides. *Physical Review B* **2012**, *86*, 085450.

[141] Perna, P.; Maccariello, D.; Radovic, M.; Scotti di Uccio, U.; Pallecchi, I.; Codda, M.; Marré, D.; Cantoni, C.; Gazquez, J.; Varela, M., et al. Conducting interfaces between band insulating oxides: The $LaGaO_3/SrTiO_3$ heterostructure. *Applied Physics Letters* **2010**, *97*, 152111.

[142] Thiel, S.; Hammerl, G.; Schmehl, A.; Schneider, C. W.; Mannhart, J. Tunable quasi-two-dimensional electron gases in oxide heterostructures. *Science* **2006**, *313*, 1942–1945.

[143] Yamada, Y.; Sato, H. K.; Hikita, Y.; Hwang, H. Y.; Kanemitsu, Y. Spatial density profile of electrons near the $LaAlO_3/SrTiO_3$ heterointerface revealed by time-resolved photoluminescence spectroscopy. *Applied Physics Letters* **2014**, *104*, 151907.

[144] Dubroka, A.; Rössle, M.; Kim, K. W.; Malik, V. K.; Schultz, L.; Thiel, S.; Schneider, C. W.; Mannhart, J.; Herranz, G.; Copie, O., et al. Dynamical response and confinement of the electrons at the $LaAlO_3/SrTiO_3$ interface. *Physical review letters* **2010**, *104*, 156807.

[145] Basletic, M.; Maurice, J.-L.; Carrétéro, C.; Herranz, G.; Copie, O.; Bibes, M.; Jacquet, É.; Bouzehouane, K.; Fusil, S.; Barthélémy, A. Mapping the spatial distribution of charge carriers in $LaAlO_3/SrTiO_3$ heterostructures. *Nature materials* **2008**, *7*, 621–625.

[146] Fix, T.; Schoofs, F.; MacManus-Driscoll, J.; Blamire, M. Charge confinement and doping at $LaAlO_3/SrTiO_3$ interfaces. *Physical review letters* **2009**, *103*, 166802.

[147] Rubi, K.; Gosteau, J.; Serra, R.; Han, K.; Zeng, S.; Huang, Z.; Warot-Fonrose, B.; Arras, R.; Snoeck, E.; Ariando, et al. Aperiodic quantum oscillations in the two-dimensional electron gas at the $LaAlO_3/SrTiO_3$ interface. *Npj Quantum Materials* **2020**, *5*, 9.

[148] Huijben, M.; Rijnders, G.; Blank, D. H.; Bals, S.; Aert, S. V.; Verbeeck, J.; Tendeloo, G. V.; Brinkman, A.; Hilgenkamp, H. Electronically coupled complementary interfaces between perovskite band insulators. *Nature materials* **2006**, *5*, 556–560.

[149] Caviglia, A.; Gariglio, S.; Cancellieri, C.; Sacépé, B.; Fete, A.; Reyren, N.; Gabay, M.; Morpurgo, A.; Triscone, J.-M. Two-dimensional quantum oscillations of the conductance at $LaAlO_3/SrTiO_3$ interfaces. *Physical review letters* **2010**, *105*, 236802.

[150] Huang, Z.; Han, K.; Zeng, S.; Motapothula, M.; Borisevich, A. Y.; Ghosh, S.; Lü, W.; Li, C.; Zhou, W.; Liu, Z., et al. The effect of polar fluctuation and lattice mismatch on carrier mobility at oxide interfaces. *Nano letters* **2016**, *16*, 2307–2313.

[151] Arras, R.; Ruiz, V. G.; Pickett, W. E.; Pentcheva, R. Tuning the two-dimensional electron gas at the $LaAlO_3/SrTiO_3(001)$ interface by metallic contacts. *Phys. Rev. B* **2012**, *85*, 125404.

[152] Vaz, D. C.; Lesne, E.; Sander, A.; Naganuma, H.; Jacquet, E.; Santamaria, J.; Barthélémy, A.; Bibes, M. Tuning Up or Down the Critical Thickness in $LaAlO_3/SrTiO_3$ through In Situ Deposition of Metal Overlayers. *Advanced Materials* **2017**, *29*, 1700486.

[153] Yu, L.; Zunger, A. A polarity-induced defect mechanism for conductivity and magnetism at polar–nonpolar oxide interfaces. *Nature communications* **2014**, *5*, 5118.

[154] Ding, J.; Cheng, J.; Dogan, F.; Li, Y.; Lin, W.; Yao, Y.; Manchon, A.; Yang, K.; Wu, T. Two-Dimensional Electron Gas at the Spinel/Perovskite Interface: Suppression of Polar Catastrophe by an Ultrathin Layer of Interfacial Defects. *ACS Applied Materials & Interfaces* **2020**, *12*, 42982–42991.

[155] Rödel, T. C.; Fortuna, F.; Sengupta, S.; Frantzeskakis, E.; Fèvre, P. L.; Bertran, F.; Mercey, B.; Matzen, S.; Agnus, G.; Maroutian, T., et al. Universal fabrication of 2D electron systems in functional oxides. *Advanced Materials* **2016**, *28*, 1976–1980.

[156] Bogorin, D. F.; Irvin, P.; Cen, C.; Levy, J. In *Multifunctional Oxide Heterostructures*; Oxford University Press: 2012.

[157] Bogorin, D. F.; Irvin, P.; Cen, C.; Levy, J. $LaAlO_3/SrTiO_3$-based device concepts. *arXiv preprint arXiv:1011.5290* **2010**.

[158] Caviglia, A.; Gariglio, S.; Reyren, N.; Jaccard, D.; Schneider, T.; Gabay, M.; Thiel, S.; Hammerl, G.; Mannhart, J.; Triscone, J.-M. Electric field control of the $LaAlO_3/SrTiO_3$ interface ground state. *Nature* **2008**, *456*, 624–627.

[159] Jany, R.; Breitschaft, M.; Hammerl, G.; Horsche, A.; Richter, C.; Paetel, S.; Mannhart, J.; Stucki, N.; Reyren, N.; Gariglio, S., et al. Diodes with breakdown voltages enhanced by the metal-insulator transition of $LaAlO_3$–$SrTiO_3$ interfaces. *Applied Physics Letters* **2010**, *96*, 183504.

[160] Woltmann, C.; Harada, T.; Boschker, H.; Srot, V.; Van Aken, P.; Klauk, H.; Mannhart, J. Field-Effect Transistors with Submicrometer Gate Lengths Fabricated from $LaAlO_3$-$SrTiO_3$-Based Heterostructures. *Physical Review Applied* **2015**, *4*, 064003.

[161] Schneider, C. W.; Thiel, S.; Hammerl, G.; Richter, C.; Mannhart, J. Microlithography of electron gases formed at interfaces in oxide heterostructures. *Applied physics letters* **2006**, *89*, 122101.

[162] Bogorin, D. F.; Bark, C. W.; Jang, H. W.; Cen, C.; Folkman, C. M.; Eom, C.-B.; Levy, J. Nanoscale rectification at the $LaAlO_3/SrTiO_3$ interface. *Applied Physics Letters* **2010**, *97*, 013102.

[163] Caviglia, A.; Gabay, M.; Gariglio, S.; Reyren, N.; Cancellieri, C.; Triscone, J.-M. Tunable Rashba spin-orbit interaction at oxide interfaces. *Physical review letters* **2010**, *104*, 126803.

[164] Lesne, E.; Fu, Y.; Oyarzún, S.; Rojas-Sánchez, J. C.; Vaz, D.; Naganuma, H.; Sicoli, G.; Attané, J.-P.; Jamet, M.; Jacquet, E., et al. Highly efficient and tunable spin-to-charge conversion through Rashba coupling at oxide interfaces. *Nature materials* **2016**, *15*, 1261–1266.

[165] Chang, C. F.; Hu, Z.; Klein, S.; Liu, X. H.; Sutarto, R.; Tanaka, A.; Cezar, J. C.; Brookes, N. B.; Lin, H.-J.; Hsieh, H. H.; Chen, C. T.; Rata, A. D.; Tjeng, L. H. Dynamic Atomic Reconstruction: How Fe_3O_4 Thin Films Evade Polar Catastrophe for Epitaxy. *Physical Review X* **2016**, *6*, 041011.

[166] Arras, R.; Calmels, L. Fully spin-polarized two-dimensional electron gas at the $CoFe_2O_4/MgAl_2O_4(001)$ polar interface. *Physical Review B* **2014**, *90*, 045411.

[167] Cheng, B.; Qin, H.; Liu, L.; Xie, J.; Hu, J. Mechanism of polar catastrophe cancelling induced by charge compensation for epitaxy γ-Fe_2O_3 film on MgO(001) substrate: A theoretical investigation. *Superlattices and Microstructures* **2018**, *120*, 377–381.

[168] Chen, Y.; Bovet, N.; Trier, F.; Christensen, D.; Qu, F.; Andersen, N. H.; Kasama, T.; Zhang, W.; Giraud, R.; Dufouleur, J., et al. A high-mobility two-dimensional electron gas at the spinel/perovskite interface of γ-$Al_2O_3/SrTiO_3$. *Nature communications* **2013**, *4*, 1371.

[169] Chen, X.-H.; Hu, Z.-X.; Gao, K.-H.; Li, Z.-Q. High-mobility two-dimensional electron gas in $\gamma-Al_2O_3/SrTiO_3$ heterostructures. *Phys. Rev. B* **2022**, *105*, 205437.

[170] Kormondy, K. J.; Posadas, A. B.; Ngo, T. Q.; Lu, S.; Goble, N.; Jordan-Sweet, J.; Gao, X. P. A.; Smith, D. J.; McCartney, M. R.; Ekerdt, J. G.; Demkov, A. A. Quasi-two-dimensional electron gas at the epitaxial alumina/$SrTiO_3$ interface: Control of oxygen vacancies. *Journal of Applied Physics* **2015**, *117*, 095303.

[171] Schütz, P.; Pfaff, F.; Scheiderer, P.; Chen, Y. Z.; Pryds, N.; Gorgoi, M.; Sing, M.; Claessen, R. Band bending and alignment at the spinel/perovskite $\gamma-Al_2O_3/SrTiO_3$ heterointerface. *Phys. Rev. B* **2015**, *91*, 165118.

[172] Ielmini, D.; Spiga, S.; Nardi, F.; Cagli, C.; Lamperti, A.; Cianci, E.; Fanciulli, M. Scaling analysis of submicrometer nickel-oxide-based resistive switching memory devices. *Journal of Applied Physics* **2011**, *109*, 034506.

[173] Mehonic, A.; Vrajitoarea, A.; Cueff, S.; Hudziak, S.; Howe, H.; Labbé, C.; Rizk, R.; Pepper, M.; Kenyon, A. J. Quantum Conductance in Silicon Oxide Resistive Memory Devices. *Scientific Reports* **2013**, *3*, 2708.

[174] Tong, S.-K.; Chang, J.-H.; Hao, Y.-H.; Wu, M.-R.; Wei, D.-H.; Chueh, Y.-L. Optimum resistive switching characteristics of $NiFe_2O_4$ by controlling film thickness. *Applied Surface Science* **2021**, *564*, 150091.

[175] Munjal, S.; Khare, N. Compliance current controlled volatile and nonvolatile memory in Ag/$CoFe_2O_4$/Pt resistive switching device. *Nanotechnology* **2021**, *32*, 185204.

[176] Li, J.; Yao, C.; Huang, W.; Qin, N.; Bao, D. Highly uniform resistive switching properties of $NiFe_2O_4$ films by embedding well-ordered pyramid-shaped Pt/Au nanostructures. *Journal of Alloys and Compounds* **2022**, *890*, 161814.

[177] Aghavnian, T. Couplages magnéto-électriques dans le système multiferroïque artificiel : $BaTiO_3/CoFe_2O_4$, Theses, Université Paris Saclay (ComUE), 2016.

[178] Schrödinger, E. An Undulatory Theory of the Mechanics of Atoms and Molecules. *Phys. Rev.* **1926**, *28*, 1049–1070.

[179] Born, M.; Oppenheimer, R. Zur Quantentheorie der Molekeln. *Annalen der Physik* **1927**, *389*, 457–484.

[180] Hartree, D. R. In *Mathematical Proceedings of the Cambridge Philosophical Society*, 1928; Vol. 24, pp 111–132.

[181] Hohenberg, P.; Kohn, W. Inhomogeneous Electron Gas. *Phys. Rev.* **1964**, *136*, B864–B871.

[182] Kohn, W.; Sham, L. J. Self-Consistent Equations Including Exchange and Correlation Effects. *Phys. Rev.* **1965**, *140*, A1133–A1138.

[183] Becke, A. D. Perspective: Fifty years of density-functional theory in chemical physics. *The Journal of chemical physics* **2014**, *140*, 18A301.

[184] Perdew, J. P.; Chevary, J. A.; Vosko, S. H.; Jackson, K. A.; Pederson, M. R.; Singh, D. J.; Fiolhais, C. Atoms, molecules, solids, and surfaces: Applications of the generalized gradient approximation for exchange and correlation. *Phys. Rev. B* **1992**, *46*, 6671–6687.

[185] Perdew, J. P.; Burke, K.; Ernzerhof, M. Generalized gradient approximation made simple. *Physical review letters* **1996**, *77*, 3865–3868.

[186] Perdew, J. P.; Ruzsinszky, A.; Csonka, G. I.; Vydrov, O. A.; Scuseria, G. E.; Constantin, L. A.; Zhou, X.; Burke, K. Restoring the density-gradient expansion for exchange in solids and surfaces. *Physical review letters* **2008**, *100*, 136406.

[187] Jones, R. O. Density Functional Theory: Past, present, ... future? *Psi-K Scientific Highlight of the month* **2014**, *124*.

[188] Perdew, J. P.; Schmidt, K. Jacob's ladder of density functional approximations for the exchange-correlation energy. *AIP Conference Proceedings* **2001**, *577*, 1–20.

[189] Anisimov, V. I.; Zaanen, J.; Andersen, O. K. Band theory and Mott insulators: Hubbard U instead of Stoner I. *Physical Review B* **1991**, *44*, 943–954.

[190] Himmetoglu, B.; Floris, A.; de Gironcoli, S.; Cococcioni, M. Hubbard-corrected DFT energy functionals: The LDA+U description of correlated systems. *International Journal of Quantum Chemistry* **2014**, *114*, 14–49.

[191] Dudarev, S. L.; Botton, G. A.; Savrasov, S. Y.; Humphreys, C. J.; Sutton, A. P. Electron-energy-loss spectra and the structural stability of nickel oxide: An LSDA+U study. *Physical Review B* **1998**, *57*, 1505–1509.

[192] Kresse, G.; Furthmüller, J. Efficient iterative schemes for ab initio total-energy calculations using a plane-wave basis set. *Phys. Rev. B* **1996**, *54*, 11169–11186.

[193] Kresse, G.; Joubert, D. From ultrasoft pseudopotentials to the projector augmented-wave method. *Phys. Rev. B* **1999**, *59*, 1758–1775.

[194] Stevanović, V.; Lany, S.; Zhang, X.; Zunger, A. Correcting density functional theory for accurate predictions of compound enthalpies of formation: Fitted elemental-phase reference energies. *Physical Review B* **2012**, *85*, 115104.

[195] Freysoldt, C.; Grabowski, B.; Hickel, T.; Neugebauer, J.; Kresse, G.; Janotti, A.; Van De Walle, C. G. First-principles calculations for point defects in solids. *Reviews of Modern Physics* **2014**, *86*, 253–305.

[196] Péan, E.; Vidal, J.; Jobic, S.; Latouche, C. Presentation of the PyDEF post-treatment Python software to compute publishable charts for defect energy formation. *Chemical Physics Letters* **2017**, *671*, 124–130.

[197] Kim, S.; Hood, S. N.; Park, J.-S.; Whalley, L. D.; Walsh, A. Quick-start guide for first-principles modelling of point defects in crystalline materials. *Journal of Physics: Energy* **2020**, *2*, 036001.

[198] Toriyama, M. Y.; Qu, J.; Gomes, L. C.; Ertekin, E. VTAnDeM: A Python Toolkit for Simultaneously Visualizing Phase Stability, Defect Energetics, and Carrier Concentrations of Materials. *Computer Physics Communications* **2023**, 108691.

[199] Lany, S.; Zunger, A. Accurate prediction of defect properties in density functional supercell calculations. *Modelling and Simulation in Materials Science and Engineering* **2009**, *17*, 084002.

[200] Makov, G.; Payne, M. C. Periodic boundary conditions in *ab initio* calculations. *Physical Review B* **1995**, *51*, 4014–4022.

[201] Stoliaroff, A.; Jobic, S.; Latouche, C. PyDEF 2.0: An Easy to Use Post-treatment Software for Publishable Charts Featuring a Graphical User Interface. *Journal of Computational Chemistry* **2018**, *39*, 2251–2261.

[202] Kosyak, V.; Mortazavi Amiri, N. B.; Postnikov, A. V.; Scarpulla, M. A. Model of native point defect equilibrium in Cu_2ZnSnS_4 and application to one-zone annealing. *Journal of Applied Physics* **2013**, *114*, 124501.

[203] Geneste, G.; Paillard, C.; Dkhil, B. Polarons, vacancies, vacancy associations, and defect states in multiferroic $BiFeO_3$. *Physical Review B* **2019**, *99*, 024104.

[204] Krasikov, D.; Knizhnik, A.; Potapkin, B.; Sommerer, T. Why shallow defect levels alone do not cause high resistivity in CdTe. *Semiconductor Science and Technology* **2013**, *28*, 125019.

[205] Heifets, E.; Kotomin, E. A.; Mastrikov, Y. A.; Piskunov, S.; Maier, J., *Thermodynamics of ABO_3-Type Perovskite Surfaces*; Moreno-Pirajan, J. C., Ed.; IntechOpen: Rijeka, 2011; Chapter 19.

[206] Wang, V.; Xu, N.; Liu, J.-C.; Tang, G.; Geng, W.-T. VASPKIT: A user-friendly interface facilitating high-throughput computing and analysis using VASP code. *Computer Physics Communications* **2021**, *267*, 108033.

[207] Huang, J.-R.; Cheng, C. Cation and magnetic orders in $MnFe_2O_4$ from density functional calculations. *Journal of Applied Physics* **2013**, *113*, 033912.

[208] Ivanov, V. G.; Abrashev, M. V.; Iliev, M. N.; Gospodinov, M. M.; Meen, J.; Aroyo, M. I. Short-range B-site ordering in the inverse spinel ferrite $NiFe_2O_4$. *Physical Review B* **2010**, *82*, 024104.

[209] Aroyo, M. I.; Perez-Mato, J. M.; Capillas, C.; Kroumova, E.; Ivantchev, S.; Madariaga, G.; Kirov, A.; Wondratschek, H. Bilbao Crystallographic Server: I. Databases and crystallographic computing programs. *Zeitschrift für Kristallographie - Crystalline Materials* **2006**, *221*, 15–27.

[210] Anderson, P. W. Ordering and Antiferromagnetism in Ferrites. *Physical Review* **1956**, *102*, 1008–1013.

[211] Jeng, H.-T.; Guo, G. Y.; Huang, D. J. Charge-orbital ordering in low-temperature structures of magnetite: GGA + U investigations. *Physical Review B* **2006**, *74*, 195115.

[212] Stevanović, V.; d'Avezac, M.; Zunger, A. Universal Electrostatic Origin of Cation Ordering in A_2BO_4 Spinel Oxides. *Journal of the American Chemical Society* **2011**, *133*, 11649–11654.

[213] Liu, J.; Wang, X.; Borkiewicz, O. J.; Hu, E.; Xiao, R.-J.; Chen, L.; Page, K. Unified View of the Local Cation-Ordered State in Inverse Spinel Oxides. *Inorganic Chemistry* **2019**, *58*, 14389–14402.

[214] Li, Z.; Lu, J.; Jin, L.; Rusz, J.; Kocevski, V.; Yanagihara, H.; Kita, E.; Mayer, J.; Dunin-Borkowski, R. E.; Xiang, H.; Zhong, X. Atomic Structure and Electron Magnetic Circular Dichroism of Individual Rock Salt Structure Antiphase Boundaries in Spinel Ferrites. *Advanced Functional Materials* **2021**, *31*, 2008306.

[215] Haas, C. Phase transitions in crystals with the spinel structure. *Journal of Physics and Chemistry of Solids* **1965**, *26*, 1225–1232.

[216] Burdett, J. K.; Price, G. D.; Price, S. L. Role of the crystal-field theory in determining the structures of spinels. *Journal of the American Chemical Society* **1982**, *104*, 92–95.

[217] Verwey, E. J. W.; De Boer, F.; Van Santen, J. H. Cation Arrangement in Spinels. *The Journal of Chemical Physics* **1948**, *16*, 1091–1092.

[218] Miller, A. Distribution of Cations in Spinels. *Journal of Applied Physics* **1959**, *30*, S24–S25.

[219] Stevanović, V.; d'Avezac, M.; Zunger, A. Simple Point-Ion Electrostatic Model Explains the Cation Distribution in Spinel Oxides. *Physical Review Letters* **2010**, *105*, 075501.

[220] O'Neill, H. S. C.; Navrotsky, A. Simple spinels; crystallographic parameters, cation radii, lattice energies, and cation distribution. *American Mineralogist* **1983**, *68*, 181–194.

[221] Seko, A.; Oba, F.; Tanaka, I. Classification of spinel structures based on first-principles cluster expansion analysis. *Physical Review B* **2010**, *81*, 054114.

[222] Fang, Y.; Zhang, S.; Ohodnicki, P. R.; Wang, G. Relation between cation distribution and chemical bonds in spinel $NiFe_2O_4$. *Materials Today Communications* **2022**, *33*, 104436.

[223] Navrotsky, A.; Kleppa, O. The thermodynamics of cation distributions in simple spinels. *Journal of Inorganic and Nuclear Chemistry* **1967**, *29*, 2701–2714.

[224] Seminovski, Y.; Palacios, P.; Wahnón, P.; Grau-Crespo, R. Band gap control via tuning of inversion degree in $CdIn_2S_4$ spinel. *Applied Physics Letters* **2012**, *100*, 102112.

[225] Santos-Carballal, D.; Roldan, A.; Grau-Crespo, R.; De Leeuw, N. H. First-principles study of the inversion thermodynamics and electronic structure of FeM_2X_4 (thio)spinels (M = Cr , Mn, Co, Ni; X = O , S). *Physical Review B* **2015**, *91*, 195106.

[226] Tielens, F.; Calatayud, M.; Franco, R.; Recio, J. M.; Pérez-Ramírez, J.; Minot, C. Periodic DFT Study of the Structural and Electronic Properties of Bulk $CoAl_2O_4$ Spinel. *The Journal of Physical Chemistry B* **2006**, *110*, 988–995.

[227] Okhotnikov, K.; Charpentier, T.; Cadars, S. Supercell program: a combinatorial structure-generation approach for the local-level modeling of atomic substitutions and partial occupancies in crystals. *Journal of Cheminformatics* **2016**, *8*, 17.

[228] Iliev, M. N.; Mazumdar, D.; Ma, J. X.; Gupta, A.; Rigato, F.; Fontcuberta, J. Monitoring *B*-site ordering and strain relaxation in $NiFe_2O_4$ epitaxial films by polarized Raman spectroscopy. *Phys. Rev. B* **2011**, *83*, 014108.

[229] Safi, R.; Ghasemi, A.; Shoja-Razavi, R.; Tavousi, M. The role of pH on the particle size and magnetic consequence of cobalt ferrite. *Journal of Magnetism and Magnetic Materials* **2015**, *396*, 288–294.

[230] Hunpratub, S.; Phokha, S.; Kidkhunthod, P.; Chanlek, N.; Chindaprasirt, P. The effect of cation distribution on the magnetic properties of $CoFe_2O_4$ nanoparticles. *Results in Physics* **2021**, *24*, 104112.

[231] Moya, C.; Fraile Rodríguez, A.; Escoda-Torroella, M.; García Del Muro, M.; Avula, S. R. V.; Piamonteze, C.; Batlle, X.; Labarta, A. Crucial Role of the Co Cations on the Destabilization of the Ferrimagnetic Alignment in Co-Ferrite Nanoparticles with Tunable Structural Defects. *The Journal of Physical Chemistry C* **2021**, *125*, 691–701.

[232] Lüders, U.; Bibes, M.; Bobo, J.-F.; Cantoni, M.; Bertacco, R.; Fontcuberta, J. Enhanced magnetic moment and conductive behavior in $NiFe_2O_4$ spinel ultrathin films. *Physical Review B* **2005**, *71*, 134419.

[233] Muhich, C. L.; Aston, V. J.; Trottier, R. M.; Weimer, A. W.; Musgrave, C. B. First-Principles Analysis of Cation Diffusion in Mixed Metal Ferrite Spinels. *Chemistry of Materials* **2016**, *28*, 214–226.

[234] Anjum, S.; Jaffari, G. H.; Rumaiz, A. K.; Rafique, M. S.; Shah, S. I. Role of vacancies in transport and magnetic properties of nickel ferrite thin films. *Journal of Physics D: Applied Physics* **2010**, *43*, 265001.

[235] Salazar-Tamayo, H.; Tellez, K. E. G.; Meneses, C. A. B. Cation Vacancies in $NiFe_2O_4$ During Heat Treatments at High Temperatures: Structural, Morphological and Magnetic Characterization. *Materials Research* **2019**, *22*.

[236] Arras, R.; Calmels, L.; Warot-Fonrose, B. Half-metallicity, magnetic moments, and gap states in oxygen-deficient magnetite for spintronic applications. *Applied Physics Letters* **2012**, *100*, 032403.

[237] Arras, R.; Warot-Fonrose, B.; Calmels, L. Electronic structure near cationic defects in magnetite. *Journal of Physics: Condensed Matter* **2013**, *25*, 256002.

[238] Shi, X.; Li, Y.-F.; Bernasek, S. L.; Selloni, A. Structure of the $NiFe_2O_4(001)$ surface in contact with gaseous O_2 and water vapor. *Surface Science* **2015**, *640*, 73–79.

[239] Wagman, D. D.; Evans, W. H.; Parker, V. B.; Schumm, R. H.; Halow, I.; Bailey, S. M.; Churney, K. L.; Nuttall, R. L. Erratum: The NBS tables of chemical thermodynamic properties. Selected values for inorganic and C1 and C2 organic substances in SI units [J. Phys. Chem. Ref. Data 11, Suppl. 2 (1982)]. *Journal of Physical and Chemical Reference Data* **1989**, *18*, 180–1812.

[240] Rák, Z.; O'Brien, C. J.; Brenner, D. W. First-principles investigation of boron defects in nickel ferrite spinel. *Journal of Nuclear Materials* **2014**, *452*, 446–452.

[241] Gutiérrez, D.; Foerster, M.; Fina, I.; Fontcuberta, J.; Fritsch, D.; Ederer, C. Dielectric response of epitaxially strained $CoFe_2O_4$ spinel thin films. *Physical Review B* **2012**, *86*, 125309.

[242] Shi, X.; Bernasek, S. L.; Selloni, A. Formation, Electronic Structure, and Defects of Ni Substituted Spinel Cobalt Oxide: a DFT+U Study. *The Journal of Physical Chemistry C* **2016**, *120*, 14892–14898.

[243] Boettger, J. C. Nonconvergence of surface energies obtained from thin-film calculations. *Physical Review B* **1994**, *49*, 16798–16800.

[244] Tasker, P. W. The stability of ionic crystal surfaces. *Journal of Physics C: Solid State Physics* **1979**, *12*, 4977.

[245] Goniakowski, J.; Finocchi, F.; Noguera, C. Polarity of oxide surfaces and nanostructures. *Reports on Progress in Physics* **2007**, *71*, 016501.

[246] Arras, R.; Gosteau, J.; Huang, D.; Nakamura, H.; Zhao, H. J.; Paillard, C.; Bellaiche, L. Spin-polarized electronic states and atomic reconstructions at antiperovskite $Sr_3SnO(001)$ polar surfaces. *Phys. Rev. B* **2021**, *104*, 045411.

[247] Noguera, C. Polar oxide surfaces. *Journal of Physics: Condensed Matter* **2000**, *12*, R367.

[248] Rushiti, A.; Hättig, C.; Wen, B.; Selloni, A. Structure and Reactivity of Pristine and Reduced Spinel $CoFe_2O_4$ (001)/(100) Surfaces. *The Journal of Physical Chemistry C* **2021**, *125*, 9774–9781.

[249] Osorio-Guillén, J.; Lany, S.; Barabash, S. V.; Zunger, A. Magnetism without Magnetic Ions: Percolation, Exchange, and Formation Energies of Magnetism-Promoting Intrinsic Defects in CaO. *Physical Review Letters* **2006**, *96*, 107203.

[250] Reuter, K.; Scheffler, M. Composition, structure, and stability of RuO_2 (110) as a function of oxygen pressure. *Physical Review B* **2001**, *65*, 035406.

[251] Handbook, R. Solubility Parameters of Organic Compounds C-732-733, 1979.

[252] Ahlawat, A.; Khan, A. A.; Deshmukh, P.; Shirolkar, M. M.; Satapathy, S.; Choudhary, R. J.; Phase, D. M. Effect field controlled magnetization in $NiFe_2O_4/SrRuO_3$/PMN-PT heterostructures for nonvolatile memory applications: XMCD study. *Applied Physics Letters* **2021**, *119*, 112902.

[253] Parkinson, G. S. Iron oxide surfaces. *Surface Science Reports* **2016**, *71*, 272–365.

[254] Ohnuma, T.; Kobayashi, T. X-ray absorption near edge structure simulation of $LiNi_{0.5}Co_{0.2}Mn_{0.3}O_2$ via first-principles calculation. *RSC Adv.* **2019**, *9*, 35655.

[255] Patel, R. K.; Patra, K.; Ojha, S. K.; Kumar, S.; Sarkar, S.; Saha, A.; Bhattacharya, N.; Freeland, J. W.; Kim J.-W. Philip J. Ryan, P. M. S. M. Hole doping in a negative charge transfer insulator. *Commun. Phys.* **2022**, *5*, 216.

[256] Dai, J.-Q.; Zhang, H.; Song, Y.-M. Interfacial electronic structure and magnetoelectric effect in M/$BaTiO_3$ (M=Ni, Fe) superlattices. *Journal of Magnetism and Magnetic Materials* **2012**, *324*, 3937–3943.

[257] Dai, J.-Q.; Song, Y.-M.; Zhang, H. Magnetoelectric coupling at the epitaxial Ni/$PbTiO_3$ heterointerface from first principles. *Physica B: Condensed Matter* **2015**, *456*, 383–387.

[258] Duan, C.-G.; Jaswal, S. S.; Tsymbal, E. Y. Predicted Magnetoelectric Effect in Fe/$BaTiO_3$ Multilayers: Ferroelectric Control of Magnetism. *Phys. Rev. Lett.* **2006**, *97*, 047201.

[259] Arras, R.; Sharma, K.; Calmels, L. Interplay between oxygen vacancies and cation ordering in the $NiFe_2O_4$ spinel ferrite. *J. Mater. Chem. C* **2024**, *12*, 556–561.

[260] Blöchl, P. E. Projector augmented-wave method. *Physical review B* **1994**, *50*, 17953.

[261] Ceperley, D. M.; Alder, B. J. Ground State of the Electron Gas by a Stochastic Method. *Phys. Rev. Lett.* **1980**, *45*, 566–569.

[262] Neugebauer, J.; Scheffler, M. Adsorbate-substrate and adsorbate-adsorbate interactions of Na and K adlayers on Al(111). *Phys. Rev. B* **1992**, *46*, 16067–16080.

Summary: During this thesis, we performed a numerical study of spinel ferrites MFe_2O_4 (M = Co, Ni) as potential materials for designing reconfigurable and energy-efficient electronic devices. Using first-principles calculations, we aimed at understanding the insulator-to-metal transition which can be induced experimentally by applying an electric field in the spinel ferrites interfaced with a ferroelectric perovskite ($BaTiO_3$). The current manuscript begins by an analysis of stoichiometric MFe_2O_4 bulk crystals properties, confirming that the inverse-spinel structure is the ground state and that cation disorder tends to decrease the band-gap width at the Fermi level. The investigation of structural defects in non-stoichiometric crystals reveals that certain substitutions or cation vacancies can induce hole conduction. The role of polar (001)-orientated surfaces in thin films is then examined, demonstrating how growth conditions stabilize metallic or insulating surfaces, influenced by atomic and electronic reconstructions and epitaxial strain. Preliminary results on a perfect $NiFe_2O_4/BaTiO_3$ interface are finally presented, showing the emergence of a significant magnetoelectric coupling and a reduction of the band-gap width at the interface.

Keywords: First-principles calculations (DFT), transition-metal oxides, insulator-to-metal transition, structural defects, surface/interface

---

Résumé : Au cours de cette thèse, nous avons réalisé une étude numérique de ferrites de structure spinelle MFe_2O_4 (M = Co, Ni) qui sont matériaux prometteurs pour la conception de dispositifs électroniques reconfigurables et efficaces sur le plan énergétique. En utilisant des calculs ab initio, nous avons cherché à comprendre la transition isolant-métal qui peut être induite expérimentalement en appliquant un champ électrique dans ces ferrites, lorsqu'elles sont interfacées avec un oxyde de structure pérovskite ferroélectrique ($BaTiO_3$). Le manuscrit de cette thèse commence par une analyse des propriétés des cristaux massifs de MFe_2O_4 stœchiométriques, confirmant que la structure spinelle inverse correspond à l'état fondamental et que le désordre des cations tend à diminuer la largeur de la bande interdite en énergie au niveau de Fermi. L'étude des défauts structuraux dans les cristaux non-stœchiométriques révèle que certaines substitutions ou lacunes cationiques peuvent induire une conduction de trous. Le rôle des surfaces polaires orientées (001) dans les couches minces est ensuite examiné, démontrant comment les conditions de croissance stabilisent des surfaces, métalliques ou isolantes en raison des reconstructions atomiques et électroniques et de la contrainte épitaxiale. Des résultats préliminaires obtenus suite à l'étude d'une interface parfaite $NiFe_2O_4/BaTiO_3$ sont finalement présentés, montrant l'émergence d'un couplage magnétoélectrique significatif et une forte réduction de la largeur de la bande interdite à l'interface.

Mots-clés: Calculs *ab initio*, oxydes de métaux de transition, transition métal-isolant, défauts structuraux, surface/interface